REPUBLIQUE ALGERIENNE DEMOCRATIQUE ET POPULAIRE

MINISTERE DE L'ENSEIGNEMENT SUPERIEUR ET DE LA RECHERCHE SCIENTIFIQUE

UNIVERSITE M'HAMED BOUGARA-BOUMERDES

Faculté des **S**ciences

Thèse de Doctorat

Filière : Chimie

Option : Chimie analytique

Présentée par

Mme MEGUELLATI-HAMIDOUCHE Zineb

Synthèse électrochimique de films d'hydroxydes doubles lamellaires sur un substrat métallique – application à l'environnement

Devant le jury :

Mme	BOUAZIZ-TERRACHET Souhila	Prof	UMBB	Présidente
Mme	GHEMMIT-DOULACHE Naima	Prof	UMBB	Directrice de thèse
M	TRARI Mohamed	Prof	USTHB	Examinateur
Mme	DJEBARRI Baya	MCA	UMBB	Examinatrice
M	LOUNICI Hakim	Prof	Univ-Bouira	Examinateur
Mme	BRAHIMI Razika	MCA	USTHB	Invitée

Année Universitaire : 2023/2024

PEOPLE'S DEMOCRATIC REPUBLIC OF ALGERIA

MINISTRY OF HIGHER EDUCATION AND SCIENTIFIC RESEARCH

University of M'hamed Bougara-Boumerdes

Faculty of Sciences

Doctoral thesis

Branch: Chemistry
Option: Analytical chemistry

Presented by

Mme MEGUELLATI-HAMIDOUCHE Zineb

Electrochemical synthesis of lamellar double hydroxide films on a metallic substrate – application to the environment

---

Jury:

Mme	BOUAZIZ-TERRACHET Souhila	Prof	UMBB	President
Mme	GHEMMIT-DOULACHE Naima	Prof	UMBB	Supervisor
Mr	TRARI Mohamed	Prof	USTHB	Examinator
Mme	DJEBARRI Baya	MCA	UMBB	Examinator
Mr	LOUNICI Hakim	Prof	Univ-Bouira	Examinator
Mme	BRAHIMI Razika	MCA	USTHB	Guest

Academic year: 2023/2024

Dedication

"And my success can only come from Allah. In Him I trust, and unto Him I look" _{Quran 11 :88}

Success doesn't come by accident; it is the result of continuous effort, prominent energy, and endless determination.

Though the hurdles never come to an end, finding inspiration to keep positive in the darkest times might be even tougher than the work itself.

But life shows us inspiring situations as much as it puts obstacles in our way.

Along these lines

To those who dreamed of entering the campus but life didn't allow them to.

To those who sacrificed their educational careers for the sake of their families.

To those who ignite hope in others so they can keep going.

To those who didn't get the chance to study but are the source of inspiration for their kids to keep learning.

I dedicate this thesis.

Zineb. M

Acknowledgment

First and foremost, I would like to express my gratitude to Allah the Almighty for enabling me to acquire knowledge and patience, as I would not have completed this work without His assistance and mercy.

The research work that is the subject of this thesis was carried out at the Laboratory for Processing and Formatting of Fibrous Polymers (LTMFP) at the University of M'Hamed Bougara, Boumerdes, under the direction of Professor GHEMMIT Naima.

First of all, I would like to thank my supervisor, Professor GHEMMIT Naima, for the support during the realisation of the thesis, for the confidence she has put in me, and for the scientific guidance.

I cannot forget to thank Mme. Brahimi Razika, who has given me enthusiasm, guidance, and dedication. I would like to thank her for transmitting her passion for research.

I would like to thank all the Ph.D. students, personnel, and teachers of the laboratory of Processing and Formatting of Polymers, and to Pr. ALIOUCHE Djamel in particular.

I thank Mme. BOUAZIZ-TIRACHET Souhila, Professor at UMBB University, for giving me the honour of chairing the jury for this thesis. I also thank Mr. TRARI Mohamed, Professor at USTHB University, Mme. DJEBARRI Baya, Class A Lecturer at UMBB University, and Mr. LOUNICI Hakim, Professor at Bouira university, for giving me the honour to examine this thesis. I also want to express my gratitude to Prof. HALFAOUI Rachid, who was supposed to be on the committee but was unable to attend due to health concerns.

A special thanks to the Ph.D. students and personnel of the Laboratory of Soft Technologies, Valorization, Physicochemistry of Biological Materials, and Biodiversity (LTDVPMBB) for their help and support during the realisation of this work.

My sincerest thanks to my husband Fahim and my son Noah for their love, encouragement, and unconditional support.

My deepest thanks to my parents, MEGUELLATI Brahim and MERIKHI Malika, and my siblings, Smail, Messouda, Houria, Fatima, and Khalil and their families, who accompanied me during the hardest time. The words are incapable of thanking you enough for the endless support.

I also want to send special thanks to my friends and relatives who supported me in one way or another and all the people who crossed my path and helped with the realisation of this thesis.

Finally, the sincerest expression of gratitude to all of those with whom I have had the pleasure to work during this and other related projects

Abstract

Abstract

The increase in chemical consumption has immensely increased the organic contamination in water resources and effluents. The objective of this work is the elaboration of lamellar double hydroxide materials using two methods and their application in the environmental field. Several physicochemical techniques, including XRD, FTIR, SEM/EDS, TGA/DTG, and electrochemical characterizations, were employed in order to assess the structural and morphological properties of MgAl-LDH, MgFe-LDH, and CoAl-LDH powders synthesised by coprecipitation method. On the other hand, MgAl-LDH and CoAl-LDH thin films were successfully electrodeposited over metallic substrates (Nickel and stainless-steel electrodes).

MgAl-LDH, MgFe-LDH, and CoAl-LDH powders were applied for the adsorption of Azocarmine G (ACG), and the experimental parameters were optimised using the response surface methodology to reach maximum experimental adsorption capacities (mg.g^{-1}) of 105.9, 101.6, and 98.66 for MgAl-LDH, MgFe-LDH, and CoAl-LDH, respectively. The adsorption behaviour of MgAl-LDH electrodeposited on a stainless-steel electrode was tested towards the removal of bromophenol blue (BPB), the effect of the experimental conditions was investigated, and the maximum adsorption capacity was 14.96 mg.g^{-1}. Several kinetic and isotherm models were applied to the experimental results to assess the adsorption process. The energetic aspect of the processes was also studied by determining thermodynamic parameters such as standard Gibbs free energy (ΔG°), enthalpy (ΔH°) and entropy (ΔS°). The regeneration of the materials is investigated by the chemical and electrochemical methods; the experiments revealed that using powders results in extremely high adsorption capacities, while the advantage of using formed films is that they are quick, simple, and effective for the regeneration.

MgFe-LDH powder synthesised via the co-precipitation method was used for the modification of graphite electrode (G/MF electrode). The modified electrode was then tested for the electrochemical selective detection of Metronidazole (MNZ) using cyclic voltammetry. The developed sensor exhibited good performance in terms of sensitivity and selectivity with a detection limit of 0.74×10^{-3} M.

Key words

Layered double hydroxide (LDH); Adsorption; Electrochemical Sensors; Coprecipitation; Electrodeposition; Azocarmine G, Bromophenol Blue; Metronidazole; Graphite modified electrode

Résumé

L'augmentation de la consommation de produits chimiques a considérablement amplifié la contamination organique des effluents aquatiques et des ressources des eaux. L'objectif de ce travail est l'élaboration des hydroxydes double lamellaires (HDL) suivant deux méthodes, et leur application dans le domaine environnemental. Plusieurs techniques physicochimiques, notamment XRD, FTIR, SEM/EDS, TGA/DTG et caractérisations électrochimiques, ont été utilisées afin d'évaluer les propriétés structurelles et morphologiques des poudres de MgAl-HDL, MgFe-HDL et CoAl-HDL synthétisées par la méthode de coprécipitation. D'autre part, des films minces de MgAl-HDL et de CoAl-HDL ont été électrodéposés avec succès sur des substrats métalliques (électrodes de Nickel et d'acier inoxydable).

Des poudres MgAl-HDL, MgFe-HDL et CoAl-HDL ont été appliquées pour l'adsorption de l'azocarmine G (ACG), et les paramètres expérimentaux ont été optimisés à l'aide de la méthode des surfaces de réponse pour atteindre des capacités d'adsorption (mg/g) expérimentales maximales de 105,9 ; 101,6 et 98,66 pour MgAl-HDL, MgFe-HDL et CoAl-HDL, respectivement. Le comportement d'adsorption du MgAl-HDL électrodéposé sur une électrode en acier inoxydable a été testé en vue de l'élimination du bleu de bromophénol (BPB), l'effet des conditions expérimentales a été étudié et la capacité d'adsorption maximale était de 4,96 mg/g. Plusieurs modèles cinétiques et isothermes ont été appliqués aux résultats expérimentaux pour évaluer les processus d'adsorption. L'aspect énergétique des processus a été également étudié en déterminant les paramètres thermodynamiques tels que l'énergie libre standard de Gibbs ($\Delta G°$), l'enthalpie ($\Delta H°$) et l'entropie ($\Delta S°$). La régénération des matériaux a été étudiée par deux voies chimiques et électrochimiques ; les expériences ont révélé que l'utilisation de poudres a permis d'obtenir des capacités d'adsorption extrêmement élevées, tandis que l'avantage de l'utilisation de film formé réside dans la rapidité, la simplicité et l'efficacité de la régénération.

La poudre de MgFe-HDL synthétisée via la méthode de coprécipitation a été utilisée pour la modification de l'électrode en graphite (électrode G/MF). L'électrode modifiée a été ensuite testée pour la détection électrochimique sélective du métronidazole (MNZ) par voltamétrie cyclique. Le capteur développé a présenté de bonnes performances en termes de sensibilité et de sélectivité avec une limite de détection de 0,74 mM.

Mots clés

Hydroxyde double Lamellaire (HDL); Adsorption; Capteurs électrochimiques; Coprécipitation ; Électrodéposition ; Azocarmine G, bleu de bromophénol ; Métronidazole ; Électrode modifiée en graphite

ملخص

أدى الإفراط في استهلاك المواد الكيميائية إلى زيادة كبيرة في التلوث العضوي في مياه الصرف الصحي والموارد المائية. كان الهدف من هذا العمل هو إعداد هيدروكسيد رقائقي مزدوج باستخدام طريقتين واستخدامها في المجال البيئي. تم استخدام العديد من التقنيات الفيزيائية والكيميائية، بما في ذلك XRD، FTIR، SEM/EDS، TGA/DTG، والتوصيفات الكهروكيميائية، من أجل تقييم الخصائص الهيكلية والمورفولوجية لمساحيق MgAl-LDH، وMgFe-LDH، وCoAl-LDH التي تم تصنيعها من خلال تقنية الترسيب المتزامن. من ناحية أخرى، تم ترسيب أغشية الرقيقة MgAl-LDH وCoAl-LDH بنجاح على ركائز معدنية (أقطاب نيكال وفولاذ مقاوم للصدأ).

تم تطبيق مساحيق MgAl-LDH، وMgFe-LDH، وCoAl-LDH لادصاص Azocarmine G (ACG)، وتم تحسين الظروف التجريبية باستخدام منهجية سطح الاستجابة للوصول إلى أقصى قدرات الادمصاص (مجم/جم) البالغة 105.9، 101.6 و98.66 لـ MgAl-LDH، وMgFe-LDH، وCoAl-LDH، على التوالي. تم اختبار سلوك الادمصاص لـ MgAl-LDH المُركب كهروكيميائيًا على قطب كهربائي من الفولاذ المقاوم للصدأ تجاه إزالة البروموفينول الأزرق (BPB) مع دراسة تأثير الظروف التجريبية، وكانت سعة الامتزاز القصوى 4.96 مجم / جم. تم تطبيق العديد من النماذج الحركية والأيسوثرمية على النتائج التجريبية لتقييم عملية الادمصاص. تمت دراسة الجانب النشط للعمليات أيضًا من خلال تحديد المعاملات الديناميكية الحرارية مثل طاقة جيبس الحرة القياسية (ΔG°)، والمحتوى الحراري (ΔH°) والإنتروبيا (ΔS°). تم دراسة إمكانية تجديد المواد باستخدام الطرق الكيميائية والكهروكيميائية. وكشفت التجارب أن استخدام المساحيق يؤدي إلى قدرات امتصاص عالية للغاية، في حين أن ميزة استخدام الأغشية المترسبة هي أنها سريعة وبسيطة وفعالة للتجديد.

تم استخدام مسحوق MgFe-LDH المُصنَّع عبر طريقة الترسيب المتزامن لتعديل قطب الجرافيت (قطب G/MF). تم بعد ذلك اختبار القطب المعدل للكشف الانتقائي الكهروكيميائي للميترونيدازول (MNZ) باستخدام التقنيات الكهروكيميائية. أظهر المستشعر المطور أداءً جيدًا من حيث الحساسية والانتقائية مع حد كشف قدره 0.74 مم.

الكلمات المفتاحية

هيدروكسيد رقائقي مزدوج (HDL)؛ الادمصاص؛ أجهزة الاستشعار الكهروكيميائية. الترسيب المتزامن. الترسيب الكهربائي؛ أزوكارمين جي، بروموفينول الأزرق؛ ميترونيدازول. قطب الجرافيت المعدل.

List of abbreviations

4-AP	4-aminophenol
4-NI	4-nitroindane
A_F	A constant which depends on the temperature and the adsorption system
P_0	Absolute pressure
T	Absolute temperature (°K)
q_t	Adsorption capacity at time t (mg.g^{-1})
AA	Ascorbic acid
ACG	Azocarmine G
θ	Bragg diffraction angle.
BPB	Bromophenol blue
CF	Carbon fibre
CNT	Carbon nanotubes
CEA	Carcinoembryonic antigen
C_e	Concentration at equilibrium
CP	Conducting polymers
CPE	Constant phase element
Dcs	Crystallite size
i	Current
CV	Cyclic voltammetry
DPV	Differential pulse voltammetry
DTG	Differential thermogravimetric
D	Diffusion coefficient in solution (cm^2 s^{-1})
DCV	Direct current voltammetry
K_d	Distribution coefficient
M^{2+}	Divalent metal
D-R	Dubinin-radushkevich
A	Electroactive area (cm^2)
EIS	Electrochemical impedance spectroscopy
EP	Emerging pollutants
ΔH^o	Enthalpy change
ΔS^o	Entropy
q_e	Equilibrium adsorption capacity (mg.g^{-1})
F	Faraday's constant (96485 C/mol)
FTO	Fluorine-doped tin oxide
FTIR	Fourier transformer infra-red
GC	Glassy carbon

GR	Graphene
GO	Graphene oxide
G	Graphite electrode
$\mathbf{\epsilon_{D\text{-}R}}$	Polanyi Potential
HPLC	High performance liquid chromatography
Z	Impedance
ITO	Indium tin oxide
$\mathbf{k_{in}}$	Inta-particle diffusion model constant ($mg.g^{-1}.min^{-1/2}$)
ISE	Ion selective electrode
ILs	Ionic liquids
$\mathbf{K_{D\text{-}R}}$	Is a constant related to the adsorption energy ($mol^2\ k.J^{-2}$)
$\mathbf{\beta_E}$	Is the desorption constant ($g.mg^{-1}$)
$\mathbf{k^0}$	Is the heterogeneous rate constant
$\mathbf{E_0}$	Is the standard potential
LDH	Layered double hydroxides
$\mathbf{Z_0}$	Magnitude
m	Mass (g)
MS	Mass spectroscopy
MBZ	Mebendazole
MNZ	Metronidazole
G/MF	MgFe-LDH modified graphite electrode
NF	Nafion
5-HT	Neurotransmitter serotonin
n	Number of electrons transfered
$\mathbf{n_i}$	Number of moles
PPCP	Personal care products
$\mathbf{\phi}$	Phase shift,
$\mathbf{PMo_{12}}$	Phosphomolybdic acid
PPV	Poly (phenylene-vinylene)
PA	Polyacetylene
PAni	Polyaniline
PP	Polyphenylene
PPy	Polypyrrole
PT	Polythiophene
$\mathbf{\phi}$	Pore size
P	Pressure
$\mathbf{K_1}$	Pseudo-first order rate constant (min^{-1})
$\mathbf{K_2}$	Pseudo-second order rate constant ($g.mg^{-1}.min^{-1}$)
$\mathbf{\omega}$	Radial frequency ($radians.s^{-1}$)
rGO	Reduced graphene oxide
$\mathbf{\alpha_E}$	Represents the initial rate of the adsorption ($mg.g^{-1}min^{-1}$)

SAF	Safinamide mesylate
SEM	Scanning electron microscopy
SWASV	Square wave anodic stripping voltammetry method
ΔG°	Standard Gibbs free energy
G	The conductance
R_L	The constant of the separation factor
K_F	The Freundlich adsorption constant
K_L	The Langmuir equilibrium constant ($L.mg^{-1}$ or $L. mol^{-1}$)
I_p	The peak current (A)
γ	The specific conductivity of the electrolyte ($S.cm^{-1}$)
C_{BL}	The thickness of the boundary layer ($mg.g^{-1}$)
V_t	The total pore volume
V_m	The volume of gas adsorbed in a monolayer
TGA	Thermogravimetric analysis
t	Time
M^{3+}	Trivalent metal
R	Universal gas constant (8.314 J/K mol)
λ	Wavelength of radiation
XRD	X-Ray diffraction
BIAN	A-diimine(bis(4-HOOC-phenyl)-acenaphthenequinonediimine
β-CD	B-cyclodextrin

List of figures

Chapter I

Chapter II

Chapter III

Chapter IV

Chapter V

List of Tables

Chapter I

Chapter II

Chapter III

Chapter IV

Table of contents

Introduction

The growing demand in technology and industry has increased chemical consumption and greatly impacted the environment. Human social evolution and the misguided perception of personal safety result in significant chemical release into land and aquatic habitats. In a world that is facing issues such as population increase, climate change, and rising water needs in agriculture and industry, water resources are of the utmost importance. Emerging pollutants released into water resources present a serious threat to living organisms. Since these contaminants are difficult to eliminate, consuming water with low levels of contaminants over an extended period of time might have negative health effects [1,2]. Organic pollutants are dangerous contaminants that have gained the attention of researchers because of their high contamination in the environment. This kind of pollutants can enter the body through ingestion, skin absorption, or inhalation and induce kidney failure, blood poisoning, and other health issues [3].

In recent years, there has been an increasing interest in the detection and analysis of organic pollutants in water springs, sludges, and effluents. Several physicochemical methods are presented, including Fourier transform infrared spectroscopy (FTIR), mass spectroscopy (MS), UV-visible spectroscopy, and high-performance liquid chromatography (HPLC) [4,5]. Despite their high sensitivity, these techniques require expensive, heavy machinery and extensive processes, making the in-situ analysis unfeasible. In light of these limitations, Scientists and engineers are concerned with the development of processes that are quick, easy, and affordable, with the particularity of being portable for the on-site sample and treatment [6].

Electroanalysis represents the largest area of applied electrochemistry. Owing to this fact, the electroanalysis can be classified as a special area of electrochemistry that focuses on the identification (qualitative characterization) and determination (quantification) of chemical substance(s) in a sample [7]. An electrochemical sensor is a type of chemical sensor that analyses particular species quantitatively and semi-quantitatively using electrochemical methods. The device consists of a working electrode as a receptor, a counter electrode, and a reference electrode; the three electrodes correspond to the transducer system [8]. The working electrode is the receptor of the electrochemical sensor and the most important part in the detection process. Thus, it should be constructed with an appropriate material for the analysis, taking into account important parameters such as its inertness, stability, affordability, and low background current over the potential window. Several materials have been reported, including conductive polymers, metals and metal oxides, carbon-based materials, and ionic liquids.

As water consumption increases, scientists are increasingly interested in issues beyond the identification and quantification of pollutants, especially since some contaminants are resistant to common water treatment methods. Therefore, more affordable and efficient treatment methods must be implemented in order to upgrade the effectiveness of wastewater treatment [9]. The development of novel environmental remediation techniques for arduous chemical pollutants is the subject of numerous studies, including coagulation, biological treatment, advanced oxidation techniques (photo-fanton, photodegradation), and natural sorption techniques (adsorption, absorption, and ion exchange) [10]. Adsorption is a technique for separating compounds from a fluid phase (aqueous or gaseous) based on the spontaneous process of phase transfer using an adsorbent with a high degree of porosity and a sizable specific surface. Adsorption is one of the methods that has been widely implemented in water and

environmental remediation owing to its low cost, ease of use, and low sludge volume. However, the choice of the adsorbent remains important to increase the efficiency of the process. According to the literature, a large number of materials are employed as adsorbents, like activated carbon, minerals, polymers, and clays [11].

Clays are very common mineral deposits that have been used by humans since early days, particularly in ceramic and pottery production. The importance of these materials has increased recently as a result of their inclusion in a variety of industrial and scientific fields [12]. Layered double hydroxides (LDH) are anionic clays with a specific lamellar structure. Their lamellas are formed by a divalent cation M^{2+} (Mg, Ni, Cu, Co, Ca…) and trivalent cation M^{3+} (Al, Fe…) along with a given cationic ratio x. The sheets hold a positive charge that is compensated by the interlamellar anion A^{n-} (CO_3^{2-}, NO_3^-, Cl^-…) and water molecules; the structure is likewise expressed as $[M^{2+}_{1-x}M^{3+}_x(OH)_2]^{x+}[A^{n-}_{x/n}(H_2O)_y]$ [13].

Literature presents a great diversity of LDHs driven by the variation of divalent and trivalent cations, intercalary anions, and the M^{2+}/M^{3+} molar ratio. LDH materials can be synthesized through several methods including co-precipitation and electrodeposition. Co-precipitation is the simultaneous precipitation of metal hydroxides ($M(OH)_2$ and $M(OH)_2^+$) by adding a base [14]. The electrodeposition process is based on the formation of hydroxide ions by a reduction reaction of the species existing in the medium. The production of OH^- ions increases the pH in the vicinity of the surface of the electrode, which allows the formation of the LDH film [15].

On account of their many advantageous characteristics, layered double hydroxides are frequently used in different fields of application. These materials possess interesting characteristics that promote their use as highly efficient adsorbents for different kinds of molecules. In addition, LDHs are increasingly incorporated in electrochemistry as working electrodes due to their electrochemical properties, especially for electrode modification in electrochemical sensors [16].

This work focused on the elaboration of LDH clays using coprecipitation and electrochemical method. The elaborated LDHs are then oriented for application as an adsorbent or an electrochemical sensor. The results are structured around three chapters.

The first chapter presents a bibliographic review of electrochemical sensors, adsorption, and lamellar double hydroxides. After a preamble on emergent pollutants, the quantification and detection of contaminants are discussed along with the electrochemical sensors. Subsequently, the treatment methods developed recently, and more precisely, the adsorption method, are detailed. Finally, a general presentation of lamellar double hydroxides is given, as are their synthesis methods, properties, and, of course, their fields of application.

The second chapter is focused on the experimental methods and protocols used for this work, the synthesis of the LDHs, the characterization methods used, as well as the experimental protocols for the parametric study of adsorption and electrochemical sensing tests.

The third chapter is devoted to the presentation of the results obtained in three main parts. The first includes the characterization techniques such as XRD, FTIR, SEM/EDS, BET, TGA/DSC, PZC determination, and electrochemical characterizations. The second part deals with the study of the adsorption behaviour of the materials synthesised by both methods. The last part scrutinises their application in electrochemical sensors.

The thesis ended with a conclusion of the main results obtained and possible prospects for the future.

References

[1]   N. Haddadou, N. Bensemma, G. Rekhila, M. Trari, K. Taïbi, *"Journal Photochem. Photobiol. A Chem.* **2018**. DOI: 10.1016/j.jphotochem.2018.03.033.

[2]   P. Singh, P. Sharma, *J. Photochem. Photobiol. A Chem.* **2021**, *408* (December), 113096. DOI: 10.1016/j.jphotochem.2020.113096.

[3]   S. Kobylewski, M. F. Jacobson, *Int. J. Occup. Environ. Health*. **2012**, *18* (3), 220–246. DOI: 10.1179/1077352512Z.00000000034.

[4]   Y. Fan, D. Pan, M. Yang, X. Wang, *Sci. Total Environ.* **2023**, *866* (September 2022), 161412. DOI: 10.1016/j.scitotenv.2023.161412.

[5]   V. Ayerdurai, M. Cieplak, W. Kutner, *TrAC - Trends Anal. Chem.* **2023**, *158*, 116830. DOI: 10.1016/j.trac.2022.116830.

[6]   H. Afsharara, E. Asadian, B. Mosta, K. Banan, S. Arjomand, D. Hatamabadi, A. Keshavarz, C. Mustansar, R. Keçili, F. Ghorbani-bidkorpeh, *Trends Anal. Chem.* **2023**, *160*, 116949. DOI: 10.1016/j.trac.2023.116949.

[7]   L. M. Moretto, K. Kalcher, *Environmental Analysis by Electrochemical Sensors and Biosensors: Fundamentals*, Vol. 1, Springer, Ontario **2014**.

[8]   R. Meng, Q. Zhu, T. Long, X. He, Z. Luo, R. Gu, *Food Control*. **2023**, *150* (October 2022), 109743. DOI: 10.1016/j.foodcont.2023.109743.

[9]   S. Sharma, G. Sharma, A. Kumar, P. Dhiman, T. S. AlGarni, M. Naushad, Z. A. ALOthman, F. J. Stadler, *Sep. Purif. Technol.* **2022**, *278* (June 2021), 119481. DOI: 10.1016/j.seppur.2021.119481.

[10]   M. Zubair, H. A. Aziz, I. Ihsanullah, M. A. Ahmad, M. A. Al-Harthi, *Environ. Technol. Innov.* **2021**, *23*, 101614. DOI: 10.1016/j.eti.2021.101614.

[11]   X. Hong, M. Xia, M. Shi, C. Liu, Y. Yan, Y. Tao, Y. Zhang, Y. Zhang, P. Du, F. Wang, *J. Colloid Interface Sci.* **2023**, *629*, 948–959. DOI: 10.1016/j.jcis.2022.09.088.

[12]   D. M. Z. Valenti, J. Silva, W. R. Teodoro, A. P. Velosa, S. B. V. Mello, *Clin. Exp. Dermatol.* **2012**, *37* (2), 164–168. DOI: 10.1111/j.1365-2230.2011.04216.x.

[13]   F. Chengqian, L. Wanbing, D. Yimin, W. Zhiheng, L. Yaqi, C. Ling, L. Bo, Y. Siwen, W. Junlong, D. Xianglong, et al., *Colloids Surfaces A Physicochem. Eng. Asp.* **2023**, *663* (November 2022), 130921. DOI: 10.1016/j.colsurfa.2023.130921.

[14]   X. Han, J. Li, J. Lu, S. Luo, J. Wan, B. Li, C. Hu, X. Cheng, *Nano Energy*. **2021**, *86* (April), 106079. DOI: 10.1016/j.nanoen.2021.106079.

[15]   M. Monti, P. Benito, F. Basile, G. Fornasari, M. Gazzano, E. Scavetta, D. Tonelli, A. Vaccari, *Electrochim. Acta*. **2013**, *108*, 596–604. DOI: 10.1016/j.electacta.2013.06.143.

[16]   M. V. Bukhtiyarova, *J. Solid State Chem.* **2019**, *269*, 494–506. DOI: 10.1016/j.jssc.2018.10.018.

Chapter I
Literature review

I.1. Sensors

I.1.1. Emerging Pollutants

The technological and industrial development of human activities in recent years have boosted the use of chemicals, causing severe pollution at all environmental levels (air, water, and soil) induced by uncontrolled urban, agricultural, and industrial discharges [1–3]. A lot of chemicals are released into aquatic and terrestrial environments as a result of human social development and a false sense of personal safety. In many countries around the world, river water is frequently used for agriculture, bathing, and drinking. Furthermore, sewage water is used for cultivation in several developing nations without any prior pretreatment. Numerous contaminants were introduced to the food chain when untreated or substandard wastewater was used for agriculture [4]. The consumption of water with low levels of contaminants over a long period of time can have adverse health consequences because some of these pollutants are persistent in nature and hard to remove. Pesticides, medications, and industrial chemicals are just a few examples of the various chemical pollutants that exist in the environment. There are more than 50 different types of environmental contaminants, with concentrations in the aquatic environment ranging from $pg.mL^{-1}$ to $mg.mL^{-1}$ [5].
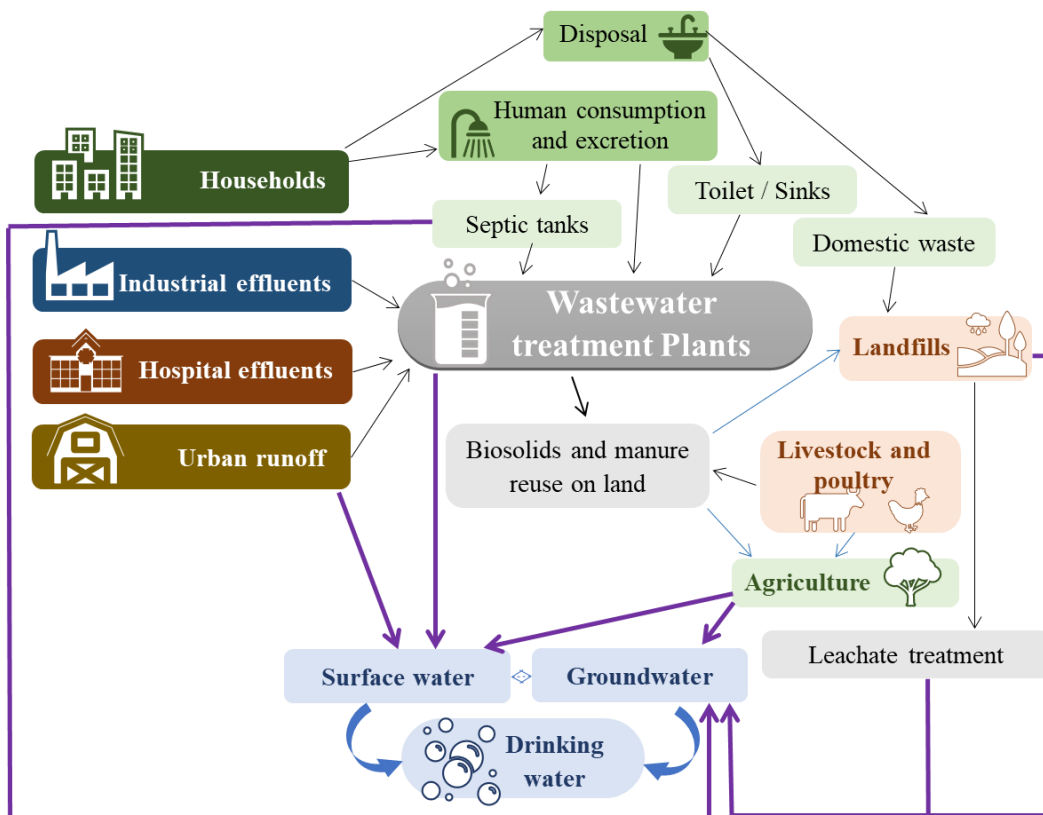
Figure I. 1. Emerging pollutants pathway [6]

Emerging pollutants released into water resources present a serious threat to living organisms. The main categories of emerging pollutants are: pharmaceuticals and personal care products (PPCPs), industrial chemicals, agricultural compounds (insecticides, pesticides, and herbicides), water disinfection by-products, disinfectants and biocides, surfactants, food additives, nanomaterials, waterborne pathogens, etc. [7,8]. However, the two typical pollutants

that have attracted the attention of researchers are organic pollutants and heavy metals. They can cause renal failure, blood poisoning, and other health problems when they enter the body by ingestion, skin absorption, or inhalation. The development of an efficient quantification system to detect pollutants seems absolutely necessary [9].

I.1.1.1. Dye Molecules

A dye is a coloured substance with a large molecular weights and complex systems of conjugated double bonds. Dyes have been used in many sectors, such as painting, textiles, tanning, printing, pharmaceutical, cosmetic, food and polymer industries. Sulphonic groups are incorporated into dye molecules to improve their solubility in water. Sulphonated dyes are important industrial products with widespread applications, they can be considered suitable anionic dyes that hold a negative charge in a wide pH range [10].

Azocarmine G is a synthetic sulphonated dye with the chemical formula of $C_{28}H_{18}N_3NaO_6S_2$. Haematology, histology, and the production of diagnostic assays are the main fields that employ it. Though, this dye is also helpful for protein determination in acidic media. The creation of a purple-red complex serves as an indicator. For microscopy, azocarmine G is a common stain. It can also be utilised as a reference standard when using high performance liquid chromatography in conjunction with a diode array detector to determine the presence of azocarmine G in food goods and beverages [11].

Arylmethane dyes are a group of stains which are formed by one carbon linked to benzene or naphthalene groups. Bromophenol Blue is an arylmethane dye with chemical formula of $C_{19}H_{10}Br_4O_5S$ [12]. This dye can be used in buffer solutions to distinguish between dead and living cells. Additionally, it has been a component of gel loading buffer as a tracking dye used in agarose or polyacrylamide gels for protein or nucleic acid electrophoresis.

I.1.1.2. Antibiotics

Antibiotics are used to treat or prevent some types of bacterial infection. They function by either eliminating bacteria or stopping their spread. The antibiotic 1-(2-hydroxyethyl)-2-methyl-5-nitroimidazole, also known as metronidazole (MNZ), from the group of nitroimidazole is a common antibacterial and anti-inflammatory drug used to treat infectious disorders that was created from anaerobic bacteria and protozoal [13,14]. Nevertheless, the overdose of MNZ exceeding 2g per day can have a number of negative side effects, such as visual neuropathy, haematuria, decreased neutrophil count, dyssynergia, mutagenicity, sputum production, and seizures [15]. MNZ is widely used and its employment generate a serious spread of wastewater contaminated with MNZ molecules which effect human health and the environment.

I.1.2. Pollutant detection and quantification

There exist several physicochemical methods for the analysis of organic molecules, such as Fourier transform infrared spectroscopy, mass spectroscopy, UV-visible spectroscopy, and high-performance liquid chromatography [8,16]. Despite their high sensitivity, these methods demand heavy equipment at a high cost and time-consuming procedures, which make in-situ analysis unfeasible. In view of these drawbacks, scientists and engineers are concerned with the

development of rapid methods that are fast, simple, and cost-effective, with the particularity of being portable for onsite sampling and treatment [17,18].

A sensor is a device that detects changes in a certain variable, such as temperature, pressure, mass, voltage, etc., and transforms them into a measurable signal. The most important parts of a sensor (Erreur ! Source du renvoi introuvable.) are the receptor that generates the information of interest, the transducer that receives the information and converts it into a signal, and a computer-assisted programme that describes the occurring process [19].

The advantage of sensors is the simplicity of the instrumentation and the facility of the sample preparation, which are two factors that minimise the analysis duration, and even the possibility to become portable and perform the onsite analysis. Moreover, sensors have high sensitivity and selectivity towards a large number of organic and inorganic pollutants. Sensors are among the recent analytical techniques that have found a large application in the environmental, agri-food, and medical sectors [20].
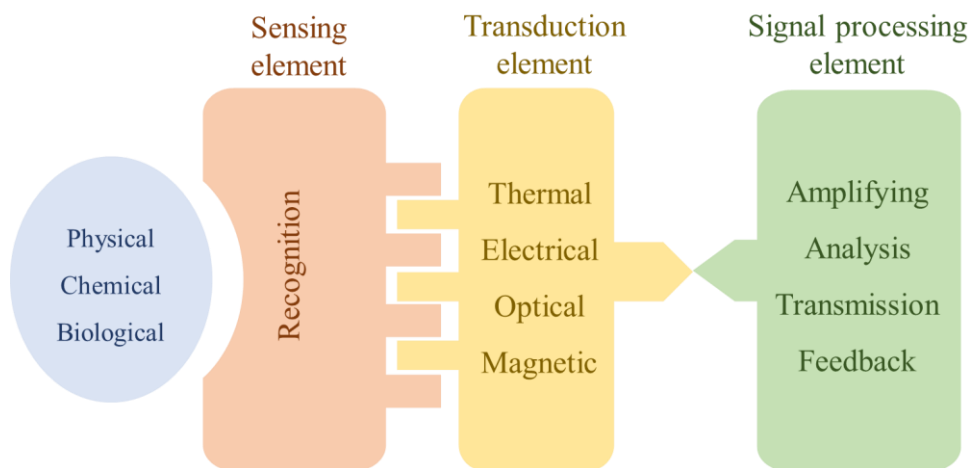
Figure I. 2. Schematic representation of the main components of a sensor [21].

I.1.3. Classification of sensors

The classification of sensors is done according to their operating procedure. This leads to optical, electrochemical, electrical, mass-sensitive, magnetic, and thermal sensors, or sensors based on other physical properties such as radioactivity [22–24]. Based on the operating procedure, sensors are divided into three main categories:

- Physical sensors where the measured information is a physical property such as absorbance, conductivity, temperature, mass change, etc.
- Chemical sensors where the signal is originated from a chemical reaction and the variable is directly related to the concentration of the target molecule. It contains a chemically active layer that arises a response
- Biosensors where the receptor is a biological sensing element such as cells, enzymes, antibodies, nucleic acids, microorganism, etc. These elements must have the particularity of binding to a target analyte.

I.1.4. Electrochemical sensors

An electrochemical sensor is a class of chemical sensors that uses electrochemical techniques for the quantitative and semi-quantitative analysis of certain species. The device consists of a working electrode as a receptor, a counter electrode, and a reference electrode; the three electrodes correspond to the transducer system [25,26]. Electrochemical sensors can be divided according to their detecting principle; this engenders three main types that are briefly discussed below.

I.1.4.1. Conductometric sensors

The principle of conductometric sensors lays on establishing the detection information from the electrical conductance G of the electrolyte between two electrodes of the same nature by applying a voltage or an alternating current. It has the expression:

$$G = \gamma . \frac{S}{l} \hspace{4cm} \text{I.1}$$

γ is the specific conductivity of the electrolyte (S.cm^{-1}), and the ratio S/l is the geometric constant of the cell (cm), represented by k.

By measuring the conductance G of the cell immersed in an electrolyte when the conductivity constant of the cell is known, the variation of the conductivity of any electrolyte may be established.

The advantage of conductometric sensors is that there is no requirement for a reference electrode which reduces the cost of the device. However, they are generally not selective, so an electrode modification is necessary to improve the selectivity of the surface [27]. The most predominant materials used in these sensors are thin films, especially for gas sensors, where the conductivity change is established due to surface chemisorption. Different kinds of thin films have been reported in the literature; for instance, conductometric methods were employed in [28] for the selective and sensitive detection of CH_4 using Ga_2O_3 thin films, and also in [29] for the sensitive detection of O_2 onto CdS thin films.

I.1.4.2. Potentiometric sensors

This kind of sensor estimates the potential difference established between a reference solution and the sample solution by means of a reference electrode [30]. The separation of the solution is done by a membrane, while the relationship between the potential difference and the target molecule's activity is given by the Nerst equation (**Eq I.2**) [23]:

$$E = E_0 + \frac{RT}{nF} Ln \frac{a^s}{a^m} \hspace{4cm} \text{I.2}$$

Where E_0 is the standard potential of sensor electrode, F is Faraday's constant, T is absolute temperature, R is universal gas constant, s is sample, n is the valency of ions and a is the target molecule's activity.

The most commonly used potentiometric sensor is the pH electrode, which is an ion selective electrode (ISE) that measures the change in the working electrode's potential

depending on the surrounding environment [31]. The ion-selective electrodes are based on a permselective, ion-conducting membrane that allows the separation of the reference solution from the sample solution (outside solution). Recent researches report the development of potentiometric sensors since they are simple and allow the on-site analysis. For example, El-Sayed et al. investigated the use of an eco-friendly copper electrode for the potentiometric determination of safinamide mesylate (SAF); the sensor was effectively implemented for the quantification of SAF in pure and pharmaceutical dosage forms [32], while the work of Parrilla et al. involved 3D-printing technology for the construction of a microneedle-based sensor that was modified with conductive inks; the system was then used for the development of a potentiometric sensor for pH monitoring [33].

I.1.4.3. Amperometric/voltametric sensors

Amperometric sensors are based on an electron transfer reaction between the solution and the working surface, which creates a measurable current while the potential is controlled with a potentiostat. The technique can use a potentiostatic detection, where the potential is kept constant in a period of time, or a potentiodynamic detection, where the potential is scanned between two values. The device in this case includes an electrochemical cell composed of three-electrode system (reference, counter, and working electrode) and a suitable electrolyte containing the detected species. The reference electrode allows the measurement of potential between the working electrode and the counter electrode [34].

The initial amperometric/voltametric technique used in an electroanalytical study is cyclic voltammetry (CV). It gives details on the locations of the electroactive compound's redox potentials and the impact of media on the redox process, while the current generated by the applied potential is measured during the potential sweep. The resulting cyclic voltammogram displays distinctive peaks brought on by the development of the diffusion layer at the electrode surface. The development of amperometric sensors is becoming increasingly widespread in different sectors because of the wide range of redox-active molecules that can be detected on-site with ease of manipulation. Amperometric sensors also present great sensitivity and selectivity and are easily modified with a wide variety of materials to match the targeted species [35]. Otherwise, their pH dependence and co-existent electro-active species interference remain hurdles during the analysis [36].
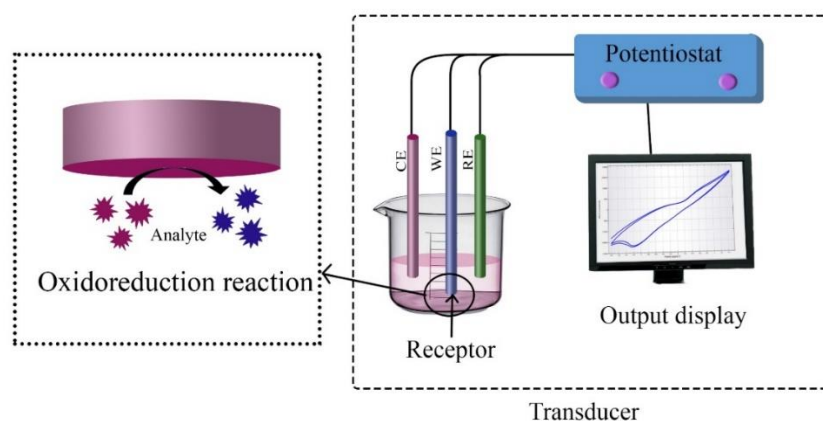
Figure I. 3. Schematic representation of a typical amperometric/voltametric sensing system

I.1.5. Types of sensors and modified electrodes

The working electrode is the receptor of the electrochemical sensor and has a major role in the detection process. For instance, the material of the working electrode should be suitable for the analysis, and its choice must consider important characteristics including its inert nature, stability, low background current over the potential window, and low cost. Several materials have been described in the literature as working electrodes with different sizes and shapes, and the list is still increasing.

I.1.5.1. Mercury electrode:

These electrodes have demonstrated excellent performance from the very beginning in the analysis of pollutants. Mercury electrodes are characterised by their renewable surface, where new drops of thin films can be easily created, the production of a pseudo-stationary state at high scan rates for linear sweep voltammetry, and the large potential range in the cathodic zone [37]. These facts are the reason for their strong performance in the analysis of pollutants. Furthermore, due to their wide cathodic potential range, which includes the standard reduction potential of the majority of ions, and their favourable signal-to-noise ratio, these devices have excellent potential for the analysis of both organic and inorganic compounds [38].

The work of Nemcova et al. demonstrated the use of a classical dropping mercury electrode for the determination of the genotoxic hydrocarbon 4-nitroindane (4-NI) using direct current voltammetry (DCV) and differential pulse voltammetry (DPV) [39]. The system was successfully applied for the determination of 4-NI in samples of drinking and river water. In [40], mercury electrodes were employed for the reduction of the herbicide chloridazon. However, the toxicity and restricted anodic potential of mercury electrodes are the major disadvantages that limit their use.

I.1.5.2. Conductive polymers

Conducting polymers (CPs) are a distinct class of polymers where the structure comprises a conjugated system allowing the delocalization of electrons through the repeated units. The regular repetition of monomers containing π electrons creates a semiconducting molecular wire architectures that grant the polymer an interesting optical and electronic properties. Conductive polymers attracted great interest in the electrochemical field owing to their corrosion resistance, low density, flexibility and controllable shape and morphology. The most prominent types of CPs are polyacetylene (PA), polypyrrole (PPy), polyaniline (PAni), polyphenylene (PP), polythiophene (PT), poly (phenylene-vinylene) (PPV) etc, these polymers can be used alone for the construction of electrodes like the work of Song et al. who investigated the electrochemical detection of carcinoembryonic antigen (CEA) on a conducting polypyrrole (PPy) nanocomposite film electrode, the biosensor exhibits satisfying sensing performance for CEA detection [41].

Conductive polymers can also be combined with other materials for better sensitivity and selectivity like the investigation of Yu et al. on polyaniline (PANI) as a hybrid component along with β-cyclodextrin (β-CD) and phosphomolybdic acid (PMo_{12}) for the construction of a sensitive electrochemical sensor which was successfully used for the detection of ascorbic acid (AA) [42]. The study [43] presented also the electrochemical sensing behavior of a gallium nitride-polyaniline-polypyrrole (GaN- PANI-PPy) hybrid composite towards mebendazole (MBZ). The drug was detected by differential pulse voltammetry using GaN-PANI-PPy modified glassy carbon electrode as working electrode which shows linear responses towards MBZ with good sensitivity.

I.1.5.3. Carbon based nanomaterials

Carbon based electrodes including carbon nanotubes (CNTs), graphene (GR) and graphene oxide, carbon nanoparticles, carbon nanofibers, and carbon nano-tubes represents a superior choice in electrochemistry owing to their inert nature, wide chemical surface, large potential window and anti-corrosive behavior. Although, some electrochemical properties depend on the composition and the synthesis method such as the background current, the electron transfer rate and the adsorption. Li et al. studied a new kind of carbon as an effective electrochemical sensor for the determination of Cd^{2+} and Pb^{2+} in water using electrochemical pre-enrichment and anodic-stripping voltammetry methods [44]. The work of Materon et al. reported the use of a screen-printed electrodes (SPE) modified with fullerene (C60), reduced graphene oxide (rGO) and Nafion (NF) (C60-rGO-NF/SPE) for the determination of the antibiotic metronidazole (MNZ) [45]. The detection was also performed in serum and urine, with recovery between 94% and 100%, which are similar to the results obtained by chromatographic method (HPLC-UV).

Carbon based electrodes can be composed of solely single carbon compound or have another substance with carbon compound, this leads to a classification into homogenous (glassy carbon, carbon nanotube, graphite) and heterogenous (carbon paste and screen-printed electrodes). Nevertheless, the drawback of these electrodes is the slow electron transfer reaction compared with the metallic electrode.

I.1.5.4. Metal and metal oxides

Metal (gold, silver, platinum…etc) and metal-oxide electrodes (tin oxide, zinc oxide, etc) have known an extensive use in electrochemistry due to their conductivity, stability, reproducibility and the broad potential window with low background current. The modification of electrodes in electrochemical sensors for the detection today makes substantial use of the metals silver (Ag), bismuth (Bi), platinum (Pt) and the metal nanomaterial of gold (Au). In the study of Maduraiveeran et al., a glassy carbon (GC) electrode modified with silver nanoparticles (Ag NPs) entrenched in silicate matrix was effectively applied for the electrocatalytic and sensor applications toward H_2O_2 [46].

However, Au nanoparticles remain the most popular among them. Tan et al. developed a fluorinated graphene/gold nanocage nanocomposite for the simultaneous detection of Cd^{2+}, Pb^{2+}, Hg^{2+}, Cu^{2+}, and Zn^{2+} in peanut and tea [47]. The electrode was suitable for the determination of heavy metal with a linear using square wave anodic stripping voltammetry method (SWASV).

For instance, many metal oxide nanoparticles have been used for the modification of electrodes to improve their selectivity and sensitivity for electrochemical sensors. The work of Koçak et al. studies the rapid, sensitive and selective determination of metoprolol using glutardialdehyde-zinc oxide modified boron doped diamond electrode [17]. Another paper presented the use Fe_3O_4 nanoparticles anchored on carbon spheres (Fe_3O_4/CSs) for the electrochemical sensing of neurotransmitter serotonin (5-HT), the results showed a high sensitivity and a low detection limit 5-HT [48].

Except for the disadvantage of forming metal oxide layer during the process for the metallic electrodes which can hinder the signal. The most notable electrodes are Indium tin oxide (ITO) and Fluorine-doped tin oxide (FTO) which are made of glass coated by a transparent metal oxide film with a great electroactive and optical properties.

I.1.5.5. Ionic liquids

Ionic liquids (ILs) represent a major scientific area as innovative fluids, they are molten salts with a melting point below 100°C, the bulky organic cation and small inorganic/organic anion are usually their main composition. ILs are excellent for a wide range of applications due to their good solvating properties, high conductivity, non-volatility, low toxicity, large electrochemical window, and good electrochemical stability. Recently, ILs-based electrochemical sensors have been developed, although, the use of ILs-modified nanomaterials instead of the materials alone demonstrates better sensing properties [49]. As illustrated in [50], modified paste electrode was employed as an electrode for Isuprel monitoring using a MgO/CNTs nanocomposite and 1-butyl-3-methylimidazolium hexafluorophosphate, the modified electrode showed great ability for the electrochemical detection of Isuprel. For the work [51], the authors reported an electrochemical carbon sensor modified with graphene oxide (GO), silver nanoparticles (AgNPs) and 1-Allyl-3- methylimidazolium dicyanamide ionic liquid. The ionic liquid- based electrochemical sensor has been successfully used for the detection of efavirenz (EFV).

I.1.5.6. Silica modified electrodes

Silica-based materials have a three-dimensional structure with interconnection of open spaces which grant them the particularity of being mesoporous, vigorous inorganic solids with high specific surface area [52]. These compounds gain certain outstanding qualities, including a broad surface area, a strong adsorption capacity, thermal stability and ease of surface modification, they also exhibit the ability to exchange ions through weakly acidic silanol groups (Si-OH) in a slightly alkaline media which would enable high diffusion rates and serve as an

effective aid for the chosen analyte to bind with greater number of readily accessible binding sites. Silica-based materials are highly employed for surface modification of electrodes in electrochemical sensors, especially given their electrochemical inertness in aquatic environment. In the work of Shetti et al., the modification of carbon-based sensor by silica gel caused a considerable increase of the potential due to the cavity structure of the sensor and also effective adsorption of acetaminophen [52]. The silica gel modified electrode was tested for the electrochemical detection of acetaminophen using cyclic voltammetry and differential pulse voltammetry. Whereas, the paper of Liu et al. [53] demonstrated the detection of 4-aminophenol (4-AP) using the indium tin oxide (ITO) electrode modified with vertically-ordered mesoporous silica- nanochannel films. By means of the differential pulse voltammetry (DPV) method, the elaborated sensor was able to detect 4-AP in a wide linear range with great limit of detection.

I.2. Adsorption

I.2.1. Preface

All life on Earth depends on water, and as its consumption expands, serious problems with water quality are emerging. The usual water treatment methods (mechanical and biological) are not effective against certain types of pollution. Therefore, it is necessary to renovate treatment methods that are more efficient and less expensive in order to improve the quality of wastewater treatment [54]. Several researches are focusing on the study and development of new environmental remediation processes proposed for arduous chemical pollutants, such as coagulation, biological treatment, advanced oxidation processes (photofanton, photodegradation), and natural sorption processes (adsorption, absorption, ion exchange) [55].

Adsorption is a technique for separating substances from a fluid phase (aqueous or gaseous), based on the spontaneous process of phase transfer, using an adsorbent which has a high degree of porosity and a large specific surface [56]. This method is applied in several fields, the liquid phase adsorption is used for the treatment of petroleum products, the elimination of organic species and various pollutants in water sources (in other words for the advanced treatment of domestic and industrial wastewater, decolorization of crude sugar syrup and vegetable oils, recovery and concentration of proteins, pharmaceuticals and bio-compounds from dilute suspensions. For gas phase adsorption, this technique is effective for recovery of organic solvent vapours, dehydration of gases, removal of toxic gases for personal protection, separation of gas mixtures, detection of gases such as CO_2 sensors [57].

I.2.2. Adsorption mechanism

Adsorption is a process in which an adsorbate (atom, molecule or ion), in liquid or gas form, accumulates on the surface of a so-called adsorbent solid by physical or chemical forces. The adsorption rate is expressed by the equilibrium adsorption capacity q_e, which is given by the equation [58]:

$$q_e = {}^n\!/\!m_a \qquad\qquad \text{I.3}$$

Where n is the adsorbed amount (in mol or mg), and m_A is the mass of the adsorbent.

The explanation of the adsorption mechanism is related to some chemical aspects such as the active functional groups on the surface of the adsorbent which contribute to the interaction, and the speciation diagram of the adsorbate. The forces responsible for the retention of the adsorbate at the surface of the adsorbent can be physical or chemical depending on the enthalpy of the system. There exist two types of adsorptions [59]:

I.2.2.1. Physical Adsorption (Physisorption)

In a physisorption, there is no exchange of electrons, the adsorbate is attached to the surface of the adsorbent by weak Van Der Walls forces (dipole-dipole interactions, dispersion forces or induction forces). The enthalpy in this case is generally less than 50 kJ/mol.

I.2.2.2.   Chemical Adsorption (Chemisorption)

The bond between the adsorbent and the adsorbate is covalent or ionic in a chemisorption and the process is irreversible. In this kind of adsorption, the electronic properties of the adsorbate are changed, the enthalpy is of an order greater than 50 kJ/mol

Based on the transfer phenomena, the migration of the adsorbate from the fluid phase until its fixation on the surface is established after four main stages (**Fig I.4**), the first is mass transfer of the solute towards the boundary layer around the particles, the second is the transfer towards the external surface, the third is the internal or the intra-particle diffusion, and finally interaction and adsorption on the active site [60].
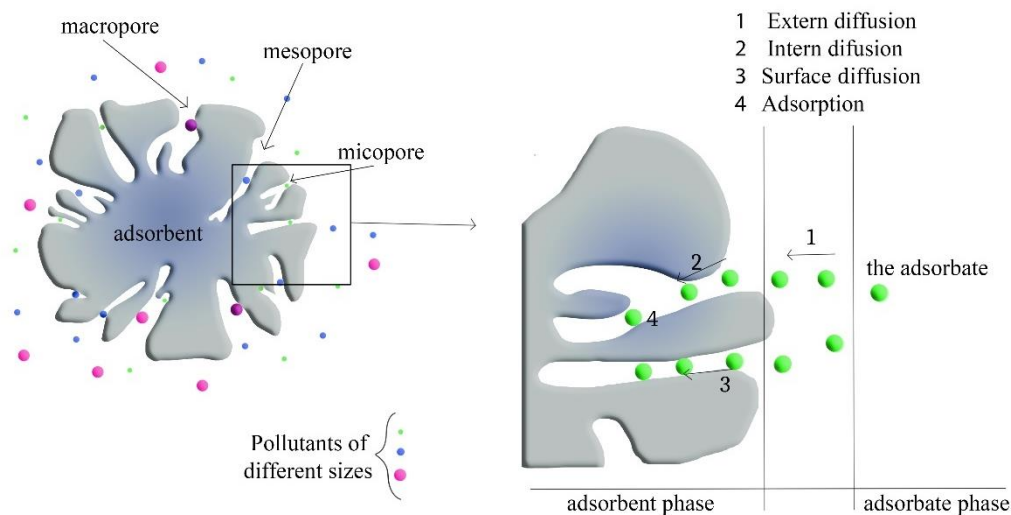
Figure I. 4. Transfer of an adsorbate to the adsorption site mechanism

I.2.3.   Chemical and structural properties of the adsorbent:

The assessment of a good adsorbent is governed by several properties. The first important characteristic is the porosity of the material, it results from a random arrangement of pores and a reticulation of macromolecular species on the grain surface. This is practically the most relevant property for adsorbents. The pore size can be divided into: micropores $\phi < 2nm$; mesopores $2 < \phi < 50nm$ and macropores $\phi > 50nm$. The latter are of primary importance for the determination of the internal volume and the adsorption capacity, while the macropores and the mesopores are responsible for the transfer of matter towards the micropores. The determination of pore size is crucial for better understanding of the kinetics and the mechanism of adsorption process [57].

The second characteristic assigned to the adsorption behaviour is the specific surface area since adsorption is a surface phenomenon. It is mainly governed by micropores and can represent in some cases up to 90% of the total specific surface. On the other side, macropores are important to facilitate access to mesopores and micropores. The specific surface depends in particular on the size of the grains also, when the size of the grains decreases, the specific

surface increases, and the number of active sites increases. The grain size is a crucial factor that influences the rate of adsorption as well [57].

Other factors are also taken into consideration such as the chemical composition including the elements that increase the polarity of the surface, the pH of the medium which affects both the charge of the adsorbate and the surface of the adsorbent, charge and hydrophobicity.

I.2.4.   Adsorption kinetics

The study of the kinetics of adsorption allowed the representation of the speed of the fixation of the molecules of the adsorbate on the surface of the grains of the adsorbent [54]. The most common kinetic models are described below:

I.2.4.1. The pseudo-first order

This model describes a liquid/solid adsorption where the adsorption rate is proportional to the difference between the adsorption capacity at the given time t (q_t) and at the equilibrium (q_e). the pseudo- first order is controlled by **Eq I.4** [61]:

$$Ln(q_e - q_t) = Lnq_e - K_1 t \qquad \text{I.4}$$

Where K_1 is the pseudo-first order rate constant (min^{-1}), t is the time, q_t and q_e are the adsorption capacity at the given time t and at the equilibrium, respectively.

I.2.4.2. The pseudo second order:

It is the most adapted model in adsorption and proposes a chemisorption behaviour for the adsorption process. This model suggests that the adsorption occurs on localised sites without interaction between the adsorbed molecules, hence, the adsorption equilibrium corresponds to the formation of a monolayer on the surface of the adsorbent. The desorption rate is neglected compared with the adsorption rate. The expression describing this model is given by **Eq I.5** [62].

$$\frac{t}{q_e} = \frac{1}{K_2 q_e^2} + \frac{1}{q_e} \qquad \text{I.5}$$

K_2 in this equation represents the pseudo-second order rate constant (g.mg^{-1}.min^{-1})

I.2.4.3. The intraparticle diffusion model

The intraparticle diffusion model is widely applied to simulate the adsorption diffusion kinetics in order to understand the effect of mass transfer and the diffusion process. When the extern diffusion and the surface reaction are the fastest [63], it can be assumed that the intraparticle diffusion is the limiting step of the adsorption, this fact appears in a multi-linearity of the q_t vs $t^{1/2}$ plot, which also corresponds to the existence of other successive steps during the adsorption process [64]. The model is expressed by **Eq I.6:**

$$q_t = K_{in} t^{1/2} + C_{BL} \qquad \text{I.6}$$

Where k_{in} is the equilibrium constant (mg.g^{-1}.min$^{-1/2}$) and C_{BL} is the thickness of the boundary layer (mg/g), if C is equal to 0, the intraparticle diffusion predominates the process.

I.2.4.4. The Elovich model

The Elovich model was originally applied to the adsorption of gases, but can also be used to describe the adsorption of aqueous-phase pollutants such as heavy metals and dyes. The model assumes that adsorption is multilayered, hence the adsorption sites increase until a maximum adsorption value. The equation of this model is [65]:

$$q_t = \frac{1}{\beta}\ln(\alpha_E . \beta_E) + \frac{1}{\beta}\ln(t) \qquad\qquad \textbf{I.7}$$

Where α_E represents the initial rate of the adsorption (mg.g^{-1}min^{-1}) and β_E is the desorption constant (g.mg^{-1})

I.2.5. Adsorption models

When an adsorbent is in contact with an adsorbate in a liquid or gaseous phase, a mass transfer takes place from bulk to the solid phase. We call an adsorption equilibrium the state in which the surface of the adsorbent is exhausted and cannot acquire more molecules. This equilibrium depends on several parameters such as the temperature, the pH of the medium, the concentration of the adsorbate and the mass of the adsorbent. For a single system, the equilibrium equation can be expressed as:

$$q_e = f(C_{eq}, T) \qquad\qquad \textbf{I.8}$$

Where q_e is the amount adsorbed relative to the mass of the adsorbate, and C_{eq} is the concentration of the adsorbate at equilibrium, T is the temperature. Considering that the temperature is held constant during the process, the equation becomes:

$$q_{eq} = f(C_{eq}), \quad T = constante \qquad\qquad \textbf{I.9}$$

To date, no universal equation describes all experimental isothermal curves with the same precision. yet, several models have been established theoretically or empirically to explain the concept of adsorption equilibrium.

I.2.6.1. Langmuir model:

This model assumes that the all the active sites of solids have the same adsorption capacity, so the adsorption mechanism is the same for all adsorbent-adsorbate bonds and the adsorption takes place in a single layer. The Langmuir model gives a theoretical explanation for the system, it proposes that the adsorbed species do not react with each other, and the surface is perfectly uniform [66], which inaccurate in practice where the surface is heterogeneous and the adsorbed molecules react with each other. This model is expressed by the following relationship:

$$q_e = \frac{q_m K_L C_e}{1 + K_L C_e} \qquad\qquad \textbf{I.10}$$

With: K_L: the Langmuir equilibrium constant (L.mg^{-1} or L. mmol^{-1}), q_m: the maximum quantity adsorbed (mg.g^{-1} or mmol.g^{-1}) and Ce: the concentration at equilibrium (mg.L^{-1} or mmol.L^{-1}).

I.2.6.2. Freundlich model:

It is a purely empirical model; it yields that the adsorption sites are heterogeneous and the process occurs only at low or intermediate concentrations. It also admits that the formation of more than one monolayer is possible and does not involve the notion of maximum adsorption. This model is governed by the **Eq I.11** [67]:

$$q_e = K_f C_e^{1/n} \qquad \text{I.11}$$

With: K_F: the Freundlich adsorption constant ((mg. g^{-1}) or (L. mg^{-1})$^{1/2}$), n: a constant linked to the adsorption intensity. These two constants are related to the adsorbate-adsorbent interaction and to the temperature. Adsorption is favourable when 1/n is less than 1.

I.2.6.3. Temkin model

The Temkin model explains linearly the reduction of the adsorption heat, in this model, the interaction energy is uniformly distributed between the particles. The equation explains this pattern [68].

$$q_e = A_F \, lnK_T + A_F \ln C_e \qquad \text{I.12}$$

With: K_T (L/mg) is the Temkin adsorption energy, A_F is a constant which depends on the temperature and the adsorption system such that:

$$A = (RT/b_T) \qquad \text{I.13}$$

With b_T a constant.

I.2.6.4. Dubinin-Radushkevich (D-R) model

The D-R Model assumes that the adsorbent size can be compared to the micropore size [69], for a given adsorbate-adsorbent system, the relation of the adsorption equilibrium can be expressed independently of temperature using the adsorption potential (ε) as shown in **Eq I.14**:

$$q_e = q_{max} \exp\left(-K_{D-R}\varepsilon_{D-R}^2\right) \qquad \text{I.14}$$

With: K_{D-R} is a constant related to the adsorption energy (mol^2 k.J^{-2}), and ε_{D-R} is the Polanyi Potential with:

$$\varepsilon_{D-R} = Ln\ (1+1/C_e). \qquad \text{I.15}$$

The determination of K from the equation leads to the calculation of the average adsorption energy using the equation:

$$E = \frac{1}{(2K)^{1/2}} \qquad \text{I.16}$$

The value obtained here gives information on the nature of the adsorption:

- If E < 8 kJ.mol^{-1}, the sorption mechanism is physical.
- If E is between 8 and 16 kJ.mol^{-1}, ion exchange is dominant.
- If E > 16 kJ.mol^{-1}, intra-particle diffusion dominates sorption.

I.2.6. Type of adsorption isotherms

The term adsorption isotherm refers to a theoretical equation describing the thermodynamic equilibrium state at a constant temperature, the study of the simplest adsorption system leads to a relationship between the adsorbed amount and the adsorbate mass. For the gas-solid phase, six types are known for the description of the isotherm as shown in **Fig.I.5**. Whereas for the liquid-solid system, four main types, C, S, L and H, are presented according to Gilles et al. [70] among which the L and H isotherms are the most frequently obtained.

I.2.7.1. Type C isotherm

This type is characterized by a constant splitting of the solute between the solution and the surface until a maximum adsorption occurs. In general, a linearity is observed when the number of free sites remains invariant during the adsorption, whereas in reality, the molecules of the solute could modify the surface of the adsorbent by activating pores which hadn't been previously activated by the solvent and creates new site.

I.2.7.2. Type L isotherm

In a diluted solution, this type rises a curvature which is explained by the decrease of vacant sites in the substrate as adsorption progresses, implying that the solute molecules are either adsorbed vertically, or there is no strong adsorption competition between the solvent and the solute. In this case the adsorbed molecules are more likely to be adsorbed flat.

I.2.7.3. Type H isotherm

This is a special case of the L curve, except that the solute has some affinity only at low concentrations, so it is fully adsorbed. The first vertical part of this isotherm is formed when the interactions between the adsorbed solute molecules and the surface of the substrate solid are very strong.

I.2.7.4. Type S isotherm

For the S-type isotherms, three experimental conditions related to the solute molecules are necessary, the latter must be monofunctional, show a moderate intermolecular attraction that makes their adsorption vertical, and response to strong competition with solvent molecules or other adsorbed species. Adsorption is therefore easier when the concentration is high.
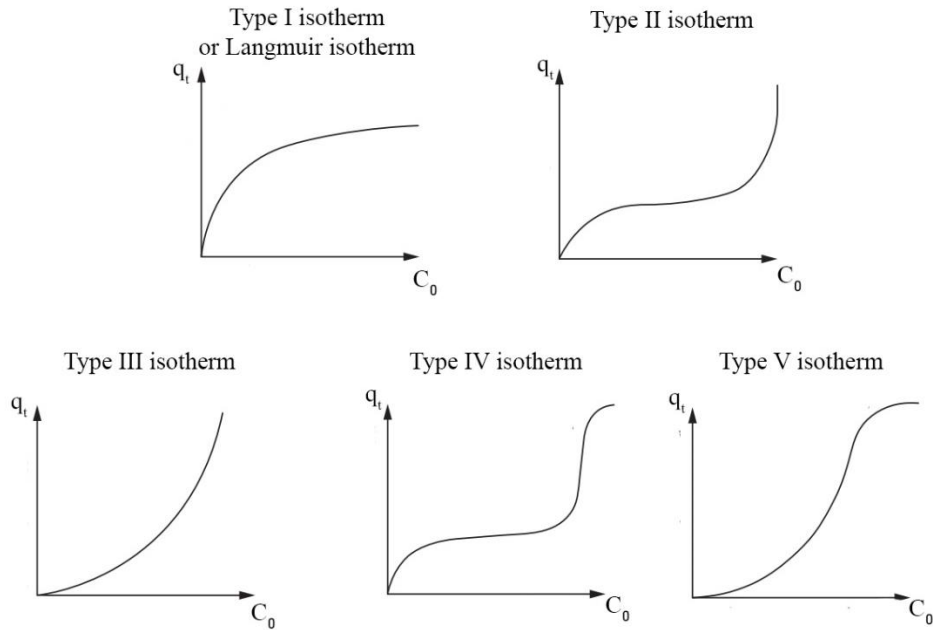
Figure I. 5. The five types of gas-solid adsorption isotherms
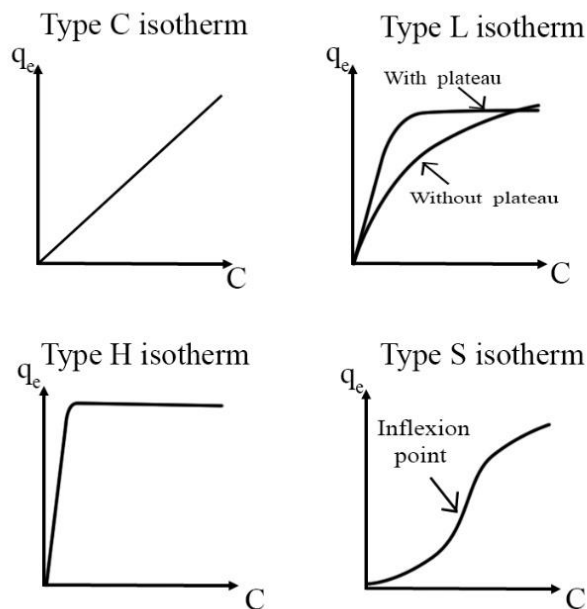
Figure I. 6. the four types of liquid-solid adsorption isotherms

I.2.7. Thermodynamics

The study of thermodynamic parameters, namely standard Gibbs free energy (ΔG^{o}), enthalpy change (ΔH^{o}) and entropy (ΔS^{o}) variations, is an essential step to understand the thermodynamic aspect of the system which can be exothermic ($\Delta H^{\circ} < 0$) or endothermic

($\Delta H°>0$). The value of the heat of adsorption $\Delta H°$ is also the main criteria for differentiating chemisorption from physisorption. The Gibbs free energy G variation is given by **Eq I.17** [56]

$$dG = -SdT + Vdp + \sum_i \mu_i dn_i + \sigma dA \qquad \text{I.17}$$

It depends on the temperature T, the pressure P, the number of moles n_i, and the surface A. in this equation, S represents the entropy, V is the volume, μ_i is the chemical potential and σ is the free energy of surface.

Since the adsorption process is spontaneous, the variation of the Gibbs free energy ΔG_{ads} has a negative value, we can give its relation with the enthalpy ΔH_{ads} and the entropy ΔS_{ads} of the adsorption by the **Eq I.18** [54]:

$$\Delta G_{ads} = \Delta H_{ads} - \Delta S_{ads} < 0 \qquad \text{I.18}$$

Standard Gibbs free energy variation ($\Delta G°$) can be calculated according to the **Eq I.20**:

$$\Delta G^0 = -RTlnK_d \qquad \text{I.19}$$

And Van't Hoff plots of ln K_d versus T^{-1} leads to the determination of $\Delta H°$ and $\Delta S°$ [71].

$$lnK_d = \frac{\Delta S^0}{R} - \frac{\Delta H^0}{RT} \qquad \text{I.20}$$

However, if the medium is aqueous, the capacity of water which is equal to 1000g/L can help with making K_d dimensionless by multiplying it by 1000, **Eq I.21** and **Eq I.22** can be rewritten as [72]:

$$\Delta G^0 = -RTln(1000K_d) \qquad \text{I.21}$$

$$ln(1000K_d) = \frac{\Delta S^0}{R} - \frac{\Delta H^0}{RT} \qquad \text{I.22}$$

I.2.8. Adsorbent materials

A wide variety of materials show a striking adsorption behaviour, these materials used as adsorbents can be of natural origin (mineral clays, zeolite, oxides or biopolymers), or synthetic.

I.2.8.1. Activated carbon

Activated carbon is produced by chemical or gaseous activation of a carbonaceous raw material such as wood and charcoal [73], lignite and lignite coke [74,75] bituminous coal [76], coconut shells [77], sawdust [78],or sunflower stalks [79]. The activation of these organic materials requires a carbonization process. Cellulose structures contain a number of functional groups containing oxygen and hydrogen, the dehydration of the raw material at high temperatures and under pyrolytic conditions removes these functional groups. Following this operation, a carbon skeleton is obtained after the destruction of the cellulosic structure. Activated carbon is the most widely used adsorbent, it has been successfully used for the removal of heavy metals [80], antibiotics [81], pesticides [82] and dyes [83].

I.2.8.2. Clays

Clay materials are mainly phyllosilicate minerals exhibiting layered structural units made up of one or two tetrahedral silica sheets around an octahedral aluminium sheet, with particle size less than 2 μm. Clays have inner surfaces, edges and surfaces-outer surfaces between the silicate layers. The interlayer and outer surfaces are susceptible to being changed during ion exchange and adsorption processes. These materials feature a wide variety of physical properties, such as fineness of particles, hardness, good plasticity, associativity, appropriate shrinkage, high refractoriness and the capacity for surface decoration [84].

Natural Clay materials can be used as demonstrates the work of Yang et al. where the kaolin clay was collected from Guizhou Province, China, then used for the removal of niobium (Nb). Clays can also be chemically synthesised as appears in the work of Xu et al. that scrutinizes the adsorption behaviour of a synthesised LTA-type zeolite for the removal of acid fuchsin [85]. In some researches, clay minerals are modified with an organic or inorganic surfactants to enhance their adsorption capacity such the paper of Abbou et al. which studies the modification of raw clay with Cetyltrimethylammonium Bromide surfactant then use it as an adsorbent for the elimination of methyl orange [86].

I.2.8.3. Metal oxides

Metal oxides consist of a metal cation and an oxide anion with a suitable hydrophilic surface, low solubility, robust mechanical structures and unique stability at different conditions against pollutants, making them among the most excellent adsorbents. Metal oxides are conceived via variable pathways including coprecipitation, hydrothermal, solvothermal, sol-gel, ultrasound-assisted, microwave-assisted, microemulsion and polyol technologies [87]. Several metal oxides have been reported for the removal of pollutants such as NiO [88], MnO_2 [89], CuO [90], Fe_3O_4 [91], V_2O_5 [92], ZnO [93].

I.2.8.4. Polymers

Polymers are a class of natural or synthetic substances composed of macromolecules obtained by the assembly of small entities called monomers. The synthesis of polymers, or the so-called polymerisation, is a process that can be grouped into two families: condensation and addition polymerizations. Polymers show an adsorption capacity similar to that of activated carbon, and their structures are similar to that of ion exchangers, although, their properties depend on the types of monomers and the method of polymerization employed in the synthesis. Polymers are employed alone as showcases the paper of Wang et al. that studies the use of polyacrolein organic gel for the successful removal of acid fuchsin [94], and can be coupled with other materials, such the work of Pandimurugan and Thambidurai where methylene blue dye removal was effected using of novel biocompatible hybrid composite of Seaweed–Zinc oxide–Polyaniline [95].

I.3. Lamellar double hydroxides

I.3.1. Preface

Clays are very common mineral deposits that have been employed in humans' activities since ancient times, especially in ceramic constructions and pottery works. Nowadays, these materials have gained more importance since they have been incorporated in a wide range of industrial and scientific sectors because of their exceptional compositional, morphological, and structural properties [96,97].

The diversity of applications of clays poses a great challenge for mineralogists to grant them a precise definition [98]. From a chemical point of view, they are lamellar materials of two-dimensional character and have a granular and malleable texture when mixed with water and a hard and brittle texture in their dry state. Their structural form is presented in the form of charged sheets separated by an intercalation space occupied by molecules, cations, or anions. The sheets are linked by weak electrostatic bonds (Van Der Waals or hydrogen bonds), which give clay materials a flexible structure and variable intercalation [99].

The classification of clays according to the charge of the sheets leads to two main types of clay. The first type is said to be cationic; its sheets are made up of a succession of tetrahedral or octahedral polyhedra of negative or neutral charge. In this case, the inter-lamellar space is occupied by cations [100]. The second type, called anionic, is the focus of this work.

I.3.2. Generalities

Anionic clays, lamellar double hydroxides (LDHs) or hydrotalcite-like compounds, are natural or synthetic lamellar materials whose layers carry an excess of positive charges induced by the replacement of a part of divalent cations by trivalent cations. The excess charge is compensated by anionic entities placed in the inter-lamellar space [101].

The term "hydrotalcite" is mainly attributed to the natural compound hydroxy-carbonate of aluminium and magnesium. The part (Hydro) means the presence of water, while its resemblance to talc explains the second part (Talcite) [102]. The discovery of the first hydrotalcite goes back to 1842 in Sweden, which was a mineral that can be easily crushed into white powder just like talc. But it was until 1915 that the Italian mineralogist E. Manasse specified its chemical formula, $[Mg_6Al_2(OH)_{16}]$ $[CO_3.4H_2O]$ [103,104]. Twenty years later, Feitknecht and Fischer were able to establish a hydrotalcite from aqueous metallic salts in a basic medium [105], while their structure is only determined by the 70s in the work of Miyata on different anionic clays [106].

LDHs are generated by the formula: $[M^{2+}_{1-x}L^{3+}_x(OH)_2]^{x+}[A^{n-}_{x/n}(H_2O)_y]$ where [107]:

- M^{2+} and L^{3+} are divalent and trivalent cations surrounded by six OH^-.
- A^{n-} is the anion intercalated between the sheets.
- x is the ratio between the number of divalent and trivalent cations.
- y is the number of water molecules in the space between the sheets.

I.3.3.   Crystallography

The structure of LDHs is of the CdI_2 type, in other words, it is a superposition of sheets composed of octahedral structural units where metal cation (divalent or trivalent) is in the centre surrounded by hydroxide ions OH- in octahedral form. the octahedra are connected to each other by their edges in such a way that the hydroxide ion is shared between three octahedra. This arrangement can be likened to brucite ($Mg(OH)_2$) except that part of the divalent metal (Mg^{2+} in this case) is replaced by a trivalent metal generating an excess of positive charges compensated by hydrated intercalary anions to ensure the neutrality of the materials. The substitution induce a distortion in the structure of the sheets due to a compression of the octahedrons of $Mg(OH)_2$, a change is then induced in the distance O-O and Mg-Mg as well as in the angles O-Mg- O [108–111]
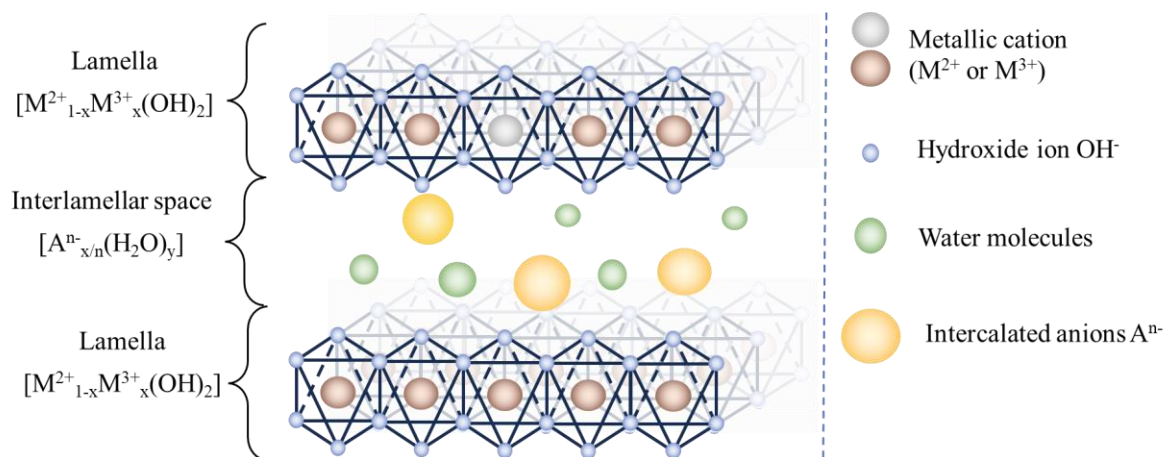
Figure I. 7. Scheme representing the structure of LDH

Table I. 1. Some names of LDHs according to their composition and crystal systems [112].

General formula	Crystal system - class	Name
$[Mg_6Al_2(OH)_{16}]$ $[(CO_3)4H_2O]$	Trigonal- Hexagonal	Hydrotalcite
$[Mg_6Al_2(OH)_{16}]$ $[(CO_3)4H_2O]$	Hexagonal- Di-hexagonal	Manasseite
$[Mg_6Fe_2(OH)_{16}]$ $[(CO_3)4H_2O]$	Trigonal- Hexagonal	Pyroaurite
$[Mg_6Fe_2(OH)_{16}]$ $[(CO_3)4H_2O]$	Hexagonal- Di-hexagonal	Sjogrenite
$[Mg_6Cr_2(OH)_{16}]$ $[(CO_3)4H_2O]$	Trigonal- Hexagonal	Stichtite
$[Ni_6Al_2(OH)_{16}]$ $[(CO_3)4H_2O]$	Trigonal- Hexagonal	Takovite
$[Ni_6Fe_2(OH)_{16}]$ $[(CO_3)4H_2O]$	Trigonal- Hexagonal	Reevsite
$[Cu_4Al_2(OH)_{12}]$ $[(SO_4)4H_2O]$	Hexagonal	Woodwardite

The dispersion of divalent or trivalent cations mainly depends on their relative proportion (the molar ratio) and follows the cationic exclusion rule in the ideal case. The repetition of cations in the plane expressed by the parameter a, is also linked to the type of cation, and consequently to the intermetallic distance [113,114]. The structure is also described by the parameter c which represents the repetition of the stack of sheets, its value depends on the inter-

sheet type [115]. According to the experimental results of the synthesized compounds, the values of α and c obtained approve that the LDHs crystallize either the rhombohedral system R or in the hexagonal system H [116–118].

In reality, the term hydrotalcite is attributed specifically to the compound MgAl-CO_3^{2-}-LDH of molar ratio 3 belonging to the trigonal crystal system, the other types of LDHs, their crystal systems, and their chemical formulas are grouped in **Table I.1**.

I.3.4.   LDHs composition
I.3.4.1.   The lamellas

From the fact that the layers of LDHs contain a divalent and a trivalent metal cation, it is possible to obtain a considerable variability of LDHs by modifying these metals or the ratio between them.

For example, Elmoubarki et al. [119] worked on two LDHs intercalated by the carbonate ion, whose trivalent cation is Fe^{3+}, but varying the divalent cation M^{2+} (Ni^{2+} and Mg^{2+}). These materials are found to be excellent dye adsorbents. Similarly, Gil et al. [113] synthesized three compounds $M^{2+}Al^{3+}$-CO^{3-} LDH such that M^{2+}= Co^{2+} ; Mg^{2+} or Ni^{2+}. The compounds showed impressive results for CO_2 sorption. On the other hand, we find in Serhal's paper [120], a variation of both the divalent cation (Mg^{2+} or Co^{2+}) and trivalent cation (Al^{3+} or Fe^{3+}) keeping the same molar ratio (=2), this work leads to four effective catalysts for the total oxidation of organic compounds.

In a few exceptions, some articles studies LDHs containing three cations, such the work [118] where the co-authors investigate the hydrogen affinity of NiFeTi-CO_3^{2-}-LDH and NiZnTi-CO_3^{2-}-LDH under ambient conditions. The integration of Zn^{2+} and Fe^{2+} in the structure increases the basicity, and thus, improves the affinity of the material.

I.3.4.2.   The interlamellar anion

For LDHs as for other clays, the ion exchange capacity of the intercalary anion opens up a wide horizon to meet the needs of specific applications (medical, catalytic, environment). In this term, several works have succeeded in achieving their goal by ion exchange.

In the article [121], the co-authors investigated the sorption capacity of ZnAl-An--LDH as a function of the spacer anion (CO_3^{2-}, NO_3^-, Cl^-), obviously, the sorption behaviour is dominated by the intercalary species which is explained by the ion exchange ability. Cavalvanti et al. [122] claims that the nature of the interlamellar anion predicts the possibility of sorption. This conclusion is in agreement with the results of Bish [99] which proposes the following order of priority for the anions occupying the space between the sheets:

$$CO_3^{2-} > NO_3^- > OH^- \approx Cl^- > SO_4^{2-}$$
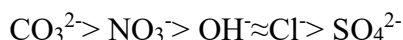
In the meantime, some studies are extended to more complex molecules (organic or mineral) to deal with more productivity. For example, Xu et al. [123] synthesized three LDHs (MgAl-A^{n-}-LDH) by varying the spacer anion (NO_3^-, NO_2^- and p-aminobenzoate), the obtained compounds present a good crystallinity and a broad distribution. Indeed, the intercalary anion

directly influences the size of the inter-lamellar space (0.37, 0.77 et 1.52 nm for intercalation by NO_3^-, NO_2^- and p-aminobenzoate respectively). In addition, this variation leads to a difference in the adsorption capacity of the obtained products.

In the same context, Marreiros et al. [124] inserted an α-diimine (bis(4-HOOC-phenyl)-acenaphthenequinonediimine) in the intercalary space of two LDHs: ZnAl-LDH and MgAl-LDH in a first step, the second step was to insert the complex ([Mo(CO)$_3$X$_2$(NCMe)$_2$] (X = I, Br)). These compounds are oriented for the epoxidation of an olefin with a 100% conversion.

I.3.4.3. Molar ratio

The molar ratio is a major factor in the crystallinity of LDHs. In the work [125], the authors studied five ZnAl-NO^{3-}LDH compounds with different molar ratios (2, 3, 4, 5 and 6). The XRD results show that the crystallinity of the compounds decreases when the cationic ratio increases, this is due to the sheet distortion due to the size difference between Zn^{2+} and Al^{3+}. On the other hand, when the ratio increases beyond 4, a ZnO phase is detected in the compound. These results are in agreement with the analysis of Sun et al. [126] who studied 4 molar ratio (1, 2, 3 and 4) of the ZnAl-Cl$^-$-LDH compound, the results show that the largest molar ratio (≈ 4) has the lowest stability and agglomeration, this is explained by its low zeta potential resulting from the low content in Al^{3+}.

The ratio M^{2+}/M^{3+} does not only influence the crystallography of the LDH compounds but also their properties. The article [127] confirms that the variation of the molar ratio induces compounds with different specific surfaces. While the work [128] shows that the basicity and the activity of MgAl-CO$_3^{2-}$-LDH increases with the molar ratio.

In general, al the previous articles confirm that the crystallinity is more important when the ratio is between 1 and 3 to ensure the stability of the compound, greater values can also cause the formation of an excess of metal hydroxide or other undesirable compound.

I.3.4.4. Conclusion

Literature presents a great diversity of LDHs driven by the variation of divalent and trivalent cations, intercalary anions, and the M^{2+}/M^{3+} molar ratio. In general, the sheets consist of two (in some exceptions three [118,129]) metal cations, the first is divalent (M^{2+}: Mg^{2+}, Zn^{2+}, Co^{2+}, Ni^{2+}...), while the second is trivalent (M^{3+}: Al^{3+}, Fe^{3+}, Cr^{3+}, Ga^{3+}...), these elements are chosen in such a way that the size of M^{3+} is close to the size of M^{2+} to keep the crystallinity and the geometry of the sheets. The proportion between the two metals is a variable factor. The spacer anion can be an inorganic or organic species. **Tables I.2** and **Table I.3** summarize the different combinations of two and three metal cations with their molar ratios and the space occupying the inter-sheet space.

Table I. 2. Summary of LDHs based on two metal cations, their molar ratios, and their methods of synthesis

$M^{2+} M^{3+}$	A^{n-}	Synthesis root	M^{2+}/M^{3+}	Reference
Mg Al	CO_3^{2-}	Co precipitation	3	[117]
	NO_3^-	Electrosynthesis	2; 3	[130]
Mg Fe	NO_3^-	Coprecipitation	2	[120]
	CO_3^{2-}	Coprecipitation	3	[119]
Zn Al	CO_3^{2-} or NO_3^-	Coprecipitation	1.25	[121]
	CO_3^{2-}	Coprecipitation	1; 2; 3; 4; 5	[131]
	NO_3^-	Coprecipitation	4	[132]
Zn Fe	Vanadate	Coprecipitation	2	[133]
	NO_3^-	Coprecipitation	3	[134]
Zn Ti	NO_3^-	Coprecipitation	2	[135]
	NO_3^-	Coprecipitation	5	[134]
Ni Al	CO_3^{2-}	Coprecipitation	2	[136]
	NO_3^-	Electrosynthesis	2; 3	[130]
	CO_3^{2-}	Hydrothermal	2; 3; 4	[137]
Ni Fe	CO_3^{2-}	Coprecipitation	3	[119]
Ni La	NO_3^-	Electrosynthesis	2; 3;4; 5;10	[138]
Ni Mn	CO_3^{2-}	Coprecipitation	2	[136]
Ni Ti	NO_3^-	Coprecipitation	2	[139]
Co Al	NO_3^-	Coprecipitation	2	[140][120]
	NO_3^-	Electrosynthesis	3	[141]
Co Fe	NO_3^-	Coprecipitation	2	[120]
Cu Cr	NO_3^-	Coprecipitation	1; 2 et 3	[142]
Cu Al	CO_3^{2-}	Coprecipitation	2	[136]
Cu Mn	CO_3^{2-}	Coprecipitation	2	[136]
Ca Cl	NO_3^-	Coprecipitation	2	[143]

Table I. 3. Summary of LDHs based on three metal cations, their molar ratios, and their methods of synthesis

$M^{2+}M^{2+}M3^+$	A^{n-}	Synthesis root	$(M^{2+}M^{2+}):M^{3+}$	Reference
Ni Fe Ti	CO_3^{2-}	Coprecipitation	2	[118]
Ni Zn Ti	CO_3^{2-}	Coprecipitation	2	[118]
Ni Zn Al	CO_3^{2-}	Coprecipitation	3	[144]
Cu Zn Al	NO_3^-	Coprecipitation	4	[145]
Cu Mg Al	CO_3^{2-}	Coprecipitation	3	[129]

I.3.5.   synthesis methods

Given the satisfactory geometric and structural properties of LDHs and the plurality of their fields of application, synthesis methods are increasingly developed to achieve the desired characteristics.

I.3.5.1. Coprecipitation

Co-precipitation is an old method that still used today for the synthesis of LDHs, it is simple and provides compounds that can be applied practically in all fields. It is the simultaneous precipitation of metal hydroxides ($M(OH)_2$ and $M(OH)_2^+$) by adding a base [106,110] according to the reaction:

$(1-x) M^{2+} + xM^{3+} + (x/n) An^- + 2OH^- + y H_2O \rightarrow [M^{2+}_{1-x} L^{3+}_x(OH)_2]^{x+} [A^{n-}_{x/n} (H_2O)_y]$ I.23
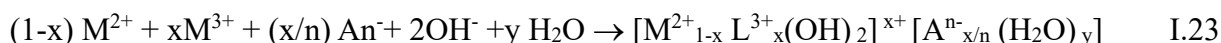
However, the following conditions are taken with caution because of their influence on the properties of the final compound [110,146]:

- Precipitation pH: crystallinity increases with pH, but very high values can produce undesirable phases [132]
- The initial concentrations of metal cations which depends on the molar ratio [131].
- The concentration of the alkaline solution: the concentration of NaOH depends on the concentrations of the metals ($C_{NaOH} = 2C_{M(II)}$; $C_{NaOH} = 3C_{M(III)}$), and the concentration of the A^{n-} precursor must be in excess of the required amount ($C_{A^{n-}} > 2C_{M(III)}$) [147].
- The aging time: a prolonged period can destroy the structure, while a short period is insufficient for good crystallization [148]
- The temperature

Co-precipitation can be divided into several types as demonstrated below:

I.3.5.1.1.   Coprécipitation at contant pH

For this type also called co-precipitation at high supersaturation, the precipitation is carried out in such a way that the pH of the medium remains constant during the synthesis. In the article [120], a solution of M^{2+} and M^{3+} nitrate ($M^{2+} = Mg^{2+}$ or Co^{2+}; $M^{3+} = Al^{3+}$ or Fe^3) is dropwise added to a solution of $NaCO_3$ (1M) whose pH is fixed at 10 by NaOH (2M), the mixture is kept under stirring after the end of precipitation for 24 hours to ensure the formation of the structure.

Another work reports the same steps for the synthesis of $ZnAl-NO_3-LDH$ ($M^{2+} / M^{3+} = 4$) but with different pH values (6, 7, 8, 9 and 10). The crystallinity of the material increases with increasing pH [132]. The results of the XRD show the presence of a new phase attributed to the compound $ZnAl-CO_3^{2-}-LDH$ in the material synthesized at pH=10, this is explained by the dissolution of CO_2 from the air in the solution which is favoured by OH^- ions. The co-precipitation at high supersaturation is used in various works for the realization of LDHs [136,142,149].

I.3.5.1.2. Coprécipitation at variable pH

This method is also called co-precipitation at low supersaturation, it consists of the dropwise adding of a basic solution to the mixture containing the metal cations, the operation increases the pH of the medium to a value high enough for the precipitation of the LDH. This process presents itself clearly in the synthesis of ZnAl-NO$_3$$^-$-LDH [150], a solution of NaOH(2M) is added to the mixture of zinc and aluminium nitrates up to a pH= 7 under constant stirring. Likewise, the work [134] gives rise to the two compounds ZnAl-NO$_3$$^-$-LDH and ZnFe-NO$_3$$^-$-LDH by increasing the pH to 7.

I.3.5.1.3. Coprecipitation by urea

Urea CO(NH$_2$)$_2$ is a base whose decomposition can be controlled by temperature and is accompanied by an increase in pH. Its use as a source of OH$^-$ gives a mono-dispersed particle size, and allows kinetic control of the coprecipitation [151]. The technique consists in dissolving the urea in a solution containing the precursors of the metals, then acting on temperature and heating rate until the precipitate is obtained, as shown in the article [139] for the synthesis of NiTi-CO$_3$$^{2-}$-LDH, or the article [152] for the synthesis of CoAl-NO$_3$$^-$-LDH.

a) Coprecipitation at variable pH

b) Coprecipitation at constant pH

Figure I. 8. The difference between co-precipitation at variable pH (a) and at constant pH (b)

I.3.5.2. Ionic exchange

The space between the sheets requires an order of priority concerning the intercalary anion according to its charge, its nature and mainly its diameter. In some cases, the solution is purged by a stream of N$_2$ to remove contamination by CO$_3$$^{2-}$ to have compounds intercalated by another anion [115,132], or use another step that leads to the desired intercalation. Among the methods applied when the LDH cannot be formed directly is ion exchange, which is the replacement of an intercalary anion by another anion following the demands of the application. The initial compound can be obtained naturally or by another synthetic route. This method is
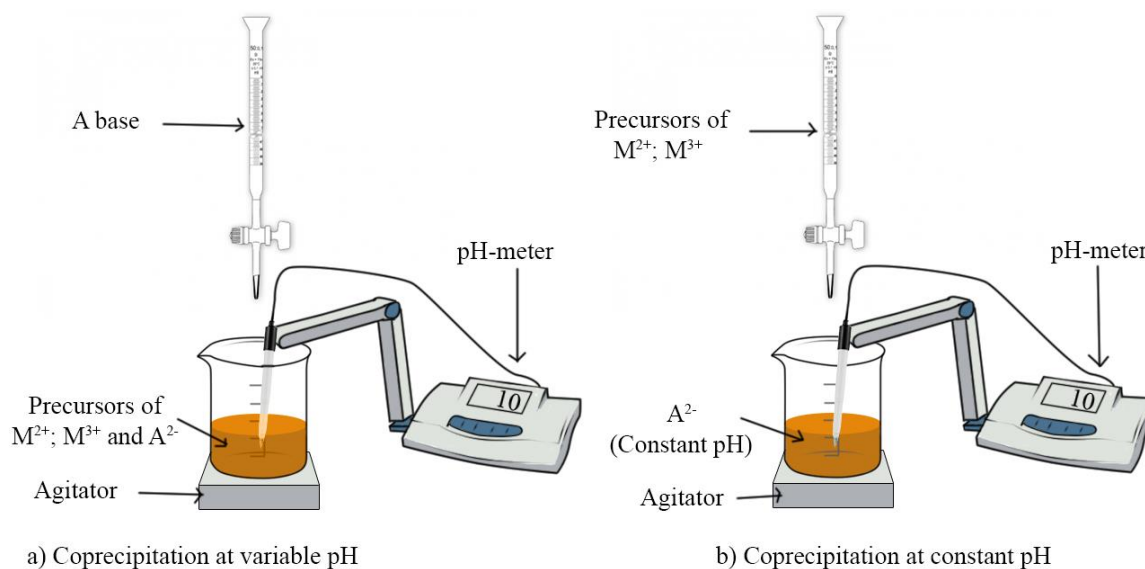
employed in the work of Brahuie et al. [150] for the intercalation of chlorogenic acid into the structure of $ZnAl-NO_3^-$- LDH.

Returning to the work of Marreiros et .al [124] who studied two LDHs, commercial $MgAl-CO_3^{2-}$-LDH and synthesised $ZnAl-CO_3^{2-}$LDH. Ion exchange is used first in the decarbonation step of $ZnAl-CO_3^{2-}$-LDH, about 1.0 g of the LDH is dispersed in 1 L of NaCl (1.0 M) and HCl (3.3 mM). The reactor is closed and purged with N_2 to eliminate all traces of CO_3^{2-}, this operation is an ion exchange of CO_3^{2-} by Cl^-. The resulting $ZnAl-Cl^-$-LDH material is then washed and treated with NaOH (1.0M) for a second ion exchange of Cl^- by hydroxide ions giving $ZnAl-OH^-$-LDH.

I.3.5.3. Hydrothermal Method

In order to synthesize a material, an additional step called "hydrothermal treatment" can be performed to improve crystallinity and particle size distribution. This operation uses a Teflon lined stainless steel autoclave to perform the reaction at the same operating temperature and pressure. In particular, we can cite the work of [153] who used this treatment at a temperature of 160°C for 24 hours to synthesize NiFe-LDH to a high degree of crystallinity.

Likewise, the authors [154] reports the use of the hydrothermal method to synthesize NiCo-LDHs on a piece of carbon fibre (FC), for this reason, the piece of FC is emerged in a solution containing the chlorides of Co and Ni and transferred to an autoclave at 120°C for 12 hours. According to [154] an average mass of 2.5-3 $mg.cm^{-2}$ of product. In addition to these two articles, the literature exposes other works involving this method [155–158].
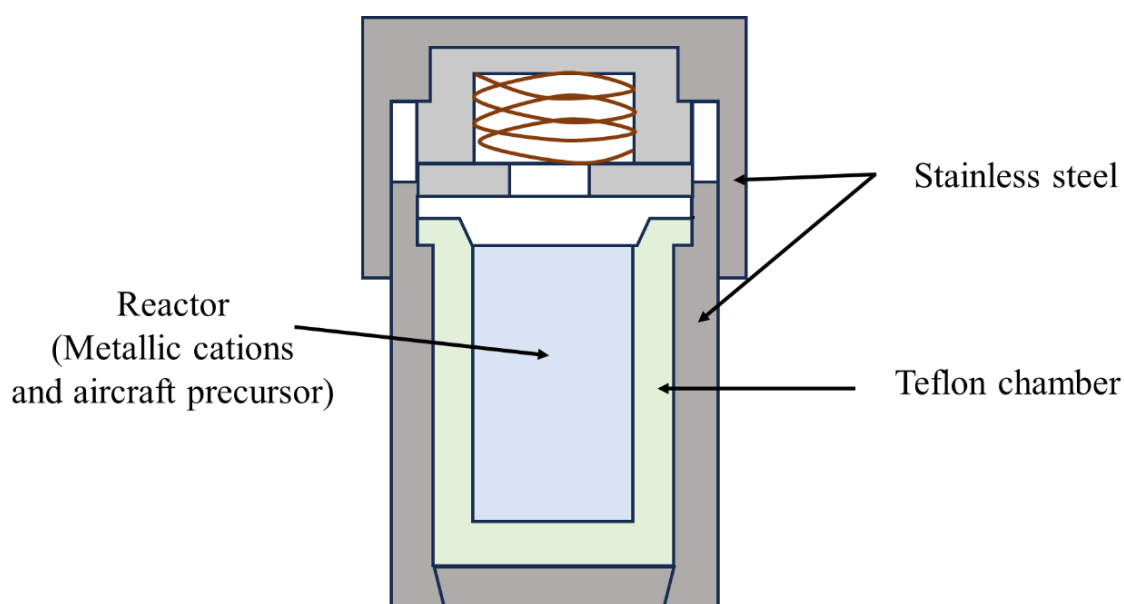
Figure I. 9. Experimental device of a Teflon-lined stainless-steel autoclave

I.3.5.4. Reconstruction from oxides

LDHs are characterized by the memory effect, this means that a structure destroyed by an external effect (calcination for example) can crystallize by resuming their original structures. For example, In the intercalation step of MgAl-CO_3^{2-}-LDH by the BIAN(α-diimine(bis(4-HOOC-phenyl)-acenaphthenequinonediimine)) in [124], the commercial product is calcined in order to eliminate the carbonates, the calcination is accompanied by the collapse of the sheets. On the other hand, the deprotonated ligand BIAN will be intercalated allowing the reconstruction of the lamellar structure. Another work which targets the memory effect of LDHs shows that the products resulting from calcination have a high adsorption [159].

I.3.5.5. Electrosynthesis

It is a promising way that involves electrochemical processes to form thin films of LDHs on a given substrate (Platinum, Nickel, Graphene...[160–162]). The first work that reports this method was carried out in 1994, a series of NiM-LDH (M= Al^{3+}, Cr^{3+}, Mn^{3+} ou Fe^{3+}) of ratio M^{2+}/M^{3+}=3, are deposited on a platinum electrode by cathodic reduction of nitrates by fixing the current at 65mA.cm^{-2} for 4 hours. This method is then delivered to the manufacture of LDH films.

Along the same lines, an Italian team presents several works concerning the electrodeposition of hydrotalcite-like compounds on platinum electrodes. In 2013, their paper [130] shows the formation of NiAl-LDH and MgAl-LDH with different cationic ratios (2/1 and 3/1) by chronoamperometry by varying the potential value from -0.5V/SCE to -1.3V/SCE. While the article [163] consider the application of this method on four different M Al-LDHs(M^{2+}=Co^{2+}, Ni^{2+}, Zn^{2+} et Mg^{2+}). Three years later, work on the electrosynthesis of CoFe-LDH and CoAl-LDH is highlighted [160], this research extends to the study of the electrochemical performance of the obtained compounds.

The electrodeposition process is based on the formation of hydroxide ions by a reduction reaction of the species existing in the medium, the production of OH^- ions increases the pH in the vicinity of the surface of the electrode which allows the formation of the LDH film [130,161,163].

$2H^+ + 2e^- \rightarrow H_2$	$\Rightarrow E°= 0.000$ V/$_{SCE}$	**I.24**
$2H_2O + 2e^- \rightarrow H_2 + 2OH^- +2é$	$\Rightarrow E°= -0.828$V/$_{SCE}$	**I.25**
$O_2 + 4e^- +2H_2O \rightarrow 4OH^-$	$\Rightarrow E°= 0.400$V/$_{SCE}$	**I.26**
$NO_3^- + 2H^+ + 2e^- \rightarrow NO_2^- + H_2O$	$\Rightarrow E°= 0.934$ V/$_{SCE}$	**I.27**
$NO_3^- + 10H^+ + 8e^- \rightarrow NH_4^+ + 3H_2O$	$\Rightarrow E°= 0.360$V/$_{SCE}$	**I.28**
$NO_3^- + H_2O + 2e^- \rightarrow NO_2^- + 2OH^-$	$\Rightarrow E°= 0.010$V/$_{SCE}$	**I.29**
$NO_3^- + 7H_2O + 8e^- \rightarrow NH_4^+ + 10OH^-$	$\Rightarrow E°= -0.120$V/$_{SCE}$	**I.30**
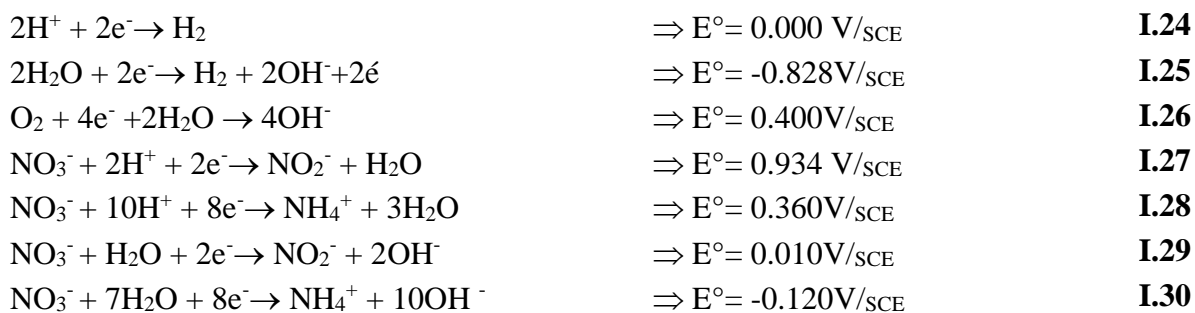
The pH is governed by the value of the applied potential, and its value increases when the potential is more cathodic, except that very negative values have an unpleasant effect on the procedure because of the formation of hydrogen bubbles on the surface [130].

Electrosynthesis is also possible for the preparation of composite or hybrid materials. For example, the work [162] report electroplating on a nickel plate of the composite material NiCo-LDH@Mn$_3$O$_4$. First, NiCo-LDH is prepared by cathodic oxidation (E=-1.0V/Ag/AgCl) for 15 minutes on a nickel plate. This procedure results in a sample with an average of 1.30 mg.cm^{-2}. The second step that leads to the NiCo-LDH@Mn$_3$O$_4$ composite is the use of the NiCo-LDH carrier nickel plate as a working electrode, the composite layer in question is manufactured with a final mass of 1.80 mg.cm^{-2} [162]. The paper [164] explains the preparation of a heterostructure of gold and LDH by the same method.

I.3.5.6. Other methods

The literature presents other methods and pathways for obtaining LDHs, among them is the sol-gel method presented in the paper [165], it consists in forming a gel by adding an oxide to the solution containing the precursors of the metal cations. The same method is employed by Prinetto et al. [166] for the realization of two materials MAl-LDH(M^{2+}= Mg^{2+} ou Ni^{2+}).

The article [167] offers a co-condensation and co-condensation-evaporation methods to synthesize the compound MgCoAl-CO$_3^{2-}$-LDH of cationic ratio: 1/0.2/1.8. The use of a condenser allows continuous solvent recovery. The second method adds a solvent evaporation step after the precipitation which leads to a gel. These synthetic pathways produce LDHs with a large specific surface area, ordered porous chains and a wide pore distribution [167].

Emulsion-mediated synthesis is a method that appears in the work of Petrilini et al. [168] to produce MgAl-LDH material. Its advantage is the ability to control the structure and increase the range of pores. Another method is presented by a Chinese team [169] in their synthesis of ZnAl-LDH, which is a substitution of Zn^{2+} by Al^{3+} in zinc hydroxide, which leads to its transformation into LDH.

I.3.6. Properties of LDHs
I.3.6.1. Ionic exchange

It is the possibility of changing the original spacer anion of the compound by another anion. This characteristic is convenient for the intercalation of LDHs with specific molecules, or even for adsorption [170]. The ion exchange is mainly the result of the excess charge induced by the presence of a trivalent cation in the structure, the additional charge must be neutralized, hence the affinity of LDHs towards molecules of anionic character [121,171]

I.3.6.2. Electrochemical properties

The analysis of the electrochemical performances of LDHs is a subject of considerable interest thanks to their advantageous characteristics. First of all, the presence of a trivalent cation in the sheets improves the electrical conductivity of the compound, this is the origin of its cyclic stability [72]. In addition, morphological variability plays an important role in its

corrosion resistance [79]. Consequently, several electrochemical performances are attributed to LDHs, which gives them a diversity of electrochemical applications [68].

I.3.6.3. Memory effect

It is a physico-chemical phenomenon that allows the material to restore its original structure when it is destroyed following calcination processes [172]. This property is generally related to the reconstruction of LDHs as a method of synthesis, but often used for other applications such as adsorption [173].
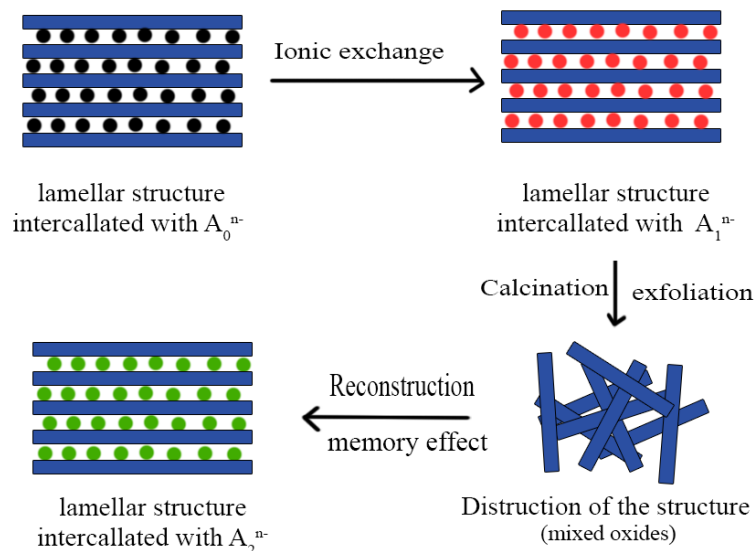
Figure I. 10. Schematic representation of the memory effect.

I.3.6.4. Magnetic properties

The magnetic character of LDHs is due to the presence of iron, iron oxide, or magnetite in their structures. Xu et al. [127] estimates this property by synthesizing Mg-Fe-CO_3-LDHs with different molar ratios of M^{2+}/M^{3+} = 2, 3 et 4, the recovery of the material is carried out by applying a magnetic field at the end of the reaction which affirms its magnetic aspect. Several other examples present the combination of LDHs materials with iron oxide (magnetite) to obtain the magnetic character. The article [174] reports the synthesis under ultrasound (100 KHz, 50W) of a magnetic LDH (Fe_3O_4-LDH) with three compositions (Mg, Cu et Al) and at different molar ratios using magnetite (Fe_3O_4). This junction is not primitive, Zhang et al. [175] were able to make a similar composite material by adding graphene oxide (OG) to the whole. The incorporation of magnetite with LDHs appears also in several other works [176,177] [178].

The separation of catalysts and their regeneration at the end of reactions is one of the difficulties facing researchers in this field. This is where the advantage of this property appears, which lies on the ease of recovery of the magnetic LDH by applying a magnetic field. This prevents catalyst loss and improves its recovery rate during the separation process [127,178].

I.3.7. Applications of LDHs

I.3.7.1. Catalytic applications

Catalysis is the acceleration or triggering of a reaction by the presence of a catalyst, which is a neutral substance in the reaction medium, and only serves to guide the kinetics of the reaction. The use of hydrotalcite-like compounds as catalysts is very well answered in the literature [124]. The work of Munonde et al. [179] presents the catalytic properties of a NiFe-LDH deposited on a black carbon plate for the oxygen evolution reaction, the exfoliation of the sheets is an additional step used to improve the performance of the catalysts. Dib et al. [117] also synthesized an LDH based on Mg and Al to catalyse the condensation reaction of 3-amino-1-phynyl-2-pyrazolin-5-one with the aromatic aldehyde.

The use of LDHs as catalysts is also reported in the following works: the deoxygenation of vanilin by CoAl-LDH/pd [152]; the oxidation of volatile organic compounds by Mg/Co-Al/Fe- LDH [120]; olefin epoxidation by ZnAl-LDH and MgAl-LDH functionalized by H_2BIA and a Mo complex [124].

I.3.7.2. Electrocatalytic application

In order to increase the kinetics of certain electrochemical reactions or even to trigger them, LDHs are frequently available to catalyse these reactions, such the reaction of oxygen devolution, in other words, the electrolysis of water is a process widely used for the production of H_2 et O_2.

In the same sense of applications, the work [180] investigates the activity of NiAl-LDH deposited on gold nanoparticles toward the electro-oxidation of methanol, the material exhibits impressive results for the reaction involved. While Wong et al. [174] expose the assemblage of magnetite with an LDH structure for application in sono-catalytic nitrate reduction. Therefore, the use of LDH-based catalysts in this field is the subject of several research[128,161,179,181].

I.3.7.3. Photocatalytic application

Heterogeneous photocatalysis is an advanced oxidation process that is gaining considerable field of study in recent years. It has the advantage of using clean, free energy (sunlight) to break down pollutants into non-toxic or less toxic products. Several papers study the photocatalytic properties of LDHs. The work of Zhu et al. [135] report the photocatalytic behaviour of silver nanoparticles coated with ZnTi-LDH, The junction shows efficiency for the photo-degradation of Rhodamine-B and NO. These results are analogous to those of Yang et al., who succeeded in degrading organic pollutants (methylene blue and tetracycline) by ZnFe-LDH and the mixed metal oxides resulting from its calcination [182]. Other papers that report the use of LDHs in photocatalysis are summarized in **Table I.4.**

Table I. 4. Recent papers reporting the use of LDH in photocatalysis.

LDH	Nature of the light	Polluant	Réf
ZnCr-LDH	Sun light	Rhodamine B Rhodamine 6G	[183]
ZnFe-LDH	Sun light	Methyl purple Malachite green	[184]
ZnTi-LDH	UV light	Methylene blue	[185]
MgAl-LDH	UV light	- Naproxen de sodium - Anti-inflammatory non-steradian - Chlorhydrate oxytetracycline	[186]
ZnAl-LDH	UV light	Methyl orange	[187]
ZnAl-LDH	High pressure xenon lamp	2-Propanol	[188]
ZnAl-LDH	mercury vapor lamp	Methylene blue	[189]
MgAlSn- LDH	UV light	Phenol	[190]
ZnAlCe-LDH	UV light	Phenol	[191]
MgAlTi- LDH	Xenon lamp	Methylene blue	[192]
ZnO/ZnFe-LDH	Xenon lamp	Acid red Chrome IV	[193]
TiO_2/MgAl-LDH	UV light	Phenol	[194]
SnO_2/MgAl-LDH	UV light	Methylene blue	[195]
TiO_2/Ag/ MgAl-LDH	Mercury vapor lamp	Phenol	[196]
CuO/CuZnAl-LDH/ZNO	UV light	Methanol	[197]

I.3.7.4. Medical application

LDHs can be used in pharmaceutical manufacturing, the article [198] demonstrates the association of a drug (Nimesulide) with an LDH in order to increase its solubility, another advantage is revealed here, it is the reduction of gastric irritation by LDHs which happens to be natural antacids. The use in the pharmaceutical field also appears in the work of Posati et al. [199] whose goal is to combine keratin with hydrotalcite nanoparticles containing diclofenac, the resulting hybrid compound confirms their use as drug delivery systems.

I.3.7.5. Application in electrochemistry

Due to the electrochemical properties of LDHs, these materials are increasingly propagated as electrodes. The specific capacitance of LDHs is an important characteristic that allows their use as supercapacitors as established by the results of Liu et al. [165]. Thus, Bai et al [200] uses a hierarchical structure resulting from the combination of LDHs with nano-files of $ZnCo_2O_4$ in order to improve their performance as super-capacitors. On another side, Guan

[201] benefits from the rhombic dodecahedral hollow morphology of CoSx/NiCo-LDH compound for this application. While Li et al. involve a sandwich structure of NiMn-LDH/reduced grapheme oxide, the compound exhibits a conserved specific capacitance for application as a supercapacitor.

In the electrochemical field, the development of resistant materials in order to coat other less resistant materials is a very important subject that conquers several researches. LDHs, with their high resistance, are applicable compounds in this respect. The paper [202] confirms the effectiveness of coating by LDHs to increase the resistance of a Mg alloy, the same concept of protection of this Mg alloy by a layer of LDH material is investigated in the article [203], but this time with the incorporation of Al_2O_3 nanoparticles deposited on the surface.

I.3.7.6. Application in electrochemical sensors

As detailed in the first part of this chapter, electrochemical sensors have widely been employed as an acceptable technique because of their instrument simplicity, timesaving, sensitivity, and in-site in situ analysis. LDHs have been used as electrode modifiers to advance the electrochemical signals.

LDHs are taking place in carbon dioxide sensor and storage technology as they are compatible and promising compounds for industrial application. The paper [204] prescribes the main characteristics of LDHs which grant them the possibility of application in this field, starting from being chemisorbents and very selective and suitable for CO_2 recovery even at high temperatures (200-500°C). Likewise, they are materials that are easy to regenerate, and have good hydrothermal and mechanical stability. Although the work [205] proposes a hydrotalcite-like compound impregnated with sodium nitrates, the impregnation of $NaNO_3$ in the LDH structure increases its basicity and influences the sorption performance towards CO_2. In addition to CO_2, LDHs are used for the detection of other molecules as summarizes table.

Table I. 5. Recent LDHs used in electrochemical sensors

Material	Technique	Target molecule	LOD	Ref
NiCo-LDH	CV	Carbendazim	0.001 μM	[206]
NiCo-LDH	CV	Lactate	0.533 mM	[207]
NiCo-LDH	CV	Dopamine	/	[208]
hydroxylated multi-walled carbon nanotubes/CoAl-LDH/	DPV	Hydroquinone Catechol	0.074 μM 0.076 μM	[209]
carbon nanodots/CoFe-LDH	CV	Hydrogen peroxide	0.04 μM	[210]
g-C_3N_4/CuAl-LDH	DPV	Diclofenac sodium	0.38 μM	[211]
Fe_3O_4/NiAl-LDH	CV	Tramadol	0.30 μM	[212]
Fe_2O_3/Ni/Al-LDH	CV	Mercury ion	0.046 μM	[35]

I.3.7.7. Application in adsorption

Due to the ion exchange property, LDHs stand out as an excellent practical adsorbent in the environmental field. The adsorption capacity of vanadium (V) by MgAl-LDH is caused mainly by ion exchange according to the explanation given by Wang et al. [213], these results are confirmed by the paper [171] by studying the adsorption of Congo red and Cr(VI) in anionic form $Cr_2O_7^{2-}$ on NiCo-LDH, this work establishes the selectivity of these compounds towards anionic pollutants. Several researches that reported the use of LDHs as adsorbents are summarized in **Table I.6**.

Table I. 6. Recent LDHs used in adsorption

$M^{2+} M^{3+}$	A^{n-}	$M^{2+}:M^{3+}$	Adsorbate	q ($mg.g^{-1}$)	Ref
MgAl	NO_3^-	2:1	Cu^{2+}, Pb^{2+}, Zn^{2+}, Ni^{2+}	/	[66]
	Sodium polyacrylate	2:1	methylene blue Pb^{2+} Hg^{2+}	210.9 345.4 142.7	[71]
	CO_3^{2-}	1:3	Phosphate anions	23.792	[214]
MgFe	CO_3^{2-}	3:1	Methylene blue Malachite green Methyl orange	18.54 108.39 62.28	[119]
	CO_3^{2-}	3:1	acid brown 14	41.7	[159]
ZnAl	NO_3^- Cl^- CO_3^{2-}	1.25:1	Phosphate anions	84 57 14	[121]
	Cl^-	3:1	Nitrate ions	295.62	[215]
	CO_3^{2-}	2:1 3:1	Methyl orange	/	[216]
NiFe	CO_3^{2-}	3:1	Methylene blue Malachite green Methyl orange	31.7 61.41 95.6	[119]
	Sulfonic Acid	3:1	Cd^{2+} Mn^{2+} Co^{2+}	266.16 175.60 106.56	[217]
	NO_3^- Chitosan	2:1	As^{3+}	93.15 /	[218]
NiCr (FA) NiCr (H_2O)	NO_3^-	2:1	Methyl orange	806 740	[219]
CoFe	CO_3^{2-}	2:1	Cr	/	[220]
NiAl	NO_3^-	1:2	Eosin yellow Malachite green	60.67 94.34	[221]
CoAl	NO_3^-	1:2	Eosin yellow Malachite green	41.52 72.20	[221]

I.3.7.8. Other applications

The Chinese team [222] used LDH-modified asphalt on more than ten kilometres of road in China to improve its resistance. The analysis of this combination after four years shows the effectiveness of LDHs in increasing the aging resistance of asphalt concrete.

Cellulose conversion is considered as an alternative to petroleum given the depletion of petroleum reserves, therefore LDHs are used by Guarin et al. [223] for the conversion of this biomass into chemicals

the authors [224] provides another dimension of application, this team investigated the properties of LDHs for the absorption of ultraviolet radiation. The research leads to an optimal compound (ZnTi-LDH) which has the best absorption properties in the UV, which opens a perspective for the application of this material for sunscreens.

I.3.8. Recapitulative

Lamellar double hydroxides or hydrotalcite-like compounds are promising materials in several fields of research. This family includes a wide variety of compounds that exhibit several properties related to their composition, morphology and chemical activity. LDHs are rarely found in nature, but relatively easy to synthesize. Moreover, there are different synthetic routes to achieve this structure, the properties of which depend on the different steps and conditions carried out according to the method chosen.

Currently, LDHs receive considerable attention in several fields of application, their plurality of characteristics and properties, giving the possibility their integration in the environmental, medical, biological and industrial fields.

References

[1] N. Haddadou, N. Bensemma, G. Rekhila, M. Trari, K. Taïbi, *"Journal Photochem. Photobiol. A Chem.* **2018**. DOI: 10.1016/j.jphotochem.2018.03.033.

[2] C. H. Nguyen, H. N. Tran, C. C. Fu, Y. T. Lu, R. S. Juang, *J. Taiwan Inst. Chem. Eng.* **2020**, *000*, 1–11. DOI: 10.1016/j.jtice.2020.02.019.

[3] K. Singh, D. Kukkar, R. Singh, P. Kukkar, N. Bajaj, J. Singh, M. Rawat, A. Kumar, K. H. Kim, *J. Ind. Eng. Chem.* **2020**, *81*, 196–205. DOI: 10.1016/j.jiec.2019.09.008.

[4] H. A. Ahmad, S. Ahmad, Q. Cui, Z. Wang, H. Wei, X. Chen, S. Q. Ni, S. Ismail, H. M. Awad, A. Tawfik, *Sci. Total Environ.* **2022**, *809*. DOI: 10.1016/j.scitotenv.2021.151926.

[5] N. Ranjan, P. K. Singh, N. S. Maurya, *Ecotoxicol. Environ. Saf.* **2022**, *247* (September), 114220. DOI: 10.1016/j.ecoenv.2022.114220.

[6] A. I. Stefanakis, J. A. Becker, *Impact Water Pollut. Hum. Heal. Environ. Sustain.* **2015**, (December 2015), 55–80. DOI: 10.4018/978-1-4666-9559-7.ch003.

[7] Q. He, B. Wang, J. Liang, J. Liu, B. Liang, G. Li, Y. Long, G. Zhang, H. Liu, *Mater. Today Adv.* **2023**, *17*, 100340. DOI: 10.1016/j.mtadv.2022.100340.

[8] Y. Fan, D. Pan, M. Yang, X. Wang, *Sci. Total Environ.* **2023**, *866* (September 2022), 161412. DOI: 10.1016/j.scitotenv.2023.161412.

[9] S. Kobylewski, M. F. Jacobson, *Int. J. Occup. Environ. Health*. **2012**, *18* (3), 220–246. DOI: 10.1179/1077352512Z.00000000034.

[10] M. Holc, **1999**, *43*.

[11] S. Bonan, G. Fedrizzi, S. Menotta, C. Elisabetta, *Dye. Pigment.* **2013**, *99* (1), 36–40. DOI: 10.1016/j.dyepig.2013.03.029.

[12] M. E. Farah, M. Maia, F. M. Penha, E. B. Rodrigues, *The Use of Vital Dyes during Vitreoretinal Surgery – Chromovitrectomy*, First Edit ed., © 2010, Elsevier Inc. All Rights Reserved. **2000**.

[13] R. Zokhtareh, M. Rahimnejad, G. Najafpour-Darzi, H. Karimi-Maleh, *Environ. Res.* **2023**, *216* (P3), 114643. DOI: 10.1016/j.envres.2022.114643.

[14] P. K. Gopi, G. Kesavan, S. M. Chen, C. H. Ravikumar, *New J. Chem.* **2021**, *45* (6), 3022–3033. DOI: 10.1039/d0nj05501h.

[15] X. Hu, Y. Zhang, T. Zeng, Q. Wan, K. Wu, N. Yang, *Diam. Relat. Mater.* **2022**, *128* (August), 109303. DOI: 10.1016/j.diamond.2022.109303.

[16] V. Ayerdurai, M. Cieplak, W. Kutner, *TrAC - Trends Anal. Chem.* **2023**, *158*, 116830. DOI: 10.1016/j.trac.2022.116830.

[17] B. Koçak, Y. Ipek, A. Keçeci, *Diam. Relat. Mater. J.* **2023**, *131* (November 2022). DOI: 10.1016/j.diamond.2022.109558.

[18] H. Afsharara, E. Asadian, B. Mosta, K. Banan, S. Arjomand, D. Hatamabadi, A. Keshavarz, C. Mustansar, R. Keçili, F. Ghorbani-bidkorpeh, *Trends Anal. Chem.* **2023**, *160*, 116949. DOI: 10.1016/j.trac.2023.116949.

[19] M. Gonçalves, L. V. De Faria, A. B. Nascimento, R. L. Germscheidt, J. A. Bonacin, R. A. A. Munoz, S. Patra, L. P. Hern, L. Angnes, *Anal. Chim. Acta*. **2022**, *1233* (September), 340362. DOI: 10.1016/j.aca.2022.340362.

[20] L. R. G. Silva, J. H. S. Carvalho, S. Stefano, G. G. Oliveira, J. Prakash, B. C. Janegitz, **2023**, *35* (April), 106142. DOI: 10.1016/j.mtcomm.2023.106142.

[21] L. Meng, *Tailoring Conducting Polymer Interface for Sensing and Biosensing*, Liu-Tryck Linkoping **2020**.

[22] X. Wang, H. Yu, S. Kold, O. Rahbek, S. Bai, *Biomim. Intell. Robot.* **2023**, *3* (1), 100089. DOI: 10.1016/j.birob.2023.100089.

[23] G. Asch, *Les Capteurs En Instrumentation Industrielle*, 7th ed., Dunod, Paris **2010**.

[24] G. Maruccio, J. Narang, *Electrochemical Sensors: From Working Electrodes to Miniaturized Devices*, Elsevier WP **2022**.

[25] J. Zoubir, N. Bougdour, C. Radaa, A. Idlahcen, I. Bakas, A. Assabbane, *Sensors Int.* **2023**, *3* (February 2022), 100160. DOI: 10.1016/j.sintl.2022.100160.

[26] R. Meng, Q. Zhu, T. Long, X. He, Z. Luo, R. Gu, *Food Control.* **2023**, *150* (October 2022), 109743. DOI: 10.1016/j.foodcont.2023.109743.

[27] N. R. Stradiotto, H. Yamanaka, M. V. B. Zanoni, **2003**, *14* (2), 159–173.

[28]   M. Fleischer, H. Meixner, *Sensors Actuators B Chem.* **1995**, *26–27*, 81–84.

[29]   V. Smyntyna, V. Golovanov, S. Kaeiulis, G. Mattogno, G. Righini, *Sensors Actuators B. Chem.* **1995**, *25*, 24–26.

[30]   X. V Chen, P. Bühlmann, *Curr. Opin. Electrochem.* **2022**, *32*, 100896. DOI: 10.1016/j.coelec.2021.100896.

[31]   J. C. Zuaznabar-gardona, A. Fragoso, *Sensors Actuators B. Chem.* **2018**, *273* (January), 664–671. DOI: 10.1016/j.snb.2018.06.103.

[32]   H. M. El-sayed, H. Ezzat, A. M. Mahmoud, H. A. M. Hendawy, O. M. El-abassy, H. Ibrahim, *Microchem. J.* **2023**, *191* (April), 108829. DOI: 10.1016/j.microc.2023.108829.

[33]   M. Parrilla, A. Vanhooydonck, M. Johns, R. Watts, K. De Wael, *Sensors Actuators B. Chem.* **2023**, *378* (September 2022), 133159. DOI: 10.1016/j.snb.2022.133159.

[34]   J. Lee, S. Kim, H. Shin, *Sensors (Switzerland).* **2021**, *21* (4), 1–15. DOI: 10.3390/s21041346.

[35]   M. Dib, A. Moutcine, H. Ouchetto, A. Chtaini, A. Hafid, M. Khouili, *Inorg. Chem. Commun.* **2021**, (April), 108624. DOI: 10.1016/j.inoche.2021.108624.

[36]   L. D. Mello, L. T. Kubota, **2002**, *77*, 237–256.

[37]   J. Barek, A. G. Fogg, A. Muck, J. Zima, *Crit. Rev. Anal. Chem.* **2001**, *31* (4), 291–309. DOI: 10.1080/20014091076776.

[38]   C. Ariño, N. Serrano, J. M. Díaz-Cruz, M. Esteban, *Anal. Chim. Acta.* **2017**, *990*, 11–53. DOI: 10.1016/j.aca.2017.07.069.

[39]   V. Němcová, V. Vyskočil, J. Barek, *Monatshefte fur Chemie.* **2016**, *147* (1), 143–151. DOI: 10.1007/s00706-015-1574-9.

[40]   M. Zimpl, M. Kotouček, K. Lemr, J. Veselá, J. Skopalová, *Anal. Bioanal. Chem.* **2001**, *371* (7), 975–982. DOI: 10.1007/s002160101044.

[41]   J. Song, H. Teng, Z. Xu, N. Liu, L. Xu, L. Liu, F. Gao, X. Luo, *Microchim. Acta.* **2021**, *188* (6), 1–9. DOI: 10.1007/s00604-021-04859-1.

[42]   X. Yu, Q. Zhou, L. Bi, *Russ. J. Appl. Chem.* **2022**, *95* (7), 1036–1047. DOI: 10.1134/S1070427222070163.

[43]   S. Munusamy, R. P. Sivasankaran, K. Sivaranjan, P. Sabhapathy, V. Narayanan, F. Mohammad, S. Sagadevan, *Electrochim. Acta.* **2023**, *448* (October 2022), 142148. DOI: 10.1016/j.electacta.2023.142148.

[44]   Y. Li, H. Huang, R. Cui, D. Wang, Z. Yin, D. Wang, L. Zheng, J. Zhang, Y. Zhao, H. Yuan, et al., *Sensors Actuators, B Chem.* **2021**, *332* (January), 129519. DOI: 10.1016/j.snb.2021.129519.

[45]   E. M. Materón, A. Wong, T. A. Freitas, R. C. Faria, O. N. Oliveira, *J. Pharm. Anal.* **2021**, *11* (5), 646–652. DOI: 10.1016/j.jpha.2021.03.004.

[46]   G. Maduraiveeran, M. Kundu, M. Sasidharan, *J. Mater. Sci.* **2018**, *53* (11), 8328–8338. DOI: 10.1007/s10853-018-2141-7.

[47]   Z. Tan, W. Wu, C. Feng, H. Wu, *Microchim. Acta.* **2020**, 187:414.

[48]   Q. Q. Xu, L. Luo, Z. G. Liu, Z. Guo, X. J. Huang, *Biosens. Bioelectron.* **2023**, *222* (December 2022), 114990. DOI: 10.1016/j.bios.2022.114990.

[49]   G. R. Chaudhary, S. Bansal, **2013**, 241–253. DOI: 10.1007/s12668-013-0094-5.

[50]   N. Zaheiritousi, H. Ali, Z. Hassan, K. Maleh, *Top. Catal.* **2022**, *65* (5), 739–746. DOI: 10.1007/s11244-022-01598-2.

[51]   N. Mavis Xhakaza, R. Chokkareddy, G. G. Redhi, *J. Mol. Liq.* **2022**, *368*, 120444. DOI: 10.1016/j.molliq.2022.120444.

[52]   N. P. Shetti, S. J. Malode, D. S. Nayak, K. Raghava, C. Venkata, K. Ravindranadh, *Microchem. J.* **2019**, *150* (August), 104206. DOI: 10.1016/j.microc.2019.104206.

[53]   X. Liu, H. Li, H. Zhou, J. Liu, L. Li, J. Liu, F. Yan, T. Luo, *J. Electroanal. Chem.* **2020**, *878*, 114568. DOI: 10.1016/j.jelechem.2020.114568.

[54]   S. Sharma, G. Sharma, A. Kumar, P. Dhiman, T. S. AlGarni, M. Naushad, Z. A. ALOthman, F. J. Stadler, *Sep. Purif. Technol.* **2022**, *278* (June 2021), 119481. DOI: 10.1016/j.seppur.2021.119481.

[55]   M. Zubair, H. A. Aziz, I. Ihsanullah, M. A. Ahmad, M. A. Al-Harthi, *Environ. Technol. Innov.* **2021**, *23*, 101614. DOI: 10.1016/j.eti.2021.101614.

[56]   E. Worch, *Adsorption Technology in Water Treatment: Fundamentals, Processes, and Modeling*, DE GRUYTER **2012**.

[57] C. Tien, *Introduction to Adsorption: Basics, Analysis, and Applications*, Elsevier **2019**.

[58] A. H. Chen, J. Lin, N. Zhang, *J. Hazard. Mater.* **2017**, (Ii). DOI: 10.1016/j.jhazmat.2017.11.002.

[59] M. El-Kammah, E. Elkhatib, E. Aboukila, *Inorg. Chem. Commun.* **2022**, *146* (September), 110062. DOI: 10.1016/j.inoche.2022.110062.

[60] S. Alvarez-Torrellas, M.Munoz, J. A. Zazo, J. A. Casas, J. García, *J. Environ. Manage.* **2016**, 1–12. DOI: 10.1016/j.jenvman.2016.08.077.

[61] Y. Chen, S. Chen, Z. Deng, X. Xu, J. Qin, X. Guo, Z. Bai, X. Chen, Z. Lu, *Colloids Surfaces A Physicochem. Eng. Asp.* **2022**, *652* (July), 129827. DOI: 10.1016/j.colsurfa.2022.129827.

[62] A. Kheradmand, M. Negarestani, S. Kazemi, H. Shayesteh, *Sci. Rep.* **2022**, 1–17. DOI: 10.1038/s41598-022-19056-0.

[63] Y. Wang, C. Lin, X. Liu, W. Ren, X. Huang, M. He, W. Ouyang, *Sci. Total Environ.* **2021**, *778*, 146353. DOI: 10.1016/j.scitotenv.2021.146353.

[64] L. Ai, C. Zhang, L. Meng, *J. Chem. Eng. Data*. **2011**, *56* (11), 4217–4225. DOI: 10.1021/je200743u.

[65] T. Duyen, T. Minh, P. Nguyen, H. T. Van, **2022**, *25*. DOI: 10.1016/j.eti.2021.102244.

[66] H. Huang, Z. Li, H. Wang, C. Xia, P. Yan, Q. Zhang, Z. Meng, *J. Environ. Chem. Eng.* **2022**, *10* (6), 108733. DOI: 10.1016/j.jece.2022.108733.

[67] I. Toumi, H. Djelad, F. Chouli, A. Benyoucef, *J. Inorg. Organomet. Polym. Mater.* **2022**, *32* (1), 112–121. DOI: 10.1007/s10904-021-02084-0.

[68] X. Luo, Z. Huang, J. Lin, X. Li, J. Qiu, J. Liu, X. Mao, *J. Clean. Prod.* **2020**, *258*, 120991. DOI: 10.1016/j.jclepro.2020.120991.

[69] J. S. Piccin, G. L. Dotto, L. A. A. Pinto, **2011**, *28* (02), 295–304.

[70] I. Theoretical, *J. Colloid Interface Sci.* **1974**, *47* (3), 755–765.

[71] M. Chen, R. Bi, R. Zhang, F. Yang, F. Chen, *Colloids Surfaces A Physicochem. Eng. Asp.* **2021**, *617* (February), 126384. DOI: 10.1016/j.colsurfa.2021.126384.

[72] A. Roghanizad, M. Karimi Abdolmaleki, S. M. Ghoreishi, M. Dinari, *J. Mol. Liq.* **2020**, *300*, 112367. DOI: 10.1016/j.molliq.2019.112367.

[73] L. Luo, Y. Yang, M. Xiao, L. Bian, B. Yuan, Y. Liu, F. Jiang, X. Pan, *Chem. Eng. J.* **2014**. DOI: 10.1016/j.cej.2014.10.087.

[74] S. K. Sriramoju, P. S. Dash, S. Majumdar, *Biochem. Pharmacol.* **2020**, 104784. DOI: 10.1016/j.jece.2020.104784.

[75] Q. He, G. Wang, Z. Chen, Z. Miao, K. Wan, *Fuel*. **2020**, *267* (January), 117140. DOI: 10.1016/j.fuel.2020.117140.

[76] F. Wang, Y. Yao, Z. Wen, Q. Sun, X. Yuan, *Fuel*. **2020**, *266* (January), 117102. DOI: 10.1016/j.fuel.2020.117102.

[77] H. K. Yagmur, I. Kaya, *J. Mol. Struct.* **2021**, *1232*, 130071. DOI: 10.1016/j.molstruc.2021.130071.

[78] S. Bhowmik, V. Chakraborty, P. Das, *Results in Surfaces and Interfaces*. **2021**, *3* (March), 100011. DOI: 10.1016/j.rsurfi.2021.100011.

[79] M. Baysal, K. Bilge, B. Yılmaz, M. Papila, Y. Yürüm, *Biochem. Pharmacol.* **2018**. DOI: 10.1016/j.jece.2018.02.020.

[80] A. Melliti, M. Yılmaz, M. Sillanpää, B. Hamrouni, R. Vurm, *Colloids Surfaces A Physicochem. Eng. Asp.* **2023**, *672* (April). DOI: 10.1016/j.colsurfa.2023.131775.

[81] M. Francoeur, C. Yacou, E. Petit, D. Granier, V. Flaud, S. Gaspard, S. Brosillon, A. Ayral, *J. Water Process Eng.* **2023**, *53* (February). DOI: 10.1016/j.jwpe.2023.103602.

[82] L. Domergue, N. Cimetière, S. Giraudet, P. Le Cloirec, *J. Environ. Chem. Eng.* **2022**, *10* (5). DOI: 10.1016/j.jece.2022.108218.

[83] S. Merrad, M. Abbas, M. Trari, *Fibers Polym.* **2023**, *24* (3), 1067–1081. DOI: 10.1007/s12221-023-00025-x.

[84] S. Gu, X. Kang, L. Wang, E. Lichtfouse, C. Wang, *Environ. Chem. Lett.* **2019**, *17* (2), 629–654. DOI: 10.1007/s10311-018-0813-9.

[85] H. Xu, L. Wu, T. Shi, W. Liu, S. Qi, *Sci. China Technol. Sci.* **2014**, *57* (6), 1127–1134. DOI: 10.1007/s11431-014-5542-0.

[86] B. Abbou, I. Lebkiri, H. Ouaddari, A. El, F. Ezzahra, L. Kadiri, A. Ouass, A. Lebkiri, E. Housseine, *Inorg. Chem. Commun.* **2023**, *155* (July), 111127. DOI:

10.1016/j.inoche.2023.111127.

[87]   L. Wang, C. Shi, L. Wang, L. Pan, X. Zhang, J.-J. Zou, *Nanoscale.* **2020**, 1–26. DOI: 10.1039/C9NR09274A.

[88]   N. Mohammed, H. Islam, G. A. Abd, E. Moemen, *J. Mater. Sci. Mater. Electron.* **2020**, (0123456789). DOI: 10.1007/s10854-020-03376-w.

[89]   T. A. Abdullah, R. T. R. T. Juzsakova, N. Al Jammal, M. A. M. L. P. Cuong, *Int. J. Environ. Sci. Technol.* **2020**, (0123456789). DOI: 10.1007/s13762-020-02956-x.

[90]   G. Mustafa, H. Tahir, M. Sultan, N. Akhtar, **2013**, *12* (47), 6650–6660. DOI: 10.5897/AJB2013.13058.

[91]   K. K. Singh, K. K. Senapati, K. C. Sarma, *J. Environ. Chem. Eng.* **2017**, *5* (3), 2214–2221. DOI: 10.1016/j.jece.2017.04.022.

[92]   A. Di Mauro, A. Landström, I. Concina, A. Di Mauro, A. Landström, I. Concina, G. Impellizzeri, V. Privitera, *J. Colloid Interface Sci.* **2018**. DOI: 10.1016/j.jcis.2018.08.070.

[93]   M. Nadeem, Q. Dar, F. Nawaz, M. Naveed, M. Iqbal, M. Faizan, *Integr. Med. Res.* **2018**, (x x), 1–13. DOI: 10.1016/j.jmrt.2018.06.002.

[94]   B. Wang, X. Wan, Z. Liu, J. Zhong, J. Tan, Y. Li, Y. F. Zhang, *J. Polym. Res.* **2022**, *29* (11), 1–9. DOI: 10.1007/s10965-022-03333-7.

[95]   R. Pandimurugan, S. Thambidurai, *Biochem. Pharmacol.* **2016**, *4* (1), 1332–1347. DOI: 10.1016/j.jece.2016.01.030.

[96]   P. Boch, J.-C. Nièpce, *Ceramic Materials. Process, Properties and Applications*, ISTE Ltd **2007**.

[97]   D. M. Z. Valenti, J. Silva, W. R. Teodoro, A. P. Velosa, S. B. V. Mello, *Clin. Exp. Dermatol.* **2012**, *37* (2), 164–168. DOI: 10.1111/j.1365-2230.2011.04216.x.

[98]   G. M. DoNascimento, *Clays, Clay Minerals and Ceramic Materials Based on Clay Minerals*, ExLi4EvA **2016**.

[99]   D. L. Bish, **1980**, *103* (May), 170–175.

[100]   A. Vaccari, *Catal. Today.* **1998**, *41* (1–3), 53–71. DOI: 10.1016/S0920-5861(98)00038-8.

[101]   A. Roy, C. Forano, K. El Malki, J. P. Besse, *Sect. Title Ind. Inorg. Chem.* **1992**, (444), 108–169. DOI: 10.1007/978-1-4684-8866-1_7.

[102]   G. Mishra, B. Dash, S. Pandey, *Appl. Clay Sci.* **2018**, *153* (June 2017), 172–186. DOI: 10.1016/j.clay.2017.12.021.

[103]   F. Cavani, F. Trifiro, A. Vaccari, *Catal. Today.* **1991**, *11*, 173–301.

[104]   E. Manasse, *Proc Verb.* **1915**, *24*, 92.

[105]   W. Feitknecht, G. Fischer, *Chim. Acta.* **1935**, *18*, 555–569.

[106]   S. Miyata, T. Kumura, *Chem. Lett.* **1973**, (006), 843–848.

[107]   J. Mittal, *J. Environ. Manage.* **2021**, *295* (June), 113017. DOI: 10.1016/j.jenvman.2021.113017.

[108]   D. G. Evans, R. C. T. Slade, *struct Bond.* **2006**, *119* (December 2005), 1–87. DOI: 10.1007/430_005.

[109]   V. Rives, *Layered Double Hydroxides: Present and Future*, Nova Science Publishers, Inc, New York **2001**.

[110]   M. V. Bukhtiyarova, *J. Solid State Chem.* **2019**, *269*, 494–506. DOI: 10.1016/j.jssc.2018.10.018.

[111]   J.-F. MARUCCO, *Chimie Des Solides*, EDP Sciences **2004**.

[112]   K. Prabir, M. Scott, A. Kathleen, *HANDBOOK of Layered Materials*, Marcel Dekker, Inc, New York **2004**.

[113]   A. Gil, E. Arrieta, M. A. Vicente, S. A. Korili, *Chem. Eng. J.* **2018**, *334* (October 2017), 1341–1350. DOI: 10.1016/j.cej.2017.11.100.

[114]   E. S. Zhitova, S. V. Krivovichev, I. V. Pekov, V. N. Yakovenchuk, Y. A. Pakhomovsky, *Appl. Clay Sci.* **2016**, *130*, 2–11. DOI: 10.1016/j.clay.2016.01.031.

[115]   S. Miyata, **1983**, *31* (4), 305–311.

[116]   S. Miyata, A. Okada, *Clays Clay Miner.* **1977**, *25* (1), 14–18. DOI: 10.1346/CCMN.1977.0250103.

[117]   M. Dib, H. Ouchetto, S. Akhramez, H. Fadili, A. Essoumhi, *Mater. Today Proc.* **2019**, (xxxx), 8–11. DOI: 10.1016/j.matpr.2019.08.106.

[118]   N. El, H. Hadj-abdelkader, B. Abdellah, **2019**, (xxxx). DOI: 10.1016/j.ijhydene.2019.02.022.

[119]   R. Elmoubarki, F. Z. Mahjoubi, A. Elhalil, H. Tounsadi, M. Abdennouri, M. Sadiq, S. Qourzal, A. Zouhri, N. Barka, *J. Mater. Res. Technol.* **2017**, *6*, 271–283. DOI:

10.1016/j.jmrt.2016.09.007.

[120] C. A. Serhal, I. Mallard, C. Poupin, M. Labaki, S. Siffert, R. Cousin, *Comptes Rendus Chim.* **2018**, *21* (11), 993–1000. DOI: 10.1016/j.crci.2018.09.012.

[121] E. M. Seftel, R. G. Ciocarlan, B. Michielsen, V. Meynen, S. Mullens, P. Cool, *Appl. Clay Sci.* **2018**, *165* (December 2017), 234–246. DOI: 10.1016/j.clay.2018.08.018.

[122] F. A. P. Cavalcanti, A. Schutz, P. Biloen, *Interlayer Accessibility in Layered Double-Metal Hydroxides*, Vol. 31, Elsevier Science Publishers B.V. **1987**.

[123] J. Xu, Y. Song, Q. Tan, L. Jiang, *J. Mater. Sci.* **2017**, *52* (10), 5908–5916. DOI: 10.1007/s10853-017-0826-y.

[124] J. Marreiros, M. Diaz-Couce, M. J. Ferreira, P. D. Vaz, M. J. Calhorda, C. D. Nunes, *Inorganica Chim. Acta.* **2019**, *486* (Ii), 274–282. DOI: 10.1016/j.ica.2018.10.062.

[125] A. A. A. Ahmed, Z. A. Talib, M. Z. Bin Hussein, A. Zakaria, *J. Solid State Chem.* **2012**, *191* (3), 271–278. DOI: 10.1016/j.jssc.2012.03.013.

[126] X. Sun, E. Neuperger, S. K. Dey, *J. Colloid Interface Sci.* **2015**, *459*, 264–272. DOI: 10.1016/j.jcis.2015.07.073.

[127] S. Xu, M. C. Liao, H. Y. Zeng, C. R. Chen, H. Z. Duan, X. J. Liu, J. Z. Du, *Appl. Clay Sci.* **2015**, *115*, 124–131. DOI: 10.1016/j.clay.2015.07.039.

[128] A. Navajas, I. Campo, A. Moral, J. Echave, O. Sanz, M. Montes, J. A. Odriozola, G. Arzamendi, L. M. Gandía, *Fuel.* **2018**, *211* (September 2017), 173–181. DOI: 10.1016/j.fuel.2017.09.061.

[129] D. Bharali, R. C. Deka, *Colloids Surfaces A Physicochem. Eng. Asp.* **2017**, *525* (April), 64–76. DOI: 10.1016/j.colsurfa.2017.04.060.

[130] M. Monti, P. Benito, F. Basile, G. Fornasari, M. Gazzano, E. Scavetta, D. Tonelli, A. Vaccari, *Electrochim. Acta.* **2013**, *108*, 596–604. DOI: 10.1016/j.electacta.2013.06.143.

[131] K. Abderrazek, N. Frini Srasra, E. Srasra, *J. Chinese Chem. Soc.* **2017**, *64* (3), 346–353. DOI: 10.1002/jccs.201600258.

[132] A. A. A. Ahmed, Z. A. Talib, M. Z. Hussein, *Mater. Today Proc.* **2016**, *3* (2), 130–144. DOI: 10.1016/j.matpr.2016.01.044.

[133] K. Nejati, A. R. Akbari, S. Davari, K. Asadpour-Zeynali, Z. Rezvani, *New J. Chem.* **2018**, *42* (4), 2889–2895. DOI: 10.1039/c7nj04469k.

[134] S. J. Xia, F. X. Liu, Z. M. Ni, J. L. Xue, P. P. Qian, *J. Colloid Interface Sci.* **2013**, *405* (3), 195–200. DOI: 10.1016/j.jcis.2013.05.064.

[135] Y. Zhu, R. Zhu, G. Zhu, M. Wang, Y. Chen, J. Zhu, Y. Xi, H. He, *Appl. Surf. Sci.* **2018**, *433*, 458–467. DOI: 10.1016/j.apsusc.2017.09.236.

[136] K. Jirátová, F. Kovanda, J. Ludvíková, J. Balabánová, J. Klempa, *Catal. Today.* **2016**, *277* (3), 61–67. DOI: 10.1016/j.cattod.2015.10.036.

[137] F. Kovanda, T. Rojka, P. Bezdička, K. Jirátová, L. Obalová, K. Pacultová, Z. Bastl, T. Grygar, *J. Solid State Chem.* **2009**, *182* (1), 27–36. DOI: 10.1016/j.jssc.2008.09.014.

[138] S. Jiang, Y. Liu, W. Xie, M. Shao, *J. Energy Chem.* **2018**. DOI: 10.1016/j.jechem.2018.08.010.

[139] P. R. Chowdhury, K. G. Bhattacharyya, *Dalt. Trans.* **2015**, *44* (15), 6809–6824. DOI: 10.1039/c5dt00257e.

[140] C. Taviot-gue, P. Vialat, F. Leroux, F. Razzaghi, H. Perrot, O. Sel, N. D. Jensen, U. G. Nielsen, S. Peulon, E. Elkaim, et al., *Chem. Mater.* **2016**, *28*, 7793–7806. DOI: 10.1021/acs.chemmater.6b03061.

[141] E. Scavetta, B. Ballarin, M. Gazzano, D. Tonelli, *Electrochim. Acta.* **2009**, *54* (3), 1027–1033. DOI: 10.1016/j.electacta.2008.07.078.

[142] J. W. Kou, S. Y. Cheng, J. W. Wang, X. M. Xie, *Chem. Eng. J.* **2017**, *323*, 565–571. DOI: 10.1016/j.cej.2017.04.125.

[143] Y. Chen, Z. Shui, W. Chen, G. Chen, *Constr. Build. Mater.* **2015**, *93* (3), 1051–1058. DOI: 10.1016/j.conbuildmat.2015.05.047.

[144] S. Zhao, H. Yi, X. Tang, D. Kang, F. Gao, J. Wang, Y. Huang, Z. Yang, *Catal. Today.* **2018**. DOI: 10.1016/j.cattod.2018.05.011.

[145] S. Chakraborty, I. Sengupta, I. Sarkar, S. K. Pal, S. Chakraborty, *Appl. Clay Sci.* **2019**, *168* (June 2018), 43–55. DOI: 10.1016/j.clay.2018.10.018.

[146] F. L. Theiss, G. A. Ayoko, R. L. Frost, *Appl. Surf. Sci.* **2016**, *383*, 200–213. DOI: 10.1016/j.apsusc.2016.04.150.

[147] W. T. Reichle, *Solide States Ionics*. **1986**, *22*, 135–141.

[148] Q. Zhang, Y. Li, X. Cui, H. Wang, Y. Guo, *J. Nanosci. Nanotechnol.* **2016**, *16* (6), 5653–5661. DOI: 10.1166/jnn.2016.11725.

[149] Y. Lu, B. Jiang, L. Fang, F. Ling, J. Gao, F. Wu, X. Zhang, *Chemosphere.* **2016**, *152*, 415–422. DOI: 10.1016/j.chemosphere.2016.03.015.

[150] F. Barahuie, M. Z. Hussein, P. Arulselvan, S. Fakurazi, Z. Zainal, *J. Solid State Chem.* **2014**, *217*, 31–41. DOI: 10.1016/j.jssc.2014.04.015.

[151] Y. Zheng, B. Cheng, W. You, J. Yu, W. Ho, *J. Hazard. Mater.* **2019**, (Vi). DOI: 10.1016/j.jhazmat.2019.02.013.

[152] C. Liao, X. Liu, Y. Ren, D. Gong, Z. Zhang, *J. Ind. Eng. Chem.* **2018**, *68*, 380–386. DOI: 10.1016/j.jiec.2018.08.012.

[153] S. Anantharaj, K. Karthick, M. Venkatesh, T. V. S. V. Simha, A. S. Salunke, L. Ma, H. Liang, S. Kundu, *Nano Energy.* **2017**, *39*, 30–43. DOI: 10.1016/j.nanoen.2017.06.027.

[154] W. Su, F. Wu, L. Fang, J. Hu, L. Liu, T. Guan, *J. Alloys Compd.* **2019**, *799*, 15–25. DOI: 10.1016/j.jallcom.2019.05.305.

[155] T. Li, R. Li, H. Luo, *J. Mater. Chem. A*. **2016**, *4* (48), 18922–18930. DOI: 10.1039/C6TA08032D.

[156] Q. Wang, S. V. Y. Tang, E. Lester, D. O'Hare, *Nanoscale.* **2013**, *5* (1), 114–117. DOI: 10.1039/c2nr32568c.

[157] A. Fahami, F. S. Al-Hazmi, A. A. Al-Ghamdi, W. E. Mahmoud, G. W. Beall, *J. Alloys Compd.* **2016**, *683*, 100–107. DOI: 10.1016/j.jallcom.2016.05.032.

[158] K. Ladewig, M. Niebert, Z. P. Xu, P. P. Gray, G. Q. (Max) Lu, *Appl. Clay Sci.* **2010**, *48* (1–2), 280–289. DOI: 10.1016/j.clay.2009.11.032.

[159] Y. Guo, Z. Zhu, Y. Qiu, J. Zhao, *Chem. Eng. J.* **2013**, *219*, 69–77. DOI: 10.1016/j.cej.2012.12.084.

[160] Y. Vlamidis, E. Scavetta, M. Giorgetti, N. Sangiorgi, D. Tonelli, *Appl. Clay Sci.* **2017**, *143* (January), 151–158. DOI: 10.1016/j.clay.2017.03.031.

[161] M. K. Kumar, K. C. Swaathini, N. S. Jha, S. K. Jha, *Electroanalysis.* **2018**, elan.201800542. DOI: 10.1002/elan.201800542.

[162] N. Zhao, H. Fan, M. Zhang, C. Wang, X. Ren, H. Peng, H. Li, X. Jiang, X. Cao, *J. Alloys Compd.* **2019**, *796*, 111–119. DOI: 10.1016/j.jallcom.2019.05.023.

[163] I. Gualandi, M. Monti, E. Scavetta, D. Tonelli, V. Prevot, C. Mousty, *Electrochim. Acta.* **2015**, *152*, 75–83. DOI: 10.1016/j.electacta.2014.11.096.

[164] A. Mignani, B. Ballarin, M. Giorgetti, E. Scavetta, D. Tonelli, E. Boanini, V. Prevot, C. Mousty, A. Iadecola, *J. Phys. Chem. C*. **2013**, *117* (31), 16221–16230. DOI: 10.1021/jp4033782.

[165] H. Liu, J. Li, M. Wang, Y. Liu, J. Liu, H. Cui, *Adv. Powder Technol.* **2019**, (xxxx), 4–11. DOI: 10.1016/j.apt.2019.04.001.

[166] F. Prinetto, G. Ghiotti, P. Graffin, D. Tichit, *Microporous Mesoporous Mater.* **2000**, *39* (1–2), 229–247. DOI: 10.1016/S1387-1811(00)00197-9.

[167] H. K. D. Nguyen, H. Van Nguyen, V. A. Nguyen, *J. Mol. Struct.* **2018**, *1171*, 25–32. DOI: 10.1016/j.molstruc.2018.05.087.

[168] D. D. Petrolini, E. A. Urquieta-González, S. H. Pulcinelli, C. V. Santilli, L. Martins, *Microporous Mesoporous Mater.* **2017**, *240*, 149–158. DOI: 10.1016/j.micromeso.2016.11.011.

[169] Z. Meng, Y. Zhang, Q. Zhang, X. Chen, L. Liu, S. Komarneni, F. Lv, *Appl. Surf. Sci.* **2017**, *396*, 799–803. DOI: 10.1016/j.apsusc.2016.11.032.

[170] X. Hong, E. Zhu, Z. Ye, K. S. Hui, K. N. Hui, *J. Electroanal. Chem.* **2019**, #pagerange#. DOI: 10.1016/j.jelechem.2019.01.046.

[171] H. Hu, J. Liu, Z. Xu, L. Zhang, B. Cheng, W. Ho, *Appl. Surf. Sci.* **2019**, (Vi). DOI: 10.1016/j.apsusc.2019.02.008.

[172] G. Mascolo, M. C. Mascolo, *Microporous Mesoporous Mater.* **2015**, *214*, 246–248. DOI: 10.1016/j.micromeso.2015.03.024.

[173] Y. Lin, Q. Fang, B. Chen, *J. Environ. Sci. (China)*. **2014**, *26* (3), 493–501. DOI: 10.1016/S1001-0742(13)60462-3.

[174] K. T. Wong, P. Saravanan, I. W. Nah, J. Choi, C. Park, N. Kim, Y. Yoon, M. Jang, *Chemosphere.* **2019**, *218*, 799–809. DOI: 10.1016/j.chemosphere.2018.11.186.

[175] F. Zhang, Y. Song, S. Song, R. Zhang, W. Hou, *ACS Appl. Mater. Interfaces*. **2015**, *7* (13), 7251–7263. DOI: 10.1021/acsami.5b00433.

[176] J. Wang, J. You, Z. Li, P. Yang, X. Jing, M. Zhang, *Nanoscale Res. Lett.* **2008**, *3* (9), 338–342. DOI: 10.1007/s11671-008-9162-0.

[177] S. Tang, L. Wang, Y. Zhang, S. Li, S. Tian, B. Wang, *Fuel Process. Technol.* **2012**, *95*, 84–89. DOI: 10.1016/j.fuproc.2011.11.022.

[178] L. D. L. Miranda, C. R. Bellato, M. P. F. Fontes, M. F. de Almeida, J. L. Milagres, L. A. Minim, *Chem. Eng. J.* **2014**, *254*, 88–97. DOI: 10.1016/j.cej.2014.05.094.

[179] T. S. Munonde, H. Zheng, P. N. Nomngongo, *Ultrason. Sonochem.* **2019**, 104716. DOI: 10.1016/j.ultsonch.2019.104716.

[180] Y. Wang, H. Ji, W. Peng, L. Liu, F. Gao, M. Li, *Int. J. Hydrogen Energy*. **2012**, *37* (11), 9324–9329. DOI: 10.1016/j.ijhydene.2012.03.024.

[181] W. Zhang, Y. Li, L. Zhou, Q. Zheng, F. Xie, K. H. Lam, D. Lin, *Electrochim. Acta*. **2019**, 134595. DOI: 10.1016/j.electacta.2019.134595.

[182] Q. Yang, S. Wang, F. Chen, K. Luo, J. Sun, C. Gong, F. Yao, X. Wang, J. Wu, X. Li, et al., *Catal. Commun.* **2017**, *99*, 15–19. DOI: 10.1016/j.catcom.2017.05.010.

[183] L. Mohapatra, K. M. Parida, *Sep. Purif. Technol.* **2012**, *91*, 73–80. DOI: 10.1016/j.seppur.2011.10.028.

[184] K. M. Parida, L. Mohapatra, *Chem. Eng. J.* **2012**, *179*, 131–139. DOI: 10.1016/j.cej.2011.10.070.

[185] M. Shao, J. Han, M. Wei, D. G. Evans, X. Duan, *Chem. Eng. J.* **2011**, *168* (2), 519–524. DOI: 10.1016/j.cej.2011.01.016.

[186] C. García-Mendoza, R. Gómez, J. M. Alvaro, G. Jácome-Acatitla, F. Tzompantzi, R. López-González, *J. Photochem. Photobiol. A Chem.* **2013**, *277*, 82–89. DOI: 10.1016/j.jphotochem.2013.12.014.

[187] G. Van Tendeloo, K. De Witte, P. Cool, E. M. Seftel, E. Popovici, M. Mertens, E. F. Vansant, *Microporous Mesoporous Mater.* **2007**, *113* (1–3), 296–304. DOI: 10.1016/j.micromeso.2007.11.029.

[188] D. Carriazo, M. Del Arco, E. García-López, G. Marc, C. Martín, L. Palmisano, V. Rives, *J. Mol. Catal. A Chem.* **2011**, *342–343*, 83–90. DOI: 10.1016/j.molcata.2011.04.015.

[189] G. Starukh, *Nanoscale Res. Lett.* **2017**, *12*. DOI: 10.1186/s11671-017-2173-y.

[190] S. Mancipe, F. Tzompantzi, H. Rojas, R. Gómez, *Appl. Clay Sci.* **2016**, *129*, 71–78. DOI: 10.1016/j.clay.2016.05.005.

[191] M. Suárez-Quezada, G. Romero-Ortiz, V. Suárez, G. Morales-Mendoza, L. Lartundo-Rojas, E. Navarro-Cerón, F. Tzompantzi, S. Robles, R. Gómez, A. Mantilla, *Catal. Today*. **2016**, *271*, 213–219. DOI: 10.1016/j.cattod.2016.01.009.

[192] K. Hosni, O. Abdelkarim, N. Frini-Srasra, E. Srasra, *Korean J. Chem. Eng.* **2014**, *32* (1), 104–112. DOI: 10.1007/s11814-014-0199-8.

[193] W. Fei, Y. Song, N. Li, D. Chen, Q. Xu, H. Li, J. He, J. Lu, *Sol. Energy*. **2019**, *188* (March), 593–602. DOI: 10.1016/j.solener.2019.06.037.

[194] S. P. Paredes, M. A. Valenzuela, G. Fetter, S. O. Flores, *J. Phys. Chem. Solids*. **2011**, *72* (8), 914–919. DOI: 10.1016/j.jpcs.2011.03.017.

[195] E. Dvininov, M. Ignat, P. Barvinschi, M. A. Smithers, E. Popovici, *J. Hazard. Mater.* **2010**, *177* (1–3), 150–158. DOI: 10.1016/j.jhazmat.2009.12.011.

[196] M. F. de Almeida, C. R. Bellato, L. D. L. Miranda, J. L. Milagres, *Ceram. Int.* **2017**, *43* (2), 1843–1852. DOI: 10.1016/j.ceramint.2016.10.143.

[197] X. Liang, X. Yang, G. Gao, C. Li, Y. Li, W. Zhang, X. Chen, Y. Zhang, B. Zhang, Y. Lei, et al., *J. Catal.* **2016**, *339*, 68–76. DOI: 10.1016/j.jcat.2016.03.033.

[198] M. Bini, F. Monteforte, V. Friuli, L. Maggi, *J. Solid State Chem.* **2019**. DOI: 10.1016/j.jssc.2019.02.001.

[199] T. Posati, D. Giuri, M. Nocchetti, A. Sagnella, M. Gariboldi, C. Ferroni, G. Sotgiu, G. Varchi, R. Zamboni, A. Aluigi, *Eur. Polym. J.* **2018**, *105*, 177–185. DOI: 10.1016/j.eurpolymj.2018.05.030.

[200] X. Bai, D. Cao, H. Zhang, *Ceram. Int.* **2019**, *45* (12), 14943–14952. DOI: 10.1016/j.ceramint.2019.04.230.

[201] X. Guan, M. Huang, L. Yang, G. Wang, X. Guan, *Chem. Eng. J.* **2019**, *372* (January), 151–162.

DOI: 10.1016/j.cej.2019.04.145.

[202] J. Chen, L. Wu, X. Ding, Q. Liu, X. Dai, J. Song, B. Jiang, A. Atrens, F. Pan, *J. Mater. Sci. Technol.* **2020**. DOI: 10.1016/j.jmst.2019.10.007.

[203] L. Wu, X. Ding, Z. Zheng, Y. Ma, A. Atrens, X. Chen, *Appl. Surf. Sci.* **2019**, *487* (January), 558–568. DOI: 10.1016/j.apsusc.2019.05.115.

[204] L. Bhatta, M. Sc, S. Subramanyam, D. Ph, M. D. Chengala, D. Ph, D. G. Manager, S. Olivera, M. Sc, K. Venkatesh, et al., *J. Clean. Prod.* **2014**, (2015). DOI: 10.1016/j.jclepro.2014.12.059.

[205] S. Kim, K. B. Lee, *Chem. Eng. J.* **2019**, *356* (August), 964–972. DOI: 10.1016/j.cej.2018.08.207.

[206] T. Kokulnathan, T. J. Wang, F. Ahmed, N. Arshi, *Surfaces and Interfaces*. **2023**, *36* (December 2022), 102570. DOI: 10.1016/j.surfin.2022.102570.

[207] Y. T. Wu, P. K. Tsao, K. J. Chen, Y. C. Lin, S. Aulia, L. Y. Chang, K. C. Ho, C. Y. Chang, H. Mizuguchi, M. H. Yeh, *Sensors Actuators B Chem.* **2021**, *346* (May), 130505. DOI: 10.1016/j.snb.2021.130505.

[208] R. C. Sahoo, S. Moolayadukkam, S. Thomas, M. Asle Zaeem, H. S. S. R. Matte, *Appl. Surf. Sci.* **2021**, *541* (September 2020), 148270. DOI: 10.1016/j.apsusc.2020.148270.

[209] Z. Liu, D. Liao, J. Yu, X. Jiang, *Microchem. J.* **2022**, *175* (November 2021), 107216. DOI: 10.1016/j.microc.2022.107216.

[210] Y. Wang, Z. Wang, Y. Rui, M. Li, *Biosens. Bioelectron.* **2015**, *64*, 57–62. DOI: 10.1016/j.bios.2014.08.054.

[211] A. K. Singh, R. K. Gautam, S. Agrahari, I. Tiwari, *Mater. Chem. Phys.* **2022**, *294* (May 2022), 127002. DOI: 10.1016/j.matchemphys.2022.127002.

[212] T. Madrakian, S. Alizadeh, M. Bahram, A. Afkhami, *Ionics (Kiel).* **2017**, *23* (4), 1005–1015. DOI: 10.1007/s11581-016-1871-2.

[213] T. Wang, Z. Cheng, B. Wang, W. Ma, *Chem. Eng. J.* **2012**, *181–182*, 182–188. DOI: 10.1016/j.cej.2011.11.053.

[214] Y. D. G. Edañol, J. A. O. Poblador, T. J. E. Talusan, L. M. P. Jr, **2020**. DOI: 10.1016/j.matpr.2020.05.059.

[215] A. Elmelouky, R. Mghaiouini, A. Mortadi, Y. Hairch, D. Saifaoui, E. Ghaouti, R. El, M. Salah, *Mater. Today Proc.* **2022**, *66*, 307–312. DOI: 10.1016/j.matpr.2022.05.314.

[216] V. D. Thite, S. M. Giripunje, *Nanotechnol. Environ. Eng.* **2022**, *7* (1), 57–66. DOI: 10.1007/s41204-021-00186-1.

[217] X. Hong, M. Xia, M. Shi, C. Liu, Y. Yan, Y. Tao, Y. Zhang, Y. Zhang, P. Du, F. Wang, *J. Colloid Interface Sci.* **2023**, *629*, 948–959. DOI: 10.1016/j.jcis.2022.09.088.

[218] K. Bisaria, S. Sinha, H. M. N. Iqbal, R. Singh, *Environ. Res.* **2022**, *212*, 113184. DOI: 10.1016/j.envres.2022.113184.

[219] Z. Jiang, F. Sun, R. L. Frost, G. Ayoko, G. Qian, X. Ruan, *J. Colloid Interface Sci.* **2022**, *617* (99), 363–371. DOI: 10.1016/j.jcis.2022.03.022.

[220] W. Liu, Y. Yu, *J. Clean. Prod.* **2022**, *370* (July), 133337. DOI: 10.1016/j.jclepro.2022.133337.

[221] M. A. Nazir, T. Najam, M. S. Bashir, M. S. Javed, M. A. Bashir, M. Imran, U. Azhar, S. Shoaib, A. Shah, A. Rehman, *Korean J. Chem. Eng.* **2022**, *39* (1), 216–226. DOI: 10.1007/s11814-021-0892-3.

[222] Y. Li, S. Wu, Q. Liu, S. Nie, H. Li, Y. Dai, L. Pang, *Constr. Build. Mater.* **2019**, *208*, 192–203. DOI: 10.1016/j.conbuildmat.2019.02.174.

[223] C. Guarín, L. Gavilà, M. Constantí, F. Medina, *Chem. Eng. Sci.* **2018**, *179*, 83–91. DOI: 10.1016/j.ces.2018.01.014.

[224] X. R. Wang, Y. Li, L. P. Tang, W. Gan, W. Zhou, Y. F. Zhao, D. S. Bai, *Chinese Chem. Lett.* **2017**, *28* (2), 394–399. DOI: 10.1016/j.cclet.2016.09.002.

Chapter II
Materials and methods

In this chapter, an overview of the substances and the techniques used to conduct experiments for the current work is provided. The experimental section is divided into several sections. First, a list of all the chemicals and reagents used is offered. Next, the synthesis of LDHs and the characterization techniques are discussed. Finally, the application of the synthesised materials in adsorption and sensors is briefly detailed.

II.1. Chemicals

The chemicals used in this study are summarized in **Table II.1**

Table II. 1. List of the chemicals used in the study

Name	Formula	Mw (g.mol^{-1})	Purity	Supplier
Coprecipitation				
Magnesium chloride	$MgCl_2.6H_2O$	203.30	>98 %	BIOCHEM
Cobalt chloride	$CoCl_2.6H_2O$	237.93	>98 %	BIOCHEM
Iron chloride	$FeCl_3.6H_2O$	270.30	98 %	SIGMA-ALDRICH
Aluminium chloride	$AlCl_3$	133.34	98%	SIGMA-ALDRICH
Sodium bicarbonate	$NaHCO_3$	84.007	99%	SIGMA-ALDRICH
Sodium hydroxide	$NaOH$	40	98-100%	BIOCHEM
Adsorption				
Azocarmine G	$C_{28}H_{18}N_3NaO_6S_2$	579.58	/	SIGMA-ALDRICH
Bromophenol blue	$C_{19}H_{10}Br_4O_5O$	669.98	/	BIOCHEM
Electrochemistry				
Ferrocyanide	$K_3[Fe\,(CN)_6]$	329.24	99.5%	BIOCHEM
	$K_4[Fe\,(CN)_6]$	422.39	99%	SIGMA-ALDRICH
Potassium Sulfate	K_2SO_4	174.26	99%	Chemicals BDH
Potassium Chloride	KCl	74.55	99.5-100%	BIOCHEM
Disodium phosphate	Na_2HPO_4	141.96	98-100%	BIOCHEM
Monopotassium phosphate	KH_2PO_4	136.09	89%	Panreac AppliChem

II.2. Synthesis of LDH

The literature review in Chapter I revealed that most studies used chemical processes to create LDHs in the form of powder. The main benefit of using this synthetic approach is the potential to get quite large quantities of the product, which can facilitate some analyses. On the other hand, the electrochemical production of these compounds directly on the surface of an

inert conductive substrate also seemed attractive because it made the processes of separation, washing, and drying easier and facilitated the linkage between indirect characterizations. electrochemical and in-situ analyses. In the present work, LDH materials were synthesised using two routes: coprecipitation and electrodeposition. The synthesised powders were characterised using several physical and chemical techniques, then applied for the detection and removal of pollutants, adsorption, and sensors.

II.2.1. The pH of precipitation:

The pH of the medium presents the main characteristic for the formation of the material, and for a considerable yield, its value must exceed the pH of precipitation of the desired compound with respect to the domains of predominance of the metal hydroxides that compose it. This last condition can be theoretically withdrawn from the Pourbaix diagrams. For Example, the aluminium hydroxide exists in pH between ≈4 and ≈9, it is then important to choose a value from this range, because a higher value leads to the transformation of the precipitate into a complex $[Al(OH)_4]$ dissolved in the medium. For iron. the desired hydroxide forms in the range between ≈5 and ≈11, these values must be respected then to ensure complete precipitation of the desired compound.

However, it is possible to determine these domains experimentally by simple complexation tests. For this purpose, we previously used 25 mL of a solution containing the designated metal chlorides with the quantities shown in **Table II.2** For the titrant solution, a strong base (NaOH) at a concentration of 0.1 M is added drop by drop to the previous mixture until the result is a sufficient pH sweep. The experiments were carried out at room temperature. At the end, a complexation curve is recorded for each metal which gives the change in pH as a function of the volume of NaOH added.

Table II. 2. The concentration used in complexation tests.

	$MgCl_2.6H_2O$	$CoCl_2.6H_2O$	$AlCl_3$	$FeCl_3.6H_2O$	$NaHCO_3$
Concentration (M)	0.03	0.03	0.01	0.01	0.005

II.2.2. Coprecipitation synthesis

The coprecipitation at high supersaturation method was used as described in the literature with slight modifications to synthesize Mg_6Al_2-CO_3-LDH, Mg_6Fe_2-CO_3-LDH and Co_6Al_2-CO_3-LDH [1]. Firstly, 500 mL of metal salt solution, with quantities shown in **Table II.3**, was dropwise added to 500 mL of $NaHCO_3$ (20 mM) under continuous stirring. The pH of the bulk was kept constant throughout the synthesis time using concentrated NaOH solution at fixed values as shown in the **Table II.3.** The resulting suspension was aged under continuous stirring at 40°C for 20 hours; the precipitate was then washed thoroughly with distilled water, collected by centrifugation, and dried for 48 h at 60°C.

Table II. 3. The concentrations and the pH values used in the coprecipitation

	Concentration (M)					pH
	MgCl$_2$.6H$_2$O	CoCl$_2$.6H$_2$O	AlCl$_3$	FeCl$_3$.6H$_2$O	NaHCO$_3$	
MgAl-LDH	0.12	×	0.04	×	0.02	8.5
MgFe-LDH	0.12	×	×	0.04	0.02	9.5
CoAl-LDH	×	0.12	0.04	×	0.02	8.5

II.2.3. Electrochemical synthesis

The electrodeposition experiments were performed in a solution containing the precursors of MgAl-LDH and CoAl-LDH following the quantities mentioned in **Table II. 2**.

All the electrochemical experiments were realised in a three electrodes electrochemical cell, such the electrodeposition of the materials, the electrochemical characterization and the electrochemical detection tests. The three electrodes electrochemical cell include saturated calomel electrode (SCE) as a reference, platinum wire as a counter electrode, and a working electrode according to the demand of the experiment, the electrochemical measurements were carried out using a AUTOLAB 4.9 potentiostat/ Galvanostat Metrohm interfaced with a PC using Nova 1.7 software. The electrochemical apparatus is shown in Erreur ! Source du renvoi introuvable.**.**
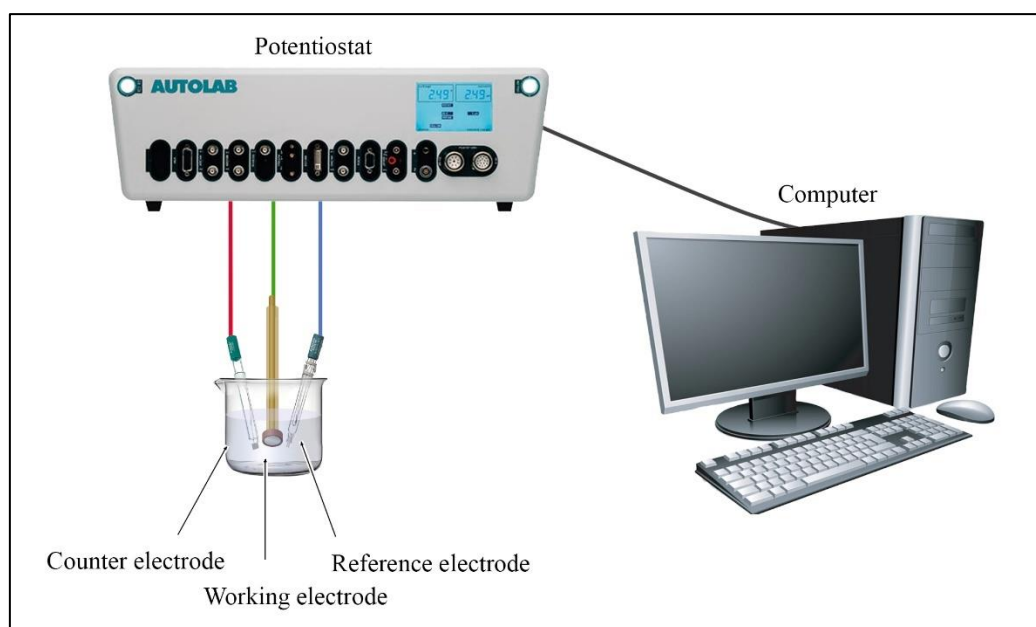
Figure II. 1. Schematic representation of a three-electrode electrochemical system

II.2.3.1.   Preparation of the electrode:

The working electrode is a metal electrode prepared rigorously to meet the electrochemical need, a circular piece of a metal (Nickel and Stainless steel) is brought into contact with a conductive wire, the assembly is coated with a non-conductive paste leaving only the surface of work as show Erreur ! Source du renvoi introuvable.. Before starting each e

lectrochemical test, a treatment was performed on the surface of the working electrode, this step is essential because it increases the producibility of the surface by creating the maximum active site, which is achieved by the elimination of any contamination or product favouring the passivation of the material. The importance of surface treatment is confirmed by electrochemical tests.
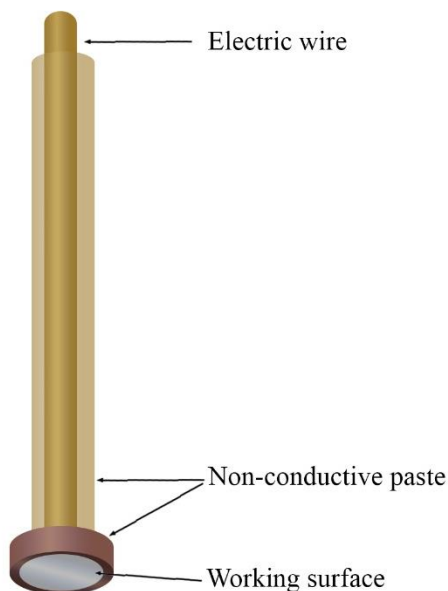
Figure II. 2. Composition of the working electrode

II.2.3.2. Linear sweep voltammetry

The linear sweep voltammetry (LSV) was used to the conditions of electrochemical synthesis. First, the curves were used to study the effect of treatment and polishing on the effectiveness of the surface and determine the range of potential which must be applied for the formation the LDH. The LSV was then performed in solution containing the precursors of MgAl-LDH and CoAl-LDH using Nickel and stainless-steel as working electrodes to determine the domain of potential that should be applied next.

II.2.3.3. Chronoamperometry CA

The electrochemical synthesis is used for the synthesis of Mg_6Al_2-CO_3-LDH and Co_6Al_2-CO_3-LDH. The synthesis is performed by chronoamperometry, which consists of imposing a constant potential during a period of time and recording the variation of the current as a function of time. The analysis of the curves obtained reveals crucial information on the kinetics and the growth of the deposits. The purpose of chronoamperometry is to increase the pH in the vicinity of the surface of the working electrode, the application of a cathodic potential involves reduction reactions of the medium elements (H_2O and O_2 as discussed in chapter I) leading to the formation of OH^- ions. Apart from this, the reduction reactions of the metals existing in the solution can compete [2].

$$M^{n+} + ne^- \rightarrow M^0 \qquad \qquad \text{II.1}$$

II.3. Physicochemical and electrochemical characterization
II.3.1. X-Ray diffraction

The analysis of the synthesized materials was performed by x-ray diffraction (XRD) analysis using Panalytical diffractometer with a CuKα radiation (λ=1.5418 A°, step size:0.001671°, scanning rate:0.071).

II.3.2. Fourier transform infrared spectroscopy

Fourier transform infrared spectroscopy was performed on a Thermo scientific FT-IR spectrophotometer within the range of 4000-400 cm-1, each LDH was used as a pellet containing 150 mg of KBr and 3 mg of the concerned powder.

II.3.3. Scanning electron microscope (SEM)

Scanning electron microscope (SEM) was performed using JSM-7610F tungsten filament (W) coupled with Energy dispersive X-ray spectrometer.

II.3.4. Thermogravimetric and Differential Thermal Analysis

Thermogravimetric and Differential Thermal Analysis (TGA/DTA) were carried out using an SDT Q600 V20.9 thermal analyzer system whose temperature is scanned from 32°C to 575°C in the presence of N_2 gas with a heating rate of 10°C/min.

II.3.5. N2 Adsorption desorption isotherm

Brunauer-Emmett-Teller (BET) surface area and porosity of LDHs were measured by N_2 adsorption-desorption isotherms at 77 K using micromeritics Gemini VII.

II.3.6. Point of zero charge

Point of zero charge (PZC) of the powder was determined using a HANNA (HI 5522) pH meter.

II.3.7. UV-Visible spectroscopy

The sample composition has an impact on this feature, potentially revealing what is in the sample and at what concentration. In order to monitor the dye adsorption capacity during adsorption testes, The samples were analyzed by a Thermo scientific ultraviolet-visible spectrophotometer. The absorbance measurement obeys the Beer-Lambert law, the maximum wavelength of which is determined by scanning the UV-Vis spectrum of the solutions.

II.3.8. Electrochemical characterization

For the electrochemical characterizations, the elaboration of the electrodes was performed in a way that, each one of the materials was compacted into a pallet and connected into a

conductive wire as shows in the drawing. All the electrochemical experiments were realised in a three electrodes cell using a solution of K_2SO_4(0.1M).

II.4. Application

II.4.1. Application in adsorption

II.4.1.1. Adsorption experiments

The study is intended to compare the adsorption behaviour of the synthesized materials; the Azocarmine G (ACG) dye was chosen as a model pollutant for the materials synthesised via Coprecipitation, while Bromophenol Blue (BPB) was chosen for the electrodeposited films.

Firstly, 200 ppm of the dye stuck solution was initially prepared then appropriately diluted into the required concentrations. the catalyst was dispersed in 20 mL of the dye solution then kept in dark with continuous stirring. To perform adsorption tests. Several experiments were performed to study the influence of the set conditions, namely: the initial pH, the initial concentration, the catalyst dose and temperature. The samples were analysed by a Thermo-scientific ultraviolet-visible spectrophotometer (λ_{ACG}=530 nm, λ_{BPB}=591 nm).

By determining the concentration throughout the adsorption process the removal efficiency was calculated by **Eq.II.2** [15]:

$$R_\% = \left[\frac{C_0 - C_f}{C_0}\right] \times 100 \qquad \text{II.2}$$

Where C_0 and C_f are respectively the initial and the final concentration of the dye.

The adsorption capacity of the material (q) can be calculated using **Eq.II.3** [16]:

$$q = \frac{(C_0 - C) \times V}{W} \qquad \text{II.3}$$

Where q_i, V and W represent respectively the amount of adsorbed dye by gramme of adsorbent (mg. g^{-1}); the volume of the aqueous solution (L) and the catalyst weight (g).

II.4.1.2. Central composite experiment design

One of the most effective statistical techniques for finding a quantitative relationship between experiment-related variables and a text index involves the Response Surface Methodology (RMS), which involves designing experiments, analysing the effects of variables, adjusting conditions, and creating models [17]. Herein, Design expert 13 software was used to optimize the relationship between the experimental parameters chosen as the independent input variables (pH, initial dye concentration (ppm) and adsorbent dose (g.L^{-1})) and the adsorption capacity (mg.g^{-1}) as the dependent response variable. A central composite design was used to analyse a set of 20 experiments including eight axial points (2 k), six replications at the centre points (n_0) and 16 factorial points (2^k), the details are presented in **Table II.4.**

$$N = 2^n + 2n + n_0 \qquad \text{II.4}$$

Table II. 4. The actual and coded values of independent variables

Variables (factors)	Symboles		Levels	
			Low (-1)	High (+1)
pH		A	5.0	9.0
Initial Concentration	ppm	B	30.0	100.0
Adsorbent dose	g.L^{-1}	C	0.1	1.0

Tables II.5 provides the experimental plan, which includes the coded and uncoded values of the variables as well as the adsorption capacity. The typical polynomial functions used in the modelling process are similar to first or second-order equations [18], the first-order, also called linear model, is presented by **Eq.II.4** or **Eq.II.5** (5):

$$Y = \beta_0 + \beta_1 X_1 + \beta_2 X_2 \qquad \qquad \textbf{II.4}$$

$$Y = \beta_0 + \beta_1 X_1 + \beta_2 X_2 + \beta_{12} X_1 X_2 \qquad \qquad \textbf{II.5}$$

The second-order model, also called quadratic model, is given by **Eq.II.6**:

$$Y = \beta_0 + \sum_{i=1}^{k} \beta_i X_i + \sum_{i=1}^{k} \beta_{ii} X_i^2 + \sum_{1 \leq i \leq j}^{k} \beta_{ijx} X_i X_j + \varepsilon \qquad \qquad \textbf{II.6}$$

Where k is the number of input variables, β_0 is the constant term, β_i is the coefficient of the linear variables, X_i is the input variables, β_{ii} is the coefficient of the quadratic parameter, β_{ij} is the interaction coefficients between input variables and ε the error associated with the experiments. Higher order models can be used in RSM modelling along with ANOVA tests to evaluate the efficiency of RSM model [18].

Table II. 5. Central composite design matrix for ACG adsorption onto MgAl-LDH, MgFe-LDH and CoAl-LDH.

	Independent input variables								
	MgAl-LDH			**MgFe-LDH**			**CoAl-LDH**		
Runs	pH	C_0 (ppm)	D (g.L^{-1})	pH	C_0 (ppm)	D (g.L^{-1})	pH	C_0 (ppm)	D (g.L^{-1})
1	9	30	0.25	5	30	0.25	5	30	0.25
2	8	30	0.25	6	65	0.10	6	30	0.25
3	8	40	0.25	9	60	0.25	7	30	0.25
4	8	80	0.25	9	30	0.25	8	30	0.25
5	8	80	0.5	9	80	0.10	9	30	0.25
6	5	30	0.25	9	80	0.5	8	30	0.25
7	8	60	0.25	7	30	0.25	8	40	0.25
8	6	30	0.25	9	100	0.25	8	60	0.25
9	8	80	0.25	7	60	0.25	8	80	0.25
10	8	80	0.25	5	80	0.75	8	100	0.25
11	8	80	0.75	5	80	1.00	8	80	0.10
12	7	30	0.25	8	30	0.25	8	80	0.25
13	8	80	0.1	8	40	0.25	8	80	0.50
14	8	30	0.25	8	60	0.25	8	80	0.75
15	8	100	1	9	80	0.75	8	80	1.00
16	9	80	0.5	5	40	0.25	9	80	0.10
17	9	80	0.1	8	100	0.25	7	80	0.10
18	6	100	0.25	5	60	0.25	8	40	0.75
19	6	60	0.25	6	30	0.25	8	40	1.00
20	6	40	0.25	5	80	0.25	8	60	0.10

II.4.1.3.   Adsorption Kinetics

With the aim to better investigate the adsorption mechanism, kinetic curves are fitted with pseudo-first order **Eq.II.7**, pseudo-second orders **Eq.II.8**, intraparticle model by **Eq.II.9** and Elovich kinetic models **Eq.II.10** [19–21]

$$\ln(q_e - q_t) = lnq_e - k_1 t \qquad\qquad\qquad \textbf{II.7}$$

$$\frac{1}{q_t} = \frac{1}{k_2 q_e^2} + \frac{t}{q_e} \qquad\qquad\qquad \textbf{II.8}$$

$$q_t = K_{in} t^{1/2} + C \qquad\qquad\qquad \textbf{II.9}$$

$$q_t = \beta \ln(t) + \beta \ln(\alpha) \qquad\qquad\qquad \textbf{II.10}$$

II.4.1.4.   Adsorption isotherms

In order to determine the properties related to the chemical affinity and surface characteristics, four isotherm models are examined [22]. The first one corresponds to Langmuir isotherm; this model is attributed to the homogeneous adsorption in form of monolayer. Its linear form is written according to the **Eq.II.11** [23]

$$\frac{C_e}{q_e} = \frac{1}{Q^0 K_L} + \frac{C_e}{Q^0} \qquad\qquad\qquad \textbf{II.11}$$

$$R_L = \frac{1}{1 + C_i K_L} \qquad\qquad\qquad \textbf{II.12}$$

The second one corresponds to the Freundlich isotherm model which comprises a multi-layered adsorption mechanism, the linearized equation is given in **Eq.II.13** [9]

$$Log\ q_e = logK_F + \frac{1}{n} logC_e \qquad\qquad\qquad \textbf{II.13}$$

n is a constant related to the adsorption intensity.

The third model is the Temkin isotherm where the description of the adsorbate–adsorbent interactions is demonstrated, its linear form is as follows **Eq.II.14** [24]

$$q_e = \frac{RT}{b_T} Ln\ A_T + \left(\frac{RT}{b_T}\right) Ln\ C_e \qquad\qquad\qquad \textbf{II.14}$$

The linear form of the fourth model attributed to Dubinin-Rushkevich (D-R) isotherm is given according to **Eq.II.15** [25]:

$$Ln\ q_e = Lnq_{max} - K_{DR}\varepsilon^2 \qquad\qquad\qquad \textbf{II.15}$$

Where ε is the adsorption potential $\varepsilon = RT\ Ln\left(1 + \frac{1}{C_e}\right)$. It is possible to estimate the system's energy from the previous isotherm using **Eq.II.16** (13):

$$E = \frac{1}{\sqrt{2K_{DR}}} \qquad\qquad\qquad \textbf{II.16}$$

II.4.1.5.   Thermodynamic parameters

The study of thermodynamic parameters of adsorption process, namely standard Gibbs free energy (ΔG°), enthalpy change (ΔH°) and entropy (ΔS°) variations [20], was realized in the range of 20-40°C, at pH=5, the calculations were performed according to the equation in Chapter I [24].

II.4.2. Application in Sensors

II.4.2.1.   Preparation of the working electrode

MgFe-LDH modified graphite electrode was homemade by a deposition of the MgFe-LDH powder, synthesised via co-precipitation method, on a graphite electrode. First of all, a graphite rod was polished with sand paper and rinsed thoroughly with distilled water. Then, the rode was covered by isolating resin leaving two contact extremities, the first for the contact with the potentiostat, and the second is the surface of the bare graphite working electrode (G). After that, 50 mg of MgFe-LDH mixed with few droplets of distilled water were mechanically deposited on the surface of the electrode with slight compression, the system is then dried at room temperature to obtain graphite modified by MgFe-LDH working electrode (G/MF) with geometric surface area of 0.15 cm^2. The fabrication process is summarized in **Fig. II.3**.

II.4.2.2.   Electrochemical experiments

For electrochemical applications, the electron transfer properties of the graphite electrode and the modified electrode were studied using CV and SIE in in PBS solution containing KCl (0.1M) and Ferricyanide couple [Fe $(CN)_6]^{3-/4-}$ (0.5mM). The modified electrode (G/MF) was tested for the detection of MNZ in aqueous medium using Linear Voltammetry (LV), Cyclic Voltammetry (CV) and Chronoamperometry (CA). Several parameters were studied like pH, the scan rate and the medium's electrolyte. The stability and the interferences effect were also investigated.
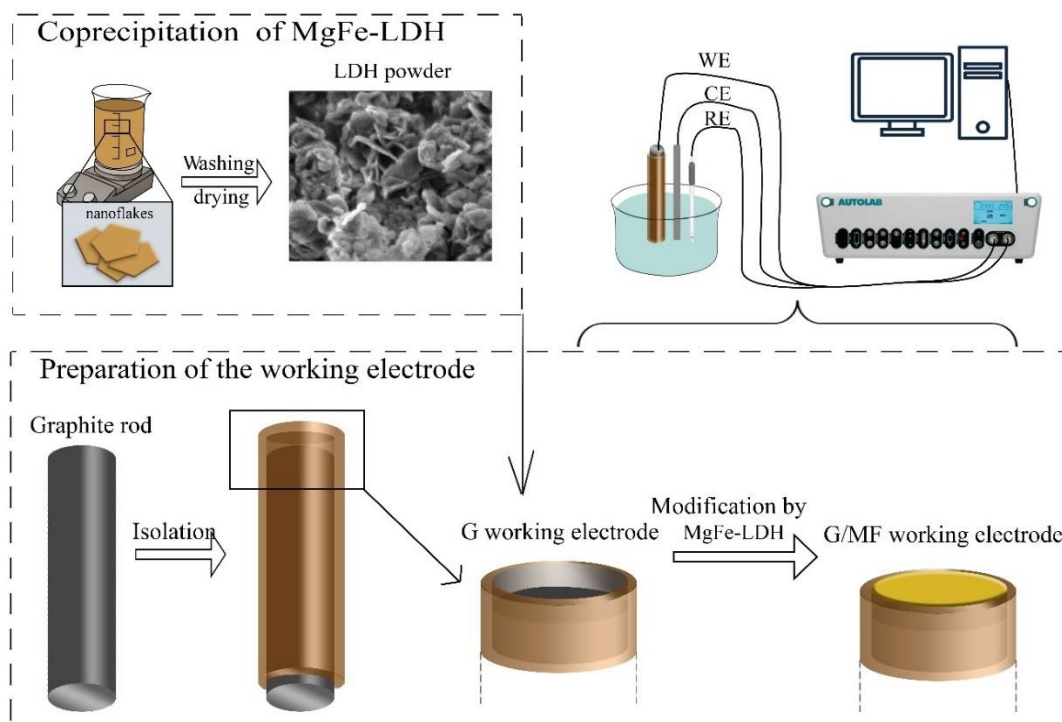
Figure II. 3. Schematic representation of the working electrode fabrication and the electrochemical experiments**.**

References

[1] F. L. Theiss, G. A. Ayoko, R. L. Frost, *Appl. Surf. Sci.* **2016**. DOI: 10.1016/j.apsusc.2016.04.150.

[2] F. Basile, P. Benito, G. Fornasari, M. Monti, E. Scavetta, D. Tonelli, A. Vaccari, *Catal. Today*. **2010**, *157* (1–4), 183–190. DOI: 10.1016/j.cattod.2010.04.039.

[3] Q. Shen, Z. Liu, Y. Hua, J. Zhao, W. Lv, A. U. H. Mohsan, *Materials (Basel)*. **2018**, *11* (6), 1015. DOI: 10.3390/ma11061015.

[4] S. Nasir, M. Z. Hussein, Z. Zainal, N. A. Yusof, S. A. Mohd Zobir, I. M. Alibe, *BioResources*. **2019**, *14* (1), 2352–2388. DOI: 10.15376/biores.14.1.Nasir.

[5] N. E. H. Hadj-Abdelkader, A.-P. Beltrao-Nunesa, F. Belkhadem, N. Benselka, R. Roy, A. Azzouza, *Appl. Clay Sci.* **2020**, *198*, 105829. DOI: 10.1016/j.clay.2020.105829.

[6] A. F. da Silva, J. L. da S. Duarte, L. Meili, *Sep. Purif. Technol. 264.* **2021**, *264*, 118353. DOI: 10.1016/j.seppur.2021.118353.

[7] M. D. Mccluskey, *Appl. Phys. Rev.* **2013**, *87* (8), 3593. DOI: 10.1063/1.372453.

[8] P. Li, L. Teng, M. I. N. Guo, M. E. I. Zhang, S. Seetharaman, *Metall. Mater. Trans. B*. **2012**, *43B* (April), 406. DOI: 10.1007/s11663-011-9611-5.

[9] M. Zubair, H. A. Aziz, I. Ihsanullah, M. A. Ahmad, M. A. Al-Harthi, *Environ. Technol. Innov.* **2021**, *23*, 101614. DOI: 10.1016/j.eti.2021.101614.

[10] E. Barsoukov, J. R. Macdonald, *Impedance Spectroscopy: Theory , Experiment , And*, 2nd ed., Wiley, John And Sons **2005**.

[11] C. M. A. Brett, **2022**.

[12] J. Wang, *ANALYTICAL ELECTROCHEMISTRY*, 2nd ed., WILEY-VCH **2000**.

[13] J. G. Manjunatha, *Electrochemical Sensors Based on Carbon Composite Materials: Fabrication, Properties and Application*, IOP Publishing, London **2022**.

[14] M. E. Orazem, B. Tribollet, *Electrochemical Impedance Spectroscopie*, WILEY, Pennington **2008**.

[15] B. S. Yadav, S. Dasgupta, *Inorg. Chem. Commun.* **2022**, *137* (December 2021), 109203. DOI: 10.1016/j.inoche.2022.109203.

[16] Z. Zhu, S. Ouyang, P. Li, L. Shan, R. Ma, P. Zhang, *Appl. Clay Sci.* **2020**, *188* (November 2019), 105500. DOI: 10.1016/j.clay.2020.105500.

[17] H. Soleimani, K. Sharafi, J. Amiri, J. Jaafari, *Heliyon*. **2023**, *9* (4), e14743. DOI: 10.1016/j.heliyon.2023.e14743.

[18] M. Hemmat, S. Majid, D. Toghraie, *Heliyon*. **2022**, *8* (June), e11944. DOI: 10.1016/j.heliyon.2022.e11944.

[19] Q. Chen, Z. Cheng, X. Li, C. Wang, L. Yan, G. Shen, *Appl. Catal. B Environ.* **2022**, *302* (June 2021), 120866. DOI: 10.1016/j.apcatb.2021.120866.

[20] S. Sharma, G. Sharma, A. Kumar, P. Dhiman, T. S. AlGarni, M. Naushad, Z. A. ALOthman, F. J. Stadler, *Sep. Purif. Technol.* **2022**, *278* (June 2021), 119481. DOI: 10.1016/j.seppur.2021.119481.

[21] H. K. Yagmur, I. Kaya, *J. Mol. Struct.* **2021**, *1232*, 130071. DOI: 10.1016/j.molstruc.2021.130071.

[22] H. Huang, Z. Li, H. Wang, C. Xia, P. Yan, Q. Zhang, Z. Meng, *J. Environ. Chem. Eng.* **2022**, *10* (6), 108733. DOI: 10.1016/j.jece.2022.108733.

[23] A. Kheradmand, M. Negarestani, S. Kazemi, H. Shayesteh, *Sci. Rep.* **2022**, 1–17. DOI: 10.1038/s41598-022-19056-0.

[24] M. Chen, R. Bi, R. Zhang, F. Yang, F. Chen, *Colloids Surfaces A Physicochem. Eng. Asp.* **2021**, *617* (February), 126384. DOI: 10.1016/j.colsurfa.2021.126384.

[25] Q. Hu, Z. Zhang, *J. Mol. Liq.* **2019**, *277*, 646–648. DOI: 10.1016/j.molliq.2019.01.005.

[26] A. Roghanizad, M. Karimi Abdolmaleki, S. M. Ghoreishi, M. Dinari, *J. Mol. Liq.* **2020**, *300*, 112367. DOI: 10.1016/j.molliq.2019.112367.

Chapter III
Synthesis and Characterizations

III.1. Materials synthesis

III.1. 1.   Precipitation tests

The determination of the formation pH and predominance areas of each metal cation are essential before proceeding with the synthesis. For this aim, preliminary experiments based on the titration of solutions containing M(II) and M(III) ions with NaOH has been carried out in order to determine the pH values at which the different LDHs precipitate as presented in the Erreur ! Source du renvoi introuvable.., showing the change in pH as a function of the volume o f NaOH.
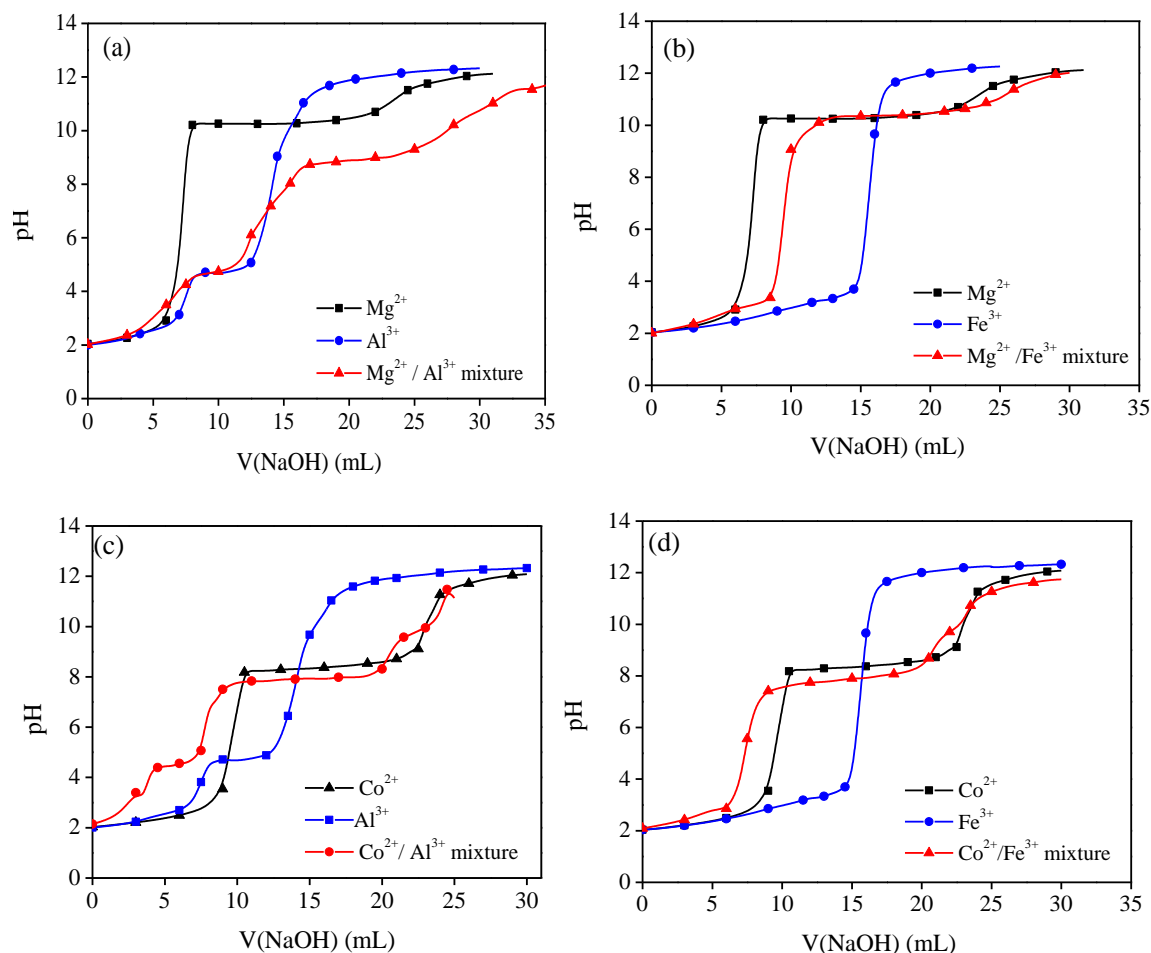
Figure III. 1. Complexation curves of the different metal cations and the corresponding LDHs

Analysis of the titration curves of simple mixtures shows that:

- For the complexation of a solution containing $MgCl_2$, $6H_2O$ and $NaHCO_3$, the plateaus of pH can be attributed to the reactions (**III.1** and **III .2**) respectively.

$$Mg^{2+}_{(aq)} + 2OH^-_{(aq)} \rightarrow Mg\,(OH)_{2(s)} \qquad K_s = 6\ 10^{-12} \qquad \textbf{III.1}$$

$$HCO_3^-_{(aq)} + OH^-_{(aq)} \rightarrow CO_3^{2-}_{(aq)} + H_2O \qquad pK_a = 10.3 \qquad \textbf{III.2}$$

- For $AlCl_3$ in the presence of $NaHCO_3$, the first plateau can be assigned to the formation of $Al(OH)_3$ precipitate following the reaction (**III.3**):

$Al^{3+}_{(aq)} + 3OH^-_{(aq)} \rightarrow Al(OH)_{3(s)}$ $\quad\quad\quad K_s = 1.33\ 10^{-33}$ **III.3**

The second one and the third one are close to each other, and can designate the formation of $[Al(OH)_4]$ complex and CO_3^{2-} as shows the reactions **III.4** and **III.2** respectively:

$Al(OH)_{3(s)} + OH^- \rightarrow [Al(OH)_4]_{(aq)}$ $\quad\quad\quad K_f = 3.0\ 10^{33}$ **III.4**

 - The first plateau in the curve of Co metal can be assigned to the formation of $Co(OH)_2$ hydroxide, while the last plateau is due to the formation of CO_3^{2-} ions.

$Co^{2+}_{(aq)} + 2OH^-_{(aq)} \rightarrow Co(OH)_{2(s)}$ $\quad\quad\quad K_s = 5.92\ 10^{-15}$ **III.5**

 - In the case of $FeCl_3$, a small plateau appeared at pH=3 and can be assigned to the following reaction:

$Fe^{3+}_{(aq)} + OH^-_{(aq)} \rightarrow Fe(OH)^{2+}_{(s)}$ **III.6**

The one noticed at higher values can be attributed to the formation of $Fe(OH)_3$ precipitate following the reaction:

$Fe^{3+}_{(aq)} + 3OH^-_{(aq)} \rightarrow Fe(OH)_{3(s}$ $\quad\quad\quad K_s = 2.79\ 10^{-39}$ **III.7**

Table III. 1. the formation pH calculated and experimental values of the corresponding hydroxides

	Ks	$[H^+]$	pH $_{calculated}$	pH $_{experimental}$
Mg(OH)₂	$2.06\ 10^{-13}$	$3.8\ 10^{-9}$	8.41	10
Co(OH)₂	$5.92\ 10^{-15}$	$2.25\ 10^{-8}$	7.64	8.29
Al(OH)₃	$1.3\ 10^{-33}$	$1.9\ 10^{-4}$	3.7	4.65
Fe(OH)₃	$2.79\ 10^{-39}$	$1.5\ 10^{-2}$	1.8	3.33

 At this stage, theoretical calculations can be performed to assess the experimental results. Using to the solubility product low (**Eq.III.8** and **Eq.III.9**), the concentration of H^+ ions can be deduced which subsequently allows the determination of the pH of formation of each metal hydroxide, it is clear in **Table III. 1.** that the theoretical values are close to the experimental data.

$$K_s = [M^{2+}] \times [OH^-]^2$$ **III.8**

Or

$$K_s = [M^{3+}] \times [OH^-]^3$$ **III.9**

 Where Ks is the solubility product, $[M^{2+}]$ and $[M^{3+}]$ are the concentrations of the divalent and trivalent ions respectively

$$pH = -\log [H^+]$$ **III.10**

For complex mixtures, the complexation curves show that:

 - In the case of the $MgCl_2$, $AlCl_3$ and $NaHCO_3$ mixture, the comparison of the neutralization curves and their corresponding pH makes it possible to attribute the first "pseudo-

plateau" to the formation of the $Al(OH)_3$ precipitate, while the second plateau should correspond to the formation of hydrotalcite phase (around 9.5) according to the reaction [1]:

$$6Mg^{2+} + 2Al(OH)_3 \text{ (s)} + 11 \text{ HO}^- + HCO_3^- \; [Mg_6Al_2(OH)_{16}]^{2+} [CO_3 \sim 4H_2O]^{2-} \qquad \textbf{III.11}$$
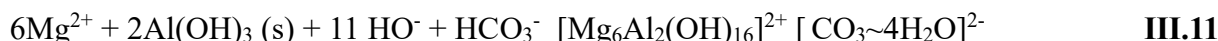
In this domain of pH, only the LDH phase can be formed. The second plateau is followed by a pH drift zone after 9.5, where there can be simultaneous formation of other solid compounds.

The previous reaction, assumes only the intercalation of carbonate ions to ensure the electroneutrality of the structure. Although, the intercalation, at least partial, of chloride ions cannot be excluded because the medium contains a significant quantity, resulting from the dissociation of metal salts. Though, according to the order of priority for the anions occupying the space between the sheets, the intercalation by Cl^- is neglected in the presence of carbonate ions [2].

- In the case of the $MgCl_2$, $FeCl_3$ and $NaHCO_3$ mixture, the first plateau can be due to the formation of $Fe(OH)_2^+$, while the second plateau at around pH= 10, correspond to the formation of the corresponding LDH, or the so-called pyroaurite, according to the reaction:

$$6 Mg^{2+} + 2 Fe(OH)_3 \text{ (s)} + 11 \text{ HO}^- + HCO_3^- \; [Mg_6Fe_2(OH)_{16}]^{2+}[CO_3 \sim 4H_2O]^{2-} \qquad \textbf{III.12}$$

- For $CoCl_2$, $AlCl_3$ and $NaHCO_3$ mixture, the first plateau is attributed to the formation of $Al(OH)_3$, while the second plateau around pH=8 is due to the formation of the CoAl-LDH according to the reaction:

$$6Co^{2+} + 2Al(OH)_3 \text{ (s)} + 11 \text{ HO}^- + HCO_3^- \; [Co_6Al_2(OH)_{16}]^{2+} [CO_3 \sim 4H_2O]^{2-} \qquad \textbf{III.13}$$

The last plateau observed in this case is attributed to the formation of the complex $[Al(OH)_4]$, which denotes that exceeding a certain value of pH will lead to the formation of undesirable product. Accordingly, the domain of formation is restricted between certain values, and the experiments shows that the LDHs phase is formed without impurities as demonstrates Erreur ! Source du renvoi introuvable.**.**
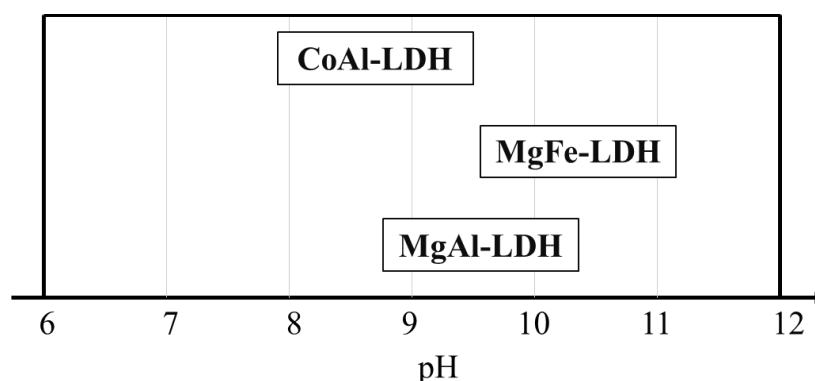
Figure III. 2. The experimental pH domain of formation of MgAl-LDH, MgFe-LDH and CoAl-LDH

III.1. 2.   Coprecipitation synthesis and characterization

In this section, several physicochemical technics were employed in order to assess the structural and the morphological properties of the synthesised materials.

III.1.2. 1. X-ray diffraction (XRD)

The X-ray pattern of the as-synthesized materials shown in Erreur ! Source du renvoi introuvable.. reveal a total coordination of crystallized LDHs with molar ratio of 3:1 in the Rhombohedral R-3m crystal system. The strong reflections of [3]:

- Mg$_6$Al$_2$-CO$_3$-LDH at 2θ = 11.42° and 22.96° corresponding to (0.0.3) and (0.0.6) planes, respectively.
- Mg$_6$Fe$_2$-CO$_3$-LDH at 2θ = 11.37° and 22.93° corresponding to (0.0.6) and (0.0.12) planes, respectively.
- Co$_6$Al$_2$-CO$_3$-LDH at 2θ = 11.50° and 23.26° corresponding to (003) and (006) planes, respectively

Using Scherrer's equation [4]; the average crystallite size (D) is calculated from the broadening β_{sample} (rd) of the strongest peaks [5–7]. The obtained values are summarized in **Table III. 2.** The final results are in good agreement with the literature and provide strong evidence on the formation of the MgAl-LDH, MgFe-LDH and CoAl-LDH phases according to the JCPDS cards N° 00-022-0700, 00-014-0293 and 00-051-0045 respectively.
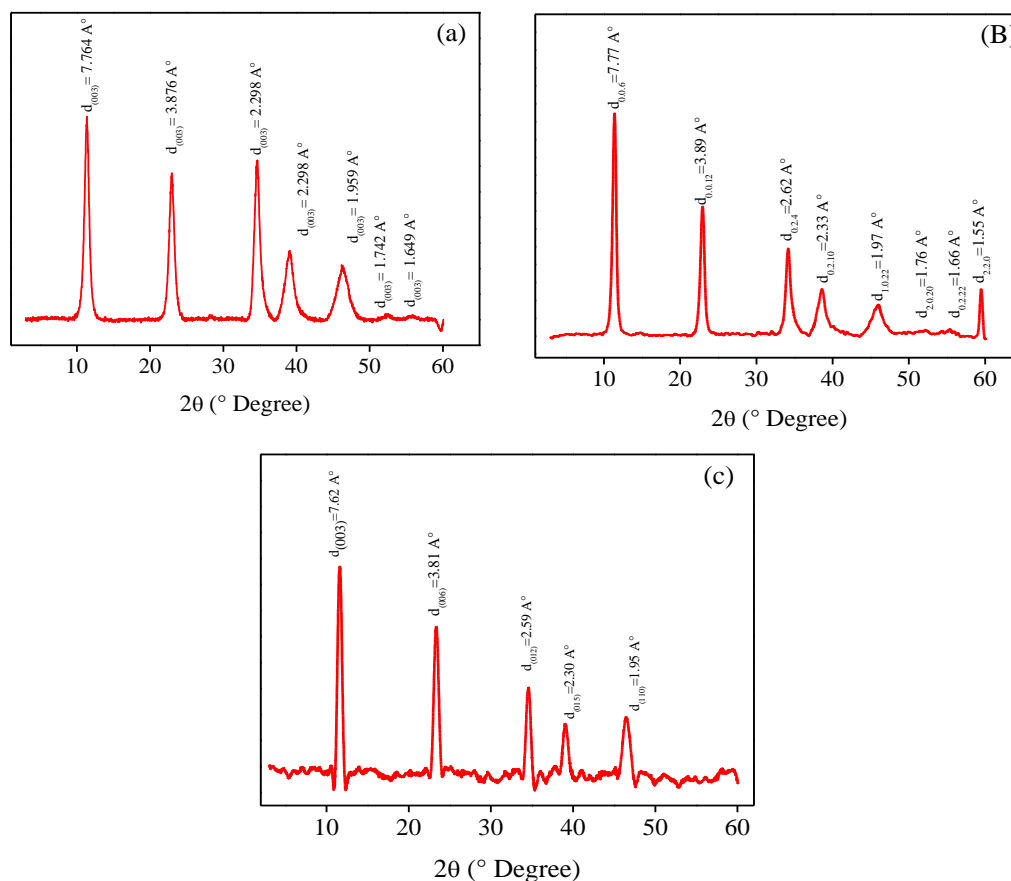
Figure III. 3. XRD patterns of: (a) MgAl-LDH, (b) MgFe-LDH (c) CoAl- LDH

Table III. 2. crystallite size and lattice strain of MgAl-LDH, MgFe-LDH and CoAl-LDH

Crystallographic parameters

	a (A°)	b (A°)	c (A°)	Position (°)	Cristallite size (A°)	Lattice strain (%)
MgAl-LDH	6.2001	6.2001	46.8550	11.419	99.32	3.561
MgFe-LDH	6.2000	6.2000	46.6000	11.374	76.38	4.650
CoAl-LDH	3.0800	3.0800	22.8000	11.607	346.59	1.004

III.1.2. 2.   Fourier Transformer Infra-Red

The FTIR spectra indicated in Erreur ! Source du renvoi introuvable.. represents similar characteristic bonds of the three samples owing to the similarity in their structure. The first large bands in the range of 2800-3600 cm^{-1} are assigned to the stretching of -OH groups in the hydroxide lamella and intercalated water molecules. The second peak at around 1670 cm^{-1} is attributed to water molecules occupying the interlamellar space. The third peak at around 1370 cm^{-1} is due to the antisymmetric stretching vibration mode of carbonate anions CO_3^{2-} in the interlamellar space. The peaks observed at lower wave numbers are corresponding to M-OH and O-M-O lattice vibrations [7,8].
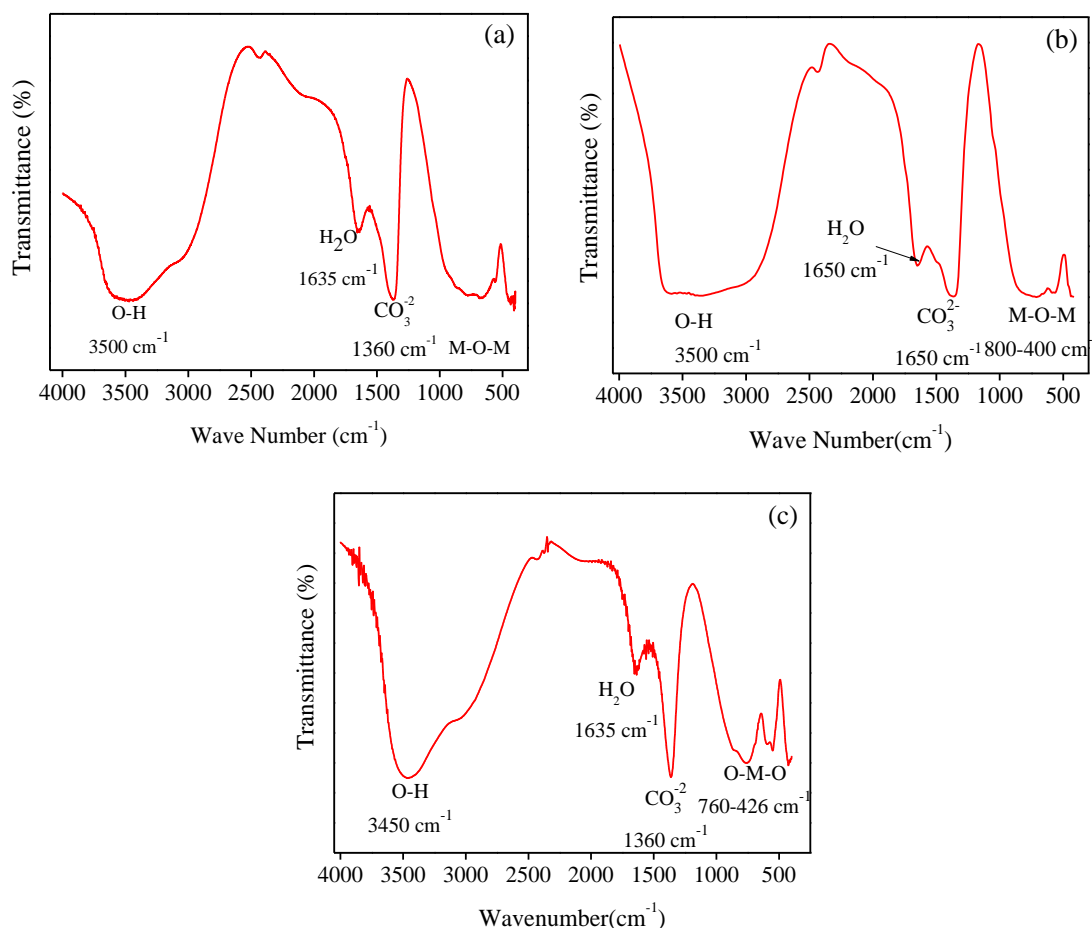
Figure III. 4. FTIR patterns of: (a) MgAl-LDH, (b) MgFe-LDH (c) CoAl- LDH

III.1.2. 3.   Scanning electron microscope (SEM)

The surface morphology of the as synthesized LDHs was observed by scanning electron microscopy, the images of the samples presented in Erreur ! Source du renvoi introuvable. show a hierarchical morphology formed by the assembly of various small nanosheets with irregular size. The higher magnification images unveil a flower-like structure with nanoflakes nanosheets on the surface of the clusters. Moreover, Energy Dispersive Spectroscopy (EDS) results shown in **Table III. 3.** reveal the corresponding composition whose the weight percentage ratios are around 1:3 [9].
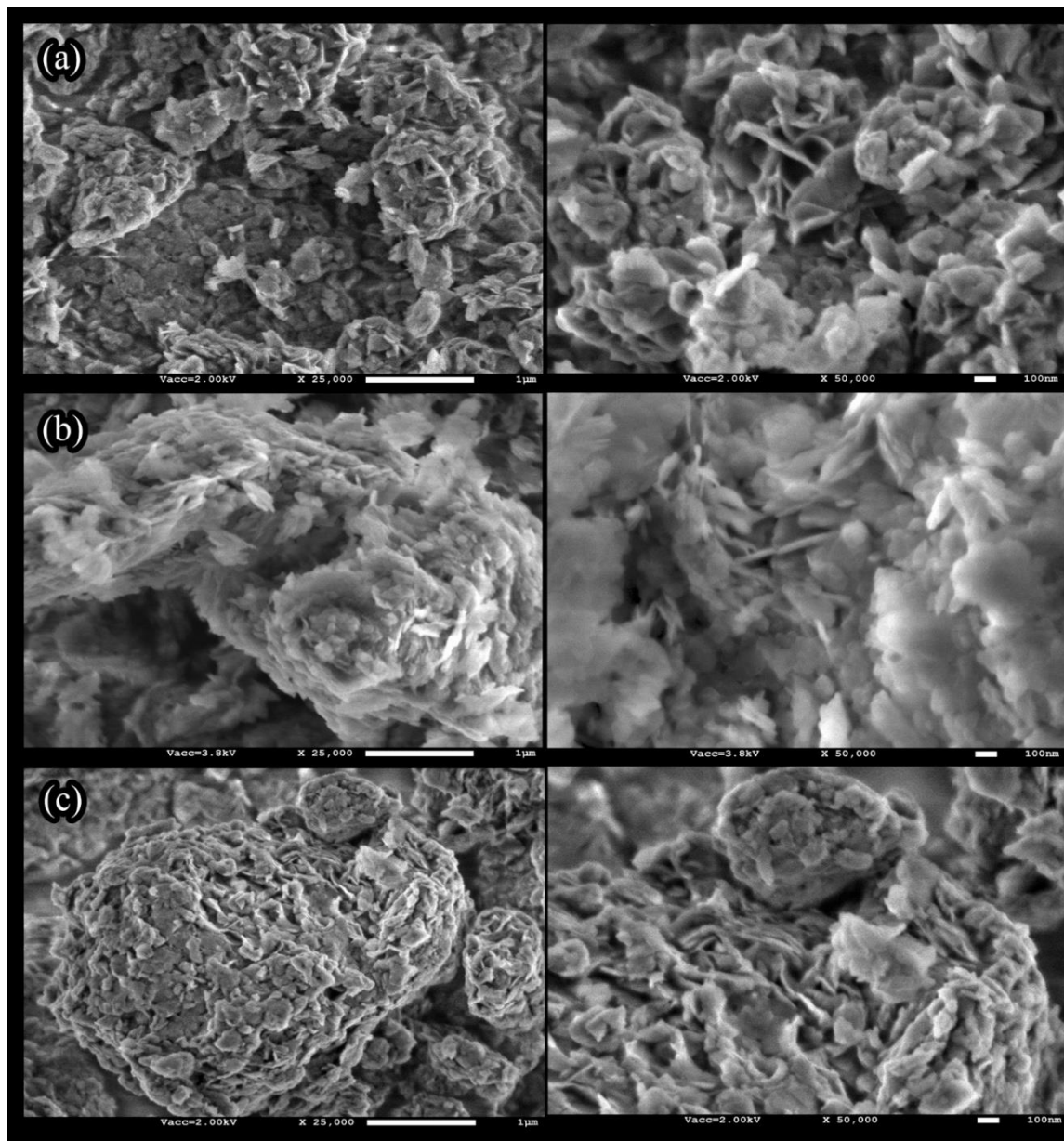
Figure III. 5. SEM images of (a) MgAl- LDH and (b) MgFe-LDH and (c) CoAl-LDH

Table III. 3. EDAX percentages of MgAl-LDH, MgFe-LDH and CoAl-LDH

MgAl- LDH			MgFe-LDH			CoAl-LDH		
Element	Masse %	Atomic %	Element	Masse %	Atomic %	Element	Masse %	Atomic %
Mg	18.72	13.05	**Mg**	14.80	18.62	**Co**	44.20	17.97
Al	7.04	4.42	**Fe**	9.71	5.32	**Al**	6.78	6.02
C	11.05	15.59	**C**	3.19	8.12	**C**	6.60	13.16
O	63.19	66.93	**O**	35.54	67.92	**O**	41.62	62.31

III.1.2. 4. N_2 adsorption-desorption isotherms (BET)

The N_2 adsorption/desorption isotherms of the samples shown in Erreur ! Source du r envoi introuvable.. were used along with the SEM images to evaluate the morphology of the materials. The type IV nitrogen adsorption and H3-type hysteresis loops for the desorption portions of the isotherms indicate the presence of the material's mesoporous structure. Using BET (Braunauere-Emmette-Teller) and BJH (Barrett-Joyner-Halenda) methods, the synthesized MgAl-LDH, MgFe-LDH and CoAl-LDH were estimated to have the surface areas and pore volumes presented in the **Table III. 4**. The radius of the pores is at the scale of nanometers which is in agreement with the morphology depicted by SEM images [10].
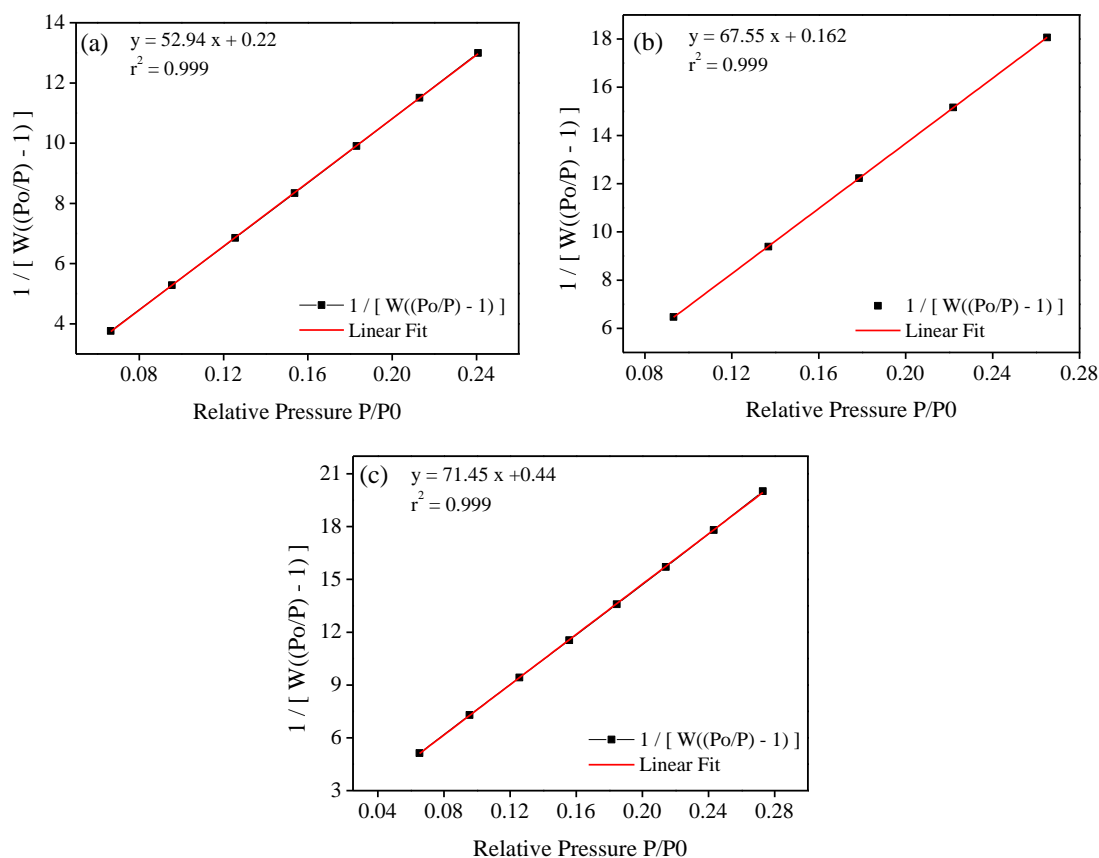
Figure III. 6. Multi-point BET Plot of (a) MgAl-LDH, (b) MgFe-LDH (c) CoAl- LDH.
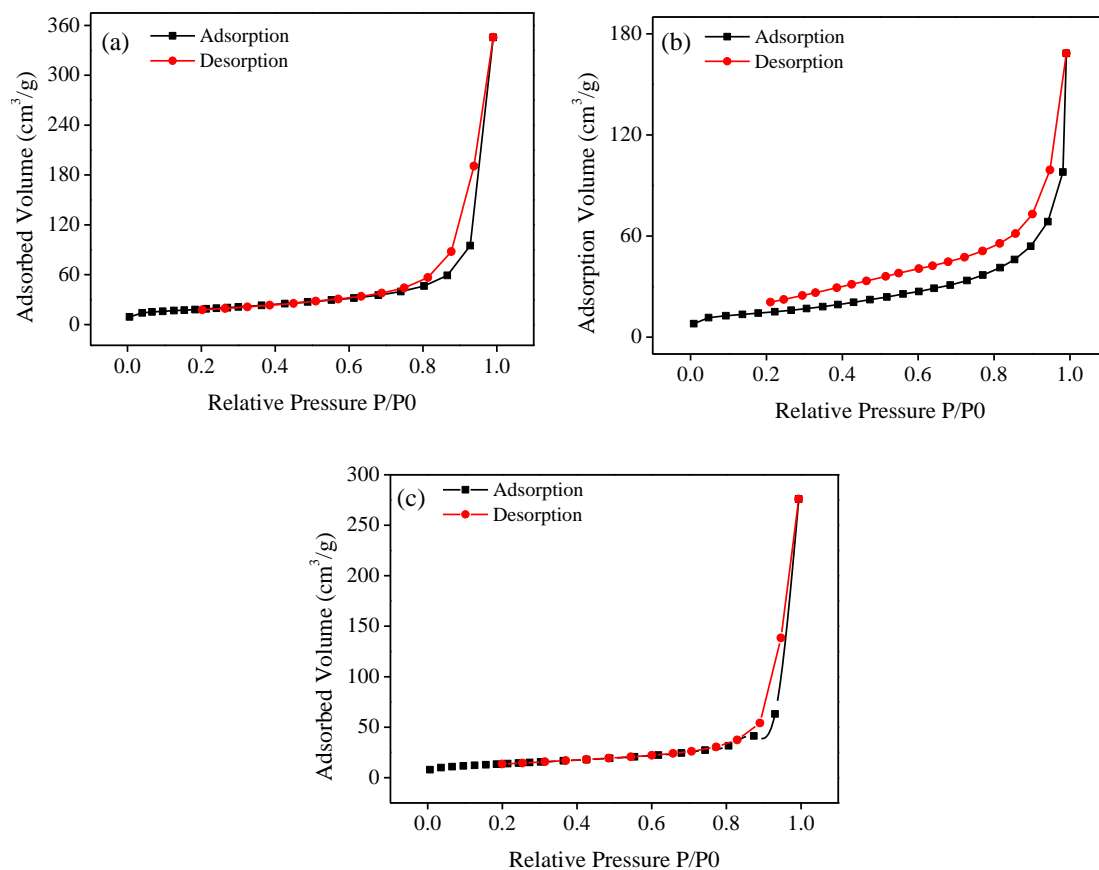
Figure III. 7. N$_2$ adsorption/desorption isotherm of (a) MgAl-LDH, (b) MgFe-LDH (c) CoAl- LDH.

Table III. 4. Textural properties of synthesized materials

	Specific surface area (m^{2}g^{-1})	V$_p$ (cm^{3}g^{-1})	R$_p$ (nm)
MgAl-LDH	65	0.523	12.50
MgFe-LDH	51	0.23	1.98
CoAl-LDH	48	0.43	14.20

III.1.2. 5.   Thermogravimetric Analysis

Erreur ! Source du renvoi introuvable.. presents the TGA/DTG weight loss curves of the p repared materials. The degradation process occurs in three steps. The first is observed below 240 °C, a weight loss of 15% accompanied with two small peaks the DTG curves is assigned to the liberation of water molecules occupying the interlamellar space. The next step in the range of 360-430 °C with a weight loss of 31% is followed by a sharp peak in the DTG curves, this stage can be attributed to the decomposition of carbonate ions and the dihydroxylation of the LDH lamellar structure. The last stage of the TGA curve displays a high loss in mass caused by the formation of oxides followed by an increase in their crystallinity [11,12].
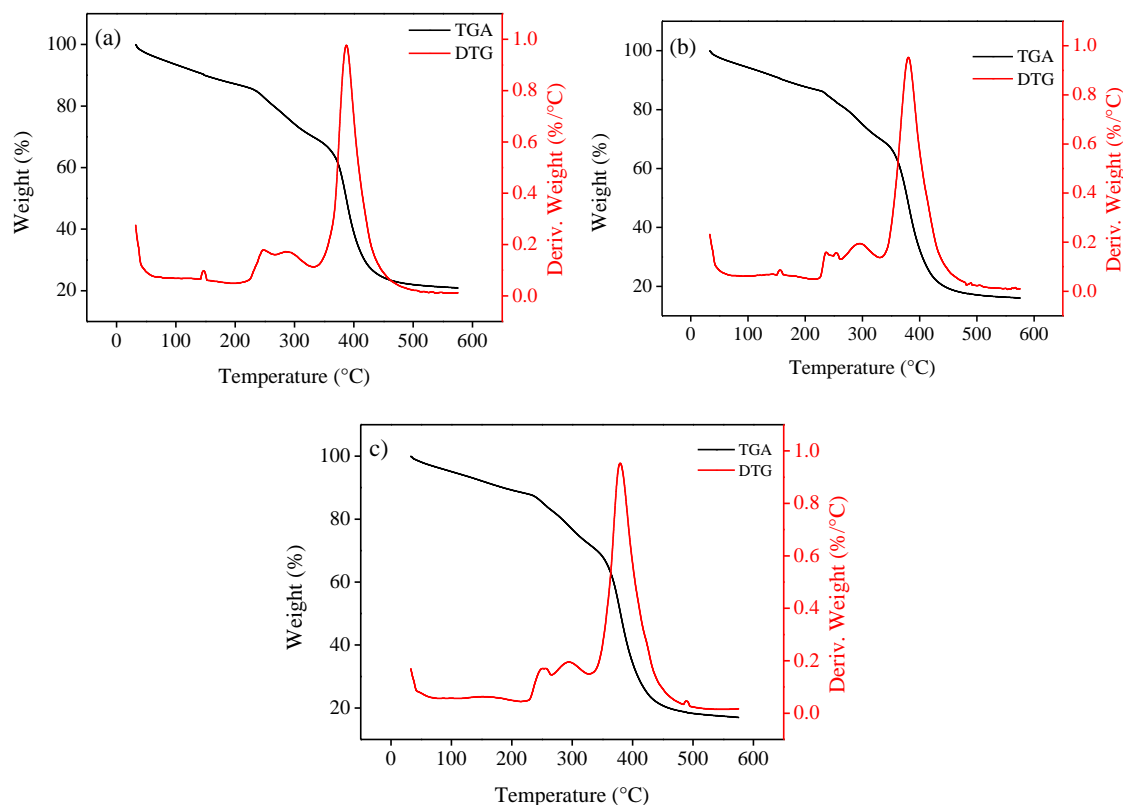
Figure III. 8. TGA / DTG patterns of (a) MgAl-LDH, (b) MgFe-LDH (c) CoAl- LDH.

III.1.2. 6.   Zero charge point

Erreur ! Source du renvoi introuvable.**.** shows the initial pH (pH_i) versus the final pH (pH_f) curves of the powders in KCl solution in order to determine the isoelectric point (PZC: zero charge point) in which the surface charge is zero. The surface charge of particles is counted positive if the pH of the solution is lower than the PZC and vice versa [13,14].
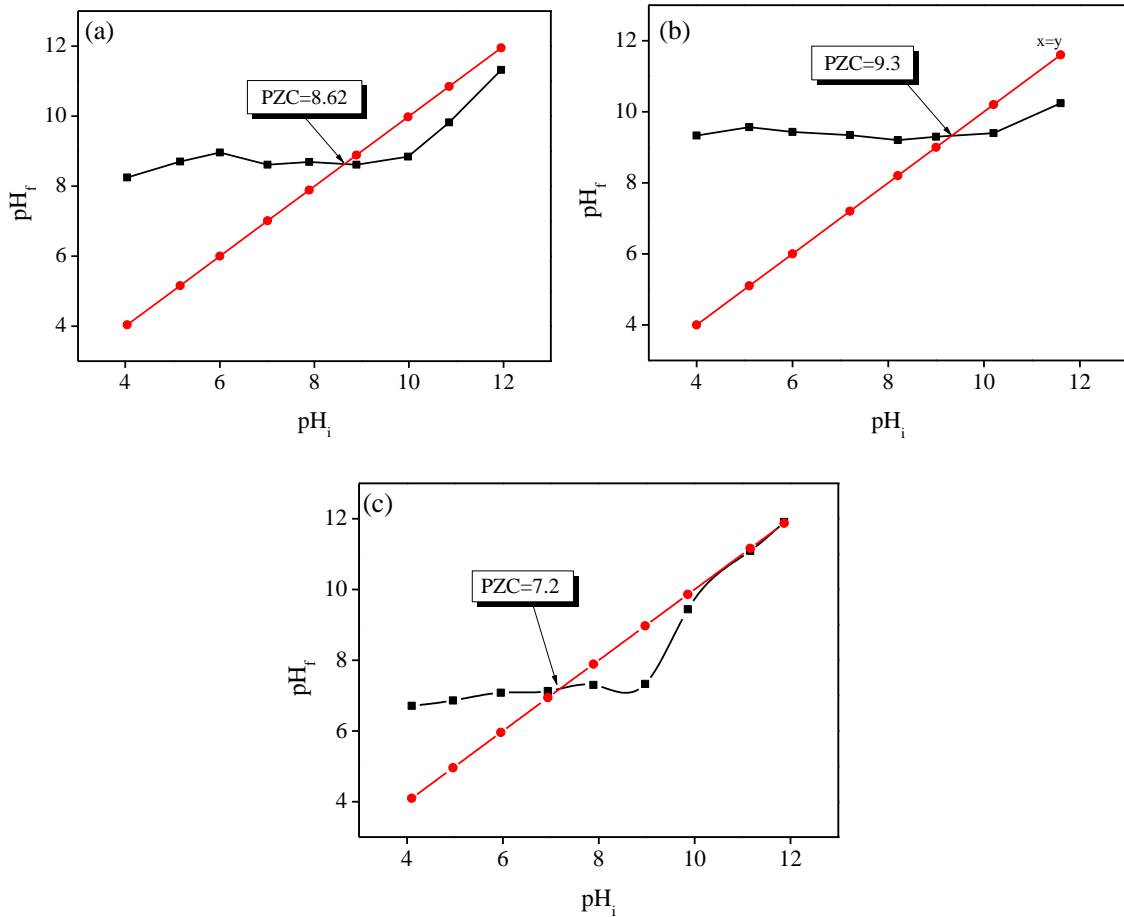
Figure III. 9. PZC determination: (a) MgAl-LDH, (b) MgFe-LDH (c) CoAl- LDH

III.1.2. 7.   Electrochemical characterization

The Open Circuit Potential (OCP) is the potential difference between the working electrode and the reference electrode. The OCP values indicate that the system has reach a "steady state" when there is no current since the circuit is not closed, The OCP value helps studying the corrosion process. Erreur ! Source du renvoi introuvable. displays the open circuit o f the systems and the OCP values are regrouped in **Table III. 5**. According to the findings, the potential changes as a function of time from more negative to less negative values, this can be explained that the system would much rather take electrons in than lose electrons, so it is more likely that reduction reactions occur.
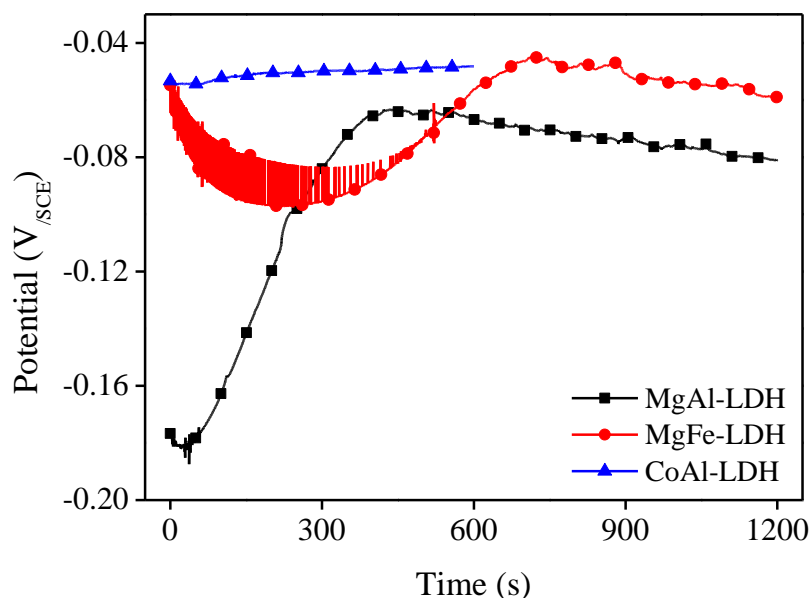
Figure III. 10. Open circuit potential curves of MgAl-LDH, MgFe-LDH and CoAl-LDH

Table III. 5. Open circuit potential values of MgAl-LDH, MgFe-LDH and CoAl-LDH

	MgAl-LDH	**MgFe-LDH**	**CoAl-LDH**
OCP (V/SCE)	-0.09	-0.066	-0.048

The electrochemical impedance spectroscopy (EIS) was used to study the charge transfer phenomena arising at the interface in the OCP potential. The measurements were carried out at the free potential (OCP) of the working electrodes in K_2SO_4(0.1M) electrolyte over a frequency range from 10^{-3} Hz to 10^5 Hz in the Nyquist plane. Experimental results were fitted to an appropriate electrical equivalent circuit, it contained a series resistor (R) and constant phase elements (CPE).

Ohmic impedance, also known as the solution resistance (R_s), is the distance from the origin of the semicircle to the Y axis. It is related to ion conduction in the electrolyte phase and electron conduction in the electrode phase, and it measures the internal resistance of the electrolyte between the reference electrode and the working electrode [15]. The semi cercles are attributed to the faradaic charge transfer between electrolyte and electrode material. The size of Nyquist semicircles are as follows: CoAl-LDH>MgAl-LDH>MgFe-LDH, a larger semicircle indicates a higher corrosion resistance in the media and the smaller radius indicates the lower interface resistance transmission of charge carriers, in other word, when the charge transfer resistance in small, the charge transfer ability is stronger, and the redox reactions of adsorption/desorption are easier. The constant phase element (CPE) represents the electric double-layer capacitance in the equivalent circuit, which is widely present in the three composite electrodes [15,16]
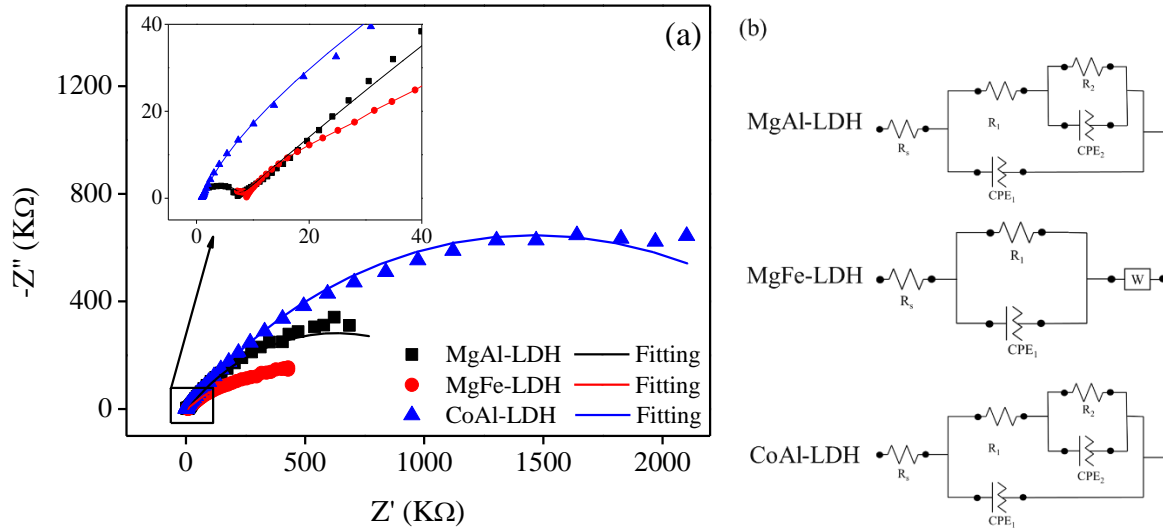
Figure III. 11. Impedance spectroscopy (a) in K_2SO_4(0.1M) of MgAl-LDH, MgFe-LDH and CoAl-LDH and the equivalent circuits (b).

Table III. 6. Electrochemical parameters in the equivalent circuits obtained from the fitted EIS plots of MgAl-LDH, MgFe-LDH and CoAl-LDH

		MgAl-LDH	**MgFe-LDH**	**CoAl-LDH**
R_s (Ω)		852.09	6909.1	967.24
R_1(Ω)		6581.5	$3.87\ 10^5$	71961
R_2(Ω)		$1.24\ 10^6$	/	$2.88\ 10^6$
CPE$_1$	Y_0	$1.4\ 10^{-9}$	$2.049\ 10^{-6}$	$2.36\ 10^{-7}$
	n	0.91	0.47	0.80
CPE$_2$	Y_0	$4.35\ 10^{-6}$	/	$1.155\ 10^{-6}$
	n	0.541	/	0.506
W	Y_0	/	2.93	/
x^2		0.23	0.20	0.085

     Polarisation tests and Tafel curves has been nominated as a reliable method in corrosion-oriented works for the study of the stability of materials, they are designed to measure the rate of uniform corrosion in units of penetration. These tests allowed to deduce the corrosion parameters of the as synthesised materials [17]. The corrosion electrokinetic parameters deduced from the Tafel method including corrosion potential (E_{corr}), corrosion current density (i_{corr}), and both anodic and cathodic Tafel slopes, b_a and b_c are collected in the **Table III.7**. The corrosion rate C_R (mm/y) was determined using the Faraday's law (Eq.).

$$C_R = \frac{3.16 \times 10^8 \times i_{corr} \times M}{n \times F \times \rho} \qquad \textbf{III.14}$$

Where i_{corr} and ρ are corrosion current density and density of the metal, respectively.
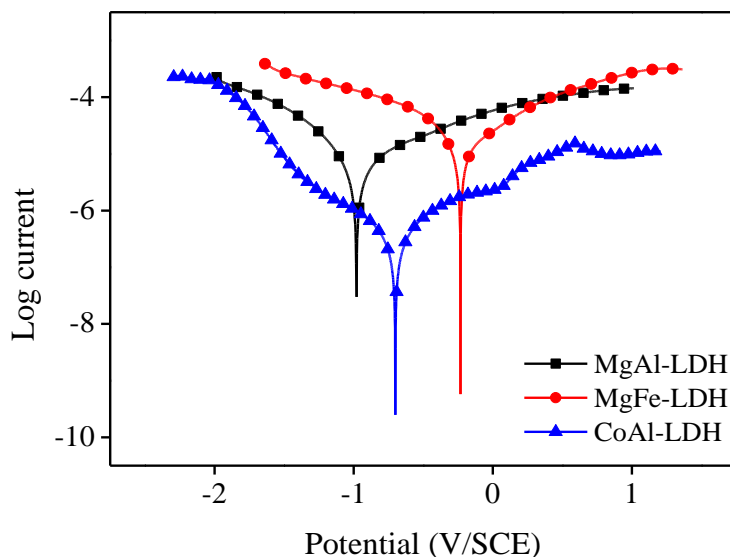
Figure III. 12. Polarization c22

urves in K_2SO_4(0.1M) (SR =5mV/s) of MgAl-LDH, MgFe-LDH and CoAl-LDH

Table III. 7. Electrokinetic parameters extracted from the polarization curves associated with MgAl-LDH, MgFe-LDH and CoAl-LDH.

	MgAl-LDH	**MgFe-LDH**	**CoAl-LDH**
b_a **(V/dec)**	0.685	0.826	1.36
b_c **(V/dec)**	2.066	1.25	1.27
E_{corr} **(Calc) (V)**	-0.980	-0.161	-0.703
C_{corr} **(Obs) (V)**	-0.979	-0.232	-0.700
j_{corr} **(Calc) ((A/cm^2)**	$13.84 \ 10^{-6}$	$28.72 \ 10^{-6}$	$0.987 \ 10^{-6}$
i_{corr} **(Obs) (A)**	$13.84 \ 10^{-6}$	$28.729 \ 10^{-6}$	$0.987 \ 10^{-6}$
Corrosion rate (mm/year)	7.04	17.336	0.838
Polarisation resistance (Ω)	$16.13 \ 10^{3}$	$7.52 \ 10^{3}$	$288.78 \ 10^{3}$
x^2	$6.06 \ 10^{-11}$	$5.54 \ 10^{-9}$	$1.12 \ 10^{-12}$

III.1. 3.   Electrochemical synthesis and characterization
III.1.3. 1.   Linear voltammetry
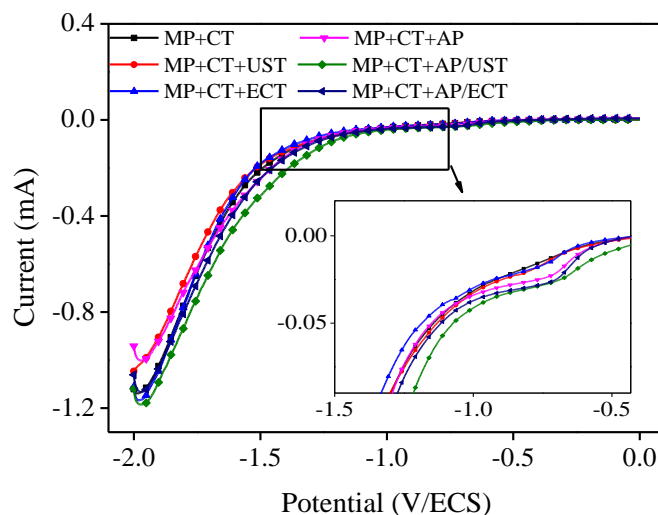
Figure III. 13. Linear sweep voltammetry of Nickel electrode in NaHCO$_3$ (0.005M, pH=5, scan rate =1mV/s), a) MP+CT; b) MP+CT + UST; c) MP+CT +ECT; d) MP+CT +AP; e) MP+CT +AP/UST; f) MP+CT +AP/ECT.

The results of linear sweep voltammetry (LSV) give important information about the conditions of electrochemical synthesis. First, these curves are used to study the effect of treatment and polishing on the effectiveness of the surface and determine the range of potential which must be applied for the formation the LDH.

The working surface is first subjected to a mechanical polishing (MP) by sand paper 1200 then 2400, followed by a chemical treatment CT (emersion for 10 min in acetone, then emersion for 15min in 40% ethanol). Subsequently, the electrode subjected to one of the following treatments [18]:

a. Ultrasound treatment (UST) in a distilled water bath for 10min.
b. Electrochemical treatment (ECT) in distilled water by applying a strong cathodic potential (-2.5V) for 10 min.
c. Polishing with alumina on a polishing cloth (AP).
d. Polishing with alumina on a polishing cloth followed by ultrasonic treatment (AP/UST).
e. Polishing with alumina on a polishing cloth followed by an electrochemical treatment AP/ECT).

The curves can be divided into four parts, the first is characterized by a rapid rise from E=-2.0V/SCE to E=-1.1V/SCE, it can be attributed to the reduction of water into H$_2$ and OH$^-$, it was noticed at this phase the formation of hydrogen bubbles on the surface of the electrode during the experiment. The second part appears as a plateau between E=-1.05V/SCE and E=-0.65V/SCE. In the third after E=-0.65V/SCE, the current increase in this part is slower than the first, it can be attributed to the reduction oxygen O$_2$ giving OH$^-$. The current vanishes when the system comes to a steady state which is due to the immunity of the electrode.

The atmosphere contains 20% oxygen which dissolves in open solution at a concentration of 10^{-4} M. OH$^-$ ions can be obtained in this system either by the reduction of water or by the reduction of oxygen:

$$2H_2O + 2e^- \rightarrow H_2 + 2OH^- + 2é \qquad \Rightarrow E° = -0.828V/SCE \qquad \textbf{III.15}$$

$$O_2 + 4e^- + 2H_2O \rightarrow 4OH^- \qquad \Rightarrow E° = 1.230V/SCE \qquad \textbf{III.16}$$
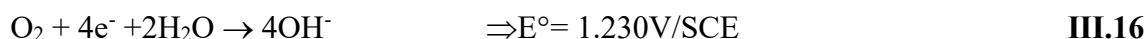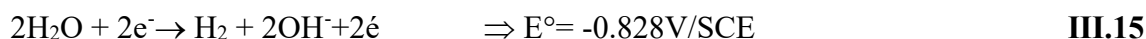
The reduction of water also produces hydrogen, which negatively affects the efficiency of the work surface, the reduction of oxygen on the other hand generates four OH$^-$ entities without hydrogen bubbles. According to the previous results, polishing with alumina on a polishing cloth followed by ultrasonic treatment (AP/UST) is the best polishing method and will be adapted before each experiment because the overpotential required for the production of OH$^-$ is lower than that of the one polished only mechanically [19].
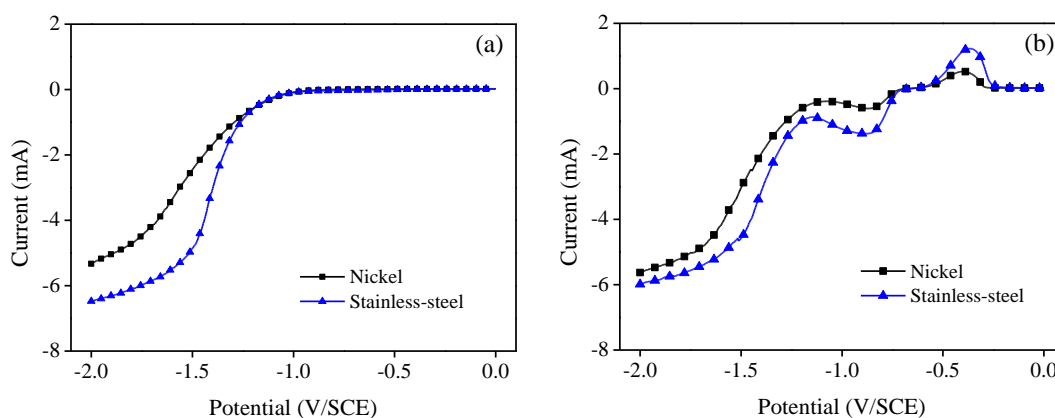
Figure III. 14. Linear sweep voltammetry (scan rate =1mV/s) of Nickel, Titan and stainless-steel electrodes in in a solution (C_T= 0.03M, pH~5) of MgAl-LDH (a) and CoAl-LDH (b).

The LSV was then performed in solution containing the precursors of MgAl-LDH and CoAl-LDH using Nickel and stainless-steel as working electrodes. The experiments performed in a solution containing MgCl$_2$, AlCl$_3$ and NaHCO$_3$ showed a similar curve to the Erreur ! S ource du renvoi introuvable.. The metal of the working electrode has a slight effect on the current which showed more negative values in the case of stainless-steel electrode, though, the general shape of the curve did not change which will not affect the domain of potential chosen for the electrodeposition. The existence of a significant current when the imposed potential is more cathodic than -1.2 V/SCE is attributed to water reduction reaction, while the domain before -0.06 is the steady state of the electrode. Subsequently, the potential between -1.2 V/SCE and -0.06 V/SCE is the domain where the LDH phase is more likely to be formed.

In the solution CoCl$_2$, AlCl$_3$ and NaHCO$_3$, a current peak appeared in addition to the water reduction wall, which is attributed to the reduction of cobalt cation according to the following reaction (**III.17**):

$$Co^{2+} + 2e^- \rightarrow Co \qquad E° = -0.28 \text{ V/SHE} \qquad \textbf{III.17}$$

The presence of this concomitant reaction limits the domain of potential for the obtention of pure LDH phase seeing that the formation of Co metal is possible in the potential region of the peak.

III.1.3. 2. Electrodeposition of MgAl-LDH on the metallic electrodes

The electrosynthesis of the materials was carried out using chronoamperometry by imposing a fixed potential on the electrode during a fixed period of time. This synthesis pathway induces the generation of OH$^-$ at the working electrode which increases the local pH and leads to the deposition of LDH from the metal salts solution [20]. The study of nucleation and growth is essential in the electrodeposition, because the driving force of nucleation can be simply varied by changing the applied potential. Generally, as long as the cathodic potential is applied, the OH$^-$ are forming and the LDH is precipitating very rapidly since the necessary pH is easily reached, the current in this case decreases from more negative values to positive values until reaching a stabilised state around 60s which is due to the nucleation process on the surface of the electrode, the decreasing part obeys the Cottrell equation [21].

Erreur ! Source du renvoi introuvable.. **(a and c)** and Erreur ! Source du renvoi in trouvable.. **(a and c)** illustrate the effect of the applied potential on the electrodeposition process, the experiments showed that the white MgAl-LDH deposit start appearing at values greater than -1.1V/SCE, more negative potentials increase the thickness of the film, which is accompanied by an increase in the residual current values. However, from -1.3V/SCE on, the process is accompanied with the formation of H$_2$ bobbles which causes the detachment of the formed grains from the surface [21]. The best deposit was obtained at the value of -1.2V/SCE.

Erreur ! Source du renvoi introuvable.. **(b and d)** and Erreur ! Source du renvoi in trouvable.. **(b and d)** illustrate the effect of time on the electrodeposition, it was noticed that the value of the residual current didn't change significantly since a stability plateau is observed after 300s. though, the increase in the time increases the nucleation process and thus, increases the thickness of the films, which effect negatively the adhesion of the material to the surface and causes its detachment. The best deposition time was 1200 s.
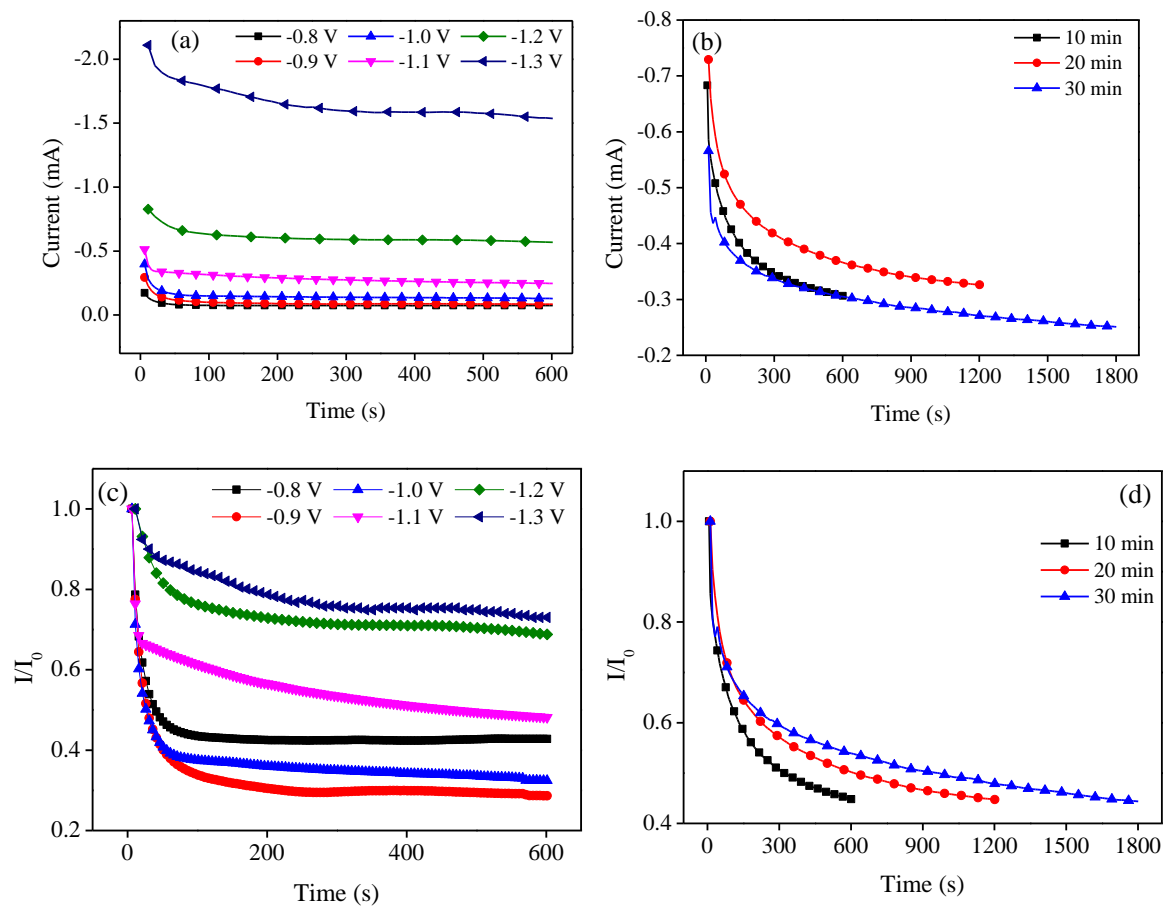
Figure III. 15. Effect of applied potential variation (a and c) and time variation (b and d) on the electrodeposition of MgAl-LDH (C_T= 0.03M, pH~4.7) on Nickel electrode.
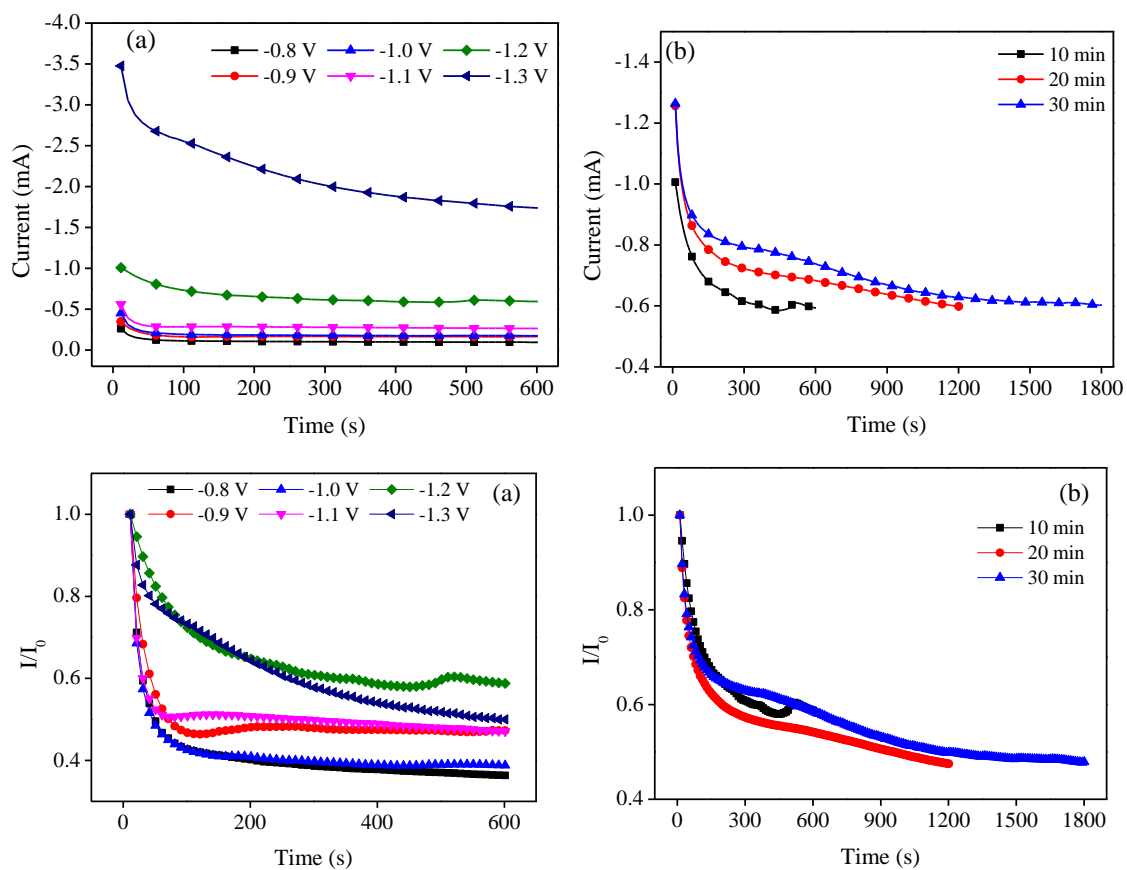
Figure III. 16. Effect of applied potential variation (a and c) and time variation (b and d) on the electrodeposition of MgAl-LDH (C_T= 0.03M, pH~4.7) on stainless-steel electrode.

Table III. 8. Initial and residual current extracted from chronoamperometric curves of MgAl-LDH electrodeposition with potential variation.

	Applied potential (V/SCE)	Initial current I_i (mA)	Residual current I_{res} (mA)	I_{res}/I_0
Nickel electrode	-0.8	-0.173	-0.074	0.428
	-0.9	-0.293	-0.084	0.287
	-1.0	-0.398	-0.129	0.324
	-1.1	-0.513	-0.247	0.481
	-1.2	-0.827	-0.569	0.688
	-1.3	-2.109	-1.537	0.729
Stainless-steel electrode	-0.8	-0.261	-0.095	0.364
	-0.9	-0.345	-0.163	0.472
	-1.0	-0.450	-0.174	0.387
	-1.1	-0.558	-0.263	0.471
	-1.2	-1.006	-0.593	0.589
	-1.3	-3.476	-1.736	0.499

Table III. 9. Initial and residual current extracted from chronoamperometric curves of MgAl-LDH electrodeposition with time variation.

	Electrodeposition time (min)	Initial current I_i (mA)	Residual current I_{res} (mA)	I_{res}/I_0
Nickel electrode	10	-0.683	-0.303	0.444
	20	-0.729	-0.326	0.447
	30	-0.567	-0.251	0.443
Stainless-steel	10	-1.006	-0.598	0.594
	20	-1.257	-0.598	0.476
	30	-1.264	-0.603	0.477

III.1.3. 3.   Electrodeposition of CoAl-LDH on the metallic electrodes

The previously described chronoamperometry was also performed for the electrochemical synthesis of CoAl-LDH on Nickel and Stainless-steel electrodes.

For the electrodeposition of CoAl-LDH shown in Erreur ! Source du renvoi introuvable. and Erreur ! Source du renvoi introuvable., the obtained results are similar to the ones obtained for MgAl-LDH, the current shows a drift from negative to more positive values and reaches a plateau after 60s, this part is accompanied with the nucleation process following an increase in the pH of the vicinity of the electrode. The variation of the applied potential and the deposition time allowed to choose -1.2 V/SCE and 1200s as best conditions. In this case, when the potential is not sufficiently negative (less than -0.9 V), the current increases into the negative side, which is due to the presence of a concomitant reaction leading to the formation of Co metal [22].
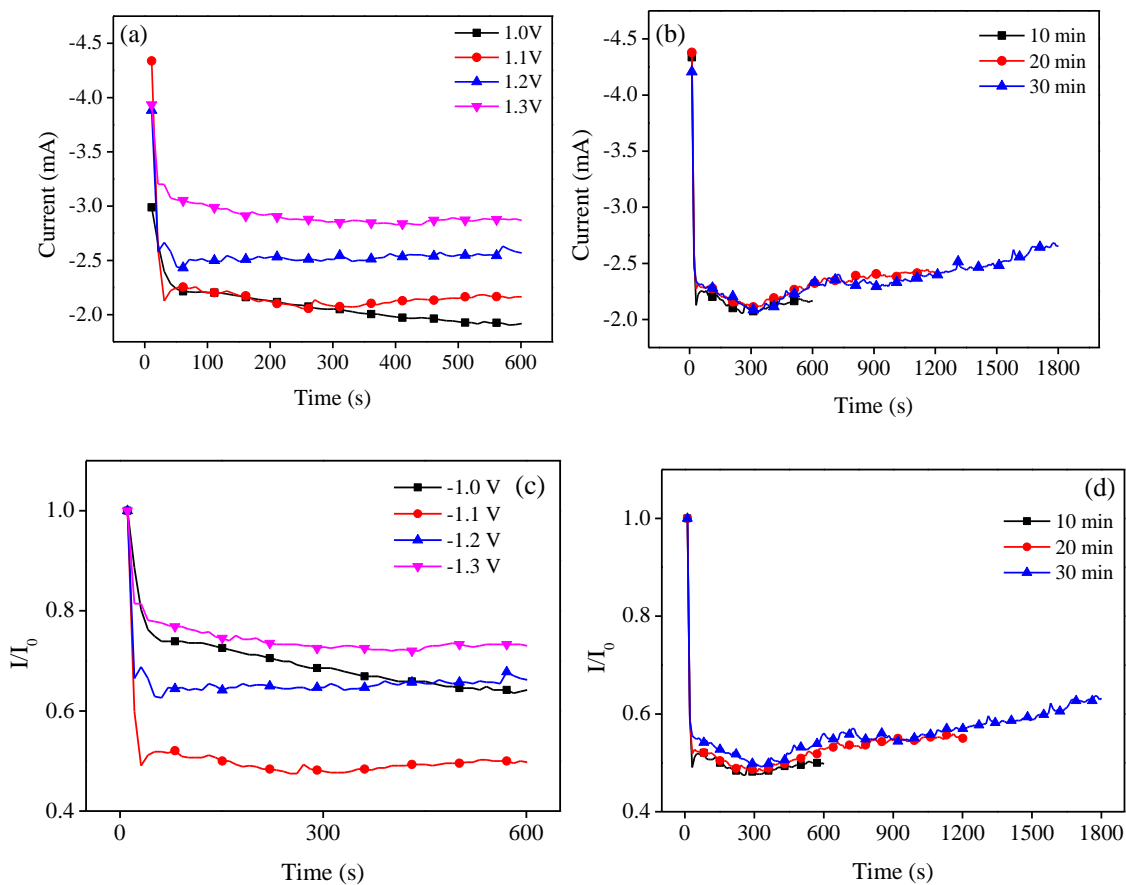
Figure III. 17. Effect of applied potential variation (a and c) and time variation (b and d) on the electrodeposition of CoAl-LDH (C_T= 0.03M, pH~4.7) on Nickel electrode.
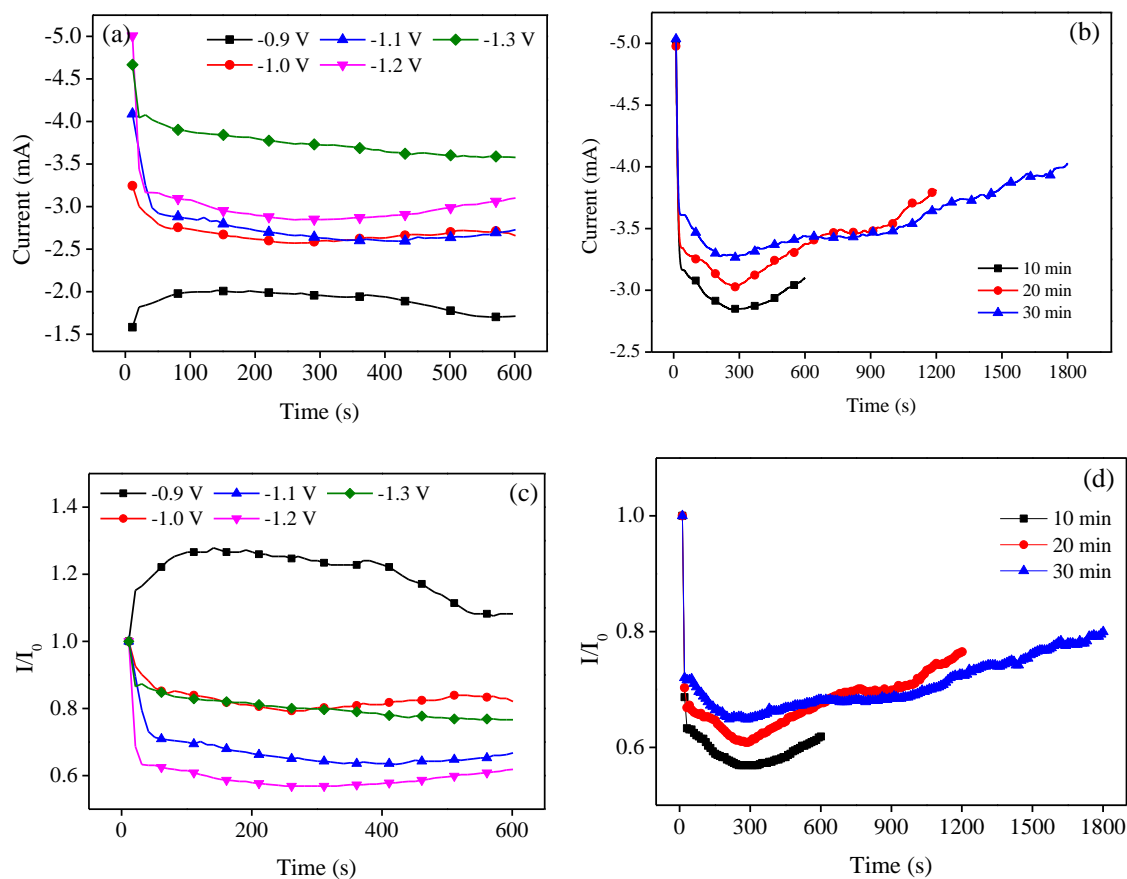
Figure III. 18. Effect of applied potential variation (a and c) and time variation (b and d) on the electrodeposition of CoAl-LDH (C_T= 0.03M, pH~4.7) on Stainless-steel electrode.

Table III. 10. Initial and residual current extracted from chronoamperometric curves of CoAl-LDH electrodeposition with potential variation.

|	Applied potential (V/SCE)	Initial current I_i (mA)	Residual current I_{res} (mA)	I_{res}/I_0
Nickel electrode	-1.0	-2.987	-1.919	0.642
	-1.1	-4.337	-2.164	0.499
	-1.2	-3.882	-2.568	0.662
	-1.3	-3.933	-2.869	0.729
Stainless-steel electrode	-0.9	-1.584	-1.712	1.081
	-1.0	-3.245	-2.658	0.819
	-1.1	-4.089	-2.728	0.667
	-1.2	-5.006	-3.101	0.619
	-1.3	-4.667	-3.578	0.767

Table III. 11. Initial and residual current extracted from chronoamperometric curves of CoAl-LDH electrodeposition with time variation.

	Electrodeposition time (min)	Initial current I_i (mA)	Residual current I_{res} (mA)	I_{res}/I_0
Nickel electrode	10	-4.337	-2.164	0.499
	20	-4.378	-2.398	0.548
	30	-4.207	-2.655	0.631
Stainless-steel	10	-5.005	-3.101	0.620
	20	-4.976	-3.812	0.766
	30	-5.035	-4.029	0.800

III.1.3. 4.   Electrochemical characterization of the electrodeposited materials

The EIS was used to study the charge transfer phenomena of the deposit compared with the bare electrode arising. The measurements were carried out at the free potential (OCP) of the working electrodes in K_2SO_4(0.1M) electrolyte over a frequency range from 10^{-3} Hz to 10^5 Hz in the Nyquist plane. Observing the curves shows that they included one semicircle and a diffusion line in some the cases as shows the Erreur ! Source du renvoi introuvable..**(a and b)**.

. The equivalent circuit diagrams used in the analysis of the EIS spectra is shown in Erreur ! Source du renvoi introuvable..**c**. where Rs represents the solution resistance, CPE r epresents the constant phase element during the charge transfer reaction, R represents the charge transfer resistance and W represents the Warburg diffusion element that models the diffusion process.

The size of the semi cercles related with the faradaic charge transfer between electrolyte and electrode surface helps to assess the corrosion resistance in the electrolyte, a larger semicircle indicates a higher corrosion resistance a smaller radius indicates a lower interface resistance transmission of charge carriers [22], the deposition process made the surfaces of the transmission of the charge carriers easier due to the charge excess in the lamellar structure of the LDHs . The constant phase element (CPE) represents the electric double-layer capacitance in the equivalent circuit, which is widely present in the deposited films [23].
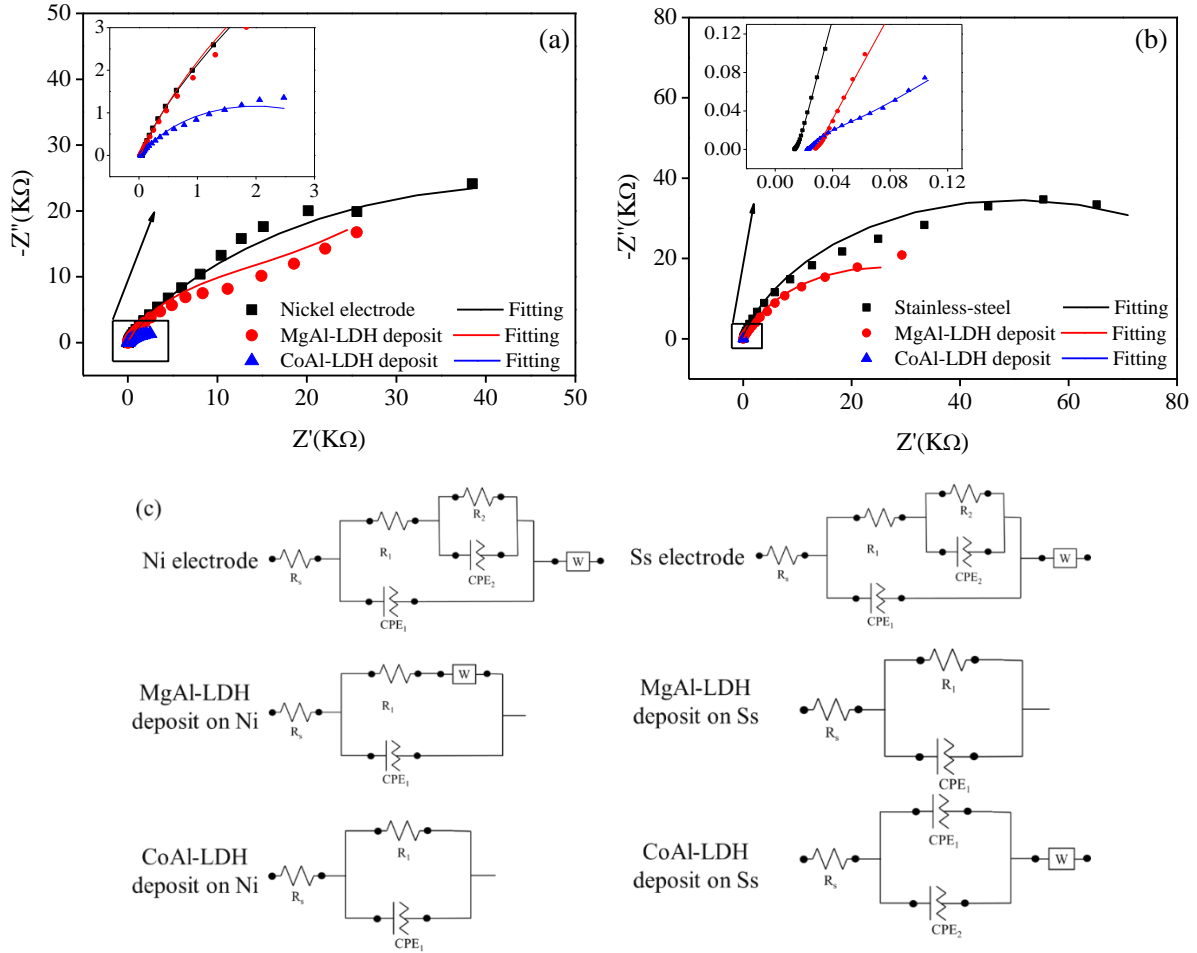
Figure III. 19. Electrochemical impedance spectra in K_2SO_4(0.1M) of MgAl-LDH/Ni, MgAl-LDH/Ss, CoAl-LDH/Ni and CoAl-LDH/Ss

Table III. 12. Electrochemical parameters in the equivalent circuits obtained from the fitted EIS plots of MgAl-LDH/Ni, MgAl-LDH/Ss, CoAl-LDH/Ni and CoAl-LDH/Ss

		MgAl-LDH/Ni	MgAl-LDH/Ss	CoAl-LDH/Ni	CoAl-LDH/Ss
R_s (Ω)		22.9	28.55	29.048	22.499
R_1(Ω)		20265	50623	3914	/
CPE_1	Y_0	6.61 10^{-5}	9.8 10^{-5}	0.00118	0.0813
	n	0.80	0.78	0.68	0.199
CPE_2	Y_0	/	/	/	0.0599
	n	/	/	/	1.1
W	Y_0	1.6 10^{-4}	/	/	0.045
x^2		0.211	0.090	0.040	0.0039

The CV curves of the bare electrodes compared with MgAl-LDH and CoAl-LDH deposits are used to assess the electrochemical behaviour of the films as presented in Erreur ! Source du r envoi introuvable.. After the water reduction wall, MgAl-LDH demonstrates the same response as the bare electrodes, this might be attributed to the high porosity of the deposited films which allow the diffusion of the solution to the metal surface, so then obtain similar response, the absence of any peaks is totally expected for this deposit since the standard potentials of Mg^{2+} and Al^{3+} existing in the film are high enough that makes their reduction excluded in this domain of potential. Contrary to the CoAl-LDH where the peak of reduction of Co^{2+} appears at around -0.88V/SCE. The CV of CoAl-LDH exhibits a very broad feature which is characteristic of both electric double layer capacitance and Faradaic pseudo-capacitance [24].
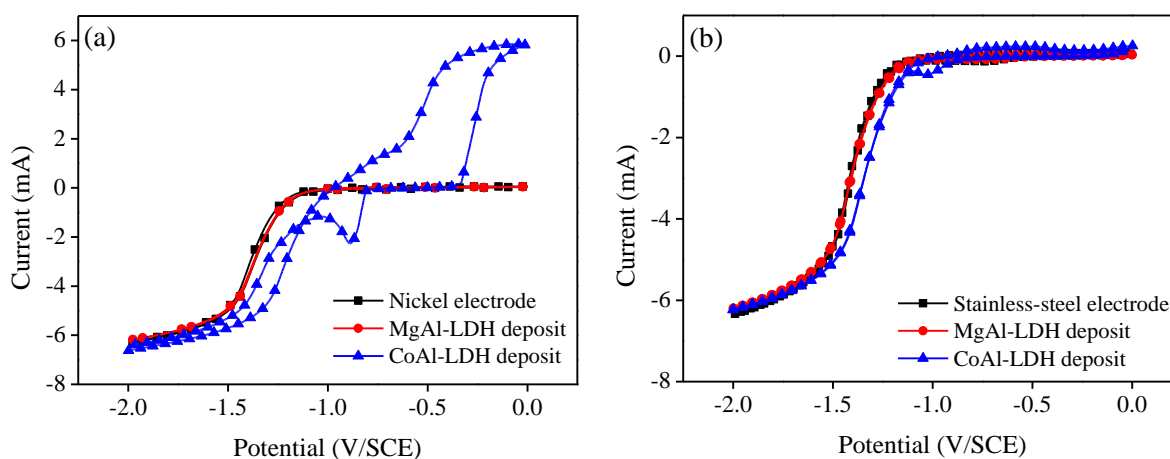
Figure III. 20. Comparison of the CV (10mV/s) curves of MgAl-LDH and CoAl-LDH deposits with the bare electrodes compared in K_2SO_4(0.1M)

References

[1] J. W. Boclair, P. S. Braterman, *Chem. Mater.* **1999**, *58* (17), 298–302.

[2] D. L. Bish, **1980**, *103* (May), 170–175.

[3] L. Wu, X. Ding, Z. Zheng, Y. Ma, A. Atrens, X. Chen, *Appl. Surf. Sci.* **2019**, *487* (January), 558–568. DOI: 10.1016/j.apsusc.2019.05.115.

[4] Y. Zhu, R. Zhu, G. Zhu, M. Wang, Y. Chen, J. Zhu, Y. Xi, H. He, *Appl. Surf. Sci.* **2018**, *433*, 458–467. DOI: 10.1016/j.apsusc.2017.09.236.

[5] K. Nejati, A. R. Akbari, S. Davari, K. Asadpour-Zeynali, Z. Rezvani, *New J. Chem.* **2018**, *42* (4), 2889–2895. DOI: 10.1039/c7nj04469k.

[6] N. E. H. Hadj-Abdelkader, A.-P. Beltrao-Nunesa, F. Belkhadem, N. Benselka, R. Roy, A. Azzouza, *Appl. Clay Sci.* **2020**, *198*, 105829. DOI: 10.1016/j.clay.2020.105829.

[7] A. F. da Silva, J. L. da S. Duarte, L. Meili, *Sep. Purif. Technol. 264*. **2021**, *264*, 118353. DOI: 10.1016/j.seppur.2021.118353.

[8] J. K. E. Tan, N. Birbilis, S. Choudhary, S. Thomas, P. Balan, *Corros. Sci.* **2022**, *205* (June), 110444. DOI: 10.1016/j.corsci.2022.110444.

[9] S. Sharma, G. Sharma, A. Kumar, P. Dhiman, T. S. AlGarni, M. Naushad, Z. A. ALOthman, F. J. Stadler, *Sep. Purif. Technol.* **2022**, *278* (June 2021), 119481. DOI: 10.1016/j.seppur.2021.119481.

[10] H. K. D. Nguyen, H. Van Nguyen, V. A. Nguyen, *J. Mol. Struct.* **2018**, *1171*, 25–32. DOI: 10.1016/j.molstruc.2018.05.087.

[11] J. Wang, L. A. Stevens, T. C. Drage, J. Wood, *Chem. Eng. Sci.* **2012**, *68* (1), 424–431. DOI: 10.1016/j.ces.2011.09.052.

[12] H. Hu, Y. Yuan, W. Shi, *Prog. Org. Coatings*. **2012**, *75* (4), 474–479. DOI: 10.1016/j.porgcoat.2012.06.007.

[13] S. Iftekhar, M. Emin, V. Srivastava, E. Repo, **2018**, *209*, 470–479. DOI: 10.1016/j.chemosphere.2018.06.115.

[14] F. P. De Sá, B. N. Cunha, L. M. Nunes, *Chem. Eng. J.* **2013**, *215–216*, 122–127. DOI: 10.1016/j.cej.2012.11.024.

[15] C. Feng, X. Wu, *J. Colloid Interface Sci.* **2023**, *635*, 316–322. DOI: 10.1016/j.jcis.2022.12.143.

[16] Y. Li, C. Ren, W. Li, X. Ma, M. Dong, L. Geng, M. Li, H. Zhou, Y. Liu, *J. Taiwan Inst. Chem. Eng.* **2023**, *146* (April), 104888. DOI: 10.1016/j.jtice.2023.104888.

[17] W. Jia, H. Cao, T. Wang, Y. Min, Q. Xu, *Surf. Coatings Technol.* **2023**, *463* (January), 129551. DOI: 10.1016/j.surfcoat.2023.129551.

[18] N. Ghemmit-Doulache, H. Khireddine, D. S. Salah, *J. Environ. Sci. Eng.* **2011**, *5*, 10.

[19] I. Gualandi, M. Monti, E. Scavetta, D. Tonelli, V. Prevot, C. Mousty, *Electrochim. Acta*. **2015**, *152*, 75–83. DOI: 10.1016/j.electacta.2014.11.096.

[20] A. Mignani, B. Ballarin, M. Giorgetti, E. Scavetta, D. Tonelli, E. Boanini, V. Prevot, C. Mousty, A. Iadecola, *J. Phys. Chem. C.* **2013**, *117* (31), 16221–16230. DOI: 10.1021/jp4033782.

[21] O. Brylev, L. Roué, D. Bélanger, *J. Electroanal. Chem.* **2005**, *581* (1), 22–30. DOI: 10.1016/j.jelechem.2005.04.006.

[22] Y. Chen, H. Yang, H. Feng, P. Yang, J. Zhang, B. Shu, *Mater. Today Commun.* **2023**, *35*

(January), 106058. DOI: 10.1016/j.mtcomm.2023.106058.

[23] Y. Luo, Y. Wang, F. Hua, M. Xue, X. Xie, Y. Xie, S. Yu, L. Zhang, Z. Yin, C. Xie, et al., *J. Hazard. Mater.* **2023**, *443* (PB), 130300. DOI: 10.1016/j.jhazmat.2022.130300.

[24] Y. Vlamidis, E. Scavetta, M. Giorgetti, N. Sangiorgi, D. Tonelli, *Appl. Clay Sci.* **2017**, *143* (January), 151–158. DOI: 10.1016/j.clay.2017.03.031.

Chapter IV
Application in Adsorption

IV.1. Adsorption behaviour of the coprecipitated LDHs

The possibility of applying the synthesized LDHs in adsorption is investigated by choosing Azocarmine G (ACG) (**Fig.IV.1.**) as a target pollutant then varying the experimental parameters such as the pH of the medium, the initial concentration of the dye, the dose of the adsorbent and the contact time. Response Surface Methodology is adopted to determine the optimal adsorption conditions and find a quantitative relationship between the parameters of the experiment and the adsorption capacity.
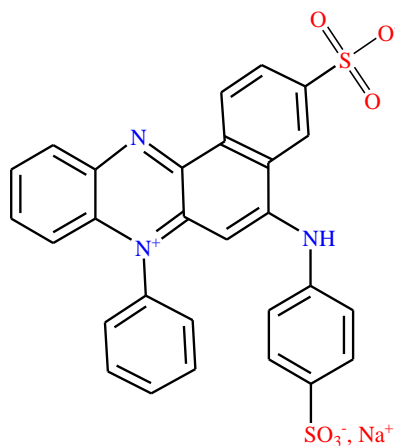
Figure IV. 1. Azocarmine G structure

IV.1. 1.   Analysis of variants (ANOVA)

The analysis of variants was tested by linear, 2FI, quadratic and cubic models. This analysis showed that the adsorption onto MgAl-LDH and CoAl-LDH fits better with the cubic model (R^2=0.96 and 0.97 respectively) while the adsorption onto MgFe-LDH showed a good fit with the quadratic model (R^2=0.85), the summary of factor interactions and all main effects are shown in **Table. IV.1**, **Table. IV.2,** and **Table. IV.3** [1,2]. The F- and P- values were used to assess the statistical importance of each parameter and predict the adequacy of the model for the adsorption behaviour. F-value > 0.05 and P-value < 0.05 provide evidence for the model's importance, which emphasises the connection between the variable and the desired result [3,4].

Table.IV.4. demonstrate the coded relationship between the studied parameters and the adsorption capacity of the materials. Where A, B and C are the independent variables (pH, initial dye concentration (ppm) and adsorbent dose (g.L^{-1})). The predicted values are plotted versus the actual experimental values, the results in **Fig.IV.2. a, b, and c** show a good agreement between the predicted and the actual values, as the difference is less than 0.2 between the maximum of residuals. For further analysis, diagnostic plots were employed to evaluate the model's accuracy, namely, the normal probability graph of the studentized residuals shown in **Fig.IV.2. d, e and, f.** The conformance of the residuals to a normal distribution is shown by the normal probability graph where a straight line should be drawn between the data points. The plot shows that the residuals are typically centred within the reference line [1,5].

Table IV. 1. ANOVA of Reduced Cubic model results for the response surface of MgAl-LDH

Source	Sum of squares	Mean square	F-value	P-value	
Model	5265.72	438.81	12.59	0.0013	significant
A	507.33	507.33	14.55	0.0066	
B	715.99	715.99	20.54	0.0027	
C	60.80	60.80	1.74	0.2282	
AB	603.72	603.72	17.32	0.0042	
BC	1079.29	1079.29	30.96	0.0008	
A²	261.33	261.33	7.50	0.0290	
B²	532.20	532.20	15.27	0.0058	
A²B	220.47	220.47	6.32	0.0401	
AB²	379.10	379.10	10.87	0.0132	
A³	105.91	105.91	3.04	0.1249	
B³	453.45	453.45	13.01	0.0087	
C³	2868.38	2868.38	82.28	< 0.0001	
Residual	244.03	34.86	/	/	
Cor Total	5509.74	/	/	/	

Table IV. 2. ANOVA of Reduced Cubic model results for the response surface of MgFe-LDH

Source	Sum of squares	Mean square	F-value	P-value	
Model	3313.14	414.14	8.03	0.0012	significant
A	4.56	4.56	0.0884	0.7718	
B	945.79	945.79	18.34	0.0013	
C	1058.93	1058.93	20.53	0.0009	
AB	190.02	190.02	3.68	0.0812	
AC	296.16	296.16	5.74	0.0355	
A²	782.46	782.46	15.17	0.0025	
B²	191.75	191.75	3.72	0.0800	
C²	313.57	313.57	6.08	0.0314	
Residual	567.31	51.57	/	/	
Cor Total	3880.45	/	/	/	

Table IV. 3. ANOVA of Reduced Cubic model results for the response surface of CoAl-LDH

Source	Sum of squares	Mean square	F-value	P-value	
Model	5351.74	445.98	21.85	0.0002	significant
A	1580.53	1580.53	77.42	< 0.0001	
B	399.38	399.38	19.56	0.0031	
C	269.76	269.76	13.21	0.0083	
AB	1365.51	1365.51	66.89	< 0.0001	
BC	365.35	365.35	17.90	0.0039	
A²	1280.29	1280.29	62.71	< 0.0001	
B²	250.77	250.77	12.28	0.0099	
C²	406.77	406.77	19.92	0.0029	
A²C	1411.71	1411.71	69.15	< 0.0001	
B²C	226.63	226.63	11.10	0.0126	
B³	205.77	205.77	10.08	0.0156	
C³	176.06	176.06	8.62	0.0218	
Residual	142.91	20.42	/	/	
Cor Total	5494.65	/	/	/	

Table IV. 4. Final equation in terms of coded factors for ACG adsorption onto MgAl-LDH, MgFe-LDH and CoAl-LDH.

MgAl-LDH		MgFe-LDH		CoAl-LDH	
Adsorption capacity=		Adsorption capacity=		Adsorption capacity=	
+115.59		+22.97		-64.00	
+28.86	*A	+0.9021	*A	+138.98	*A
-160.68	*B	+14.13	*B	-88.52	*B
+23.60	*C	-19.55	*C	-76.98	*C
+72.03	*AB	-7.74	*AB	+129.92	*AB
-211.81	*BC	+12.25	*AC	-76.39	*BC
-29.40	*A²	+17.48	*A²	+359.78	*A²
+52.21	*B²	+9.39	*B²	-161.89	*B²
-28.43	*A²B	+21.11	*C²	+20.35	*C²
+66.11	*AB²			+551.44	*A²C
-18.21	*A³			-224.52	*B²C
+77.17	*B³			-24.53	*B³
+97.43	*C³			-21.29	*C³

Table IV. 5. Central composite design matrix with experimental and predicted values for MgAl-LDH adsorption of ACG

Runs	Independent input variables			Response variable	
	A	B	C	Adsorption capacity (mg.g^{-1})	
	pH	Initial concentration (ppm)	Adsorbent dose (g.L^{-1})	Experimental	Predicted
1	9	30	0.25	68.68	69.26
2	8	30	0.25	74.48	74.45
3	8	40	0.25	88.68	84.43
4	8	80	0.25	107.76	101.56
5	8	80	0.5	86.56	92.98
6	5	30	0.25	59.20	59.78
7	8	60	0.25	73.12	75.95
8	6	30	0.25	60.00	56.05
9	8	80	0.25	107.76	101.56
10	8	80	0.25	96.00	101.56
11	8	80	0.75	68.03	64.35
12	7	30	0.25	62.00	65.49
13	8	80	0.1	52.16	55.39
14	8	30	0.25	74.48	74.45
15	8	100	1	**60.28**	**60.28**
16	9	80	0.5	80.00	81.79
17	9	80	0.1	46.00	44.21
18	6	100	0.25	85.00	85.20
19	6	60	0.25	62.00	60.58
20	6	40	0.25	75.00	77.83

Table IV. 6. Central composite design matrix with experimental and predicted values for MgFe-LDH adsorption of ACG

|	Independent input variables			Response variable	
	A	B	C	Adsorption capacity (mg.g^{-1})	
Runs	pH	Initial concentration (ppm)	Adsorbent dose (g.L^{-1})	Experimental	Predicted
1	5	30	0.25	60.35	57.65
2	6	65	0.10	72.00	73.67
3	9	60	0.25	48.00	54.87
4	9	30	0.25	54.87	58.60
5	9	80	0.10	84.00	74.22
6	9	80	0.5	50.00	46.89
7	7	30	0.25	40.86	40.64
8	9	100	0.25	66.00	71.38
9	7	60	0.25	38.00	43.55
10	5	80	0.75	45.08	40.69
11	5	80	1.00	36.78	39.96
12	8	30	0.25	43.90	45.25
13	8	40	0.25	50.00	43.58
14	8	60	0.25	48.00	44.84
15	9	80	0.75	48.00	46.75
16	5	40	0.25	58.68	59.30
17	8	100	0.25	63.00	65.77
18	5	60	0.25	55.03	67.20
19	6	30	0.25	48.10	44.77
20	5	80	0.25	90.16	81.23

Table IV. 7. Central composite design matrix with experimental and predicted values for CoAl-LDH adsorption of ACG.

| Runs | Independent input variables | | | Response variable | |
| | A | B | C | Adsorption capacity (mg.g^{-1}) | |
	pH	Initial concentration (ppm)	Adsorbent dose (g.L^{-1})	Experimental	Predicted
1	5	30	0.25	36.67	35.68
2	6	30	0.25	45.64	46.09
3	7	30	0.25	48.00	52.59
4	8	30	0.25	55.77	55.16
5	9	30	0.25	51.28	53.80
6	8	30	0.25	58.32	55.16
7	8	40	0.25	59.20	53.36
8	8	60	0.25	60.00	66.12
9	8	80	0.25	77.95	77.76
10	8	100	0.25	59.97	60.84
11	8	80	0.10	109.85	108.42
12	8	80	0.25	77.95	77.76
13	8	80	0.50	59.44	55.41
14	8	80	0.75	46.69	50.01
15	8	80	1.00	40.79	39.64
16	9	80	0.10	**62.00**	**62.00**
17	7	80	0.10	**59.00**	**59.00**
18	8	40	0.75	42.00	41.16
19	8	40	1.00	38.00	38.56
20	8	60	0.10	**70.00**	**70.00**
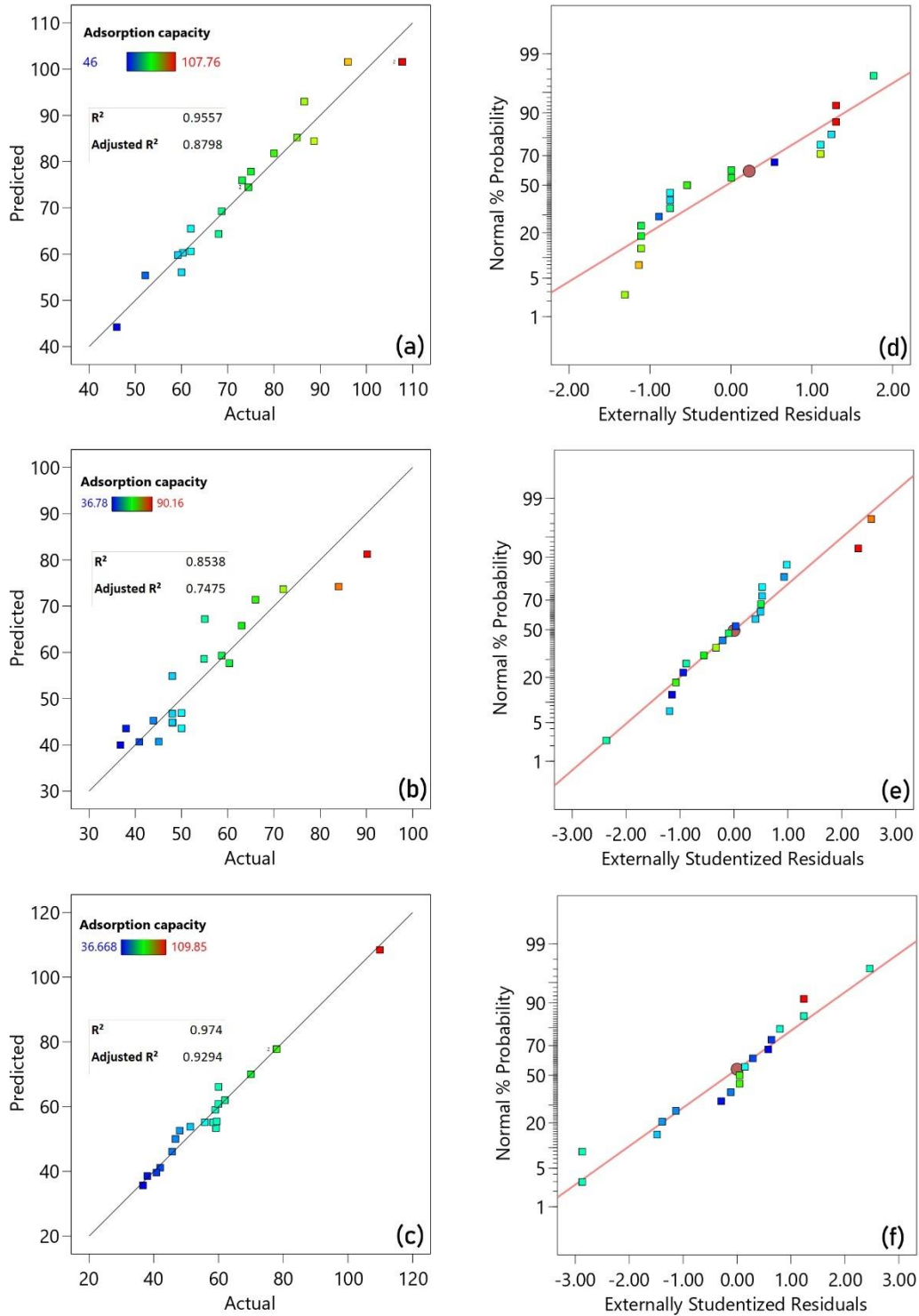
Figure IV. 2. The actual value obtained from the experiments versus the predicted values (a), (b) and (c) and Normal plot of residuals (d), (e) and (f).

IV.1. 2. Parameters assessment using the response surface methodology

The graphic representations of the response surface (3D) in **Fig.IV.3.** were utilised to further examine the interaction between the experimental conditions and identify the ideal level of each variable to an increase in adsorption capacity.

The pH of the solution has an essential role At the solid-liquid interface in the adsorption process as it changes the ionization degree of the adsorbent charge and the molecular structure of the adsorbates [6]. The best adsorbed capacities are obtained at pH < PZC for the three materials, the surface of the particles is positively charged ate this value unlike ACG molecules which are negatively charged according to their pKa (7.8) leading to an increase in the attraction between them, and thus increases the adsorption quantity. It is important to note that the low adsorption quantities at higher pH values is doubtlessly caused by the competition with OH$^-$ ions of the solution [7].

The adsorption capacity is also related to the dye concentration owing to the pulse between molecules at high concentration values. In general, the increase in dye concentration involves the increase in the adsorption quantity until a critical limit where the active sites of the adsorbent particles become saturated [8,9]

Another crucial factor that affects the adsorption process is the catalyst's mass. Theoretically, increasing the dose of an adsorbent should result in an increase in the amount of adsorbed material because more active sites on the surface of the material will be available to ACG molecules, allowing more species to fill the unoccupied sites [10]. A certain limit can be observed where the adsorption quantity starts to decrease, this fact is due to the maximum adsorption that had already occurred for the same amount of dye molecules [11].

Following the optimisation and the evaluation of the models using Design Expert software, the optimal operating conditions for maximum adsorption capacity of ACG on the materials, as determined by the CCD approach, are given in **Table IV.8.**, the experimental test realised in close conditions revealed close adsorption capacities therefore, it can be said that this method has a good efficacity for adsorption efficiency prediction toward dye removal.

Table IV. 8. Optimal conditions for ACG adsorption onto MgAl-LDH, MgFe-LDH and CoAl-LDH.

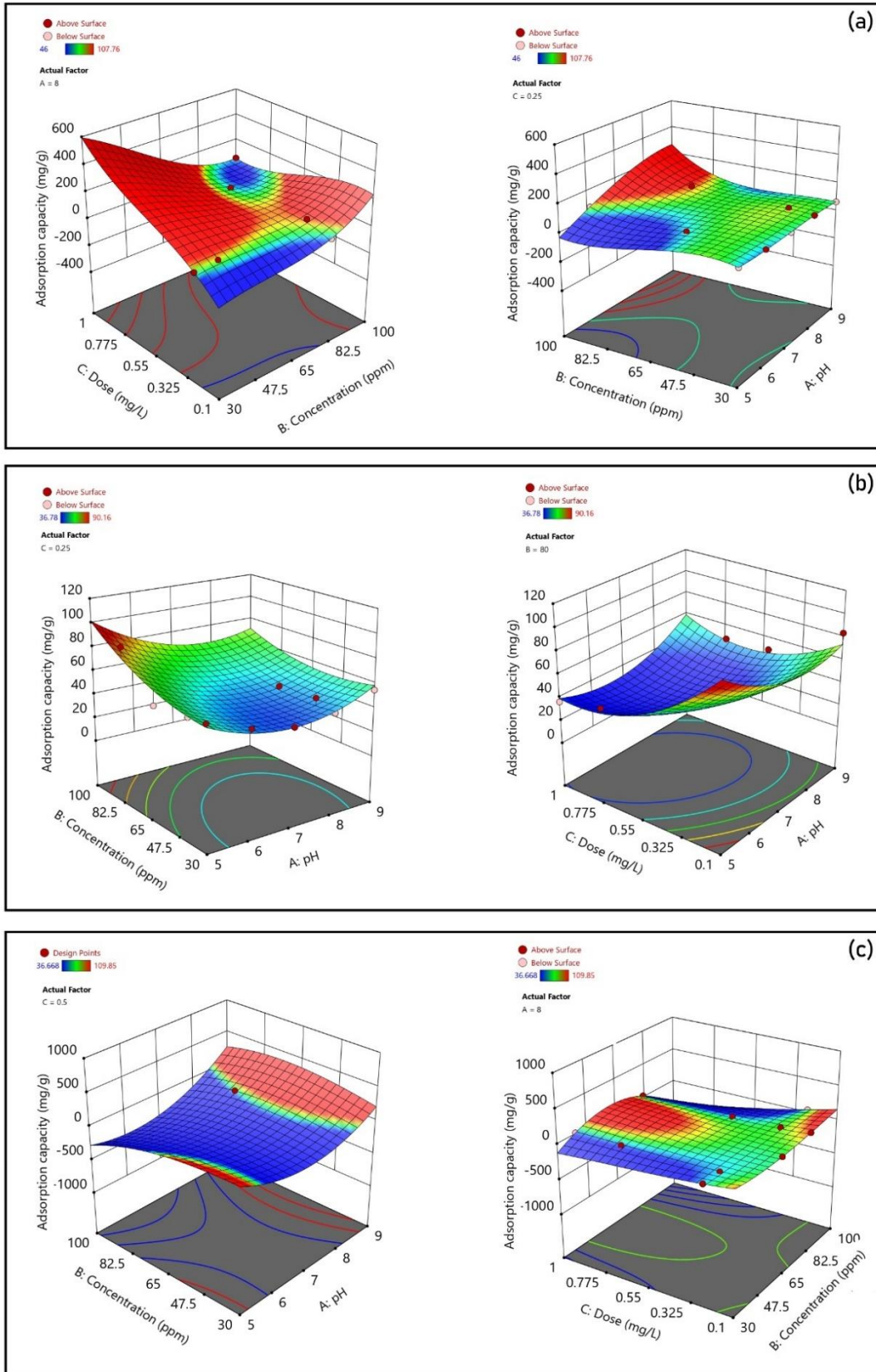|		pH	Concentration (ppm)	Dose (mg.L^{-1})	Adsorption capacity (mg.g^{-1})
MgAl-LDH	Predicted	8.2	40	0.29	110
	Experimental	8.0	80	0.25	105
MgFe-LDH	Predicted	5.4	90	0.13	100
	Experimental	5.0	80	0.25	90
CoAl-LDH	Predicted	7.0	40	0.11	105
	Experimental	8.0	80	0.10	98.6

Figure IV. 3. 3D response surface plots of ACG removal using: a) MgAl-LDH, b) MgFe-LDH and c) CoAl-LDH

IV.1. 3. Adsorption kinetics

The contact time is another parameter that allows to assess the adsorption equilibrium. The plots in **Fig. IV.4.** show a quick increase in the adsorbed quantity due to the availability of the active sites, after that, the equilibrium starts to forge and a maximum adsorption quantity is reached, at this point, further time contact will not enhance the adsorption process.
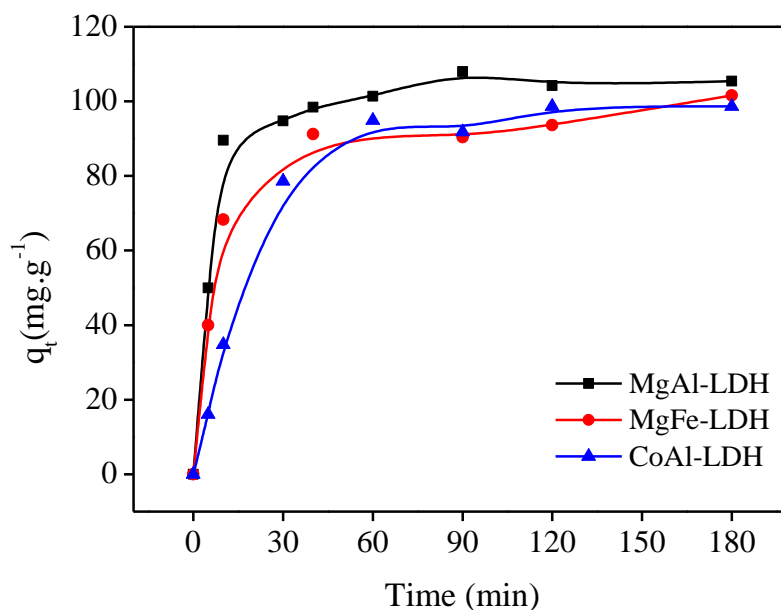

Figure IV. 4. Study of time effect following the optimal conditions on the adsorption of ACG on MgAl-LDH, MgFe-LDH and CoAl-LDH

The fitting of kinetic curves using pseudo-first order, pseudo-second orders, intraparticle model and Elovich kinetic models revealed the data summarized in **Table IV.9.** it should be emphasized that the second order model, is the most suitable for all the systems with R^2 equals to 0.99. In addition, the obtained theoretical adsorption capacities are the highest and the closest to the experimental results. This model implies that chemisorption is the rate-limiting phase, it involves valence forces through the sharing or exchanging of electrons between the adsorbent and adsorbate, in other words, the availability of adsorption sites (functional groups) on the sorbent had a significant impact on the rate of ACG adsorption [12,13].

For the intraparticle diffusion model, it is assumed that the system is dominated by intraparticle diffusion process when a line passing through the origin is observed, whereas a process dominated by surface adsorption is indicated by a large intercept [14]. For all the materials, the results showed two linear segments indicating that the adsorption process is limited by multiple steps, The first is explained by boundary layer diffusion carried on by mass transfer from the dye solution to the exterior of the adsorbent particles, whilst the second signifies dye molecule intraparticle diffusion across the porous adsorbent surface. The process is dominated by surface adsorption, as seen by the large intercepts observed [15,16].

Table IV. 9. Adsorption kinetic parameters of ACG adsorption onto MgAl-LDH, MgFe-LDH and CoAl-LDH

		MgAl-LDH		MgFe-LDH		CoAl-LDH	
Experimental data	$q_{max\ 1}$ (mg/g)	105.9		101.6		98.66	
Pseudo-first order	$q_{max\ 1}$ (mg/g)	34.56		52.77		72.96	
	K_1(min^{-1})	-1.4 10^{-4}		-1.5 10^{-4}		-1.9 10^{-4}	
	R_1^2	0.69		0.68		0.93	
Pseudo-second order	$q_{max\ 2}$ (mg/g)	108.1		103.2		108.22	
	K_2 (g/mg min^{-1})	2.5 10^{-3}		1.3 10^{-3}		6.4 10^{-4}	
	R_2^2	0.99		0.99		0.99	
Intraparticle model	C	-2.47	86.99	-3.14	64.71	-21.59	62.07
	K_{in}(g/mg min$^{-0.5}$)	27.23	1.64	21.5	2.8	12.19	1.31
	R_{in}^2	0.94	0.74	0.97	0.76	0.99	0.67
Elovich model	β (g/mg min^{-1})	6.26		10.28		17.12	
	α (g/mg min^{-1})	1.66 10^5		552.36		0.626	
	R_E^2	0.85		0.86		0.78	
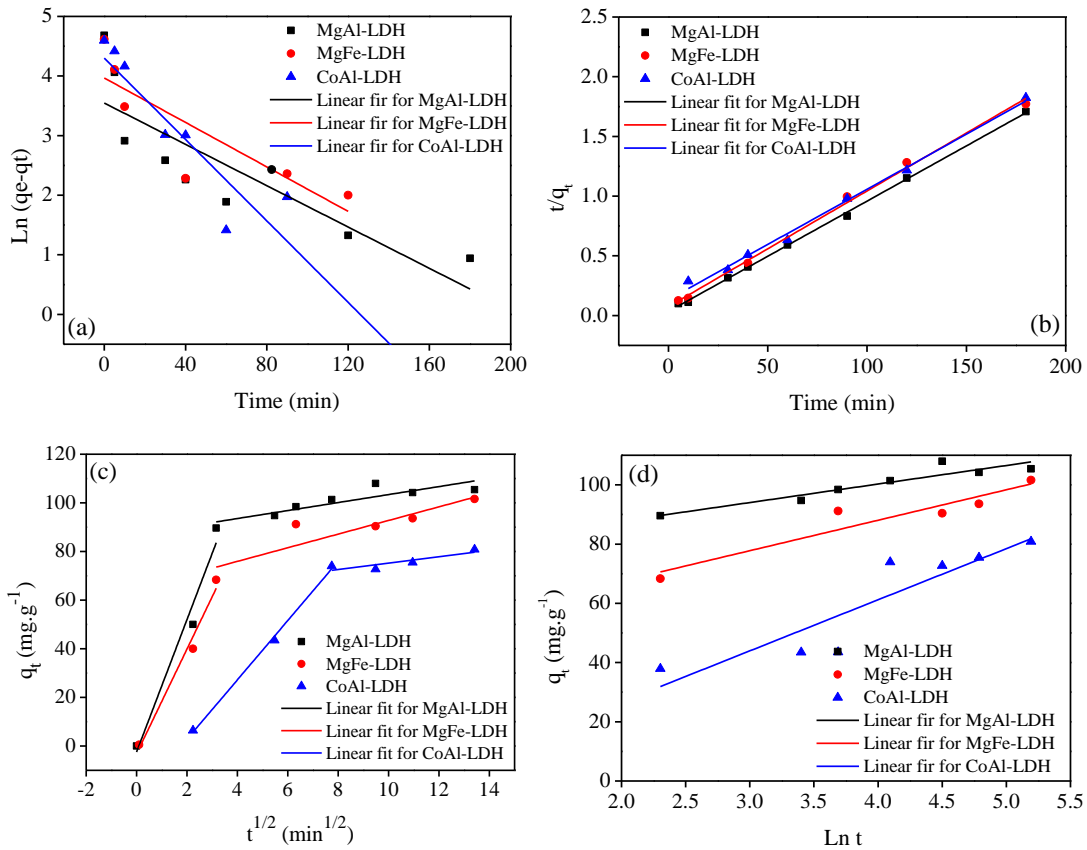
Figure IV. 5. Kinetic Data fitting by a) pseudo-first-order; b) pseudo-second-order; c) Intraparticle model and d) Elovich model of ACG adsorption on MgAl-LDH, MgFe-LDH and CoAl-LDH.

IV.1. 4. Adsorption isotherm models

The main interest of this part is to interpret the common interactions through the validity of the models of isotherms to deduce the constants of the models and the maximum adsorption capacities. The application of the different theoretical models to the experimental results is shown in **Fig.IV.6**. The maximum adsorption quantities, the constants and the correlation coefficients obtained after linearization of the isotherms are summarised in **Table IV.10.** The characteristic isotherm of the process shows an L-type shape according to the literature, showing a high affinity of the ACG molecules towards the materials, followed by the saturation of the active sites until the obtainment of a plateau.

The choice of the fitted model is based on the determination coefficients (R^2), for MgAl-LDH and CoAl-LDH, Langmuir and D-R models exhibited the highest R^2, whereas for MgFe-LDH, it is Langmuir and Temkin that fitted best the adsorption process. The Langmuir process suggest that the system exhibit a monolayer adsorption process and the value of R_L ($0 < R_L < 1$) describes the favourability of the process. The theoretical maximum adsorption capacity from Langmuir isotherm was found to be satisfactory compared with literature as shows the **Table IV.11**. Unlike Langmuir isotherm which does not take into account the constant adsorption potential, the D-R model is based on the adsorption potential theory and assumed that the adsorption process was related to micropore volume filling rather than layer-by-layer adsorption on pore walls [17]. The sorption energy calculated is less than 8 kJ/mol suggesting that the adsorption process is physical, if the magnitude of E was between 8 and 16 kJ mol^{-1}, the adsorption process would be chemical [18].

Table IV. 10. Langmuir, Freundlich, Temkin and D-R isotherm's parameters of ACG adsorption on MgAl-LDH, MgFe-LDH and CoAl-LDH.

		MgAl-LDH	MgFe-LDH	CoAl-LDH
Langmuir Model	q_{max} (mg. g^{-1})	238.66	131.58	65.91
	K_L (L.mg^{-1})	0.033	0.304	0.337
	R_L	0.375	0.40	0.056
	R^2	0.975	0.989	0.91
Freundlich Model	$1/n$	2.94	1.37	20.16
	K_F (L.g^{-1})	2.19	5.37	1.12
	R^2	0.801	0.981	0.81
Temkin Model	B_T	31.5	29.6	5.98
	K_T (L.mg^{-1})	1.27	0.3	680.5
	R^2	0.882	0.975	0.75
D-R Model	q_{max} (mg. g^{-1})	109.94	85.63	60.94
	K_{DR}	2.63 10^{-5}	2.77 10^{-5}	2.19 10^{-6}
	E (kJ.mol^{-1})	0.137	0.134	0.476
	R^2	0.932	0.903	0.95

Table IV. 11. Comparison of the Langmuir maximum adsorption capacity of ACG with literature

Adsorbent	Adsorption capacity (mg.g^{-1}) (at T = 298 K)	Equilibrium time (min)	Ref
Nano-silica from kaolinitic clay	41.29	30	[19]
Fe$_3$O$_4$-Carbon-Based Composite	239.6	/	[20]
MgAl-LDH	238.66	180	**This work**
MgFe-LDH	131.58	180	**This work**
CoAl-LDH	65.91	180	**This work**
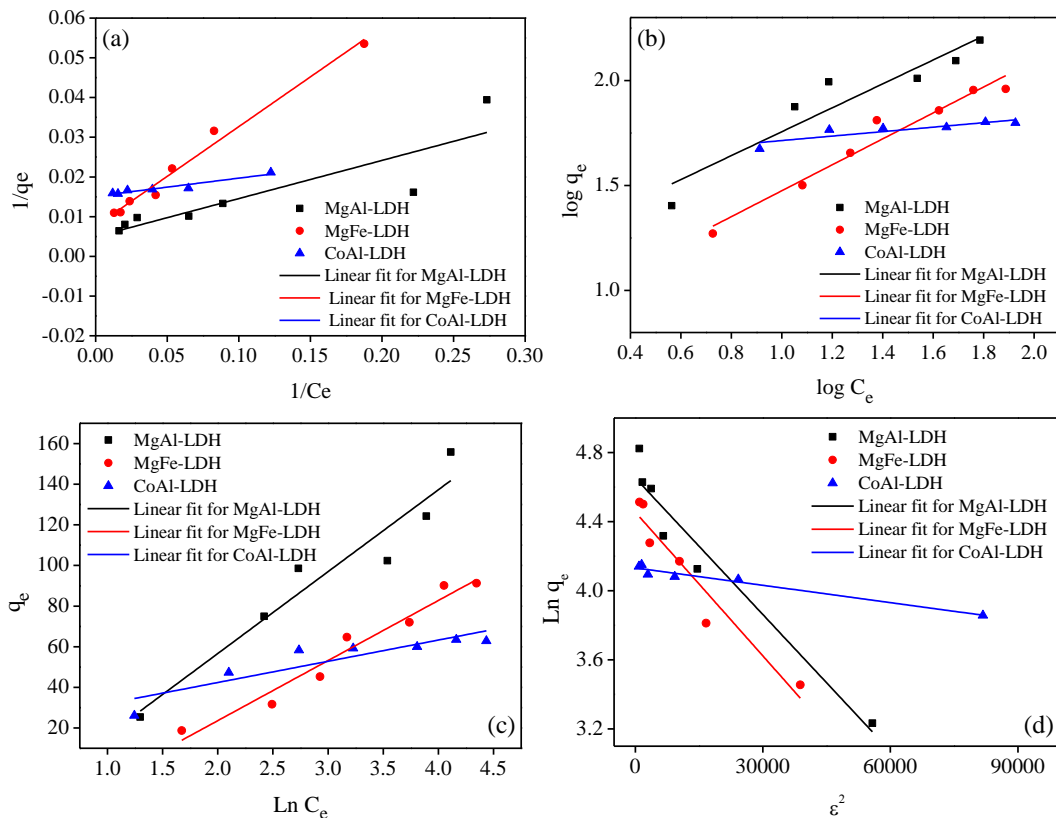
Figure IV. 6. Isotherms modelling by Langmuir (a), Freundlich (b) and Temkin (c) and D-R (d) of ACG adsorption on MgAl-LDH, MgFe-LDH and CoAl-LDH.
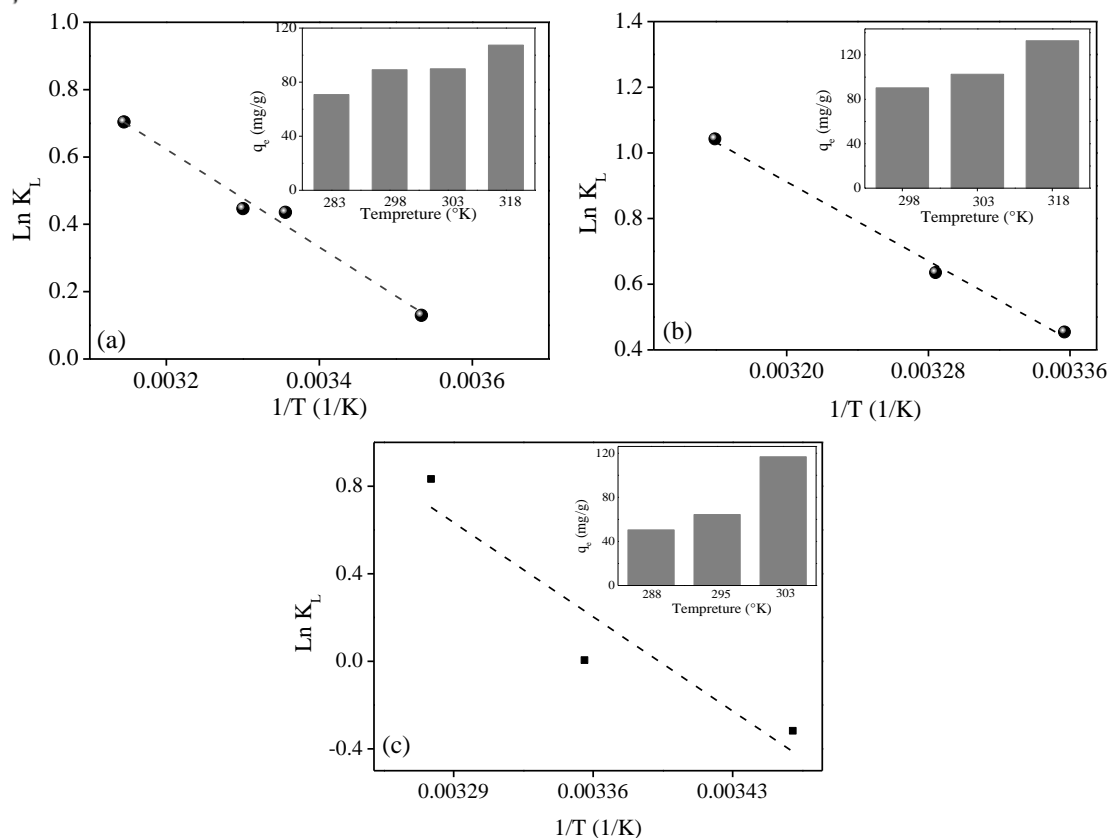
IV.1. 5.   Thermodynamic parameters

The determination of the thermodynamic parameters of the system was carried out to better understand the adsorption mechanism, to assess the energy aspect of the involved reactions and to determine the nature of adsorption (physical or chemical). The thermodynamic parameters including enthalpy $\Delta H°$, entropy $\Delta S°$ and free enthalpy $\Delta G°$ have been determined and regrouped in **Tabe IV.12**.

From Van't Hauff plot in **Fig.IV.7.** The obtained $\Delta G°$ values from Van't Hoff plots are negative which confirms that the reaction occurs spontaneously. The positive values of $\Delta H°$ belonging to the range of 1 - 93 kJ.mol^{-1} confirms the physisorption behavior of the system with an endothermic reaction. The positive values of the entropies ($\Delta S°$) of the systems describes the favorability of the adsorption process because of the affinity between the adsorbent and the dye molecules.

Table IV. 12. Thermodynamic parameters for the adsorption of ACG on MgAl-LDH, MgFe-LDH and CoAl-LDH

|	T ($°K$)	q_e (mg. g^{-1})	K_L	$\Delta G°$(KJ.mol^{-1})	$\Delta H°$(KJ.mol^{-1})	$\Delta S°$(JK^{-1}.mol^{-1})
MgAl-LDH	283	70.88	1.14	-0.304		
	298	89.20	1.54	-1.079		
	303	89.89	1.56	-1.124	12.083	43.81
	318	107.44	2.02	-1.861		
MgFe-LDH	298	90.40	1.57	-1.125		
	303	102.60	1.89	-1.609	25.053	87.75
	318	132.77	2.84	-2.743		
CoAl-LDH	289	50.488	-0.32	0.764		
	298	64.46	0.0051	-0.013	51.150	173.51
	305	116.82	0.83	-2.112		

**Figure IV. 7.** Vant Hoff plots of ACG adsorption on MgAl-LDH (a), MgFe-LDH (b) and CoAl-LDH (c)

IV.1. 6. Mechanistic insights

In order to identify the functional groups involved in the adsorption mechanism, the FTIR was carried on the materials at the end of the adsorption experiment by gathering, rinsing and drying the powder. The spectra in **Fig. IV.8.** revealed two additional peaks around 1220 cm^{-1} and 1030 cm^{-1} that can be attributed to the elongation of S=O and C-N existing on the adsorbed azocarmine G molecules, respectively. Some of the peaks in the spectra before adsorption showed also a remarkable decrease such as O-M-O, O-H and H-O-H which can be explained by the participation of these groups in the adsorption mechanism mainly by electrostatic forces and hydrogen bonds [21].

The interactions involved in the adsorption process between the adsorbent and the target molecules are the chemical and the electrostatic interactions. The functional groups on the surface of the adsorbent and the speciation diagram of dye molecules, which are directly related to the pH of the medium, are two important chemical properties that are included in the explanation of the adsorption mechanism. [22]. The results propose that the retention of dye molecules is governed from a part by electrostatic forces between the positive charge of the lamellas induced by Al^{3+} or Fe^{3+} and the negatively charged sulfonate groups on ACG molecules, and from another part by hydrogen bonds with O-H of the lamellas (**Fig. IV.9**) [7].
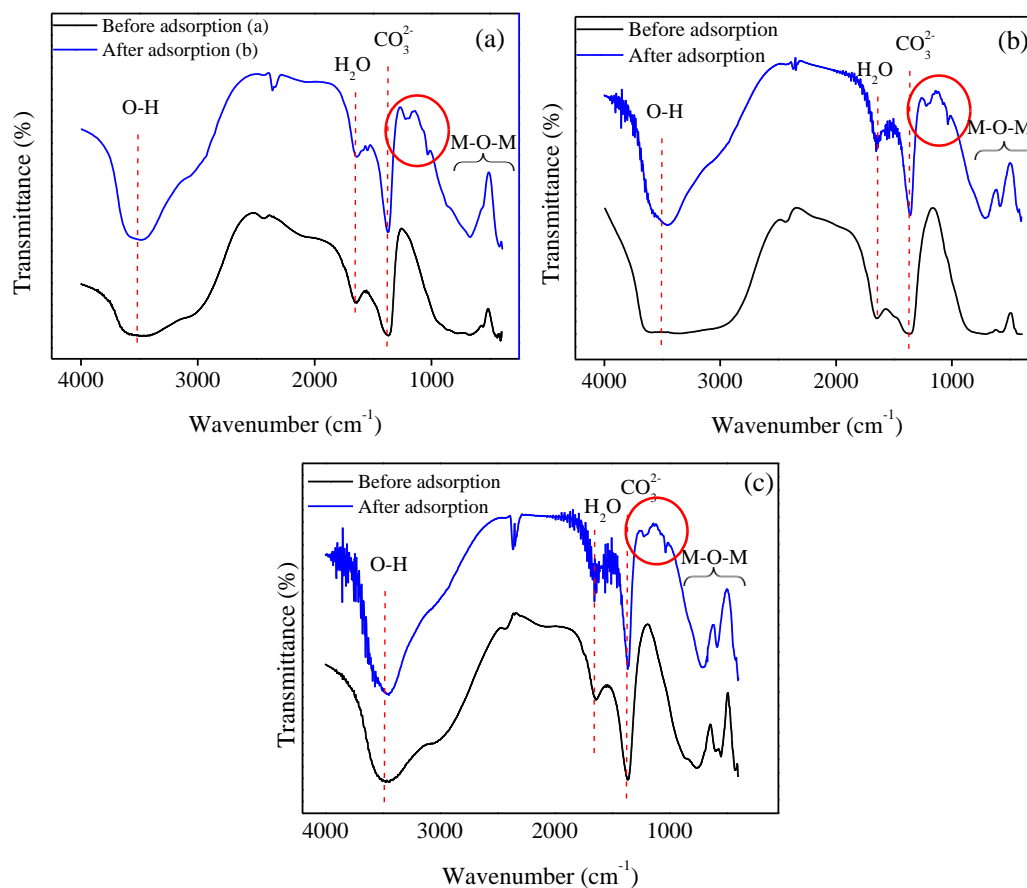
Figure IV. 8. FTIR spectra before and after adsorption of MgAl-LDH (a), MgFe-LDH (b) and CoAl-LDH (c)
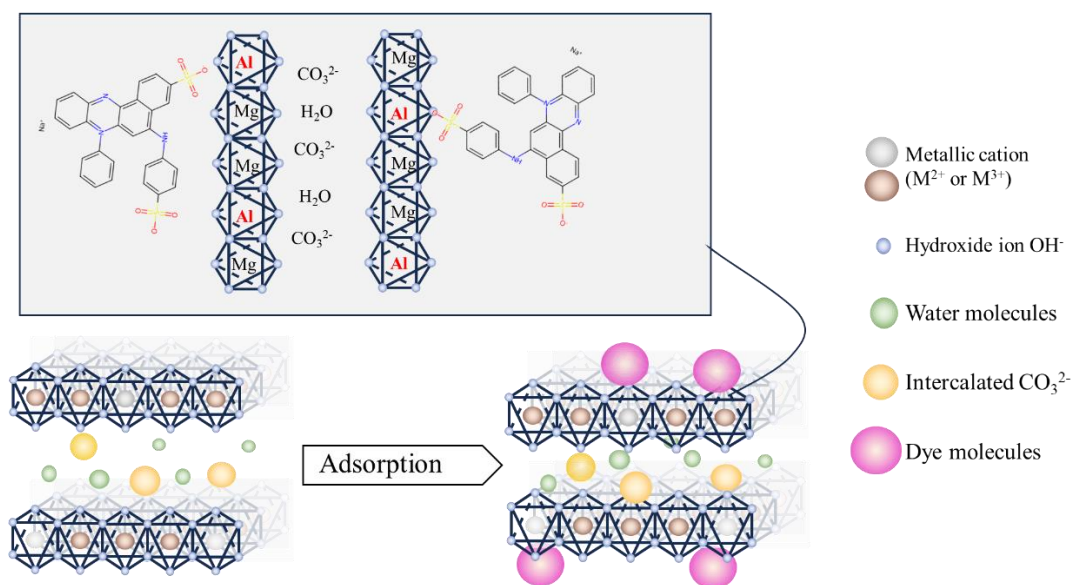
Figure IV. 9. Proposed mechanism for adsorption removal of ACG using the synthesised materials

IV.2. Adsorption behaviour of the electrodeposited MgAl-LDH

The adsorption behaviour of the electrochemically synthesised MgAl-LDH electrodeposited on stainless-steel electrode was tested choosing bromophenol blue (BPB) as a target molecule. The effect of the experimental conditions including the pH of the medium, the initial concentration of the dye, the dose of the adsorbent, and the contact time were studied.
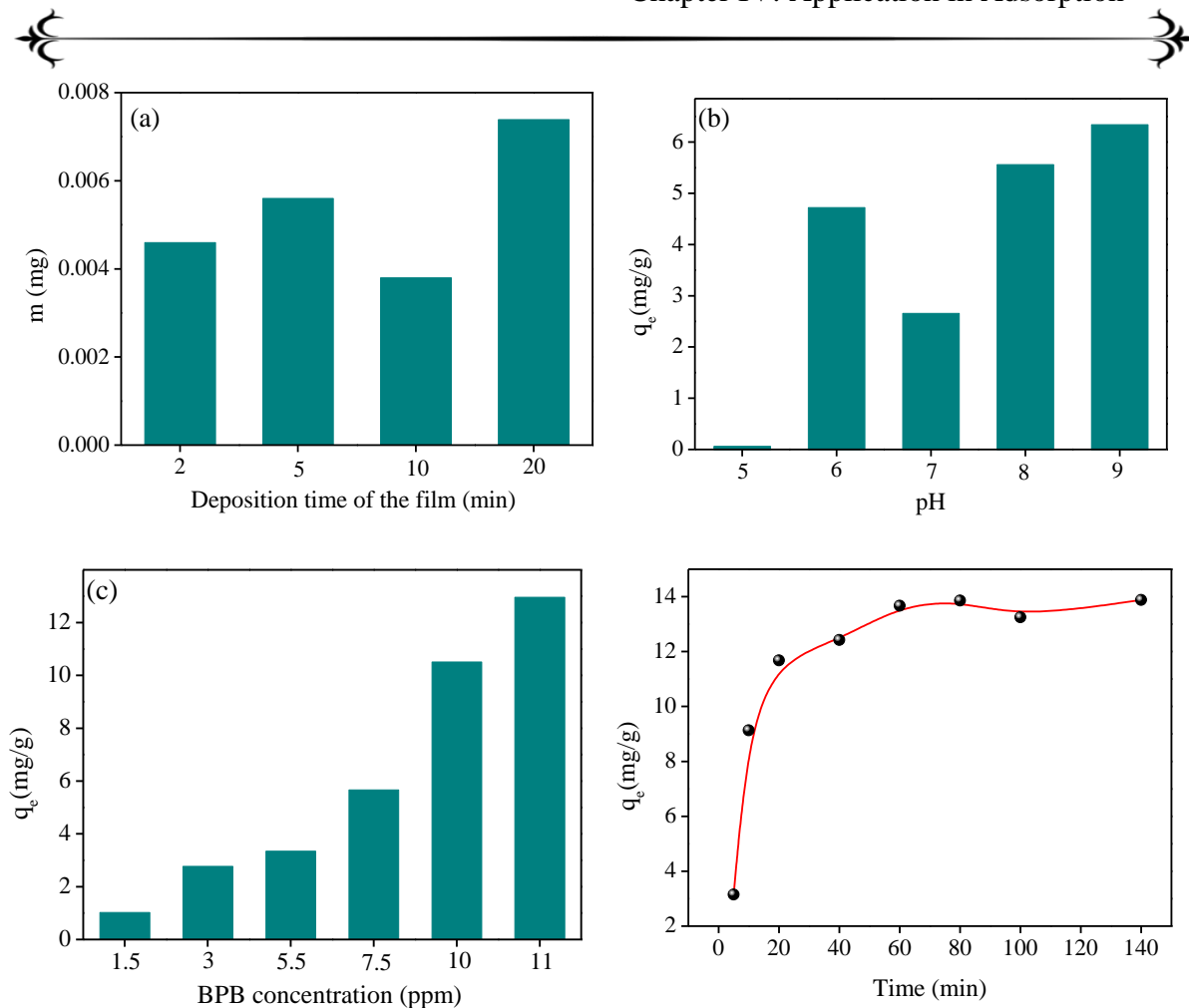
IV.2. 1. Parameters effect

The adsorption of BPB onto the electrodeposited MgAl-LDH was carried out at different conditions to investigate the effect of each parameter (**Fig.IV.10**). The first parameter was the deposition time of the film. The investigations revealed that the film deposited during 20 minutes had the highest quantity of adsorption because the electrodeposition is greatly influenced by time, and as time increases the film is created. Note in this case that the graphs are plotted using the adsorbed masse (mg) instead of the adsorption capacity (mg/g), this is due to the weight of the films deposited at short time which could not been determined and required more sophisticated equipment (microbalance), however, it was only possible to determine the mass of the film deposited after 20 min as 1.2 mg, and used for the rest of the calculations.

The pH of the solution has an essential effect on the adsorption process at the solid-liquid interface, as it changes the ionization degree of the adsorbent charge and the molecular structure of the adsorbates [6]. For this study, the best adsorbed quantity is obtained at pH=9.

For the third parameter, the increase in dye concentration leads to the increase in the adsorption quantity until a critical limit where the sites of the adsorbent particles become saturated [8,9]. The adsorption of BPB onto the film increases until an optimal value of 11 ppm where the adsorption capacity is 13.8mg/g.

The contact time during the adsorption is another parameter that allows to assess the adsorption regression. In response to the availability of the active sites, the plot shows a rapid increase in the amount of adsorbed molecules. Once the equilibrium has formed and the maximum amount of adsorption has been attained, further time contact will not accelerate the adsorption process.
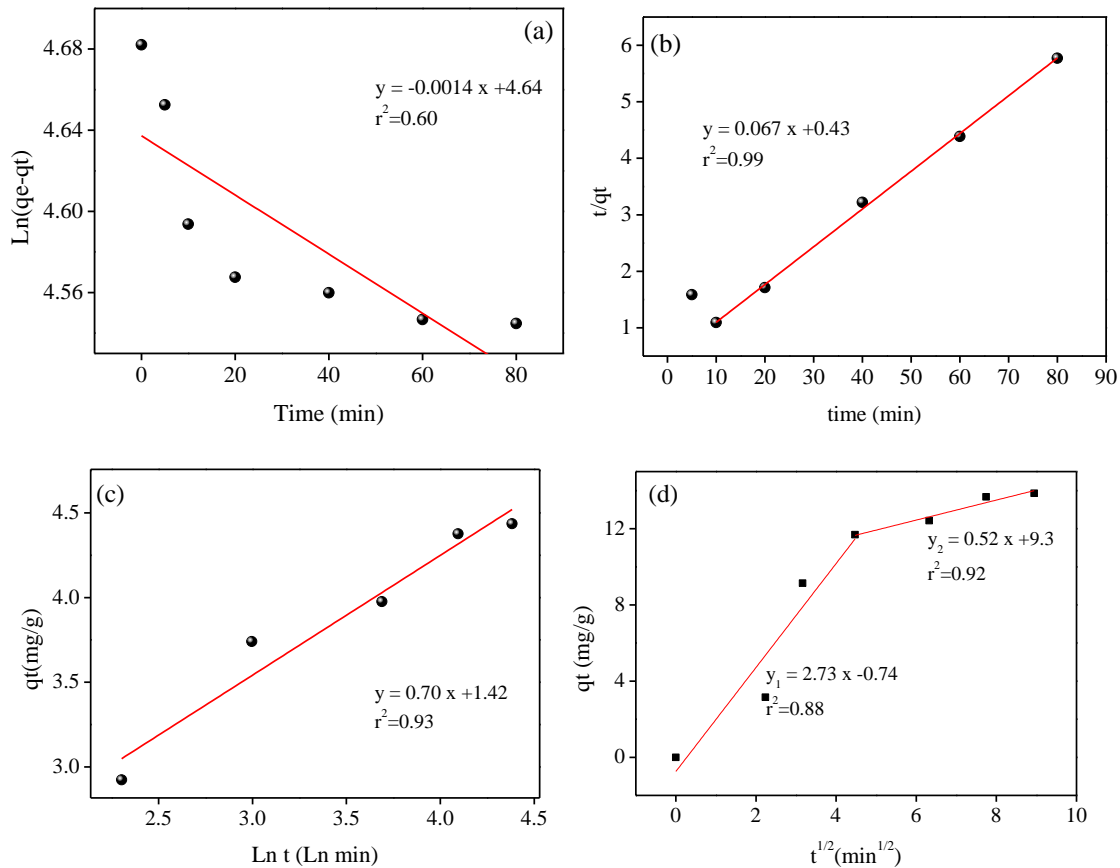
Figure IV. 10. Study of parameters effect on the adsorption of BPB onto the electrodeposited MgAl-LDH (t=140 min, V=10 mL) (a) the deposition time of the film, (b) the pH, (c) BPB initial concentration and (d) contact time.

IV.2. 2. Adsorption Kinetics

The fitting of the kinetic curves is an important step to enquire the adsorption mechanism. The data summarized in **Table IV.13**. revealed that the second order model is the most suitable for the system with a correlation coefficient (R^2) of 0.999 and theoretical adsorption capacities closest to the experimental results (14.96 mg/g). Hence the rate limiting phase of the adsorption process is the involving valence forces through the sharing or exchanging of electrons between the adsorbate and the adsorbent [12,13]. The intraparticle diffusion model revealed two linear segments denoting that multiple steps govern the adsorption process. The large intercept obtained indicate that the process is dominated by the surface adsorption (**Fig.IV.11**) [15,16].

Table IV. 13. Adsorption kinetic parameters of BPB adsorption on the electrodeposited MgAl-LDH

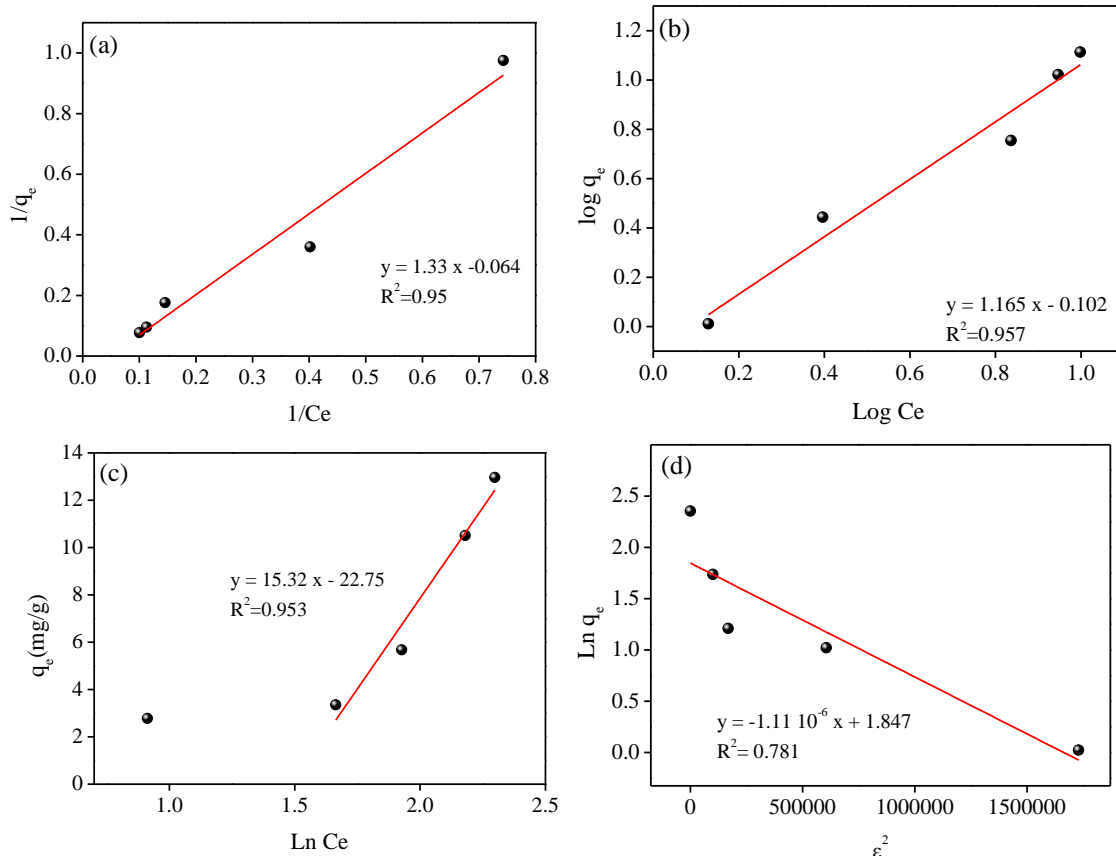| Experimental data			$q_{max\,1}$ (mg/g)			
			13.67			
Pseudo-first order	$q_{max\,1}$ (mg/g)		K_1 (min^{-1})		R_1^2	
	103.26		-1.82 10^{-5}		0.59	
Pseudo-second order	$q_{max\,2}$ (mg/g)		K_2 (g/mg min^{-1})		R_2^2	
	14.96		0.1037		0.99	
Intraparticle model	C		K_{in} (g/mg min$^{-0.5}$)		R_{in}^2	
-0.74	9.3	2.73	0.52	0.87	0.92	
Elovich model	β (g/mg min^{-1})		α (g/mg min^{-1})		R_E^2	
	0.7		7.60		0.94	

Figure IV. 11. Kinetic Data fitting by a) pseudo-first-order; b) pseudo-second-order; c) Intraparticle model and d) Elovich model of BPB adsorption on the electrodeposited MgAl-LDH.

IV.2. 3. Adsorption Isotherm Models

The previously described isotherm models were employed to study the properties related to the chemical affinity and surface characteristics. The calculations and the fittings showed that the system follows the Langmuir model with the highest R^2. The sorption energy calculated is less than 8 kJ/mol suggesting that the adsorption process is physical (**Table IV.14, Fig IV.12**) [18].

Table IV. 14. Langmuir, Freundlich, Temkin and D-R isotherm's parameters of BPB adsorption on the electrodeposited MgAl-LDH

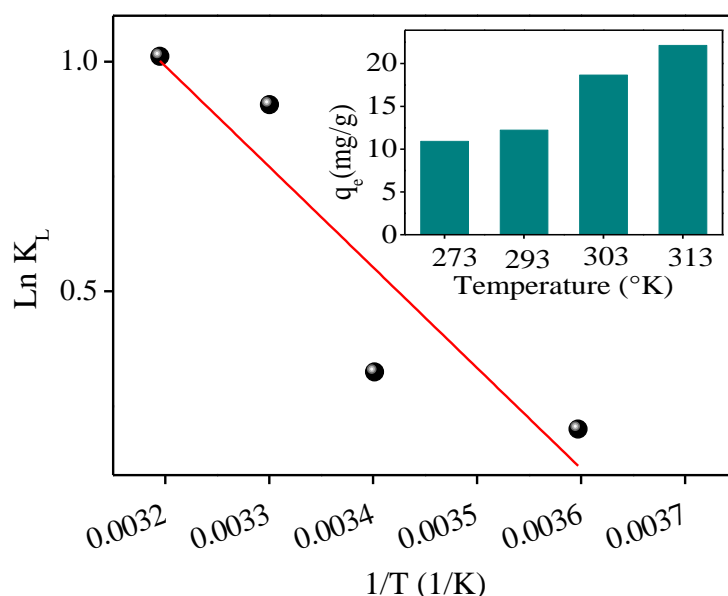| Langmuir Model	q_{max} (mg. g^{-1})	K_L(L/g)	R_L	R^2
	15.62	-0.0481	-0.711	0.958
Freundlich Model	**1/n**	**K_F (L/g)**		**R^2**
	0.858	14.62		0.957
Temkin Model	**B_T**	**K_T (L/g)**		**R^2**
	15.32	0.226		0.95
D-R Model	**q_{max} (mg. g^{-1})**	**K_{DR}**	**E (kJ.mol^{-1})**	**R^2**
	6.33	1.11 10^{-6}	0.671	0.78

Figure IV. 12. Isotherms modelling by Langmuir (a), Freundlich (b) Temkin (c) and D-R (d) of BPB adsorption on the electrodeposited MgAl-LDH

IV.2. 4. Thermodynamic parameters

The effect of temperature on the adsorption behavior of the deposited films towards BPB was investigated (**Fig.IV.13**), the adsorption quantity showed a remarkable increase in higher temperature values, which allow to predict the endothermic behavior of the reaction. This allowed to determine important thermodynamic parameters such as standard Gibbs free energy (ΔG°), enthalpy change (ΔH°) and entropy (ΔS°). The values of ΔG° (**Table IV.15.**) are negative which confirms that the reaction occurs spontaneously. The positive values of ΔH° belonging to the range of 1 - 93 kJ.mol^{-1} confirms the physisorption behavior of the system with an endothermic reaction. The positive values of the entropies (ΔS°) of the systems describes the favorability of the adsorption process because of the affinity between the adsorbent and the dye molecules.

Table IV. 15. Thermodynamic parameters for the adsorption of BPB adsorption on the electrodeposited MgAl-LDH

T (°K)	q_e (mg. g^{-1})	K_L	ΔG°(KJ.mol^{-1})	ΔH°(KJ.mol^{-1})	ΔS°(JK^{-1}.mol^{-1})
278	10.92	1.22	-0.462		
294	12.23	1.38	-0.793		
303	20.23	2.47	-2.282	18.227	66.56
313	22.13	2.75	-2.632		

Figure IV. 13. Vant Hoff plot of of BPB adsorption on the electrodeposited MgAl-LDH

IV.3. Regeneration

The adsorption regeneration reported in literature is generally performed in acidic medium, but since LDHs materials are instable in the acidic pH, their regeneration is slightly difficult and requires a basic medium; only. Following the adsorption study, the regeneration

tests of the LDH synthesised by coprecipitation were performed using chemical cleaning, the powders were gathered after the adsorption, rinsed thoroughly with distilled water, then dispersed in a solution of $NaHCO_3$ (0.1M, pH=9) for 4 hours, the powder is then rinsed again with distilled water and dried for 48 hours, the re-use of the powders revealed regeneration percentages of 58.6%, 57.2% and 54.0% for MgAl-LDH, MgFe-LDH and CoAl-LDH respectively. Therefore, the process of desorption from powder seems arduous, time consuming and not really effective.

The MgAl-LDH deposited film was also regenerated using a different technic, the electrode was first rinsed by distilled water, then cleaned through an electrochemical process by imposing a cathodic potential (-2V) for 30s in a solution of $NaHCO_3$(0.1M) [23]. The potential will cause the reduction of water molecules in the vicinity of the electrode which is accompanied by the production of H_2 bobbles that helps the desorption of dye molecules. Three tests were performed and the regeneration percentages were 84%, 79% and 77%.

Considering that the adsorption is performed for water remediation, it was striking that the chemical cleaning requires water quantities that are greater than the initial treated quantity, while the electrochemical regeneration requires only about twenty millilitres of bicarbonate solution that can be used for several rounds. Moreover, the electrochemical regeneration showed better regeneration percentages and interesting simplicity regarding the experimental process. It can be concluded that the use of electrodeposited films in adsorption is advantageous by being quick, simple and effective for the regeneration from the solution.

References:

[1]   S. Sharafinia, A. Farrokhnia, E. Ghasemian, *Colloids Surfaces A Physicochem. Eng. Asp.* **2022**, *634* (December 2021), 128039. DOI: 10.1016/j.colsurfa.2021.128039.

[2]   Z. Meguellati, N. Ghemmit-Doulache, R. Brahimi, *Inorg. Chem. Commun.* **2023**, *157* (February), 111226. DOI: 10.1016/j.inoche.2023.111226.

[3]   B. Saha, A. Debnath, B. Saha, *J. Indian Chem. Soc.* **2022**, *99* (9), 100635. DOI: 10.1016/j.jics.2022.100635.

[4]   N. Ayshah, M. Azmier, T. Ubaidah, *Inorg. Chem. Commun.* **2023**, *153* (April), 110844. DOI: 10.1016/j.inoche.2023.110844.

[5]   M. Gun, H. Arslan, M. Saleh, M. Yalvac, N. Dizge, *Int. J. Environ. Res.* **2022**, *16* (2), 1–13. DOI: 10.1007/s41742-022-00399-5.

[6]   M. A. Nazir, T. Najam, S. Jabeen, M. A. Wattoo, M. Sohail, S. Shoaib, A. Shah, *Inorg. Chem. Commun.* **2022**, *145* (May), 110008. DOI: 10.1016/j.inoche.2022.110008.

[7]   M. A. Nazir, T. Najam, M. S. Bashir, M. S. Javed, M. A. Bashir, M. Imran, U. Azhar, S. Shoaib, A. Shah, A. Rehman, *Korean J. Chem. Eng.* **2022**, *39* (1), 216–226. DOI: 10.1007/s11814-021-0892-3.

[8]   A. Kheradmand, M. Negarestani, S. Kazemi, H. Shayesteh, *Sci. Rep.* **2022**, 1–17. DOI: 10.1038/s41598-022-19056-0.

[9]   J. Wang, W. Wang, Z. Ai, M. Li, H. Li, W. Peng, Y. Zhao, S. Song, *Appl. Clay Sci.* **2021**, *210* (May), 106153. DOI: 10.1016/j.clay.2021.106153.

[10]   Y. Zhang, C. Jing, J. Zheng, H. Yu, Q. Chen, L. Guo, D. Pan, N. Naik, Q. Shao, Z. Guo, *Colloids Surfaces A Physicochem. Eng. Asp.* **2021**, *628* (July), 127279. DOI: 10.1016/j.colsurfa.2021.127279.

[11]   M. Chen, R. Bi, R. Zhang, F. Yang, F. Chen, *Colloids Surfaces A Physicochem. Eng. Asp.* **2021**, *617* (February), 126384. DOI: 10.1016/j.colsurfa.2021.126384.

[12]   M. S. A. A. Alazba, M. T. Amin, *Arab. J. Sci. Eng.* **2022**, *47* (5), 5613–5627. DOI: 10.1007/s13369-021-05576-w.

[13]   H. K. Yagmur, I. Kaya, *J. Mol. Struct.* **2021**, *1232*, 130071. DOI: 10.1016/j.molstruc.2021.130071.

[14]   S. Bhowmik, V. Chakraborty, P. Das, *Results in Surfaces and Interfaces*. **2021**, *3* (March), 100011. DOI: 10.1016/j.rsurfi.2021.100011.

[15]   M. Baysal, K. Bilge, B. Yılmaz, M. Papila, Y. Yürüm, *Biochem. Pharmacol.* **2018**. DOI: 10.1016/j.jece.2018.02.020.

[16]   A. S. A. Ahmed, M. M. S. Sanad, A. Kotb, A. N. R. M. Negma, M. H. Abdallaha, *Mater. Adv.* **2023**. DOI: 10.1039/d3ma00226h.

[17]   M. El Haddad, *J. Taibah Univ. Sci.* **2016**, *10* (5), 664–674. DOI: 10.1016/j.jtusci.2015.08.007.

[18]   L. D. L. Miranda, C. R. Bellato, M. P. F. Fontes, M. F. de Almeida, J. L. Milagres, L. A. Minim, *Chem. Eng. J.* **2014**, *254*, 88–97. DOI: 10.1016/j.cej.2014.05.094.

[19]   G. Tchanang, C. N. Djangang, F. Abi, D. Laure, M. Moukouri, G. Trésor, N. Djabo, J. M. Kepdieu, P. Blanchart, *Ann. Civ. Environtal Eng.* **2022**, *6*, 008–018. DOI: 10.29328/journal.acee.1001034.

[20]   G. H. Al-hazmi, H. A. Saad, M. S. Refat, A. M. A. Adam, *Crystals*. **2022**, *12*, 1355.

[21]   S. Merrad, M. Abbas, M. Trari, *Fibers Polym.* **2023**, *24* (3), 1067–1081. DOI: 10.1007/s12221-023-00025-x.

[22]   M. El-Kammah, E. Elkhatib, E. Aboukila, *Inorg. Chem. Commun.* **2022**, *146* (September), 110062. DOI: 10.1016/j.inoche.2022.110062.

[23]   N. Ghemmit-Doulache, H. Khireddine, D. S. Salah, *J. Environ. Sci. Eng.* **2011**, *5*, 10.

Chapter V
Application in Sensors

V. 1. Metronidazole

Metronidazole (MNZ) is an antibiotic from the group of nitroimidazole [1,2] commonly used as an antibacterial and anti-inflammatory drug [3]. However, the use of this antibiotic generates a serious spread of wastewater which effect human health and the environment. Due to this, it is mandatory to develop a quantitative techniques for the detection of MNZ [4].

V. 2. Electrochemical characterization

Recently, a great focus is concerned with the electrochemical investigation of modified electrodes to assess the electron transfer properties. Herein, the CV curves of G/MF electrodes were recorded in PBS (pH=7)/KCl (0.1M) containing 0.5mM [Fe (CN)$_6$]$^{3-}$ with variation of the scan rate from 10mV/s to 200mV/s. The resulting voltammograms in **Fig.V.1.a** shows that the G/MF electrode exhibited an activity towards [Fe (CN)$_6$]$^{3-/4-}$ redox couple. It is possible to calculate the electroactive surface area (A) of the working electrode using Randles-Sevcik equation [5–7]. For 5.0 mM [Fe (CN)$_6$]$^{3-}$, D is equal to 7.6×10^{-6} cm^2 s^{-1} [8]. From the slope of I$_p$ versus the square root of the scan rate, and according to the above-mentioned equation, the calculated electroactive surface area of G/MF was 0.0156 cm^2 which represents 10% of the real surface area of the working electrode.
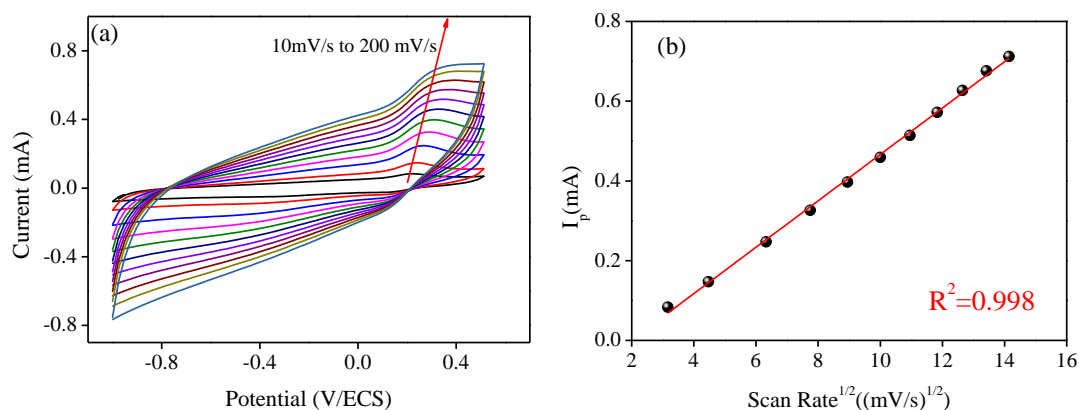
Figure V. 1. (a) CV of G/MF in PBS/KCl (0.1M) containing 0.5mM [Fe (CN)$_6$]$^{3-}$ with scan rate variation (10; 20; 40; 60; 80; 100; 120; 140; 160; 180; 200 mV/s) (b) Linear plot of I$_{pa}$ vs $\upsilon^{1/2}$

In order to determine the effectiveness of the MgFe-LDH modification of the graphite electrode, G and G/MF electrodes were first examined by CV in the blank solution (PBS). Generally speaking, the total current in CV plots incorporate the faradaic current (caused by faradaic reactions) and the non-faradaic current (capacitive current). In the absence of the analyte, only the background current caused by the capacitive behaviour of the double layer charging is registered [9,10]. As shown in **Fig.V.2,** the background current of G/MF electrode is higher than that of bare G electrode, which can be attributed to the increase of the active surface area, due to the fact that the surface area is proportional to the number and accumulation of positive and negative charged particles, thus the capacitive behaviour of the double layer increases when the active surface area increases [11].
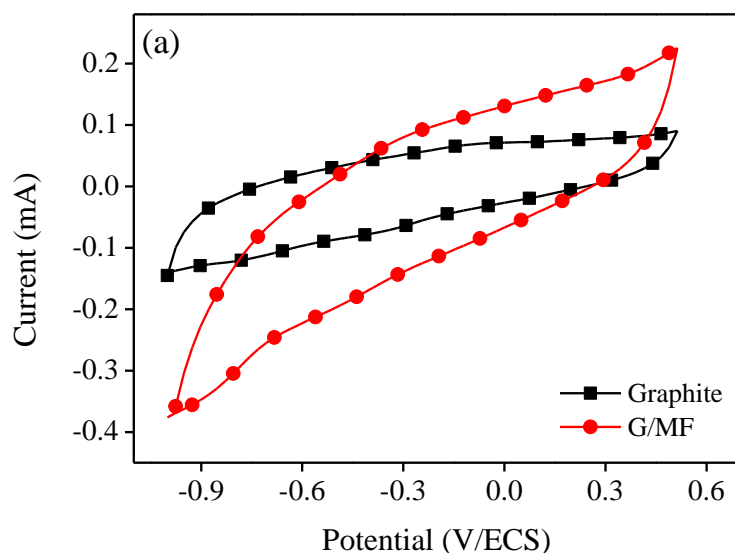
Figure V. 2. CV of G and G/MF electrodes (SR= 20 mV/s) and in PBS/KCl (0.1M) containing 0.5mM [Fe $(CN)_6]^{3-}/^{4-}$.
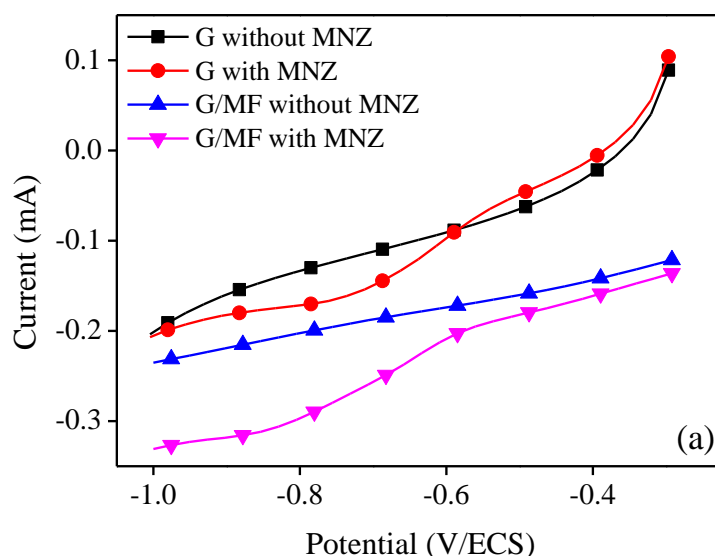
V. 3. Electrochemical detection of MNZ

To ensure the reduction of MNZ on the surface of G/MF electrode, the Linear Voltammetry (LV) was performed in the presence and the absence of 1.6mM MNZ. The curves of G/MF display a reduction peak at -0.7V in the presence of MNZ compared to its response in blank solution, which confirms that the peak is attributed to the reduction of MNZ as shown in **Fig V.3**.[12].

Furthermore, electrochemical performance of bare graphite G and G/MF electrode toward the detection of MNZ was examined. As shown in **Fig.V.4.**, the modification of the electrode increased the peak's current by 1.71 times compared to the unmodified graphite, this increase in current assumes that the use of MgFe-LDH to modify the graphite electrode may accelerate the electron transportation in the reduction of MNZ owing to the increase in the effectiveness of surface area by increasing electroactive sites. Hence, MgFe-LDH could be used as electrode modifier for the detection of MNZ.
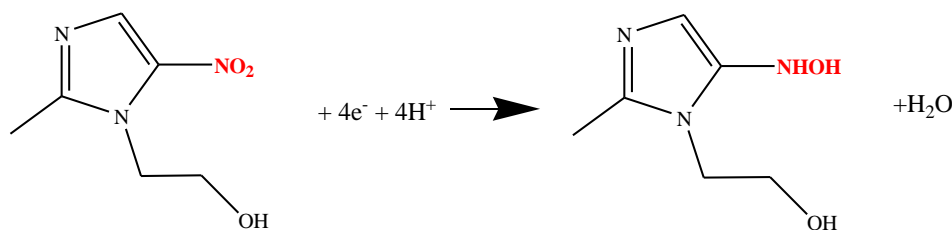
**Figure V. 3.** The reduction mechanism of MNZ

Figure V. 4. Linear voltammetry response in PBS (pH=7) (a) the presence and (b) the absence of MNZ(1.6mM).

V. 4. Effect of conditions parameters:

The electrochemical detection ability is highly effect by the experimental conditions; thus, it is mandatory to determine the optimal conditions for the best sensor performance. First of all, the influence of the pH of the medium was investigated using CV experiments over the pH range of 4.0 to 10.0 as shown in Fig. 6. (a-b). The reduction peak current increased by increasing the solution pH until reaching its maximum at the value 7, while the current showed lower values for higher pH. The peaks showed also a slight shift of the peak's potential (E_p) towards less cathodic potentials when the medium is more acidic which is due to the coexistence of protons involved in the reduction process [3,4,13].

The CV was then performed in PBS (pH=7) solution containing 1.6 mM MNZ in order to study the effect of scan rate (v) as shown in **Fig. V.5**.a The response showed that the reduction peak's current |i_p| increases and the peak's potential shifts toward more negative values with the increase in the scan rate, the curves presented only one reduction peak denoting that the reduction of MNZ is irreversible[4]. In the domine of 10 mV/s to 140 mV/s, the plot of (i_p) versus ($v^{1/2}$) yields a semi-linear relationship which proves that the reduction of MNZ over G/MF electrode is a half diffusion-controlled process. Moreover, the slope of (log i_p) versus (log v) has a great significant regarding the process's mechanism, a slope of 1.0 indicates adsorption-controlled process, a slope of 0.5 indicates diffusion-controlled process, and a slope between 0.5 and 1.0 indicates both diffusion and adsorption controlled one, in this case, the plot resulted in a linear relationship with a slope of 0.56 ($r^2 = 0.93$) which gives another evidence that the process is half adsorption half diffusion-controlled process [14].
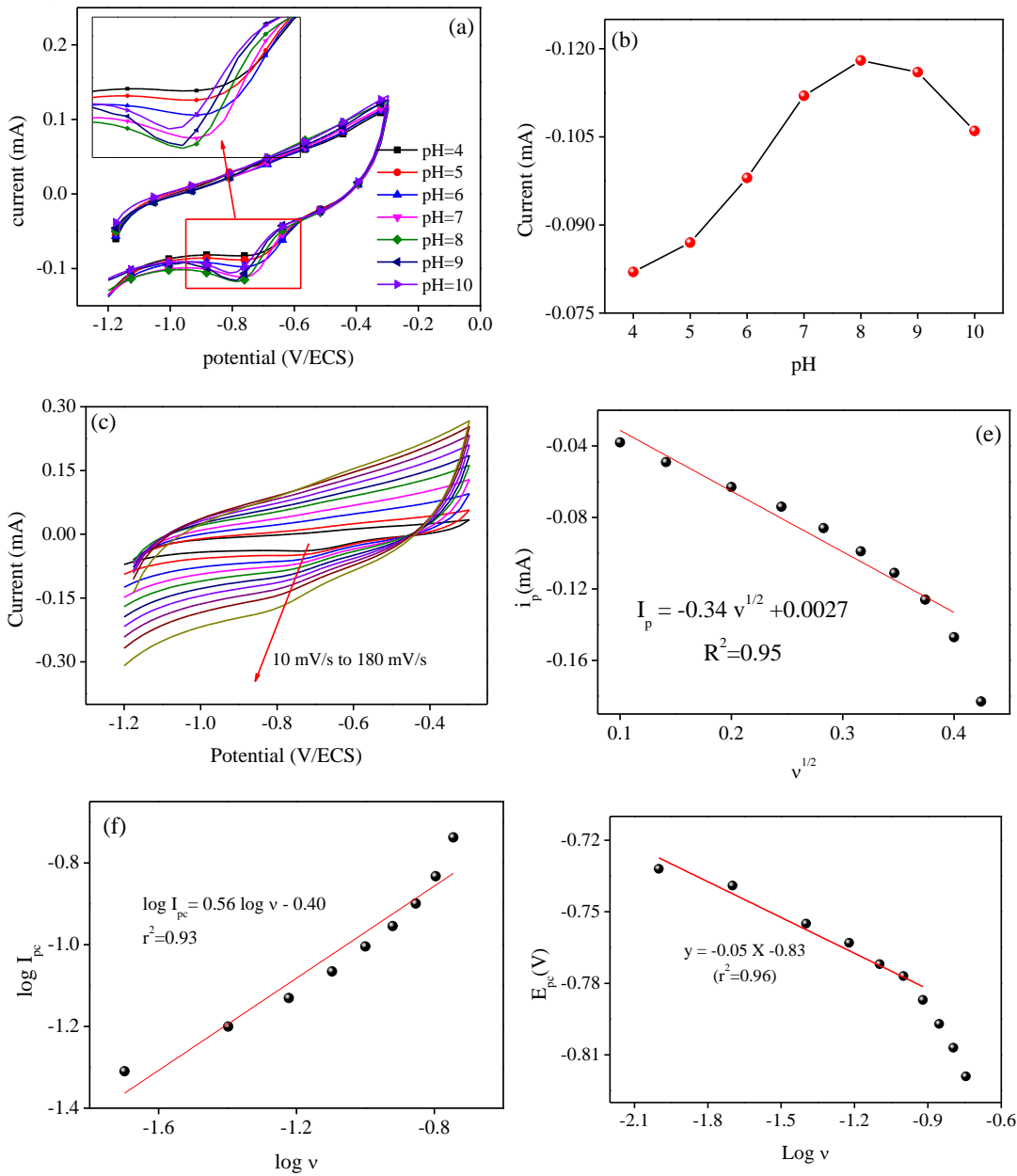
Figure V. 5. CV Response of 1.6 mM MNZ on a Graphite/MgFe-LDH in PBS: (a-b) effect of pH and (c-f) scan rate effect of (ν) (10; 20; 40; 60; 80; 100; 120; 140; 160; 180 mV/s).

Following the optimized conditions, the CV technique was used to assess the effect the analyte's concentration [MNZ] on the reduction peak. It is was clear that increasing the concentration induce an increase in the peak's current with an excellent linear response for MNZ. The calibration plot presented a linear relationship between i_p and [MNZ] following the equation $i_p=-0.039[MNZ]-0.070$ ($R^2=0.99$). The limit of detection (LOD) and the limit of quantification (LOQ) were calculated to be 0.74 mM and 2.4 mM, respectively (LOD = 3.3 S_b/m and LOQ = 10 S_b/m; where S_b is the standard deviation of the blank and m is the slope of the calibration curve) [15,16].
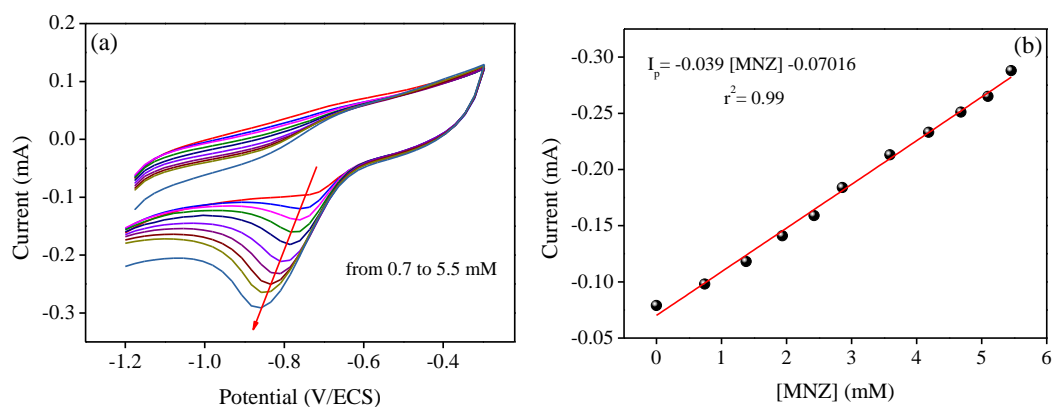
Figure V. 6. CV curves of MNZ with different concentrations in PBS (pH 8.0) (a) and the calibration curve of the cathodic peak current and the concentration of MNZ (b).

The repeatability of G/MF was studied by performing the previously described experiment for five rounds in PBS medium containing 1.6 mM MNZ. Analysing the results divulged a relative standard deviation of 3.99% confirming that the modified electrode displays a good repeatability.

Furthermore, the selectivity towards MNZ was investigated using chronoamperometry in order to visualize the effect of adding possible interfering compounds (Fusidate of Na^+; Spiramycin; Co^{2+}; Cr^{6+} and Hg^{2+}. Applying a potential of (E=-0.7V/SCE), it seems that the current response was not affected by adding the interferences, MNZ was the only molecules that perturbated the curve's current which means that the other molecules and ions do not interfere with the detection of MNZ, this can assume that the electrode has good selectivity for it.
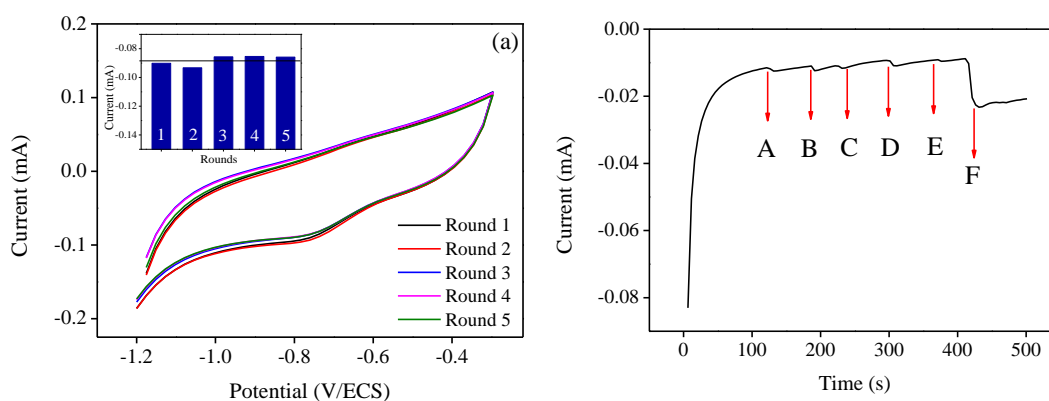
Figure V. 7. (a) Repeatability tests 1.6 mM MNZ in PBS (pH=7) and (b) chronoamperometry (E=-0.7V/SCE) to test the interferences effect (fusidate of Na^+(A); Spiramycin (B); Co^{2+} (C); Cr^{6+}(D); Hg^{2+}(E); MNZ(F))

References

[1]   R. Zokhtareh, M. Rahimnejad, G. Najafpour-Darzi, H. Karimi-Maleh, *Environ. Res.* **2023**, *216* (P3), 114643. DOI: 10.1016/j.envres.2022.114643.

[2]   P. K. Gopi, G. Kesavan, S. M. Chen, C. H. Ravikumar, *New J. Chem.* **2021**, *45* (6), 3022–3033. DOI: 10.1039/d0nj05501h.

[3]   X. Hu, Y. Zhang, T. Zeng, Q. Wan, K. Wu, N. Yang, *Diam. Relat. Mater.* **2022**, *128* (August), 109303. DOI: 10.1016/j.diamond.2022.109303.

[4]   K. Zhu, X. F. Chao, Y. Liu, Y. H. Luo, D. E. Zhang, *J. Solid State Chem.* **2022**, *314* (May), 123406. DOI: 10.1016/j.jssc.2022.123406.

[5]   H. Jin, J. Dong, X. Qi, X. Sun, M. Wei, B. He, Z. Suo, *Bioelectrochemistry*. **2023**, *149* (October 2022), 108312. DOI: 10.1016/j.bioelechem.2022.108312.

[6]   X. Zhang, J. Zhu, Z. Wu, W. Wen, X. Zhang, S. Wang, *Anal. Chim. Acta*. **2023**, *1239* (December 2022), 340743. DOI: 10.1016/j.aca.2022.340743.

[7]   J. Wang, *ANALYTICAL ELECTROCHEMISTRY*, 2nd ed., WILEY-VCH **2000**.

[8]   P. K. Kalambate, N. Larpant, R. P. Kalambate, W. Niamsi, V. Primpray, C. Karuwan, W. Laiwattanapaisal, *Sensors Actuators B Chem.* **2023**, *378* (December 2022), 133103. DOI: 10.1016/j.snb.2022.133103.

[9]   C. M. A. Brett, A. N. A. Maria, O. Brett, *ELECTROCHEMISTRY: Principles , Methods , and Applications*, OXFORD UNIVERSITY PRESS **1994**.

[10]   R. Pruna, M. Lópeza, F. Teixidor, *R. Soc. Chem.* **2019**, 276–284. DOI: 10.1039/c8nr07908k.

[11]   A. Tootoonchi, S. Saeed, H. Davarani, *J. ofThe Electrochem. Soc.* **2018**, (December 2019). DOI: 10.1149/2.0051805jes.

[12]   E. M. Materón, A. Wong, T. A. Freitas, R. C. Faria, O. N. Oliveira, *J. Pharm. Anal.* **2021**, *11* (5), 646–652. DOI: 10.1016/j.jpha.2021.03.004.

[13]   F. Rezaei, N. Ashraf, G. H. Zohuri, *Microchem. J.* **2023**, *185* (December 2022), 108260. DOI: 10.1016/j.microc.2022.108260.

[14]   H. A. M. Noureldin, A. M. Abdel-Aziz, M. M. Mabrouk, A. H. K. Saad, I. H. A. Badr, *RSC Adv.* **2023**, 844–852. DOI: 10.1039/d2ra06768d.

[15]   S. W. M. M. Carvalho, T. B. S. Santana, C. R. S. Matos, L. P. Costa, E. M. Sussuchi, I. F. Gimenez, *J. Braz. Chem. Soc.* **2019**, *30* (6), 1266–1275. DOI: 10.21577/0103-5053.20190021.

[16]   T. Madrakian, S. Alizadeh, M. Bahram, A. Afkhami, *Ionics (Kiel).* **2017**, *23* (4), 1005–1015. DOI: 10.1007/s11581-016-1871-2.

Conclusion and perspectives

Conclusion

The objective of this work was the elaboration of lamellar double hydroxide materials using different methods and their application in the environmental field. The first method was the traditional co-precipitation, which consist of the simultaneous precipitation of metal hydroxides ($M(OH)_2$ and $M(OH)_2^+$) by adding a base. While the second method incorporates electrochemical techniques (chronoamperometry) to enhance a reduction reaction of the species existing in the medium to increase the pH in the vicinity of the electrode and induce the electrodeposition of LDH thin films. The process is based on the formation of hydroxide ions on the surface of the electrode, which allows the formation of the film LDH[1].

Several physicochemical techniques were employed in order to assess the structural and morphological properties of the synthesised MgAl-LDH, MgFe-LDH, and CoAl-LDH. The XRD patterns reveal a total coordination of crystallised LDHs with a molar ratio of 3:1 in the rhombohedral R-3m crystal system. The FTIR spectra confirmed the existence of the characteristic with similar characteristic bonds in the three samples. The surface morphology was observed by scanning electron microscopy, which revealed a flower-like structure with nanoflakes and nanosheets on the surface of the clusters, while EDS analysis revealed the corresponding composition. The synthesised MgAl-LDH, MgFe-LDH, and CoAl-LDH were estimated to have surface areas of 65 $m^2.g^{-1}$, 51 $m^2.g^{-1}$, and 48 $m^2.g^{-1}$ using the N_2 adsorption/desorption isotherms. The thermogravimetric analysis (TGA/DTG) allowed for the determination of the weight loss stages. The electrochemical characterizations reported important characteristics such as the stability of the materials, their charge transfer phenomena. The electrosynthesis of MgAl-LDH and CoAl-LDH was carried out using chronoamperometry technic. The obtained results allowed to choose -1.2 V and 1200 s as the best conditions.

MgAl-LDH, MgFe-LDH, and CoAl-LDH were applied for the adsorption of Azocarmine G (ACG) as a target pollutant. Important parameters such as pH, adsorbent dosage, contact time, and initial concentration were optimised using the response surface methodology. The central composite analysis showed that the adsorption onto MgAl-LDH and CoAl-LDH fits better with the cubic model ($R^2=0.96$ and 0.97 respectively) while the adsorption onto MgFe-LDH showed a good fit with the quadratic model ($R^2=0.85$). The fitting of kinetic curves with different models revealed that all the systems follow the pseudo-second order with maximum experimental adsorption capacities (mg/g) of 105.9, 101.6 and 98.66 for MgAl-LDH, MgFe-LDH and CoAl-LDH respectively.

The investigation of isotherms proved that for MgAl-LDH and CoAl-LDH, Langmuir and D-R models exhibited the highest R^2, whereas for MgFe-LDH, it is Langmuir and Temkin that fitted best the adsorption process. Gibbs free energy was determined at different temperatures and found to be negative in all cases, thus confirming the spontaneity of the process, the energetic variations of the systems were anticipated by calculating the enthalpy values $\Delta H°$ (12.1 $KJ.mol^{-1}$, 25.1 $KJ.mol^{-1}$ and 51.15 $KJ.mol^{-1}$) and the entropy values $\Delta S°$ (43.8 $JK^{-1}.mol^{-1}$, 87.7 $JK^{-1}.mol^{-1}$ and 173.5 $JK^{-1}.mol^{-1}$). In order to identify the functional groups involved in the adsorption mechanism, FTIR was carried out on the materials at the end of the adsorption experiment. The obtained results propose that the retention of dye molecules is

governed in part by electrostatic forces between the positive charge of the lamellas and the negatively charged ACG molecules and, in another part, by hydrogen bonds with the OH⁻ of the lamellas.

The adsorption behaviour of the electrochemically synthesised MgAl-LDH electrodeposited on a stainless-steel electrode was tested, choosing bromophenol blue (BPB) as a target molecule. The effect of the experimental conditions, including the pH of the medium, the initial concentration of the dye, the dose of the adsorbent, and the contact ime, was also evaluated. The fitting of the kinetic curves revealed that the second-order model is the most suitable for the systems, with a correlation coefficient (R^2) of 0.999 and theoretical adsorption capacities closest to the experimental results (14.96 mg.g^{-1}). The calculations and the fittings of the isotherm models showed that the system follows the Langmuir model. The effect of temperature on the adsorption behaviour of the deposited films towards BPB was investigated and allowed to determine important thermodynamic parameters, mainly standard Gibbs free energy (ΔG^o from -2.632 to -0.462KJ.mol^{-1}), enthalpy change (ΔH^o = 18.227KJ.mol^{-1}) and entropy (ΔS^o = 66.56JK^{-1}.mol^{-1}).

The regeneration tests performed on the LDHs synthesised by coprecipitation showed regeneration percentages of 58.6%, 57.2%, and 54.0% for MgAl-LDH, MgFe-LDH, and CoAl-LDH respectively. The MgAl-LDH deposited film was also regenerated using electrochemical techniques by applying a fixed potential to the surface after adsorption. The tests revealed an average regeneration percentage of 80%. As a result, using powders results in extremely high adsorption capacities due to their massive surface areas, while the advantage of using electrodeposited films is that they are quick, simple, and effective for the regeneration from the solution.

MgFe-LDH powder synthesised via the co-precipitation method was used for the modification of graphite electrode (G/MF electrode). The modified electrode was then tested for the electrochemical selective detection of Metronidazole (MNZ) using cyclic voltammetry. When compared to the bare graphite electrode G, the cyclic voltammetry of the G/MF electrode revealed a noticeably higher peak current in the presence of MNZ. The developed sensor exhibited good performance in terms of sensitivity and selectivity. After the study of the effect of different conditions such as pH, scan rate, and medium electrolyte, G/MF was tested for the dependence of the peak on the concentration of MNZ; indeed, it showed a linear relationship between the peak's current I_p and the concentration [MNZ] with a detection limit of 0.74 mM.

Perspectives

The work carried out in this thesis could be promoted in various promising directions, thus offering the possibility of meeting major environmental challenges and providing innovative solutions in the field of environment, in particular:

- The synthesis of other verities of LDHs by varying the divalent and the trivalent metals and their molar ratio.
- The synthesis of LDH using other technics and comparison between their activities.
- The use of LDH as host materials and incorporation of active molecules in the intercalary space to increase their activity for specific applications.
- Study of the influence of synthesis conditions on the effectiveness of the LDHs.
- For the electrodeposition, the possibility of monitoring the PH during the electrodeposition process.
- The use of LDHs as adsorbent for the removal of other organic or inorganic pollutants.
- Enhance the adsorption process by imposing an electrochemical potential.
- The use of LDHs for the detection of other molecules.
- The application of LDH materials in other sectors such as biology, electrochemistry, energy stockage, medicine… etc.
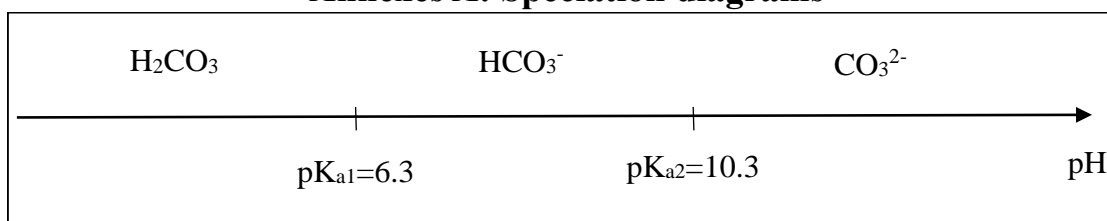
Annexes

Annexes A: Speciation diagrams

| H₂CO₃ | HCO₃⁻ | CO₃²⁻ |

$$H_2CO_3 \qquad HCO_3^- \qquad CO_3^{2-}$$

pK$_{a1}$=6.3   pK$_{a2}$=10.3   pH

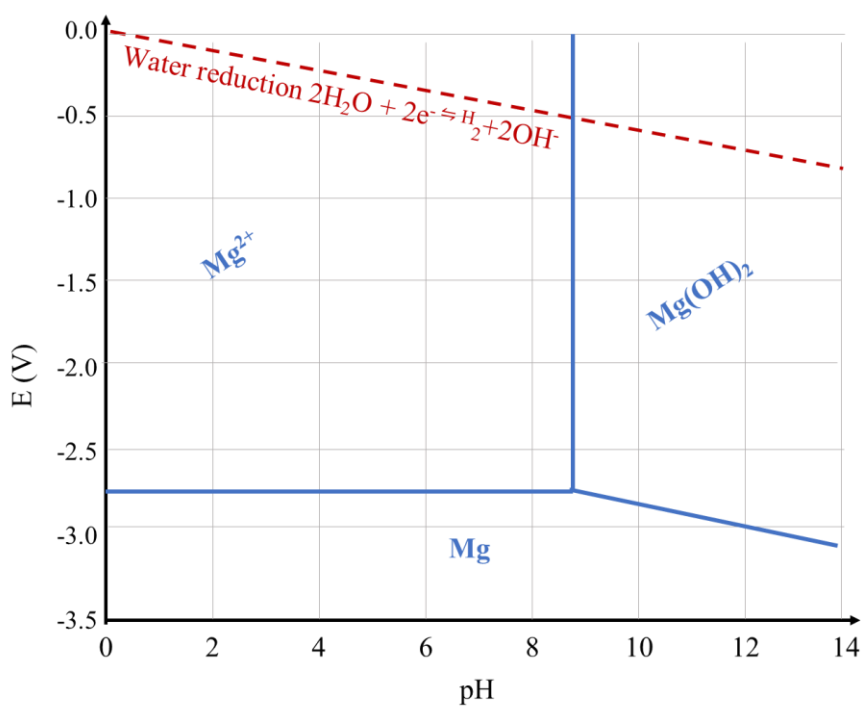**Figure A.1.** Speciation diagram of H_2CO_3

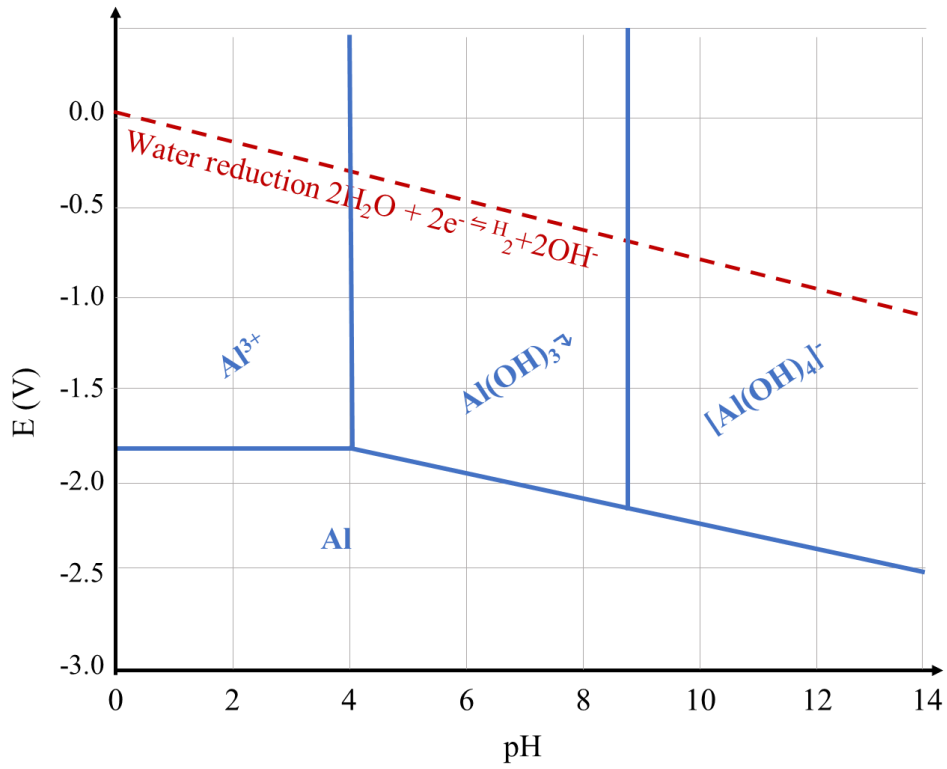**Figure A.2.** Speciation diagram of Magnesium

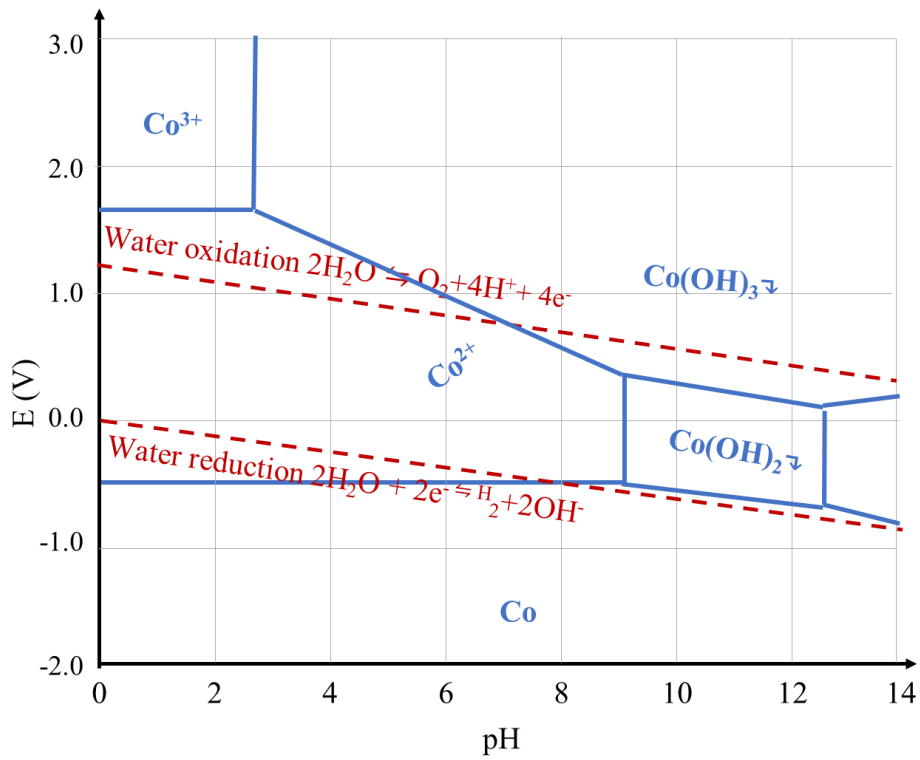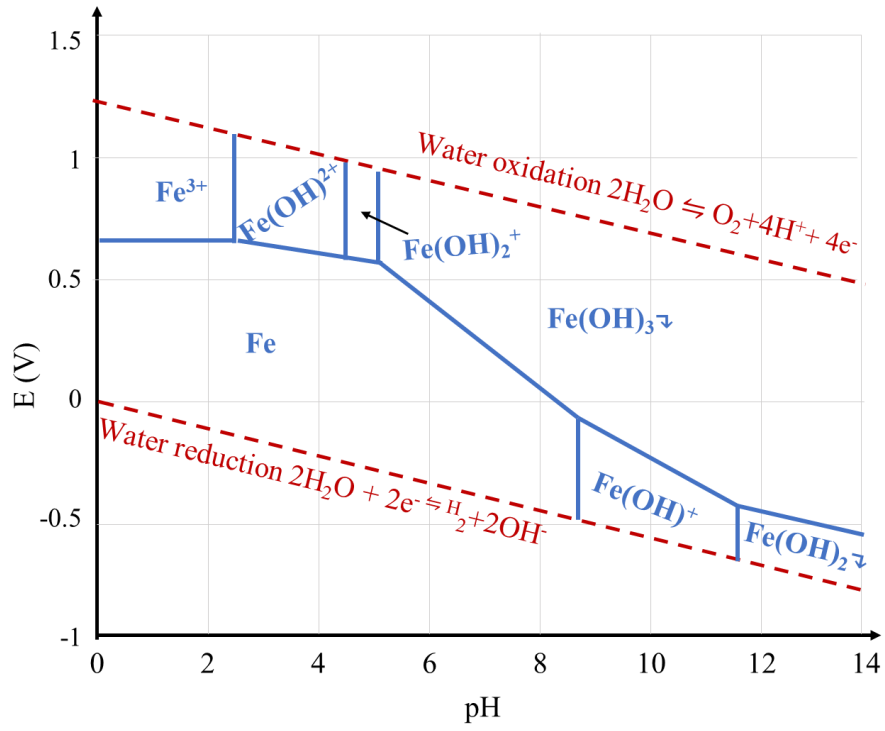**Figure A.3.** Speciation diagram of Aluminium

Figure A.4. Speciation diagram of Cobalt

Figure A.5. Speciation diagram of Iron

Annexes B : Materials and Methods
B.1. Electrochemical Methods
B.1.1. Linear sweep voltammetry

In this type of voltammetry, the current of the working electrode is measured when a potential between this electrode and the reference electrode is varied linearly with time. The curve of current as a function of potential obtained gives qualitative and quantitative information on the species studied by analysing the behaviour of the current and of potential of the peaks obtained.
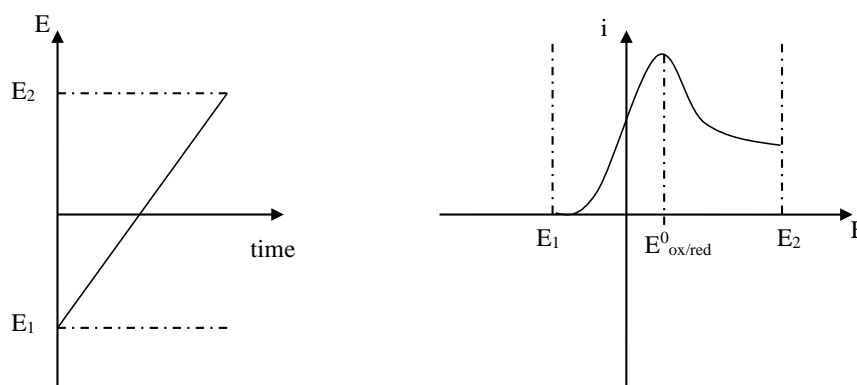

Figure B. 1. Principle graphs of a linear voltammetry

B.1.2. Chronoamperometry

Chronoamperometry is an electrochemical technique in which the potential applied to the working electrode is kept constant while the resulting current from the faradaic processes that occur at the electrode (caused by the potential step) is monitored as a function of time I=f(t).

According to Cottrel equation at a planar electrode, the current i (A) decays with time (t) as shown in **Eq.B.1**.

$$i(t) = \frac{nFACD^{1/2}}{\pi^{1/2}t^{1/2}} \tag{B.1}$$

where i is the current (A), A is the electroactive area (cm^2) and D is the diffusion coefficient in solution ($cm^2\ s^{-1}$).

B.1.3. Electrochemical Impedance spectroscopy

The term impedance refers to a quantity that includes the resistance, the capacitive reactance and the inductive reactance of an electrical system comprising elements of a different nature, it is an opposition force to electrical current in a circuit that is analogous to Ohm's law of resistance, Electrochemical Impedance Spectroscopy (EIS) relies on the measurement of the impedance characteristics of an electrical system at different frequencies of an applied perturbation [2].

Electrochemical impedance spectroscopy consists of superimposing on the voltage applied a sinusoidal voltage of low amplitude, generally of the order of 10 to 50 mV, between

the working electrode and the reference electrode, then analysing the response current, by varying the frequency for example in a range from 0.1 mHz to 100 kHz. The response obtained at high frequencies only accounts for fast phenomena and that at low, or even very low frequencies, of the entire process (fast and slow phenomena). It is thus possible to separate the various contributions of a reaction mechanism by their kinetics: stages of charge transfer, diffusion, adsorption, desorption [3].

The impedance can be expressed according to Ohm's law as:

$$Z = \frac{E_t}{I_t} = \frac{E_0 \sin(\omega t)}{I_0 \sin(\omega t + \phi)} = Z_0 \frac{\sin(\omega t)}{\sin(\omega t + \phi)} \qquad \textbf{B.2}$$

which can be represented as a complex number:

$$Z = \frac{E_t}{I_t} = Z_0 \exp(j\phi) = Z_0(cos\phi + jsin\phi) \qquad \textbf{B.3}$$

where Z is impedance (Ω), Z_0 is a magnitude, E_t is the potential at time t (V), I_t is the current at time t (A), ϕ is a phase shift, ω is a radial frequency (radians/s). $\omega = 2\pi f$, where f is frequency (Hz).

In practice, the current at each frequency is recorded by the potentiostat and transformed by a software using **Eq.B.2** to calculate the real and imaginary parts of the total impedance as presented in equation **Eq.B.3**

The Nyquist plot or the Bode plot can be used to display the EIS data. The Nyquist plot **(Fig. B.2.a)** is a graph that contrasts the real impedance (x-axis), which is always positive, with an imaginary impedance that is always negative. The phase angle or impedance magnitude (|Z|) is displayed against the frequency or frequency logarithm in the Bode plot (**Fig. B.2.b**). Typically, EIS data analysis involves fitting an equivalent circuit using software to comprehend what transpired in the under-investigation system, several electrical elements including resistor, capacitor, inductor, Warburg, and constant phase element (CPE), can be used in series or/and parallel to provide a complex equivalent circuit model.
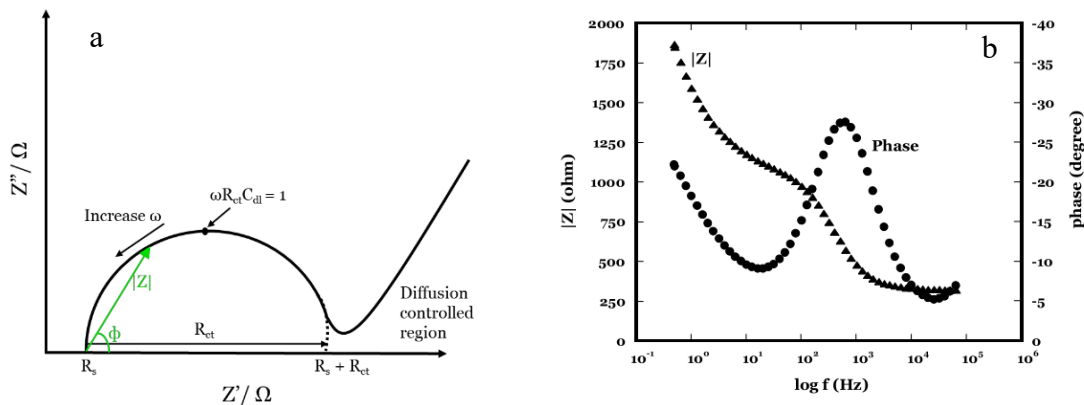
Figure B. 2. Nyquist plot of impedance spectra (a) and Bode plot of the impedance spectra (b)**.**

B.1.4. Cyclic Voltammetry

Cyclic voltammetry is a widely used electrochemical tool to learn about the thermodynamics of redox reactions, electron transfer kinetics, and coupled chemical reactions[4]. It consists of a linear sweep as a function of time of the potential from an initial value to a final value and vice versa (Fig. II.9) in the electrolyte in question, then measuring the variation in current. The resulting curve is the variation of current as a function of the applied potential. This technique was first discovered by the Czech scientist Jaroslav Heyrovsky 1920s. It mainly includes the variation of the potential (E) then the measurement of the current (I) flow through a working electrode submerged in a solution having an electroactive sample to be scrutinized. With the application of the required potential, a redox reaction takes place at the surface of the working electrode resulting from the flow of current [5].
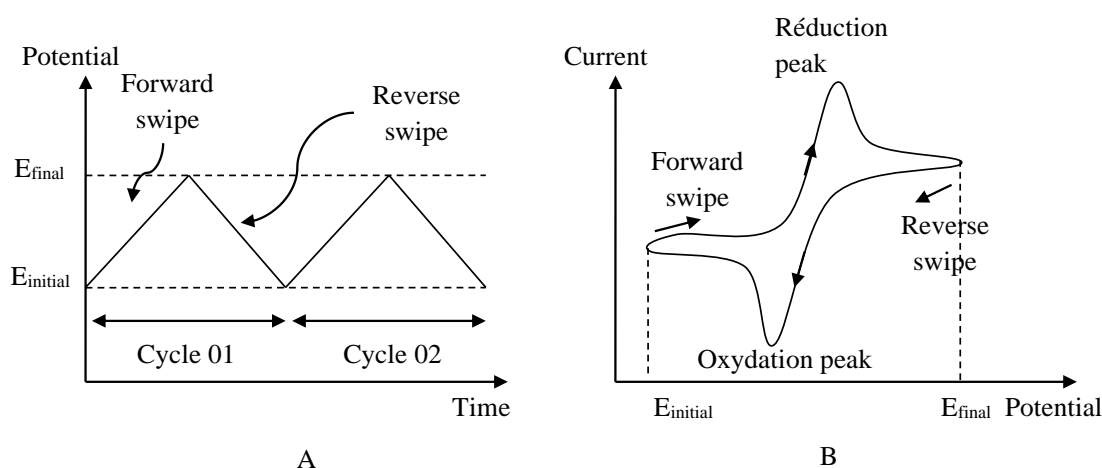
Figure B. 3. Process of cyclic voltammetry: A) variation of potential as a function of time; B) the shape of the curve of current as a function of the potential of a single cycle

Fick's law describes the relationship between the redox current and material flux at the solution–electrode interface where diffusion plays an important role (this current is also called the Faradaic current). On the other hand, Nerst or Butler–Volmer equations suggest that the concentrations of the redox species at the electrode surface are controlled by the potential applied and the rate of the reaction (ko) respectively. Accordingly, in a reversible electrochemical reaction given as Ox +ne⁻↔Red, the applied potential (E) forces the concentrations of Ox and Red at the electrode surface to a ratio following The Nerst equation:

$$E = E_0 + \frac{RT}{nF} Ln \frac{C_{Red}^0}{C_{Ox}^0}$$
$$\text{B.4}$$

The Butler-Volmer equation linking potential, concentration, and current is given by:

$$\frac{i}{nFA} = k^0 \{C_{Ox}^0 exp[-\alpha\theta] - C_{Red}^0 exp[(1-\alpha)\theta]\}$$
$$\text{B.5}$$

Where $\theta = nF \frac{(E-E^0)}{RT}$, k^0 is the heterogeneous rate constant, α is the transfer coefficient.

In the case of a reversible system, the anodic and cathodic peaks' currents (I_{pa} and I_{pc}) are identical, proportional to the concentration of electroactive species. They increase with the square root of the slew rate according to the following equation also known as the Randlès-Sevich equation:

$$I_p = 2.69 \times 10^5 AD^{1/2}n^{3/2}\gamma^{1/2}C \qquad \textbf{B.6}$$

where I_p is the peak current (A), D is the diffusion coefficient in solution ($cm^2\ s^{-1}$), and γ is the potential scan rate ($V\ s^{-1}$).

B.1.5.   Tafel plot

The region of kinetic control of electrochemical reactions is characterized by current densities that are exponential functions of potential, Tafel equations in which the current is an exponential function of potential are explained bellow[6].

When the overvoltage is very positive, the reduction current becomes negligible compared to the oxidation current, the polarization is said to be anodic.

$$i = i_a = i_{cor}(\exp\left(\frac{\alpha nF\eta_a}{RT}\right)) \qquad \textbf{B.7}$$

From this equation we can deduce β_a the anodic slope of Tafel:

$$\beta_a = \frac{2.3RT}{\alpha nF} \qquad \textbf{B.8}$$

And when the overvoltage is very negative, the anode component becomes non-existent, in this case the polarization is called cathodic.

$$-i = i_c = i_{cor}(\exp\left(\frac{\beta nF\eta_c}{RT}\right)) \qquad \textbf{B.9}$$

The slope of the cathodic branch of Tafel is given by:

$$\beta_c = \frac{-2.3RT}{\beta nF} \qquad \textbf{B.10}$$

β_a are β_c are the anodic and cathodic slopes of Tafel which makes it possible to determine Tafel's law and the polarization resistance:

$$|\eta| = (\alpha + \beta)log|i| \qquad \textbf{B.11}$$

$$R_p = \frac{1}{2.3}\left(\frac{\beta_a\beta_c}{\beta_a+\beta_c}\right)\frac{1}{i_{cor}} \qquad \textbf{B.12}$$

B.2.   Physicochemical methods
B.2.1.   X-Ray diffraction

The principle of the XRD method is the interaction of the matter with X-radiation of wavelength λ of the order of Å, this order is the same with the interatomic distances of the sample, the atoms reemit part of the incident beam in directions in space specific to the structure of the sample, if the latter is an ordered crystal. The diffraction cone of a single incident X-ray beam is formed after diffraction in the atomic planes of crystal structure (also called crystallographic plane hkl) as presented in **Fig.B.4** [7].
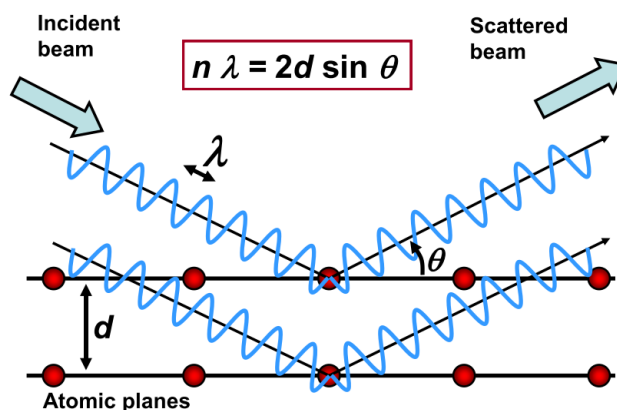
Figure B. 4. Schematic representation of the principle of X-ray diffraction [8]

The X-ray crystallographic analysis was carried out in order to identify the formed phases, to index the peaks and to calculate the lattice parameters by comparing them with those of the ASTM sheets taken from the X'pert HIGHSCORE

X-ray diffraction (XRD) analysis was performed using Panalytical diffractometer with a CuKα radiation. software. the average crystallite size (D_{cs}) is calculated from the broadening β_{sample} (rd) of the strongest peaks using Scherrer's equation [9,10].

$$D_{cs} = \frac{K\lambda}{\beta_{sample}\ Cos\theta} \qquad\qquad \textbf{B.13}$$

Where K is the crystal shape factor, λ is the wavelength of radiation and θ is the Bragg diffraction angle.

B.2.2.   Fourier Transformer Infra-Red

Fourier-transform IR (FTIR) spectroscopy is a characterization technique widely used in physics, chemistry, and biology. The fundamental principle of infrared (IR) spectroscopy is that most molecules absorb light in the infrared region of the electromagnetic spectrum, this absorption is then converted into molecular vibration. The bonds in the molecule that are present correspond precisely to this absorption. The infrared spectrum is viewed as the "chemical identity card of the molecule". This technic has the advantages of high spectral resolution, good signal-to-noise ratios, and the ability to measure a broad region of the spectrum in a short amount of time.

Speaking about the instrumentation (**Fig.B.5**), the Michelson interferometer is the main component in an IR spectrometer. A parallel beam of collimated light is directed towards a semitransparent beam splitter from a broadband source. A moveable mirror reflects one of the two beams, and a fixed mirror reflects the other beam. At the beamsplitter, the two beams are recombined. They then pass through the sample and strike a detector. The detector signal is proportional to the intensity of the interfered beam [11]. When the interferogram is Fourier trans- formed the resulting function is a plot of the spectrum in frequency space.

In this work, the chemical bonds were studied through Fourier transform infrared (FTIR) spectroscopy (Thermo scientific FTIR spectrophotometer) within the range of 4000-400 cm^{-1}, each LDH was used as a pellet containing 150 mg of KBr and 3 mg of the concerned powder
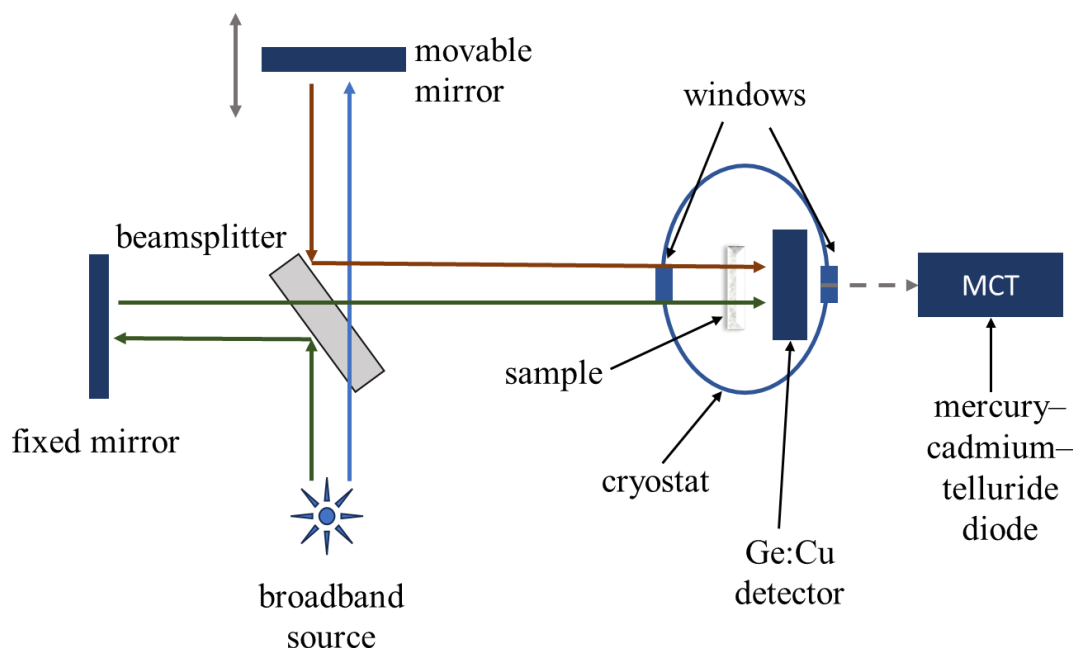
Figure B. 5. Schematic diagram of a FTIR spectrometer [11].

B.2.3.   Scanning Electron Microscope

The scanning electron microscopy (SEM) is a morphological technique that creates high resolution images for the sample surface by scanning it with a high energy stream of electrons, SEM provides information about surface morphology and composition of materials together with the energy-dispersive X-ray (EDX), which is a detecting technique that can generate more information about the sample. With SEM technique, many signals provide various information about a specific sample. For instance, while secondary electrons produce topographic data about the material, backscattered electrons produce pictures with contrast that contain information about the changes in atomic number. However, X-rays can also be employed as a signal to provide chemical information when SEM is coupled with an EDX detector.
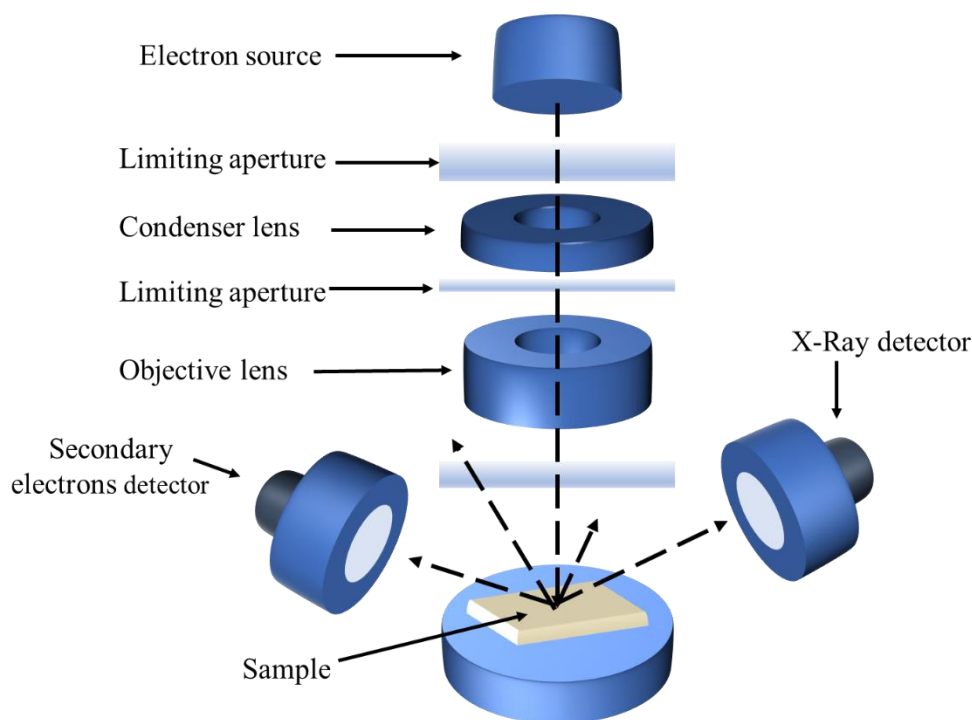
Figure B. 6. Schematic diagram of a SEM [11]

For the analysis of the prepared materials, JSM-7610F tungsten filament (W) coupled with Energy dispersive X-ray spectrometer was used to provide the morphology and determine the atomic percentage of the elements present in the material.

B.2.4. Thermogravimetric analysis

Thermogravimetric analysis (TGA) is a thermal analytical method that enables measurement of a sample's mass losses following various temperature-dependent decompositions in an inert or controlled environment. It enables the estimation of the range of thermal stability of materials as well as the temperatures related to chemical processes [12].

Based on the measurement of heat flow as a function of time, differential scanning calorimetry (DSC) analysis represents the amount of heat (Qp) proportionate to the temperature difference (T) between the sample and the reference. The measurement method entails precisely placing a predetermined mass of the sample into a crucible that is mounted on a measuring rod and placed inside of a furnace that contains a purging gas.
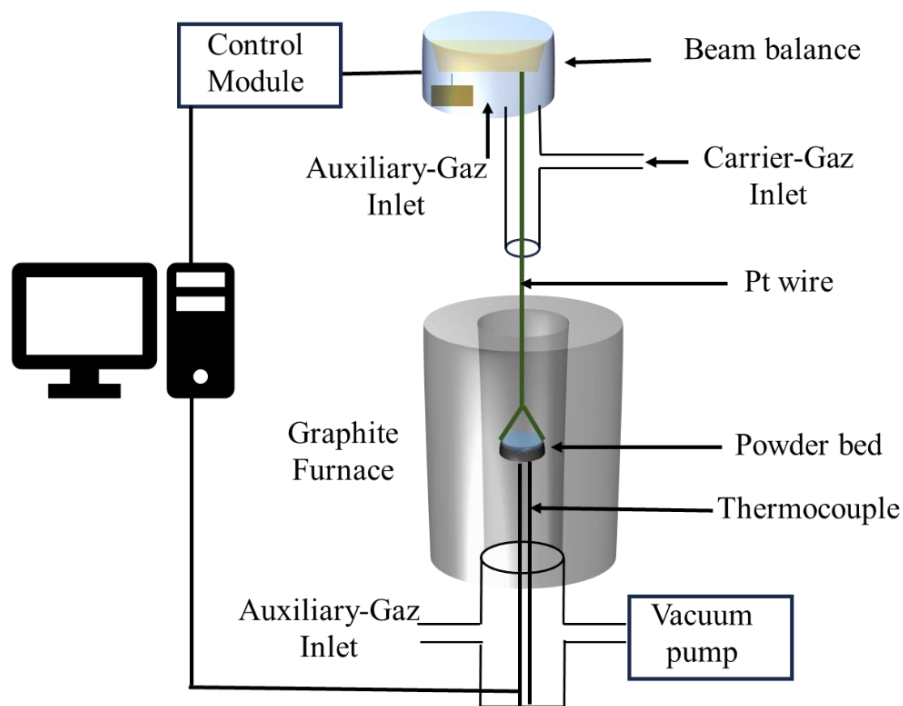
Figure B. 7. Schematic representation of the TGA technique [12].

Thermogravimetric and Differential Thermal Analysis (TGA/DTA) were carried out using an SDT Q600 V20.9 thermal analyzer system whose temperature is scanned from 32 °C to 575 °C in the presence of N_2 gas with a heating rate of 10 °C/min.

B.2.5. N_2 adsorption isotherm

The standard method used for the determination of the internal specific surface is by the adsorption of a gas (nitrogen) at low temperature, then the application of the isotherm of Brunauer-Emmett-Teller (BET) [13]. This model assumes that the adsorption is multilayer on a non-porous grain of the adsorbent without interaction between the adsorbate and the adsorbent. The volume of gas adsorbed in a monolayer V_m (volumetric method) is determined from the linear form given by equation II.3, the slope of which is $\frac{C-1}{C\,V_m}$ and the intercept is $\frac{1}{V_m C}$.

$$\frac{P/P_0}{V(1-P/P_0)} = \frac{1}{V_m C} + \frac{C-1}{C}\frac{P/P_0}{V_m}$$
 B.14

The determination of the specific surface and the total pore volume can be carried out from the adsorption branch. Using the area occupied by an adsorbed gas molecule (S_{N_2} = 0.162 nm^2), it is possible to estimate the specific surface area of the material (S_{BET}) from equation II.7 as follows:

$$S_{BET}(m^2/g) = \frac{6.022*10^{23}}{22414} V_m * \sigma_m$$
 B.15

To calculate the various structural parameters, it is necessary to introduce the conversion density factor, which is calculated using the following relationship:

$$Conversion\ factor_{(gaz-liquide)} = \frac{M}{\rho\,V_m} = \frac{28}{0.808} \times \frac{1}{22400} = 0.001547 \qquad \text{B.16}$$

The total pore volume V_t is determined, from the adsorption isotherm, at saturation by multiplying the value of the volume at (P/P$_0$) ~1 by the conversion coefficient as indicated below:

$$V_t = 0.001547 \times V_{(P/P_0)\sim1} \qquad \text{B.17}$$

The porous distribution is obtained using the t-plot method, which consists of comparing two materials of identical origin, one is non-porous and the other porous. This method makes it possible to establish a relationship between the volume of adsorbed nitrogen and the thickness of the adsorbed nitrogen layer (Å), according to the following equation:

$$t = \left(\frac{13.99}{0.034 - \log\left(\frac{p}{p_0}\right)} \right)^{0.5} \qquad \text{B.18}$$

The microporous volume and the surface of the mesopores by plotting the curve $V_a = f(t)$, the microporous volume of which is determined by multiplying the ordinate at the origin by the conversion factor:

$$V_{mic} = Conversion\ factor_{(gaz-liquide)} \times intercept \qquad \text{B.19}$$

As for the external surface, it is calculated using the same straight line from the following relation:

$$S_{ext} = 0.001547 \times 10^3 \times slope \qquad \text{B.20}$$

The distribution of pore diameters as a function of pore volumes was estimated from the adsorption isotherm using the BJH method.

The specific surface area measurements of the catalysts are calculated by the BET method (Brunauer, Emmet, Teller) from the quantity of nitrogen adsorbed at 77 K using micromeritics Gemini VII.

B.2.6. Point of zero charge determination

In a material, the positive and negative charges of the atoms are arranged in such a way that each charge compensates for the other. On the other hand, on the surface of the grains, this distribution is disturbed and the charges must be compensated by other ions. In an aqueous medium, protons neutralize negative charges and hydroxide ions neutralize positive charges. We find ourselves with a surface covered with OH$^-$ groups which undergoes protonation or deprotonation as follows:

$$\equiv\text{S-OH} + \text{H}^+ \leftrightarrow \equiv\text{S-OH}_2{}^+ \qquad \text{B.21}$$

$$\equiv\text{S-OH} \leftrightarrow \equiv\text{S-O}^- + \text{H}^+ \qquad \text{B.22}$$

In this equation, ≡S-OH represents the surface of the material. From the equation, the surface is predicted to be positive at low pH, and negative at high pH. There is a value in which the charge of the surface is equal to zero, this point is called point of zero charge pHpzc.

Annexes C : illustrations

Figure C.1. Synthesised MgAl-LDH, MgFeLDH, and CoAl-LDH before and after adsorption of ACG
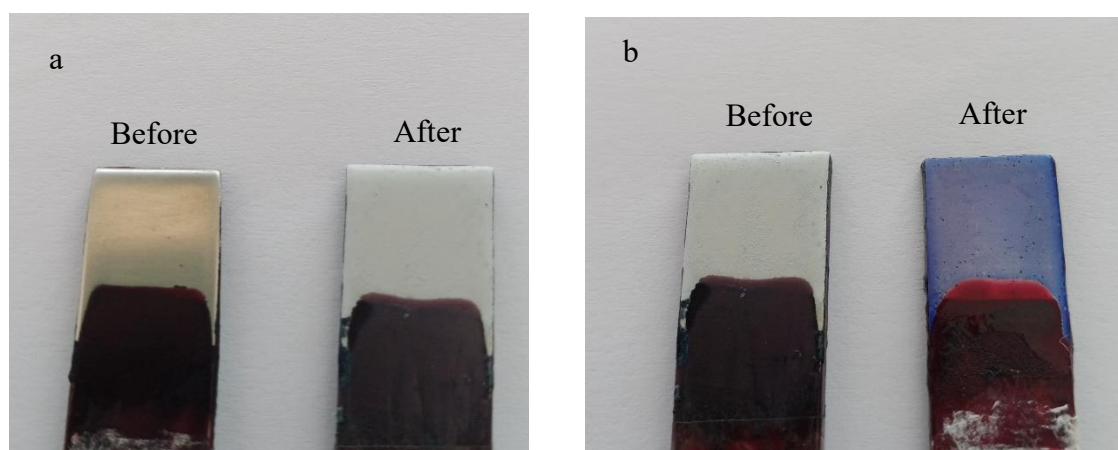
Figure C.2. Stainless steel electrode before and after electrodeposition of MgAl-LDH (a); MgAl-LDH deposit before and after adsorption of BPB

References

[1] M. Monti, P. Benito, F. Basile, G. Fornasari, M. Gazzano, E. Scavetta, D. Tonelli, A. Vaccari, *Electrochim. Acta*. **2013**, *108*, 596–604. DOI: 10.1016/j.electacta.2013.06.143.

[2] E. Barsoukov, J. R. Macdonald, *Impedance Spectroscopy: Theory , Experiment , And*, 2nd ed., Wiley, John And Sons **2005**.

[3] C. M. A. Brett, **2022**.

[4] J. Wang, *ANALYTICAL ELECTROCHEMISTRY*, 2nd ed., WILEY-VCH **2000**.

[5] J. G. Manjunatha, *Electrochemical Sensors Based on Carbon Composite Materials: Fabrication, Properties and Application*, IOP Publishing, London **2022**.

[6] M. E. Orazem, B. Tribollet, *Electrochemical Impedance Spectroscopie*, WILEY, Pennington **2008**.

[7] Q. Shen, Z. Liu, Y. Hua, J. Zhao, W. Lv, A. U. H. Mohsan, *Materials (Basel)*. **2018**, *11* (6), 1015. DOI: 10.3390/ma11061015.

[8] S. Nasir, M. Z. Hussein, Z. Zainal, N. A. Yusof, S. A. Mohd Zobir, I. M. Alibe, *BioResources*. **2019**, *14* (1), 2352–2388. DOI: 10.15376/biores.14.1.Nasir.

[9] N. E. H. Hadj-Abdelkader, A.-P. Beltrao-Nunesa, F. Belkhadem, N. Benselka, R. Roy, A. Azzouza, *Appl. Clay Sci.* **2020**, *198*, 105829. DOI: 10.1016/j.clay.2020.105829.

[10] A. F. da Silva, J. L. da S. Duarte, L. Meili, *Sep. Purif. Technol. 264*. **2021**, *264*, 118353. DOI: 10.1016/j.seppur.2021.118353.

[11] M. D. Mccluskey, *Appl. Phys. Rev.* **2013**, *87* (8), 3593. DOI: 10.1063/1.372453.

[12] P. Li, L. Teng, M. I. N. Guo, M. E. I. Zhang, S. Seetharaman, *Metall. Mater. Trans. B*. **2012**, *43B* (April), 406. DOI: 10.1007/s11663-011-9611-5.

[13] M. Zubair, H. A. Aziz, I. Ihsanullah, M. A. Ahmad, M. A. Al-Harthi, *Environ. Technol. Innov.* **2021**, *23*, 101614. DOI: 10.1016/j.eti.2021.101614.